NMR STUDIES OF THE HEAT SHOCK PROTEIN 90 N-TERMINAL DOMAIN

by

Reza M Salek

A thesis submitted in partial fulfilment for
the Degree of Doctor of Philosophy in the Faculty of Science
University of London

Department of Biochemistry and Molecular Biology
University College London
Gower Street
London
WC1E 6BT

ProQuest LLC
789 East Eisenhower Parkway
P.O. Box 1346
Ann Arbor, MI 48106-1346

For my Parents

زدانش به اندر جهان چیز نیست
تن مرده و جان نادان یکی است

فردوسی طوسی

"There is nought in the world better than knowledge,
Without this the lifeless body and ignorant soul are one"

Ferdowsi, Persian poet, 940 - 1020 A.D.

I would like to take this opportunity to thank my colleagues in the Ladbury research group. The foremost of these are Dr Mark Williams, whose guidance and expertise have been invaluable, and my supervisor, Professor John Ladbury, for his enthusiasm throughout this project. Their endless patience and support has made my time at the UCL most enjoyable and productive.

I have been fortunate to work with many other colleagues who I will not easily forget. In particular, Arsen Petrovic, who I thank for the many insightful scientific discussions we have had over the years. I also thank Dr Matt Cliff for his critical reading of some sections of this manuscript. I would also like to thank Professor Lawrence Pearl and Dr Chris Prodromou from the Institute of Cancer Research for providing the plasmid and mutants used in experiments that are presented here.

I would also like to thank colleagues in the UCL/LICR NMR laboratory, especially Dr Paul Driscoll for the valuable discussions held during NMR group meetings. Dr Geoff Kelly from the MRC Biomedical NMR centre at The National Institute for Medical Research, Mill Hill, also deserves a special mention for all his help in running experiments using their 800 MHz Varian spectrometer.

Finally I would like to thank my family for their unfailing support and encouragement throughout the course of my PhD, especially that of my wife Soheila, who always found the time and resources to support me.

The Hsp90 based chaperone is a ubiquitous protein-folding system in the cytoplasm of eukaryotes. Several signal transduction systems and cell cycling pathways utilise an interaction with Hsp90 as an essential component. The Hsp90 chaperone is an ATP dependent chaperone, which is active as a dimer. The N-terminal domain of Hsp90 itself has very weak ATPase activity and plays an essential role in the mechanism of dimerisation.

This study attempts to elucidate the nucleotide binding effects on the Hsp90 N-terminal domain by NMR. Accomplishing backbone assignments of the apo- and AMP-PNP bound forms provided a system for which individual residues could be investigated. About 200 backbone amide peaks in the $^{1}H^{15}N$ HSQC were observed out of a reported 207 residues for the Hsp90 N-terminal domain. Out of these, 192 for the apo- and 182 for the AMP-PNP bound forms were assigned. Assignments were also obtained for the HN, N, Cα, Cβ and CO nuclei. Comparison of apo and AMP-PNP HSQC spectra showed large shift differences in areas where the nucleotide binds and in a conserved loop, which has been proposed to act as a lid to the active site. The chemical shift pattern of the AMP-PNP bound form compared to that of the ADP bound form showed a different local environment for at least 30 residues, suggesting that different nucleotide bound conformations are more than just nucleotide structural differences. Analysing the NMR results suggests that binding of AMP-PNP to the Hsp90 N-terminal domain is not sufficient to cause lid closure as previously thought.

Relaxation studies highlighted regions that had different local motions in the apo- and nucleotide bound form based on individual residues within the Hsp90 N-terminal domain. The protein rotational correlation time was measured at 12.5 ns in the apo and 14 ns in the AMP-PNP bound form. No interaction between the labelled N-terminal domain and non-labelled middle domain of Hsp90 was observed. The antibiotic, novobiocin, which inhibits other members of the GHKL superfamily, was also shown not to bind to the N-terminal domain, consistent with previous studies. The study of two mutants, A107N and T101I, showed the effects of mutation in the lid region of the N-terminal domain causing chemical shifts of between 20-30 residues. Neither of these two mutants were able to bind AMP-PNP. In all nucleotide bound X-ray crystal structures solved to date, no difference between the ADP and ATP bound forms has been observed and only one conformation was found. The results presented here suggest that the structure in solution is much more variable than previously envisaged.

Table of Contents

	Page
Title	**I**
Dedication	**II**
Quotation	**III**
Acknowledgements	**IV**
Abstract	**V**
Table of Contents	**VI**
List of Figures	**IX**
List of Tables	**XVI**
Abbreviations	**XIX**
Amino acid abbreviations	**XX**
Chapter 1. Introduction	**1**
1.1 Molecular chaperone classification	**2**
1.2 The 90-kDa molecular chaperone family	**4**
1.3 Functions of Hsp90	**5**
1.3.1 Hsp90 as a part of the chaperone machinery in cytosol	**6**
1.3.2 Hsp90 interaction with substrates	**7**
1.3.2.1 Hsp90 partner proteins	**9**
1.3.3 Hsp90 as a capacitor for morphological evolution	**12**
1.4 Hsp90 domains and characterisation	**13**
1.4.1 The structure of the N-terminal domain of Hsp90	**16**
1.4.1.1 Nucleotide (ATP/ADP) interaction with the Hsp90 N-terminal domain.	**16**
1.4.1.2 Comparison of Geldanamycin (GM) to the nucleotide bound to the N-terminal domain	**20**
1.4.2 The ATPase cycle mechanism and activity of the N-terminal domain (the lid hypothesis)	**22**
1.4.2.1 Hsp90 homologues	**23**
1.4.2.2 Mutation studies of the Hsp90 N-termini	**28**
1.4.3 Residues involved in dimerisation and the role of the middle domain	**29**
1.5 Kinetic studies of Hsp90 and its N-terminal domain	**32**
1.6 Aims of this research	**34**
Chapter 2. Materials and Methods	**35**
2.1. Transformation and purification	**36**
2.1.1 The expression system	**36**
2.1.2 Preparation of $CaCl_2$ competent cells	**37**
2.1.3 Transformation	**38**
2.1.4 Plasmid purification	**38**
2.2 Expression of the Hsp90 N-terminus in Minimal Media	**39**
2.3 Expression of the Hsp90 N-terminus in LB media	**40**
2.4 Expression of the Hsp90 N-terminus in ^2H_2O	**41**
2.5 Purification of the Hsp90 N-terminus	**41**

2.6 Protein concentration measurements **43**
2.7 Buffer screening **45**
2.8 Acquiring nuclear magnetic resonance (NMR) spectra **48**
2.8.1 Spectra recorded for single and double labelled protein samples **48**
2.8.2 Spectra recorded for the apo and AMP-PNP bound backbone assignment using a triple labelled sample **49**
2.9 Processing NMR data **51**
2.10 Relaxation experiments **51**
2.10.1 Acquiring and processing the $^{15}NT_1$, $^{15}NT_2$, $^{15}N\{^1H\}$ heteronuclear-NOE relaxation experiments **51**
2.10.2 Calculating the R_1 and R_2 auto - relaxation rates **54**
2.10.3 Calculating the $\{^1H\}$-^{15}N heteronuclear NOE cross - relaxation rates **55**
2.10.4 Calculating the isotropic rotational correlation time **55**
2.11 Measuring translational diffusion coefficients using one-dimensional ^1H NMR **56**
2.12 Titration by NMR **57**

Chapter 3. The sequential backbone assignment of the Hsp90 N-terminal domain **60**

3.1 Chapter overview **61**
3.2 One-dimensional experiments **62**
3.3 Two-dimensional ^1H-^{15}N Heteronuclear Single Quantum coherence (HSQC) experiments **64**
3.4 Sequential assignment using single and double labelled samples **66**
3.4.1 Three-dimensional HNCA **69**
3.4.2 Three-dimensional HN(CO)CA **71**
3.4.3 Three-dimensional NOESY HSQC **74**
3.4.4 Three-dimensional HN(COCA)HA **75**
3.4.5 Three-dimensional TOWNY HSQC **77**
3.5 Assignments of the double-labelled N-terminal sample and preparation for expression in D_2O **78**
3.6 Deuterium labelling strategies **80**
3.7 Resonance assignment of the Hsp90 N-terminal domain using a ^2H,^{13}C,^{15}N-labelled sample **84**
3.7.1 A three-dimensional HNCA spectrum for the ^2H,^{13}C,^{15}N-labelled sample **84**
3.7.2 A three-dimensional HN(CO)CA spectrum for the triple-labelled sample **85**
3.7.3 A three-dimensional HN(CA)CB experiment **89**
3.7.4 A three-dimensional HN(COCA)CB experiment **90**
3.7.5 A three-dimensional HNCO experiment **93**
3.7.6 A three-dimensional HN(CA)CO experiment **95**
3.8 Sequential connection and assignment of the resonances **97**
3.9 Secondary structure prediction using nuclei chemical shifts **114**
3.10 Chapter summary **118**

Chapter 4. Dynamic studies of the Apo Hsp90 N-terminal domain using relaxation experiments 120

4.1 Chapter overview **121**
4.2 Analysis of the $^{15}NT_1$ and $^{15}NT_2$ **122**
4.3 Analysis of the $\{^1H\}$-^{15}N heteronuclear NOE **125**
4.4 Calculation of the isotropic correlation time (τ_c) of the Hsp90 N-terminal domain **129**
4.5 Measurement of the translational diffusion coefficient **134**
4.6 Temperature titration **141**
4.7 Chapter summary **146**

Chapter 5. Nucleotide Binding Studies 147

5.1 Chapter overview **148**
5.2 Titration of Mg^{2+} **149**
5.3 Comparison of apo- and ADP/ATP bound spectra in phosphate buffer **152**
5.4 ATP time course titration in Tris buffer **154**
5.5 Nucleotide bound spectra in Tris buffer recorded at 25°C **158**
5.6 The backbone assignment of the Hsp90 N-terminal domain bound to AMP-PNP **161**
5.7 Chemical shift difference of the apo- and AMP-PNP bound spectra **181**
5.8 Secondary structure prediction using chemical shifts **187**
5.9 Relaxation studies of the AMP-PNP bound Hsp90 N-terminal Domain **193**
5.10 Chapter summary **200**

Chapter 6. Applications of backbone assignments 202

6.1 Chapter overview **203**
6.2 Titration of novobiocin **203**
6.3 Investigating the interaction of the middle domain (T560) construct with the N-terminal domain of Hsp90 **203**
6.4 Investigating the 'ATP-lid' using mutants of the Hsp90 N-terminal domain **213**
6.5 Chapter summary **221**

Chapter 7. Discussion 222

7.1 Observations for residues 1 to 28 **227**
7.2 The second α-helix **228**
7.3 The first nucleotide binding pocket loop and its neighbouring secondary structures **230**
7.4 Observation for the third helix and second nucleotide binding pocket loop **231**
7.5 Future Perspectives **234**

Appendix Publications arising from this research **237**
References **240**

List of Figures

Page

Chapter 1:

Figure 1.1 Domain structure and dimer formation of Hsp90, induced by heat or presence of ATP **14**

Figure 1.2 Comparison of the nucleotide shapes in the Hsp90 N-terminal domain with other heat shock proteins and location of its binding in the crystal structure **17**

Figure 1.3. Schematic diagram of ADP interacting with the N-terminal domain of Hsp90 **18**

Figure 1.4. Two open and closed conformations of the human Hsp90 N-terminal domain with bound GM **20**

Figure 1.5 Schematic diagram of GM interacting with the N-terminal domain of Hsp90 **21**

Figure 1.6 Structural comparison of ATP binding domains of DNA gyrase, MutL and Hsp90 and EnvZ **24**

Figure 1.7 Comparison of the formation of the proposed lid in the GHKL superfamily **25**

Figure 1.8 Comparison of the monovalent binding site in BCK, MutL, GyrB, human Hsp90 and CheA **27**

Figure 1.9 Dimerisation of Hsp90 based on the DNA GyraseB model **31**

Chapter 2:

Figure 2.1 Single letter abbreviation of the amino acid sequence for 207 residues of the Hsp90 N-terminal domain from *S.Cerevisiae* **37**

Figure 2.2 A 12% Tris-Tricine SDS PAGE gel displaying aliquots collected during purification of the Hsp90 N-terminal **43**

Figure 2.3 A baseline corrected UV/Vis spectrum for the purified Hsp90 N-terminal **44**

Chapter 3:

Figure 3.1 A one-dimensional experiment of the Hsp90 N-terminal domain with DSS **63**

Figure 3.2 The $^{1}H^{15}N$ amide nuclei in a protein backbone structure recorded in the HSQC experiment **65**

Figure 3.3 A $^{1}H^{15}N$ HSQC spectrum of the N-terminal ATPase domain of yeast Hsp90 obtained at 800 MHz at 25°C **67**

Figure 3.4 Through bond heteronuclear coupling along the polypeptide backbone chain as used in multidimensional NMR experiments. **68**

Figure 3.5 The HN amide and Cα nuclei involved in the HNCA experiment in the protein backbone **69**

Figure 3.6 A $^{1}H^{15}N$ two-dimensional projection of the three-dimensional HNCA experiment **71**

Figure 3.7 Active nuclei recorded in an HN(CO)CA experiment and those used in the magnetisation transfer **72**

Figure 3.8 Sequential connection of the HNCA and HN(CO)CA experiments **73**

Figure 3.9 The protons detected in an NOE experiment **75**

Figure 3.10 Two slices of the three-dimensional NOESY-HSQC experiment in an ANSIG session **76**

Figure 3.11 The nuclei and coupling constants involved in the HN(COCA)HA experiment **77**

Figure 3.12 Two separate correlated window of an ANSIG session displaying the 3D^{15}NHSQC-NOESY, TOWNY-HSQC and HN(COCA)HA crosspeaks. **79**

Figure 3.13 Effect of perdeuteration on the two-dimensional $^{1}H^{15}N$ HSQC spectrum of the Hsp90 N-terminal domain. **82**

Figure 3.14 Comparison of $^{1}H^{13}C$ HSQC data from protonated and deuterated samples **83**

Figure 3.15 Comparison of the two-dimensional (^{13}Cα,NH) projections from three-dimensional HNCA spectra for a protonated and deuterated sample **86**

Figure 3.16 A two-dimensional (^{15}N,NH) projection of the three-dimensional HNCA experiment from protonated and deuterated samples **87**

Figure 3.17 A two-dimensional (^{13}Cα,NH) projection of the three-dimension HN(CO)CA spectrum **88**

Figure 3.18 A two-dimension (^{15}N,NH) projection of the three-dimension HN(CO)CA spectrum **88**

Figure 3.19 The nuclei and the coupling constants involved in the HN(CA)CB experiment **89**

Figure 3.20 A two-dimensional (^{13}Cβ,NH) projection of the three-dimensional HN(CA)CB spectrum **91**

Figure 3.21 A two-dimensional (^{15}N,NH) projection of the three-dimension HN(CA)CB spectrum **91**

Figure 3.22 The nuclei and the coupling constants involved in the HN(COCA)CB experiment **92**

Figure 3.23 A two-dimensional ($^{13}C\beta_{(i-1)}$,NH) projection of the three-dimensional HN(COCA)CB spectrum. **93**

Figure 3.24 The nuclei, direction of the magnetisation transfer and the coupling constants involved in the HNCO experiment **94**

Figure 3.25 A two-dimensional ($^{13}CO_{(i-1)}$,NH) projection of the three-dimensional HNCO spectrum. **94**

Figure 3.26 The nuclei, direction of the magnetisation transfer and the coupling constants involved in the HN(CA)CO experiment **96**

Figure 3.27 Two-dimensional ($^{13}CO_{(i)(i-1)}$,NH) projection of the three-dimensional HN(CA)CO spectrum **96**

Figure 3.28 A snapshot from an ANSIG session used for sequential assignment of the apo Hsp90 N-terminal domain **100**

Figure 3.29 Strip plots from the three-dimensional HNCA, HN(CO)CA, HN(CA)CB and HN(COCA)CB correlation spectra used for sequential assignment of apo Hsp90 N-terminal **101**

Figure 3.30 Strip plots from the three-dimensional HNCO and HN(CA)CO correlation spectra used for sequential assignment of apo Hsp90 N-terminal **102**

Figure 3.31 A $^{1}H^{15}N$ HSQC spectrum of Hsp90 N-terminal domain from a ^{15}N-labelled sample using a 800MHz proton frequency spectrometer recorded at 25°C **104**

Figure 3.32 Assigned residues plotted on the X-ray crystal structure of the Hsp90 N-terminal domain **106**

Figure 3.33 The graphic CSI output for consensus secondary structure prediction for the Hsp90 N-terminal domain **115**

Chapter 4:

Figure 4.1 Backbone NH ^{15}N R_1 relaxation of $^1H^{15}N$-labelled Hsp90 N-terminal at 25°C recorded at 600 MHz **123**

Figure 4.2 Backbone NH ^{15}N R_2 relaxation of $^1H^{15}N$-labelled Hsp90 N-terminal at 25°C recorded at 600 MHz **124**

Figure 4.3 Backbone NH $^1H^{15}N$ heteroneuclear NOE relaxation of $^1H^{15}N$-labelled Hsp90 N-terminal at 25°C recorded at 600 MHz **127**

Figure 4.4 The $^1H^{15}N$ Heteronuclear NOE values mapped on the X –ray crystal structure of the Hsp90 N-terminal domain **128**

Figure 4.5 Estimation of the correlation time **132**

Figure 4.6 Backbone NH ^{15}N R_2/R_1 ratios of the $^1H^{15}N$-labelled Hsp90 N-terminal at 25°C recoded at 600 Mhz **133**

Figure 4.7 Example of signal decay in one-dimensional diffusion experiments with decreasing gradient strength from a ^1H Hsp90 N-terminal domain sample **135**

Figure 4.8 Comparison of two parameter with three parameter data fitted using Equation 4.5 **137**

Figure 4.9 A linear fit of molecular weight versus the reciprocal of their translational diffusion coefficient to the 3rd power ($1/D_S^3$) **139**

Figure 4.10 The change in water viscosity at different temperatures **139**

Figure 4.11 NMR diffusion experiments carried out at temperatures ranging from 10°C to 35°C using a three-parameter fit of Equation 4.4 **140**

Figure 4.12 Temperature titration spectra from 10°C to 35°C for the Hsp90 N-terminal domain **143**

Figure 4.13 Superposition of the temperature titration from 5°C to 35°C for the Hsp90 N-terminal domain **144**

Chapter 5:

Figure 5.1 The $^1H^{15}N$ HSQC spectra recorded during different steps of Mg^{2+} titration **150**

Figure 5.2 The result of overlapping the HSQC spectra from the Mg^{2+} titration **151**

Figure 5.3 Comparison of apo-, ADP and ATP spectra in phosphate buffer **153**

Figure 5.4 Seven out of twelve ATP time course titration points, recorded as a series of HSQC spectra **156**

Figure 5.5 Superimposition of all twelve ATP time course titration points using a ^{15}N-labelled sample of the Hsp90 N-terminal domain **157**

Figure 5.6 Comparison of the AMP-PNP bound with the ADP bound spectrum **159**

Figure 5.7 Superimposition of the AMP-PNP bound with the ADP bound spectra **160**

Figure 5.8 Comparison of the AMP-PNP bound to the ATP bound spectrum carried out on the N-terminal domain of Hsp90 at 25°C **162**

Figure 5.9 Comparison of the ADP bound spectrum with the ATP bound spectrum **162**

Figure 5.10 The 2D (^{13}Cα,NH) projections from 3D HNCA spectra for a deuterated sample **165**

Figure 5.11 A 2D (^{13}Cβ,NH) projection of the 3D HN(CA)CB spectrum **165**

Figure 5.12 A 2D (^{15}N,NH) projection of the 3D HNCA experiment from the deuterated samples **166**

Figure 5.13 A 2D (^{15}N,NH) projection of the 3D HN(CA)CB spectrum **166**

Figure 5.14 A 2D ($^{13}CO_{(i-1)}$,NH) projection of the 3D HNCO spectrum from an AMP-PNP bound sample **167**

Figure 5.15 A 2D (^{15}N,NH) projection of the 3D HNCO spectrum from an AMP-PNP bound sample **167**

Figure 5.16 A 2D ($^{13}CO_{(i-1)}$,NH) projection of the 3D HN(CO)CA spectrum **168**

Figure 5.17 A 2D (^{15}N,NH) projection of the 3D HN(CO)CA spectrum **168**

Figure 5.18 The sequential backbone assignment of the AMP-PNP bound, Hsp90 N-terminal domain displayed using an 800 MHz proton frequency spectrum **170**

Figure 5.19 Comparison of $^{1}H^{15}N$ HSQC spectra recorded on a 500 and 800 MHz spectrometer on the same triple-labelled sample, from the Hsp90 N-terminal domain with AMP-PNP **171**

Figure 5.20 The ΔδNH of the apo- and AMP-PNP bound Hsp90 N-terminal domain extracted from the HSQC experiments **182**

Figure 5.21 The $\Delta\delta^{13}C$ of the apo- and AMP-PNP bound Hsp90 N-termianl domain from averaged $\Delta\delta^{13}C\alpha$, $\Delta\delta^{13}C\beta$ and $\Delta\delta^{13}CO$ **185**

Figure 5.22 Graphical representation of the CSI structure predication from apo- and AMP-PNP bound Hsp90 N-terminal domain compared to the X-ray crystal structure **191**

Figure 5.23 Residues predicted different using chemical shifts from apo- and AMP-PNP bound forms highlighted on the X-ray crystal structure of the Hsp90 N-terminal domain **192**

Figure 5.24 Backbone NH ^{15}N R_1 relaxation of $^1H^{15}N$-labelled Hsp90 N-terminal with AMP-PNP bound at 25°C **194**

Figure 5.25 Backbone NH ^{15}N R_2 relaxation of $^1H^{15}N$-labelled Hsp90 N-terminal with AMP-PNP bound at 25°C **195**

Figure 5.26 Backbone NH $\{^1H\}^{15}N$ heteronuclear NOE relaxation of $^1H^{15}N$-labelled Hsp90 N-terminal with AMP-PNP bound, at 25°C recorded at 600 MHz **196**

Figure 5.27 The relaxation rate difference of ΔR_1, ΔR_2 and ΔR from the apo- and AMP-PNP bound HSP-90 N-terminal are compared **197**

Figure 5.28 The $\{^1H\}^{15}N$-Heteronuclear NOE values from the AMP-PNP bound protein mapped on the X –ray crystal structure of the Hsp90 N-terminal domain **199**

Chapter 6:

Figure 6.1 Six out of nine titration points for novobiocin in a ^{15}N-labelled sample of the Hsp90 N-terminal domain at pH 8.0, 25°C **205**

Figure 6.2 Superposition of all titration point for novobiocin against a ^{15}N-labelled sample of the Hsp90 N-terminal domain **206**

Figure 6.3 Superposition of the Mg^{2+} titration points in a ^{15}N-labelled sample of the Hsp90 N-terminal domain with novobiocin **207**

Figure 6.4 The structures of the Geldanamycin and Radicicol are compared to that of the Novobiocin. **208**

Figure 6.5 Comparison of the apo- Hsp90 N-terminal domain (blue) to that of the N-terminal and middle domain of Hsp90 (red) **210**

Figure 6.6 Comparison of the AMP-PNP bound Hsp90 N-terminal domain (blue) to that of the N-terminal and middle domain of Hsp90 (red) with AMP-PNP **211**

Figure 6.7 Comparison of the ADP bound Hsp90 N-terminal domain (blue) to that of the N-terminal and middle domain of Hsp90 (red) with ADP **212**

Figure 6.8 The locations of the two mutants shown in the X-ray crystal structure of the Hsp90 N-terminal domain **214**

Figure 6.9 Comparison of the $^{1}H^{15}N$ HSQC apo- wild-type (black) to the T101I mutant (red) spectra **216**

Figure 6.10 Comparison of the $^{1}H^{15}N$ HSQC apo- wild-type (black) to the A107N mutant (blue) spectra **216**

Figure 6.11 Areas affected by the mutation for the T101I (a) and A107N (b) mutants **218**

Figure 6.12 Comparison of the T101I mutant apo- with AMP-PNP spectra **220**

Figure 6.13 Comparison of the A107N mutant apo- with AMP-PNP spectra **220**

Chapter 7:

Figure 7.1 Various regions of the Hsp90 N-terminal domain highlighted on a tube representation **226**

List of Tables

Page

Chapter 1:

Table 1.1 Conserved families of molecular chaperones and their co-chaperones **3**

Table 1.2 Localisation and homologues of the Hsp90 molecular chaperone family found in eubacteria, yeast, plants and mammals **5**

Table 1.3 Some of the most important Hsp90 substrates based on biochemical evidence for interaction **8**

Table 1.4 Examples of the most important Hsp90 substrates with their homologues in eukaryotes and yeast **9**

Table 1.5 Residues involved in the binding of nucleotides compared with those involved in binding GM **21**

Table 1.6 Activities of mutants T101I and A107N compared to wild type Hsp90 **28**

Table 1.7 Different kinetic values compared for Hsp90 wild type and the N-terminal domain of Hsp90 **33**

Chapter 2:

Table 2.1 Phosphate and Tris buffer screening for the non labelled Hsp90 N-terminal protein **46**

Table 2.2 Sodium acetate and bis-tris buffer screening for the non labelled Hsp90 N-terminal protein **47**

Table 2.3 3D experiments recorded on proton and deuterated samples **50**

Table 2.4 Delay times for ^{15}N relaxation experiments carried out on Hsp90 N-terminal samples **53**

Table 2.5 PFG pulse values used in the diffusion experiment **57**

Chapter 3:

Table 3.1. The Hsp90 N-terminal residues assigned in the $^{1}H^{15}N$ HSQC spectrum. **106**

Table 3.2 Residues assigned for the $^{13}C\alpha$ nuclei,$^{13}C\beta$ nuclei and ^{13}CO nuclei. **107**

Table 3.3 Chemical shifts derived from the $^{1}H^{15}N$ HSQC experiment **109**

Table 3.4 The $^{13}C\alpha$ nucleus chemical shifts from HNCA and HN(CO)CA experiments **110**

Table 3.5 The $^{13}C\beta$ nucleus chemical shifts from HN(CA)CB and HN(COCA)CB experiments **112**

Table 3.6 The ^{13}CO nucleus chemical shifts from HNCO and HN(CA)CO experiments **113**

Table 3.7 The $^{1}H\alpha$ nucleus chemical shifts from the $^{1}H^{15}N$ HSQC NOESY experiment **114**

Table 3.8 The secondary structure prediction of the apo- Hsp90 N-terminal domain using CSI, version 2, compared to the secondary structure from X-ray crystal studies **118**

Chapter 4:

Table 4.1 Average values for R_1, R_2 and heteronuclear NOE before and after application of the filter to calculate the isotopic rotational correlation time **131**

Table 4.2 Estimation of diffusion coefficients from a three and two parameter fit using Equation 4.5 **137**

Table 4.3 The Ds for the Hsp90 N-terminal at different temperatures with estimated molecular weight **138**

Chapter 5:

Table 5.1 The Hsp90 N-terminal AMP-PNP bound residues assigned in the $^{1}H^{15}N$ HSQC spectrum **173**

Table 5.2 Residues assigned for the (a) $^{13}C\alpha$ nuclei (b) $^{13}C\beta$ nuclei and (c) ^{13}CO nuclei in the Hsp90 N-terminal domain with bound AMP-PNP **174**

Table 5.3 Chemical shifts derived from the ^{1}H ^{15}N HSQC experiment of the Hsp90 N-terminal domain AMP-PNP bound **175**

Table 5.4 The $^{13}C\alpha$ nucleus chemical shifts from HNCA and HN(CO)CA experiments in the AMP-PNP bound Hsp90 N-terminal domain **176**

Table 5.5 The $^{13}C\beta$ nucleus chemical shifts from HN(CA)CB and HN(COCA)CB experiments **179**

Table 5.6 The ^{13}CO nucleus chemical shifts from HNCO and HN(CA)CO experiments of the AMP-PNP bound Hsp90 N-terminal domain **180**

Table 5.7 Residues involved in the nucleotide binding in the yeast Hsp90 N-terminal domain **180**

Table 5.8 The secondary structure prediction of the apo- and AMP-PNP bound Hsp90 N-terminal domain using CSI, version 2, compared to the secondary structure from X-ray crystal studies **190**

1D	one-dimensional
2D	two-dimensional
3D	three-dimensional
$\Delta\delta^{13}C$	chemical shift differences for backbone nuclei
$\Delta\delta NH$	chemical shift differences for amide protons
$\Delta\delta[X]$	chemical shift difference for any nuclei
${}^{n}J_{xy}$	n-bond scalar coupling between nuclei x and y
τ_C	rotational correlated time
t_1	first incremented delay in N-dimensional spectroscopy
t_2	second incremented delay in N-dimensional spectroscopy
A107N	alanine-107 asparagine
ADP	adenosine diphosphate
Aha1/Hch1	activator of Hsp90 ATPase/high copy Hsp90 suppressor
AMP-PNP	5'-adenylamido-diphosphate
apo-	from Greek *apo,* meaning 'away from / off'
ATP	adenosine triphosphate
AU	absorbance units
BCK	mitochondrial branched-chain α-ketoacid dehydrogenase kinase
Bis-Tris	bis(2-hydroxyethyl)aminotris (hydroxymethyl) methane
^{13}C	carbon-13
CAB	carbenicillin
CAP	chloramphenicol
CheA	chemotaxis histidine kinase
CHIP	carboxyl terminus of Hsc70- interacting protein
CSI	chemical shift index
DNA	deoxyribonucleic acid
DSS	sodium 2,2-dimethyl-2-silapentane-5-sulfonate
E.coli	Escherichia coli
EnvZ	*E.coli* histidine kinase
ER	endoplasmic reticulum
F_1	first indirectly detected dimension in N-dimensional spectroscopy
F_2	second indirectly detected dimension in N-dimensional spectroscopy
FID	free induction decay
GHKL	Gyrase, Hsp90, histidine Kinase and MutL
GM	geldanamycin
Grp96	glucose-regulated protein 94- kDa (previously Grp94)
GyrB	DNA gyrase B
^{1}H	proton
^{2}H	deuterium
H^N	amide proton
Hip	Hsc70 interacting protein
HNCA	amide proton to nitrogen to α-carbon correlation
HN(CO)CA	amide proton to nitrogen to α-carbon (via carbonyl) correlation
HN(CA)CB	amide proton to nitrogen to β-carbon (via α-carbon) correlation
HN(COCA)CB	amide proton to nitrogen to β-carbon (via α-carbon and carbonyl) correlation
HNCO	amide proton to nitrogen to carbonyl correlation
HN(CA)CO	amide proton to nitrogen to carbonyl (via α-carbon) correlation
HN(CACO)HA	amide proton to nitrogen to α- proton (via α-carbon and carbonyl) correlation

Hop	Hsp organising protein
Hsc70	70kDa heat shock cognate protein
Hsc90	collective Hsp90α and Hsp90β isoforms
Hsp75	heat shock protein 75kDa
Hsp90	heat shock protein 90 kDa
HSQC	heteronuclear single quantum coherance
HtpG	high temperature protein G (Hsp90 eubacteria homologue)
IPTG	isopropyl-β-D-thiogalactopyranoside
LB	Luria Bertani media
M9	minimal medium
MutL	DNA-mismatch repair enzyme
^{15}N	Nitrogen-15
NMR	nuclear magnetic resonance
NOE	nuclear overhauser effect
NOESY	nuclear overhauser effect spectroscopy
p23	23 kDa acidic protein
p50(cdc37)	50 KDa phosphoprotein, mammalian/cell cycle control protein 37
PFG	pulse field gradient
PMS2	a MutL homolog
RF	radio frequency
SDS PAGE	sodium dodecyl sulphate sulfate-polyacrylamide gel electrophoresis
SHRs	steroid hormone receptors
Sti1	the yeast homologue of Hop
T_1	longitudinal or spin-lattice relaxation time
T_2	transverse or spin-spin relaxation time
T101I	threonine-101 isoleucine
TRAP-1	tumour necrosis factor receptor associated proteins 1
TPR	tertratricopeptide repeat
TOWNY	'clean' TOCSY
TROSY	transverse relaxation optimised spectroscopy
TOCSY	total correlated spectroscopy

Amino Acid Abbreviations

Nonpolar Amino Acids (hydrophobic)

amino acid	three letter code	single letter code
glycine	Gly	G
alanine	Ala	A
valine	Val	V
leucine	Leu	L
isoleucine	Ile	I
methionine	Met	M
phenylalanine	Phe	F
tryptophan	Trp	W
proline	Pro	P

CHAPTER 1

INTRODUCTION

1.1 Molecular chaperone classification

The term 'molecular chaperone' was published first in 1978 by Laskey and his colleagues to describe the properties of the nuclear protein 'nucleoplasmin' in assisting the *in vitro* assembly of nucleosomes from isolated histones and deoxyribonucleic acid (DNA) (Laskey *et al.*, 1978). Molecular chaperones have been defined as "proteins that bind to and stabilise an otherwise unstable conformer of another protein and, by controlled binding and release, facilitate its correct fate *in vivo*: be it folding, oligomeric assembly, transport to a particular subcellular compartment, or disposal by degradation" (Hartl, 1996).

Molecular chaperones complete the translation of polypeptide chains in their life cycle, during folding in the cytosol by preventing or reversing off-pathway interactions and assisting in its translocation across endoplasmic reticulum (ER) or mitochondrial membranes. Molecular chaperones do not change the folding fate of a polypeptide but rather shift the equilibrium of the folding reaction toward the folded state and away from the aggregated state under physiological and stress conditions (Buchner, 1996). Several major classes of molecular chaperones have been identified and characterized as polypeptide-binding proteins with low sequence specificity. Molecular chaperones are grouped into families based on their evolutionary conservation. Many are determined and grouped according to their approximate molecular weight, e.g. the 70-kDa chaperone heat shock protein termed Hsp70. Other members of the Hsp70 chaperone family have kept the name provided to them on the basis of their historical discovery with different names for different species, as shown in Table 1.1 (Buchner, 1999). Molecular chaperones can be found in various sub-cellular compartments in different oligomeric (e.g.

monomer, dimer) states working together or with various other co-chaperones to achieve their goal.

Group	Other Names		Location	Native form	Comments
	Prokaryotes	Eukaryotes			
Hsp110		Apg-1 Hsp105	Cytosol Cytosol		mouse
Hsp100	ClpA, ClpB, ClpX, ClpY	Hsp104, Hsp87	Cytosol		
Hsp90	HptG	Hsp83 Grp94, gp96 TRAP-1	Cytosol ER Mitochondria	Dimer	Hsp90α, Hsp90β in human
Hsp70	DnaK, HscA (Hsc66)	Ssa1-4 Ssb1-2 Ssc1p Scd1p / Kar2 BiP or Grp78 Hsp72 Hsp73 Clathrin- uncoating ATPase mtHsp70/Grp75	Cytosol Cytosol Mitochondria ER ER Cytosol/nucleus Cytosol/nucleus - Cytosol Chloroplast Mitochondria	Monomers and Dimers	ATPase Activity
Hsp60, Hsp10 or Chaperonins	Cpn60 (GroEL) Cpn10 (GroES)	- - TCP-1 Hsp60 Cpn60 Cpn21	Cytosol Cytosol Cytosol Mitochondrion Chloroplast Chloroplast	14-mer 7-mer 16-18-mer 14-mer 14-mer	Weak ATPase Activity
Small Hsps	HtrC	Hsp27 & Hsp28 Hsp15 & Hsp30	Cytosol ER	Oligomer Oligomer	
Others	DnaJ GrpE	Hsp40,Ydj1 Mgel1p	Cytosol Cytosol/Mito	Dimer Dimer	Co- Chaperone of Hsp70

Table 1.1 Conserved families of molecular chaperones and their co-chaperones. Different molecular chaperones are grouped according to their molecular weight, splices and location in the cell. Similar chaperones have different names in the same species according to their historical discovery name. Data extracted from Bukau (1999).

Some of the molecular chaperones are also known as heat shock proteins, hence the abbreviation Hsp, arising from an increase in their expression level when the cells experience environmental stresses such as heat shock, oxidation, ethanol, metabolic poisons and glucose starvation. These proteins act with a protective

function, in order to assist the recovery and survival of the cell, which in general is known as the stress response (Bukau, 1999).

1.2 The 90-kDa molecular chaperone family

The members of the 90-kDa molecular chaperone family or Hsp90, as is the more familiar term, are ubiquitous chaperones found in eubacteria and eukaryotes but are absent in archea (Buchner, 1999). Hsp90 is one of the most abundant cytosolic proteins in eukaryotes, and contributes about 1-2 % of soluble protein even in the absence of stress (Welch and Feramisco, 1982). Functional Hsp90 is essential for viability in eukaryotes such as yeast and *Drosophila melanogaster* but its *Escherichia coli* (*E.coli*) homologue has been found to be not essential, even under stress (Spence *et al.,* 1990). The eubacteria homologue, the prokaryotic high temperature protein G (HtpG), has not been characterised as well as its eukaryotic counterparts. The cytoplasmic Hsp90 or the 94-kDa glucose-regulated protein Grp94 localised in the endoplasmic reticulum (ER) is also known as GP96. These two proteins are 50% identical, and their existence is most probably a result of a gene duplication that occurred at a very early stage in the evolution of the eukaryotic cell (Gupta, 1995). Another homologous protein is the tumour necrosis factor receptor associated protein 1 (TRAP-1) known previously as Hsp75 (Song *et al.,* 1995). TRAP-1 is a distant eukaryotic relative of Hsp90, resembling both size and structural organisation of the Hsp90 protein especially in the N-terminal region, but lacks the charged region. Despite these similarities, TRAP-1 is incapable of binding to Hsp90 co-chaperones such as p23 (Chen *et al.,* 1996). The

Hsp90 homologues can be found in sub-cellular compartments and according to their discovery have different names, as summarised below in Table 1.2.

	Archea	Eubacteria	Yeast	Plants	Mammals
Cytoplasm	– –	HtpG	Hsc83p Hsp83	Hsp90	Hsp90α (Hsp86) Hsp90β (Hsp84)
ER/periplasm	–	–	–	Grp94	GRP94/GP96
Mitochondria			–	–	TRAP1/HSP75
Chloroplasts				cpHsp82	

Table 1.2 Localisation and homologues of the Hsp90 molecular chaperone family found in eubacteria, yeast, plants and mammals. Homologues are shown here with their different names assigned according to its discovery. No homologue has been found in archea to this date.

Human Hsp90 has two isoforms, Hsp90α and Hsp90β, which are 76% identical and are theorised to be the consequence of a gene duplication that occurred around 500 million years ago (Krone and Sass, 1994). The Hsp90β is moderately larger than Hsp90α and also less inducible. The human Hsp90α and Hsp90β isoforms were denoted as Hsp86 and Hsp84 respectively and are sometimes collectively known as Hsc90 (Hickey *et al.*, 1989).

1.3 Functions of the Hsp90

In general three different roles for Hsp90 have been suggested. Firstly, a general chaperone role together with other chaperones in the cell such as Hsp70/Hsp40 which target misfolded bulk proteins during stress; and secondly targeting of selected protein substrates that are mostly involved in housekeeping roles and stabilising their metastable conformer, together with other Hsp90 co-factors and helpers. A final role involves acting as a capacitor for morphological evolution as suggested by Rutherford and Lindquist (1998). These diverse roles of

Hsp90, as well as being a target for various anticancer drugs, all emphasise the importance of studying this protein.

1.3.1 Hsp90 as a part of the chaperone machinery in cytosol

In vitro studies with purified Hsp90 have shown that it suppresses the aggregation of unstable proteins and reverses the partially denatured, or in some cases, the unfolded protein (Jakob *et al.,* 1995; Scheibel *et al.,* 1998). Peptide binding, limited chaperone ability and prevention of aggregation of thermally denatured protein have all been shown for fragments of Hsp90 *in vitro*, suggesting an active cooperation or function between the multiple domains of the Hsp90 protein (Johnson *et al.,* 2000). The chaperone role of the Hsp90 takes place in cooperation with other chaperone proteins as part of a refolding system. For example, it is generally believed that an unfolded polypeptide substrate associates with the Hsp70 system first and is then targeted to Hsp90 via the Hsp organising protein (Hop), a tertratricopeptide repeat (TPR) protein that interacts with both Hsp70 and Hsp90 (Johnson *et al.,* 1998). However recent studies on the steroid hormone receptors (SHRs), as a model believed to be similar for most of the Hsp90/Hsp70-based chaperone activities, showed the presence of a focal attack site on the surface of the ligand-binding domain. Such focal regions are a general topological feature of virtually all proteins in their native conformation. The possibility that the Hsp90/Hsp70-based chaperone machinery functions on these focal points in the native conformation rather than promoting the refolding of partially denatured protein must be considered (Pratt and Toft, 2003).

1.3.2 Hsp90 interaction with substrates

The cytoplasmic Hsp90 has a regulatory effect or chaperone activity for a wide range of client proteins (nearly 100 proteins to date) (Pratt and Toft, 2003; Caplan *et al.,* 2003). Generally Hsp90 interacts with diverse but highly selective unstable substrates and keeps these metastable proteins poised for activation until they are stabilised by conformational change (Buchner, 1999; Mayer and Bukau, 1999). Hsp90 interacts with its substrate through repeated cycles of low affinity binding and release (Smith, 1993). Most of these client proteins are involved in signal transduction such as: transcriptional factors, protein kinases, cell cycle regulation proteins and an increasing number of various other client proteins including the tumour suppressor p53, dioxin receptors, histones and telomerase (Pratt and Toft, 2003). Some of the well established Hsp90 substrates are shown in Table 1.3. There are no apparent structural similarities among the Hsp90 substrates. The best-studied *in vivo* substrates of Hsp90 are the SHRs (Pratt and Toft, 1997; 2003) as well as various kinases (Buchner, 1999). Hsp90 interacts with the inactive conformation of the protein prior to the final processing step (ligand binding in the case of SHRs, and membrane attachment in the case of v-src for example) which is involved in the maturation of the client protein (Pratt and Toft, 1997; 2003). As mentioned, these two classes of classical Hsp90-substrate proteins (SHRs and kinases) do not share obvious structural motifs, therefore the conformational state of the protein and its folding characteristics – rather than a sequence or defined structural motif – could be the key determinant for interactions with Hsp90 (Buchner, 1999). The list of proteins, whose folding is known to be affected by

binding of Hsp90 *in vivo,* has been growing considerably over the past years as research unfolds (Table 1-3).

In mammalian cells, the tumour-suppressor protein p53 (Blagosklonny *et al.,* 1996), nitric-oxide synthase (Garcia-Cardena *et al.,* 1998), heat-shock factor (Zou *et al.,* 1998) and a reverse transcriptase (Hu *et al.,* 1997) fold in an Hsp90-dependent way. In the case of reverse transcriptase, retroviruses not only rely on the host chaperone machinery in the cytosol of infected cells, but also specifically take Hsp90 and partner proteins aboard the virus (Hu *et al.,* 1997).

The most common Hsp90 substrates	
Steroid hormone receptors	**Others**
Progesterone receptor	Cytoskeleton: actin, tubulin, myosin
Glucocorticoid receptor	Calmodulin
Glucocorticoid-receptor HBD	Histones H1, H2A, H2B, H3 and H4
Estrogen receptor	Heat-shock factor, HSF 1
Androgen receptor	Nitric-oxide synthase, eNOS
Mineralocorticoid receptor	p53
Kinases	Reverse transcriptase
SRC tyrosine	Tumour necrosis factor
pp60v-src, c-src	Macrophage scavenger receptor
Wee1, Swe1	Luciferase
Casein kinase IIα	Dihydrofolate reductase
RAF-1, BRAF 1, Ste 11	β-Galactosidase
Cdk4, Cdk6, Cdk9	Citrate synthase
elF-2α kinase, ErbB2	Insulin receptors
Gcn2	Telomerase
Calcineurin	DNA polymerase α
MOK, MAK, MRK	Proteasome

Table 1.3. Some of the most important Hsp90 substrates based on biochemical evidence for interaction (n.b. experiments based on geldanamycin were not considered)

Hsp90 and its co-chaperone p23 are reportedly both required for efficient telomerase assembly *in vitro* and *in vivo* (Forsythe *et al.,* 2001). Hsp90 also binds to histones H1, H2A, H2B, H3 and H4 (Schnaider *et al.,* 1999). In all, this demonstrates a variety of different roles for the Hsp90 protein.

1.3.2.1 Hsp90 partner proteins

Hsp90 partner proteins or co-chaperones are proteins involved in interacting with Hsp90 substrates that can be divided into two functional classes: (1) scaffold proteins for the Hsp90 complexes; and (2) cofactors that assist protein folding directly (Buchner, 1999). The co-chaperones or cofactors bind to different regions on Hsp90 and can have a regulatory effect directly or in conjunction with other chaperones, cofactors or even its client proteins. Some of the most common cofactors that Hsp90 cooperates with to accomplish its role are: Sti1/Hop/p60, the immunophilins FKBP51/54 and FKBP52, cyclophilin 40, p50(cdc37), Sba1/p23, CHIP (carboxyl terminus of Hsc70- interacting protein), the recently categorised Aha1/Hch1 (activator of Hsp90 ATPase/high copy Hsp90 suppressor) and finally Hsp70, all of which participate as a part of a multichaperone machine.

Some of the Hsp90-partner proteins			
General name	**Name in higher eukaryotes**	**Name in yeast**	**Function**
Hsp70	Hsp70	Ssa1p	Chaperone, interacts with Hsp90
p23	p23 ,tsp23	Sba1/p	Chaperone, binds to ATP domain of Hsp90
Hsp40	Hsp40, Hsj1b,DnaJ	Ydj1p	Cofactor, chaperone
Hop	Hop, p60	Sti1/p	Assembly factor for Hsp90 and Hsp70 Binds via TPR motif
FKBP51	FKBP51, p54, FKBP54	–	Immunophilin, binds via TPR motif
FKBP52	FKBP52, p59, p56, HBI, Hsp56, FKBP73, FKBP77	–	Immunophilin, binds via TPR motif
Cyp40	Cyp40	Cpr6,Cpr7	Immunophilin, chaperone
PP5	PP5	PPT1	Immunophilin, protein-serine phosphatase
Cdc37	p50	Cdc37p	Kinase-specific cofactor, binds to p50 site
CHIP			Binds via TPR motif
Aha1		Hch1	Regulation of ATPase in Hsp90

Table 1.4. Examples of the most important Hsp90 substrates with their homologues in eukaryotes and yeast. A brief function of each substrate is described in the last column. Data derived from (Buchner, 1999; Pratt and Toft, 2003; Lotz *et al.*, 2003).

Table 1.4 summarises most of the cofactors, which bind to Hsp90 and its homologue in eukaryotes and yeast, with their relevant function and binding motif.

Among the cofactors, the two partner proteins Hip (Hsc70 interacting protein) and Hop (Hsp90 organising protein) seem to be responsible mainly for proper association of the protein components of chaperone complexes. Hip is an Hsp70-specific cofactor that also regulates the ATPase activity of Hsp70 (Frydman and Hohfeld, 1997) whereas Hop acts as an assembly factor, linking together the Hsp70 and Hsp90 machineries (Chen and Smith, 1998). Hop binds independently via an N-terminal TPR domain to Hsp70 and via a central TPR domain to Hsp90 (Pratt and Toft, 2003). Studies by Richter *et al.* (2003) have shown that, Sti1, the yeast homologue of Hop, has a non-competitive inhibitory mechanism on the ATPase activity of Hsp90. This protein binds to the N- and C-terminal part of Hsp90, preventing the N-terminal dimerisation reaction that is required for efficient ATP hydrolysis. They have also demonstrated that the first 24 amino acids of Hsp90 seem to be important for this interaction.

Large immunophilins such as FKBP51, FKBP52 or cyclophilin 40, interact specifically with non-native proteins and suppress the aggregation of unfolding proteins, maintaining chemically denatured proteins in a state competent for refolding (i.e. they have a chaperone activity similar to that of Hsp90 itself) (Buchner, 1999). Large immunophilins, and their smaller counterparts, contain a domain that can catalyse the isomerisation of prolyl-peptide bonds in proteins. The TPR domain present in the large immunophilins is required for interaction with Hsp90 and hence folding of Hsp90-client proteins. Hop and the TPR domain of the immunophilins compete with each other for the TPR domain of the Hsp90 located in its C-terminal (Pratt and Toft, 2003).

The p23 cofactor is a 23 kDa acidic protein, which regulates the nucleotide binding domain of Hsp90 and stabilises Hsp90 substrate complexes. The p23 co-

chaperone does not bind to Hsp90 in its native state, rather it binds to Hsp90 only when Hsp90 is in its active conformation, induced by the binding of ATP *in vitro* (Sullivan *et al.,* 2002). Once the p23-Hsp90 complex is formed it is very stable upon the removal of ATP, with a half-life of about 45 min (Sullivan *et al.,* 2002). Both p23 and molybdate enhance and stabilise the nucleotide bound state of Hsp90, and this state is maximised by the presence of both agents. It has been suggested by Sullivan and colleagues (1997) that molybdate occupies the binding site of the γ-phosphate after ATP hydrolysis, thus keeping the Hsp90 in its ATP bound conformation. However, there is evidence of molybdate affecting the C-terminal domain where it interacts with its substrates (Hartson *et al.,* 2000). A model was later suggested by Sullivan *et al.* (2002) whereby the binding of ATP induces a conformational transition in Hsp90 that traps the nucleotide and is committed to ATP hydrolysis. p23 specifically recognises this state and may also facilitate subsequent steps in the chaperoning cycle. Studies on fragments of Hsp90 have shown that the isolated nucleotide binding domain of Hsp90 cannot bind to p23, rather Hsp90 needs to be in a dimeric state in order to bind to the protein (Chadli *et al.,* 2000).

Cooperation between Hsp90, other chaperones and their cofactors is required for interaction with certain cell-cycle kinases. A kinase-specific cofactor of Hsp90, mammalian 50 kDa phosphoprotein (p50) and its homologue in yeast, the cell cycle control protein 37 (cdc37), exhibits chaperone properties *in vitro* and can rescue a kinase-maturation defect, caused by lack of Hsp90 *in vivo* (Kimura *et al.,* 1997). Studies on p50(cdc37) showed that it does not simply serve as a passive structural bridge between Hsp90 and its kinase substrates, but rather acts as a non-exclusive Hsp90 machinery which responds to Hsp90's nucleotide-regulated

conformational change during the generation of the Hsp90-kinase-p50(cdc37) heterocomplex (Hartson *et al.,* 2000). p50(cdc37) is not a TPR protein and binds directly to Hsp90 at a different site in the C-terminal, yet despite having a different binding site, still exhibits competition with TPR proteins particularly Hop (Silverstein *et al.,* 1998). This suggests that the p50-binding site is next, or close, to the TPR binding domain. There are also contradictory reports stating the p50(cdc37) has been co-adsorbed with large immunophilins and Hop, suggesting that they bind simultaneously to the same Hsp90 dimer (Hartson *et al.,* 2000).

CHIP (carboxyl terminus of Hsc70- interacting protein) is a 35 kDa protein that has been shown to be an interacting partner with Hsc70. CHIP interacts directly with a TPR acceptor site on Hsp90, being incorporated into Hsp90 heterocomplexes and evoking release of the regulatory cofactor p23 (Connell *et al.,* 2001). CHIP is part of the quality control mechanism in Hsp90/Hsp70 and its substrate, which decides the fate of the protein as whether to refold or degrade.

The Aha1 (activator of Hsp90 ATPase) and its homologue Hch1 (high copy Hsp90 suppressor) are the more recent cofactors investigated that have been shown to bind to the middle domain of Hsp90 and to regulate its ATPase activity (Lotz *et al.,* 2003).

1.3.3 Hsp90 as a capacitor for morphological evolution

Studies by Lindquist and co-workers on *Drosophila melanogaster* suggested that environmental stress could reveal genetic variations, presumably by compromising the buffering system that the chaperone Hsp90 can serve (Rutherford and Lindquist, 1998). They have proposed that Hsp90 allows storage

and release of the genetic variations in *Drosophila* as a result of its chaperone function on regulators of growth and development and that this role in buffering the expression of genetic variation is conserved across plant and animal kingdoms (Queitsch *et al.,* 2002). Hsp90 does this by functioning at the interface between genotype and environment (Queitsch *et al.,* 2002). If the function of Hsp90 is compromised either by mutation or drugs, the buffer breaks and the previously unavailable phenotypic variants would reveal. These traits were retained even after the Hsp90 function was restored (Rutherford and Lindquist, 1998). This is a unique role whereby Hsp90 can influence the dynamic nature of the developmental process.

1.4. Hsp90 domains and its characterisation

Sequence alignments and limited proteolytic digestion has shown that Hsp90 has a modular structure, which consists of two well-conserved regions that are connected by a highly charged linker of variable length, Figure 1.1(a). The native protein is an elongated dimer, established by the presence of a constitutive dimer site in the C-terminal region and an ATP-dependant dimerisation of the amino-terminal domain, Figure 1.1(b). The dimerisation in the N-terminal domain can also be induced by heat-shock temperatures as shown by electron microscopy studies (Yonehara *et al.,* 1996; Maruya *et al.,* 1999). Electron microscopy studies by Maruya and co-workers (1999) showed that the transformation of the linear Hsp90 dimer into a ring-shaped structure happens in the presence of ATP but not ADP, Figure 1.1(b). The dimer seems to be quite flexible, because different shapes of the molecule were detected, suggesting that rigid body movements of domains

around a hinge region could be the basis of these re-arrangements. Figure 1.1(a) shows the highly conserved regions in different Hsp90 homologues. The charged region (shown in dark grey) can be variable in length and this region is almost completely missing in prokaryotic (HtpG) and some eukaryotic Hsp90-family members as well as its mitochondrial homologue TRAP1 (Felts *et al.*, 2000).

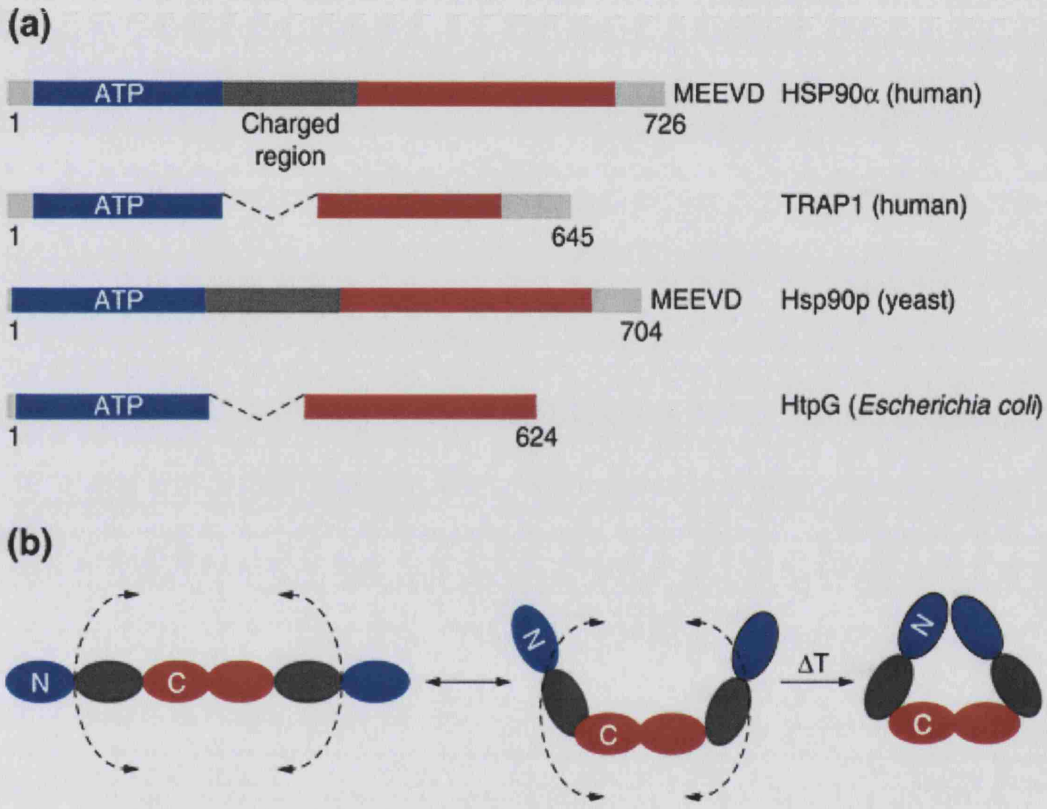

Figure 1.1 Domain structure (a) and dimer formation (b) of Hsp90 induced by heat or presence of ATP. (a) Compares different Hsp90 homologues with the conserved N-terminal domain in blue and the C-terminal domain in red with a variable linker region, which is highly charged shown in dark grey. The light grey area highlights the C-terminal TPR binding region. (b) Induction of the N-terminal domain by ATP or heat causes a second dimerisation in the N-terminal domain. Picture adapted from Buchner (1999).

Studies on the charged region suggest that the linker region causes an increase in the affinity of the N-terminal domain for non-native protein and establishes a crosstalk between the peptide and the ATP binding site. Therefore, it was proposed that the charged region must play an important role in regulating the chaperone function of Hsp90 (Scheibel *et al.*, 1999). Dimer formation occurs

through antiparallel association of C-terminal regions. The relative orientation of the domain allows Hsp90 to adopt different conformations. An increase in temperature leads to the appearance of a closed conformation (Figure 1.1.b). It has been previously reported that Hsp90 oligomerises at high temperatures and that this is associated with a novel chaperone activity (Yonehara *et al.,* 1996). Both ATP and geldanamycin (GM) which bind to the N-terminal domain of Hsp90 have an inhibitory effect on the oligomerisation, whereas molybdate and vanadate are its activators (Chadli *et al.,* 1999). Several cofactors (p60, Hop, immunophilins) have protein domains containing TPR motifs which mediate binding to the conserved C–terminus of Hsp90 (a domain about 12-kDa with a conserved MEEVD amino acid sequence) (Young *et al.,* 1998). This domain has several roles from regulatory effects to binding to various cofactors. These cofactor TPR domains have similar X-ray crystallographic structures and target co-chaperone binding to the MEEVD sequence at the C-terminal end of Hsp90. There are several reports suggesting presence of a second nucleotide binding site in the C-terminal of Hsp90 (Marcu *et al.,* 2000; Langer *et al.,* 2002; Garnier *et al.,* 2002 and Soti *et al.,* 2003). Studies by Soti *et al.* (2003) have suggested that the C-terminal binding site is much more non-specific and that interaction with both purine and pyrimidine nucleotides occur. Marcu *et al.* (2000), have shown that novobiocin binds to a site that resides in the C-terminus of the chaperone. Novobiocin also interferes with the autophosphorylation of Hsp90, suggesting that the C-terminal ATP-binding site is required for autophosphorylation (Langer *et al.,* 2002). What is clear is that the C-terminal region of Hsp90 is essential for trapping bound ATP and for maximum ATPase activity as well as Hsp90 dimerisation (Prodromou *et al.,* 2000; Weikl *et al.,* 2000).

1.4.1 The structure of the N-terminal domain of Hsp90

The X-ray crystal structures for the N-terminal domain of yeast (Prodromou *et al.,* 1997) and human (Stebbins *et al.,* 1997) proteins have been determined. The N-terminal domain is highly conserved among all Hsp90 domains with sequence identity of 69%, from yeast to human species. The tertiary structure of these two domains are extremely similar, consisting of an α/β sandwich of eight β-sheets, covered on one face by nine to ten α-helices and loops, Figure 1.2 (a) and (b). In the human Hsp90 N-terminal, four out of nine helices are of the 3_{10} type, making about 11.2% of the amino acids, which is significantly higher than the 3.4% average in protein databases (Stebbins *et al.,* 1997). At the centre of this helical face, a deep pocket about 15 Å deep with an entrance width of 8 Å to 12 Å exists. The buried β-sheet forms the bottom of the pocket and is the binding site for nucleotides and the anti-tumour drugs in a complex with the N-terminal domain, Figure 1.3 (Stebbins *et al.,* 1997; Prodromou *et al.,* 1997). The isolated N-terminal domain does not dimerise and binds nucleotides with a weak ATPase activity (about 1/10 ATPase activity of the full-length protein, Prodromou *et al.,* 2000).

1.4.1.1 Nucleotide (ATP/ADP) interaction with the Hsp90 N-terminal domain.

Nucleotides bind to the pocket centred at the middle of the N-terminal domain of Hsp90 as observed in the X-ray crystal structure solved and characterised by Pearl and co-workers (Prodromou *et al.,* 1997). Figure 1.2 (a) and

(b) show the X-ray crystal structures of the yeast Hsp90 N-terminal domain with bound nucleotides shown in yellow.

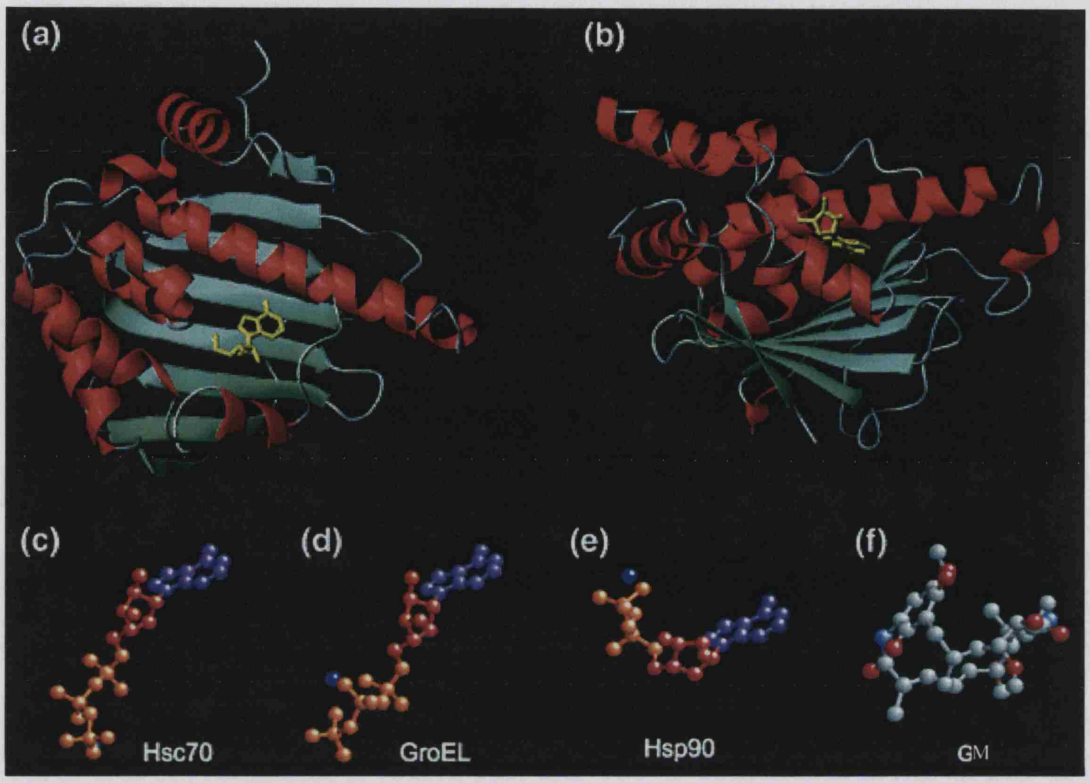

Figure 1.2 Comparison of the nucleotide shapes in the Hsp90 N-terminal domain with other heat shock proteins and location of its binding in the crystal structure. (a) and **(b)** show two views of the structure of N-terminal domain of yeast Hsp90 (helices in red, β-sheets in geen) bound to ADP (in yellow). **(c-e)** show different conformations of ATP bound in different chaperones compared to Hsp90 and **(f)** shows geldenamycin conformation bound to the Hsp90 N-terminal domain. Picture adapted from Buchner (1999).

In the Hsc70 and its homologue GroEL, the bound nucleotide adopts a fully extended conformation as shown in Figure 1.2 (c) and (d) while the nucleotide in the Hsp90-ATP/ADP complex, has a much more compacted kinked shape conformation, Figure 1.2 (e) (Prodromou *et al.,* 1997). This shape was also adapted when GM and radicicol bind to the pocket (Stebbins *et al.,* 1997; Roe *et al.,* 1999). This kinked conformation of nucleotide could explain earlier negative nucleotide binding results to the N-terminal domain of Hsp90 with some forms of the nucleotide (immobilised ATP, azido-ATP and three fluorescent ADP analogues)

(Jakob *et al.,* 1996). These negative results were probably due to the inability of these nucleotides to adopt this kinked conformation.

The nucleotide is bound to the pocket with a single direct hydrogen bond between the adenine base, from the exo-cyclic N6 amino acid, to the carboxyl side chain of Asp-79 at the bottom of the pocket, whereas all other hydrogen bonds of the adenine base take place through water interaction. This can be seen in Figure 1.3. Among these are residues; Leu-34 which binds to adenine N6, the side chains of Asp-79 and Thr-171 hydrogen bonded to adenine N1 and Gly-83 peptide nitrogen hydrogen bonded to adenine N1, all bonded through water molecules.

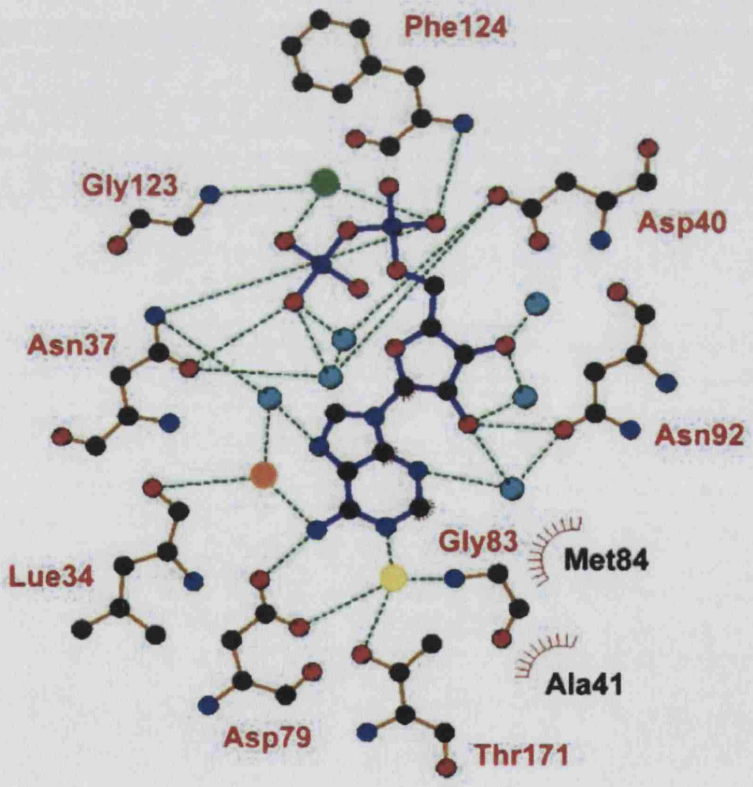

Figure 1.3. Schematic diagram of ADP interacting with the N-terminal domain of Hsp90. Hydrogen bonds are shown as green dotted lines and van der Waals contacts as purple 'spokes'. The magnesium ion is shown as a green sphere; the tightly bound water molecule is shown as a yellow sphere; the water molecule bound to Leu 34 is shown as an orange sphere and other water molecules are shown in turquoise. Picture adapted from Prodromou and Pearl, (2003).

The residue Asn-92 is bound through water molecules to N3 of the adenine and 02' of the ribose, with a second connection to 02' of the ribose directly connected to its side chain (Figure 1.3). The side chain of residue Asn-37 is bound to the N7 of the adenine, again through water interaction. One hydrophobic face of the adenine ring has a van der Waals contact with the side chain of Met-84 while the other face is exposed to solvent. At the top of the pocket, the α-phosphate group forms hydrogen bonds with the side chain of Asn-37 and the peptide nitrogen of Phe-124. The β-phosphate group forms an ion-pair hydrogen-bonding interaction with the side chain of Lys98 and interacts with several solvent molecules bound at the mouth of the pocket. The side-chain amide oxygen of Asn-37 and three other solvent molecules form an approximate octahedral co-ordination, which is identified as the Mg^{2+} ion-binding site (Prodromou *et al.,* 1997).

The structural studies on the N-terminal domain of Hsp90 suggest that despite binding Mg^{2+}-ADP/ ATP it has no inherent Mg^{2+}-binding site (Prodromou *et al.,* 1997). The base of the pocket in yeast Hsp90 is formed by residues; Ile-77, Asp-79, Val-136, Ser-138, Thr-171, and Ile-173, whose side chains project up from the buried face of the β-sheet. In the X-ray crystal structure, the electron density maps for nucleotides bound to the N-termini of Hsp90 were clear for the base, sugar, and α-phosphate groups but were weaker for the β-phosphate with fewer contacts. No significant electron density was observed for the γ-phosphate in complex with ATP (Prodromou *et al.,* 1997). They were also unable to characterise or observe the γ-phosphate in their crystal structures and there were no significant changes between the structure of the protein in ADP or ATP complexes other than the arrangement of the Lys-98 side-chain (Prodromou *et al.,* 1997).

1.4.1.2 Comparison of Geldanamycin (GM) to the nucleotide bound to the N-terminal domain

GM acts as an ADP/ATP mimetic and almost all of the polar interactions described between GM and human Hsp90 have a precise equivalent in yeast Hsp90 with ADP/ATP as shown in Table 1.5. The termed "open" and "closed" apo forms of the human Hsp90 N-terminal domain with GM co-ordinates superimposed on the apo- structures are shown in Figure 1.4. The difference in the two structures was found in 34 amino acids forming helices four, five and six and also the second loop (residues 100 to 134) of the human Hsp90 (Stebbins *et al.*, 1997).

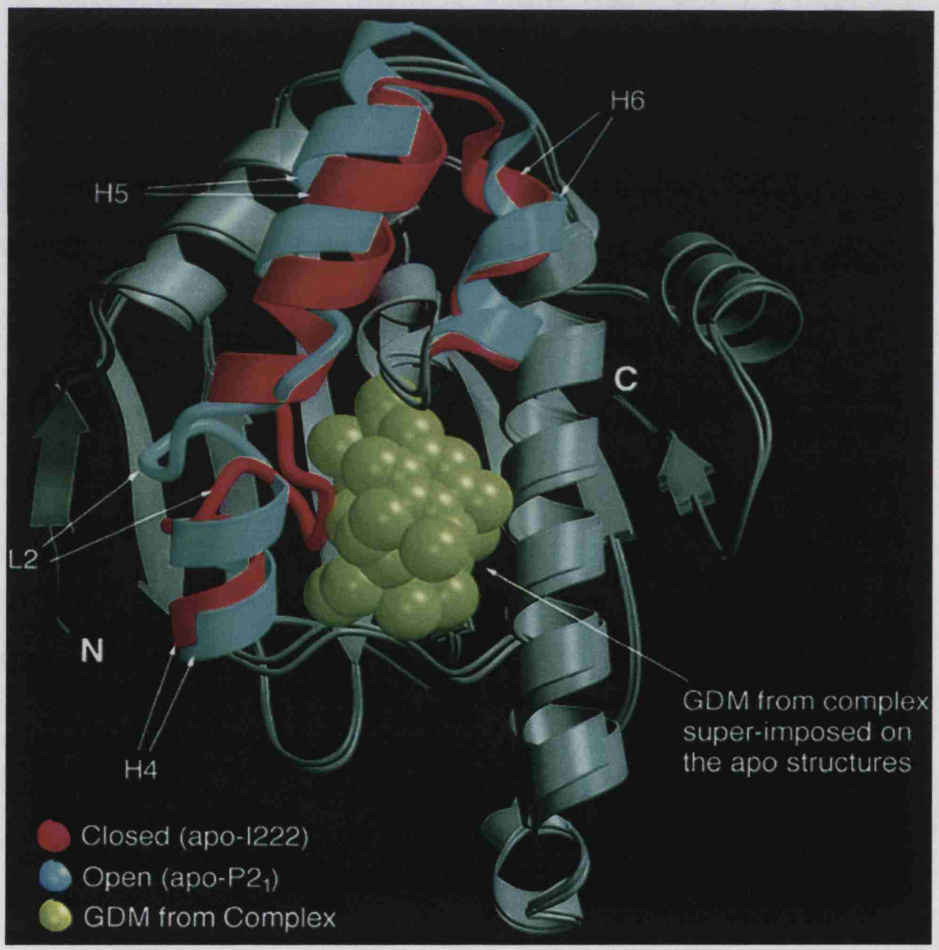

Figure 1.4. Two open (green) and closed (red) conformations of the human Hsp90 N-terminal domain with bound GM. The second loop (L2) has the biggest movement of about 9 Å. Picture adapted from Stebbins *et al.* (1997).

ADP ATP	**Interaction**	GM	Interaction
Asp-79	Direct H-bond to adenine N6	Asp-93	Direct H-bond to carbamate nitrogen
Asp-79	Through water interaction adenine N1	Asp-93	Through water interaction carbamate
Gly-83	Through water interaction adenine N1	Gly-97	Through water interaction carbamate
Thr-171	Through water interaction adenine N1	Thr-184	Through water interaction carbamate
Phe-124	H-bond to oxygen in α phosphate	Phe-138	H-bond to amide carbonyl
Lys-98	H-bond /ion pair to β phosphate	Lys-112	H-bond to benzoquinone oxygen
Lys-44	Not direct equivalent, binds to 02' and 03' oxygens of the ribose sugar	Lys-58	H-bond to methoxy and carbonyl oxygens

Table 1.5. Residues involved in the binding of nucleotides compared with those involved in binding GM. All the residues are sequentially equivalent in yeast and human with exception of Lys-44 and Lys-58 which are not direct equivalents. Data extracted from (Prodromou*et al.*, 1997a; Stebbins *et al.*, 1997).

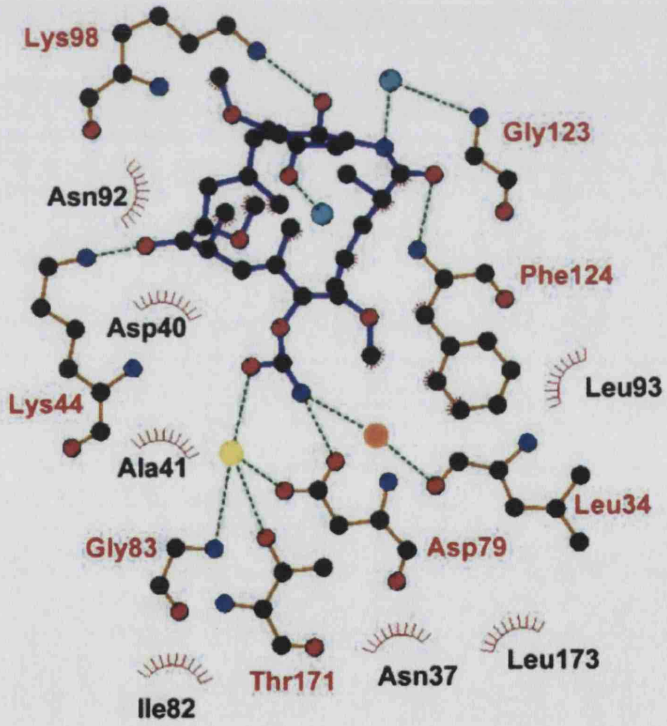

Figure 1.5. Schematic diagram of GM interacting with the N-terminal domain of Hsp90. Hydrogen bonds are shown in green dotted lines and van der Waals contacts in purple 'spokes'. The tightly bound water molecule is shown as a yellow sphere; the water molecule bound to Leu 34 is shown as an orange sphere and other water molecules are shown in turquoise. Picture adapted from Prodromou and Pearl, (2003).

Stebbins *et al.* (1997) suggested two "open" and "closed" conformations, based upon different pocket sizes and accessibility, with the open conformation being compatible with GM binding (Figure 1.4). The movement of the second loop was calculated to be about 9 Å, which displaces helix four and comes in contact with GM by forming one of the pocket walls. The motion of the second loop was facilitated by a portion of helices four and five undergoing helix-to-coil and reverse transitions, as well as being displaced by about 6 Å. This action of the second loop works as a gate of the pocket by changing its width from 8 Å to 12 Å upon drug binding (Stebbins *et al.,* 1997). Figure 1.5 shows GM interacting with the residues of the Hsp90 N-terminal domain.

1.4.2 The ATPase cycle mechanism and activity of the N-terminal domain (the lid hypothesis).

It has been suggested that the rate-limiting step of the ATPase cycle is the hydrolysis of ATP, where ATP becomes trapped and committed to hydrolyse during the cycle (Weikl *et al.,* 2000). Prodromou *et al.* (2000) suggested that the ATPase cycle of Hsp90 drives a molecular 'clamp' via transient dimerisation of the N-terminal domains and that C-terminal truncation mutants lacking inherent dimerisation displayed reduced ATPase activity. The authors have also shown that the 5'-adenylamido-diphosphate (AMP-PNP) promotes association of N-termini in intact Hsp90. In conclusion they suggested a model in which nucleotide binding in the N-terminal domain of Hsp90 caused a conformational change in a segment of the N-terminus that provided a 'lid' for the nucleotide-binding pocket resulting in association of the N-terminal domains. Enforced dimerisation provided by the C-

terminus drives an ATPase-coupled 'clamp' mechanism essentially identical to those proposed for DNA gyrase B (GyrB), a DNA topoisomerase II, and the DNA-mismatch-repair enzyme (MutL) (Prodromou *et al.,* 2000). Based on the model from GyrB and MutL, the authors suggested a model in which a loop segment folds over the nucleotide bound in the N-terminal domain, acting as an 'ATP-lid' on the nucleotide-binding pocket. The exposed surface of the lid forms a dimer interface, and with the ATP-bound conformation, stabilises the interface, which finally promotes ATP-dependent dimerisation (Wigley *et al.,* 1991; Ban *et al.,* 1999; Prodromou *et al.,* 2000). Therefore it is hypothesised that lid closure could be achieved for Hsp90 by hinging at Gly100 and Gly121, which are the conserved glycines in Hsp90 and in its homologues, GyrB and MutL.

1.4.2.1. Hsp90 homologues

A novel ATP-binding superfamily that includes diverse protein families such as molecular chaperones Hsp90, DNA topoisomerase II and DNA-mismatch-repair enzymes, was first suggested by Bergerat *et al.* (1997). Later, bacterial histidine and mitochondrial serine protein kinases were also added to this family, hence the name GHKL, which stands for Gyrase, Hsp90, histidine Kinase and MutL was proposed (Dutta and Inouye, 2000). The mitochondrial branched-chain α-ketoacid dehydrogenase kinase (BCK) is another member of this superfamily (Machius *et al.,* 2001). The most prominent feature of this superfamily is the unconventional "Bergerat" ATP-binding fold. Despite little primary sequence identity (less than 15%) between the various members, the structures of their ATP-binding domains are essentially superimposable, especially with respect to the

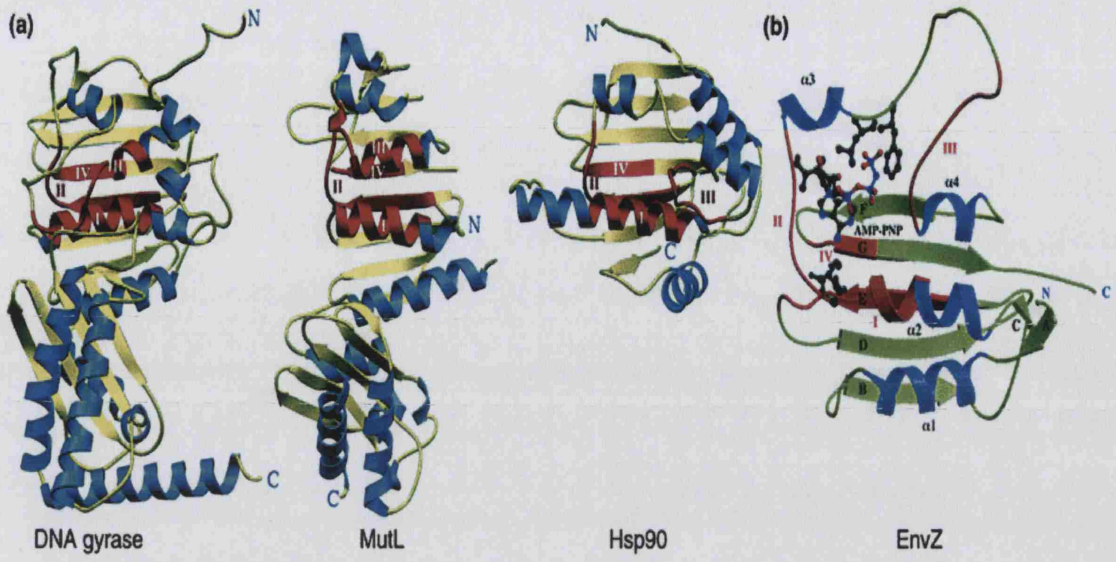

Figure 1.6 Structural comparison of ATP binding domains of DNA gyrase, MutL Hsp90 and EnvZ (a) The conserved ATP binding motif is shown in red, helices in blue, β-sheets in yellow and loops in green. **(b)** In EnvZ bound with AMP-PNP, the β-sheets are in green and helices in blue with the conserved region in red Picture adapted from (Dutta and Inouye, 2000).

novel ATP-binding fold (Figure 1.6) (Dutta and Inouye, 2000).

MutL, its human homolog PMS2 (Guarne *et al.,* 2001) and GyrB have the highest structural similarity (Ban and Yang, 1998). The highest degree of structural similarity in the GHKL superfamily exists in the nucleotide-binding domains of the family members (Figure 1.6, shown in red). The ATP-lid has a strategic location with regards to the ATP-binding pocket. The composition and conformation of the ATP-lid distinguishes the four different classes of proteins in the GHKL superfamily (Figure 1.7).

The ATP-lid of GyrB is a long loop structure (L4) that completely encloses the nucleotide (Figure 1.7) (Wigley *et al.,* 1991). In MutL, this loop is broken by a short helix (α′) and the ATP-lid is partially exposed to the solvent (Ban *et al.,* 1999). Hsp90, on the other hand, has two helices in the ATP-lid (loop 4) in all the crystal structures solved so far points away from the ATP pocket, leaving the

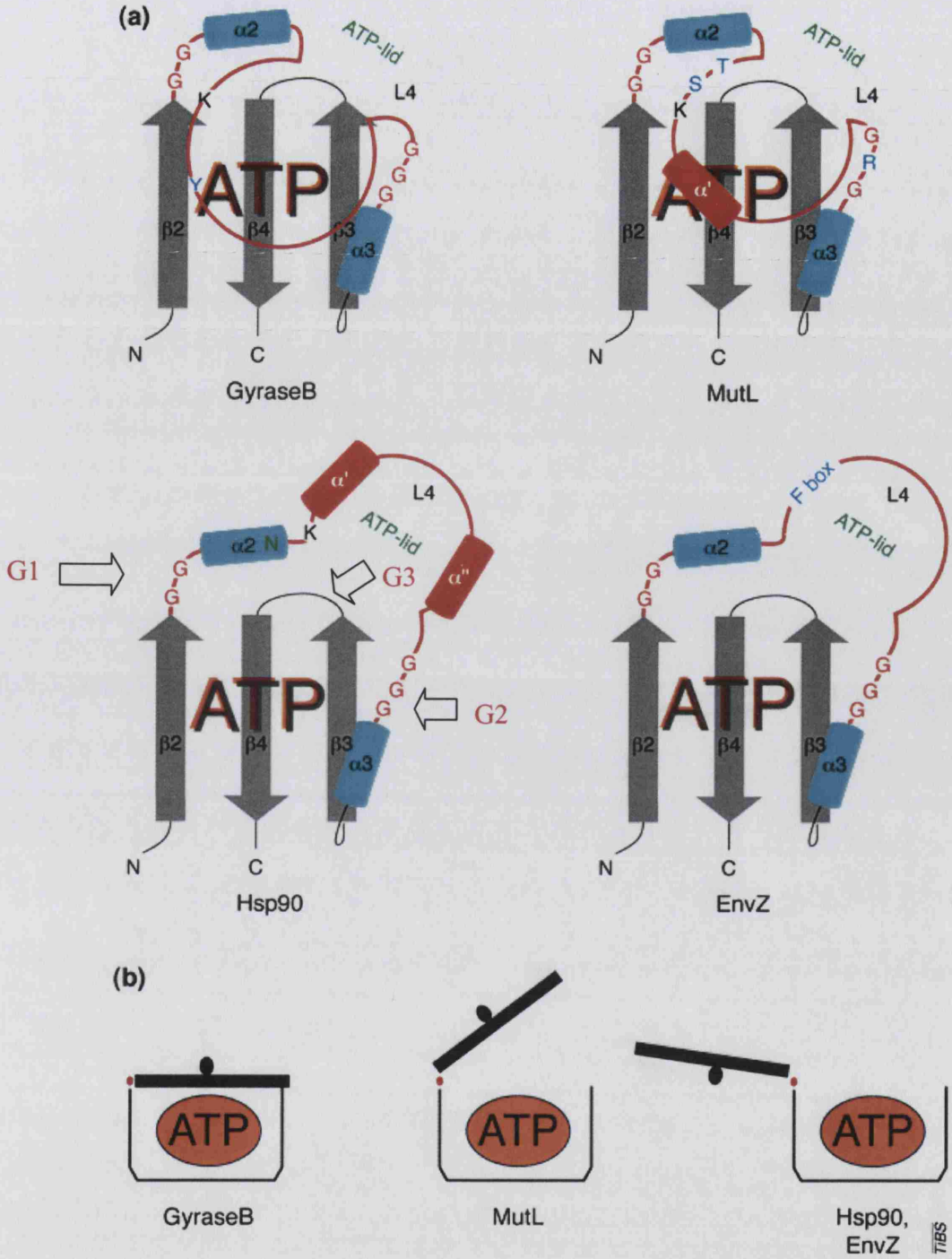

Figure 1.7. Comparison of the formation of the proposed lid in the GHKL superfamily (a) The Bergerat ATP- binding fold in individual members of the GHKL superfamily **(b)** Different conformation of the ATP-lid found in solved structure of member families of the GHKL superfamily. Picture adapted from (Dutta *and* Inouye, 2000).

nucleotide completely exposed (Prodromou *et al.,* 1997). The Hsp90 ATP-lid is considerably longer than in other family members, consisting of 25 residues

compared to the average of 17, and is therefore more structured. The ATP-lid in EnvZ is also extended away from the rest of the molecule and thus the bound nucleotide is exposed. Several different motifs and conserved residues in this area are shown in Figure 1.7. The "Bergerat" ATP binding fold is an α/β sandwich consisting of a four strand mixed β-sheet and three α-helices, forming a deep pocket for nucleotide binding. This pocket is bordered by α-helices 1, 2 and 3, and loops 3 and 4. The bottom of this pocket consists of β-sheets 2, 3 and 4.

Members of this superfamily share four conserved sequence motifs essential for ATP binding that are unrelated to the Walker A and Walker B motifs present in many other ATPases. The conserved motifs of the "Bergerat" ATP-binding fold are the N motif (Motif I) in helix α2 and conserved glycines, known as G1 (Motif II), G2 (Motif III) and G3 (Motif IV) boxes, as shown in Figure 1.7. Three of four conserved sequence motifs (I, II and IV) form a concave ATP binding pocket, while motif III, also known as an F-G2 motif, forms a flexible lid that encloses the bound ATP. Nucleotide binding appears to induce an additional intermolecular interaction causing the ATP-binding domains of GyrB and MutL to dimerise and form a 'molecular clamp' (Ban *et al.,* 1999; Wigley *et al.,* 1991; Prodromou *et al.,* 1997). The structural units that are involved in this inter-subunit interaction are conserved among GyrB, MutL and Hsp90, therefore it seems likely that Hsp90 also dimerises upon nucleotide binding (Prodromou *et al.,* 2000). The hole created within the clamp has been proposed to accommodate a length of double-stranded DNA in the case of GyrB and MutL, or an unfolded length of peptide in Hsp90. Hydrolysis of ATP is necessary to release the bound macromolecule. This series of events forms an essential part of the catalytic cycle of ATPases in GyrB, Hsp90 and MutL (Dutta and Inouye, 2000).

It has been shown that ATP hydrolysis increases in the presence of all monovalent salts in the GHKL superfamily (except for LiCl in MutL) and that it is highest in the presence of NaCl (1.5 to 3 times higher) (Hu *et al.*, 2003). Based on the conserved secondary structure surrounding the monovalent cation-binding site, Hu *et al.* (2003) suggested that a monovalent cation associates with binding of ATP in members of the GHKL family, which might be a common feature of all GHKL proteins. The diversity of the protein sequence at the position equivalent to Pro-341 of BCK, Ala-l00 of MutL and Ser-l21 of GyrB may influence the specificity of monovalent cation selection. This position is occupied by a conserved residue in mitochondrial protein kinases (proline) and the Hsp90 (tyrosine), but by variable residues in MutL, type II topoisomerases and the bacterial histidine kinase families (Hu *et al.*, 2003). The monovalent cations appear to stabilise the ATP lid in both BCK and MutL (Figure 1.8).

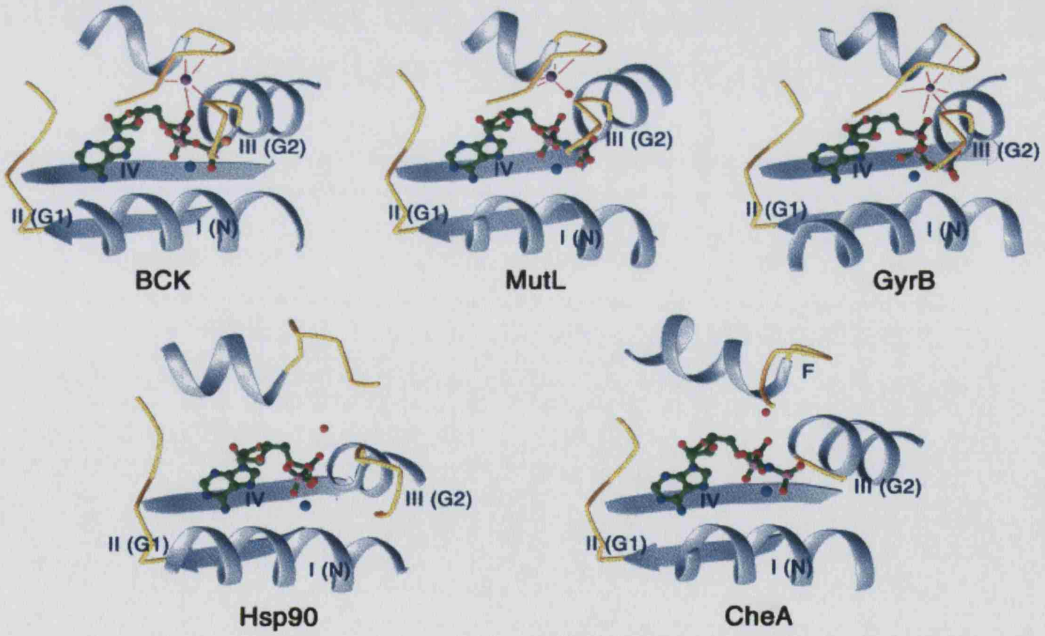

Figure 1.8 Comparison of the monovalent binding site in BCK, MutL, GyrB, human Hsp90 and CheA. The ATP binding site secondary structure is shown in grey with different motifs highlighted. The two hinges of the ATP lid (motif III) are shown in yellow. Nucleotides are represented as a ball stick model. Divalent and monovalent cations are shown in blue and purple respectively and water oxygens is shown in red. Picture adapted from Hu *et al.* (2003).

Due to the absence of the γ-phosphate of ATP in the crystal structures of Hsp90 and with the lid being disordered in histidine kinases EnvZ and CheA, the hinge of the ATP lid that potentially co-ordinates the monovalent cations, has a different conformation where no monovalent cations are observed (Figure 1.8). However, a water molecule has been observed in place of the cations suggesting that it might be replaced by monovalent cations once ATP binding is fully formed (Hu *et al.*, 2003).

1.4.2.2 Mutation studies of the Hsp90 N-termini

Two of the several mutants studied by Prodromou *et al.* (2000) which are related to the lid hypothesis are discussed here. The two mutants are Thr-101-Ile (T101I) and Ala-107-Asp (A107N) which were introduced in the full length protein. The purpose of these studies was to create mutants where one favours the open conformation of the nucleotide binding domain and the other favours the closed conformation (Prodromou *et al.*, 2000). Table 1.6 shows the activities studied for the two mutants.

Construct	**K_d AMP-PNP-Mg^{2+}** (μM)	**ATPase activity** (% of wild type)	**ATPase activity** (Mol/min/mol)
Wild Type	33	100%	0.75
T101I	37	9.4%	-
A107N	37	Increase over wild type	3.81

Table 1.6. Activities of mutants T101I and A107N compared to wild type Hsp90 at 37°C. Data extracted from Prodromou *et al.* (2000).

The residue Thr-l0l is part of a lid segment, which in GyrB closes over the bound ATP (Wigley *et al.*, 1991). The T101I mutation did not affect the stability of the protein or its affinity for AMP-PNP (Table 1.6). Nonetheless, the ATPase

activity of T101I is <5% that of wild type over the temperature range (22-45°C) studied suggesting that the mutation affects the ATPase at a step subsequent to ATP binding. Thus, the T101I mutant which binds AMP-PNP with wild-type affinity has a diminished ability to dimerise in its N-terminal domain in the ATP-bound form. The side chain of Thr-101 packs into a hydrophobic region formed by the side chains of Ile-12 and Leu-15, and the Cα and Cβ of Glu 11. Lid closure necessitates disruption of this interaction and exposes the side chain of Thr-101 on the top surface of the lid. Mutation of threonine to isoleucine would stabilise the hydrophobic interaction in the open lid conformation and destabilise the exposure of the side chain when the lid is closed. Hence the mutation favouring the open lid conformation would disfavour dimerisation and consequently ATP hydrolysis, producing the lower ATPase activity observed in the T101I mutation.

The A107N mutation in yeast Hsp90 has produced no change in AMP-PNP affinity relative to wild type. However, the ATPase activity of this mutant was substantially increased over wild type to an even greater degree than with the thermo-sensitive mutant Thr-22-Ile. Increased ATPase activity of A107N, accompanied by its enhanced dimerisation in the presence of nucleotide, is consistent with improved interactions stabilising lid closure, where in turn closure of the 'clamp' is required for efficient ATPase activity.

1.4.3 Residues involved in dimerisation and the role of the middle domain.

The amino acids corresponding to the first 24 amino acids of Hsp90 represent the first β-strand and the following α-helix, and were found to be

involved in inter-molecular interactions of the N-terminal domains that control the overall turnover of the ATPase cycle (Richter *et al.,* 2002). The known structures of GyrB and MutL and their dimerisation were used as a model to predict the regions involved in the N-terminal dimerisation reaction (Richter *et al.,* 2002). In these proteins, approximately the first 30 residues are involved in N-terminal domain dimerisation (Ban and Yang, 1998, Ban *et al.,* 1999; Brino *et al.,* 2000). Meyer and colleagues (2003) by solving the 35 kDa crystal structure of the middle segment of Hsp90, along with homology studies of the GyrB and MutL, suggested a model where Hsp90 ATPase activity takes place using independent domains in the same molecule to achieve ATP hydrolysis. They identified Arg-380, Asn-377 and Gln-384 as probable ATP catalytic residues contributed by the middle segment of Hsp90, and have showed their involvement in ATPase activity *in vitro* and in chaperone function *in vivo*, Figure 1.9 (b) and (c). The "catalytic loop" bearing the Arg-380 and Gln-384 residues exhibits significant conformational plasticity varying between a helical structure, where the catalytic residues are directed back into the middle segment, to an extended loop in which they could reach the N-terminal domain toward the γ-phosphate of ATP, Figure 1.9 (c).

Overall, the model Meyer and colleagues suggested for the mechanism of Hsp90 action, is that firstly the lid segment in the N-terminal domain of Hsp90 closes upon binding of nucleotide. Closure of the lid segment exposes a hydrophobic surface buried underneath the lid in its open conformation. This buried hydrophobic surface together with the hydrophobic face of the lid itself makes a hydrophobic interaction site that, with its equivalent partner, can form a dimer. This ATP dependant conformational change was hypothesised to represent structural basis for the dimerisation of the N-terminal domains (Prodromou *et al.,*

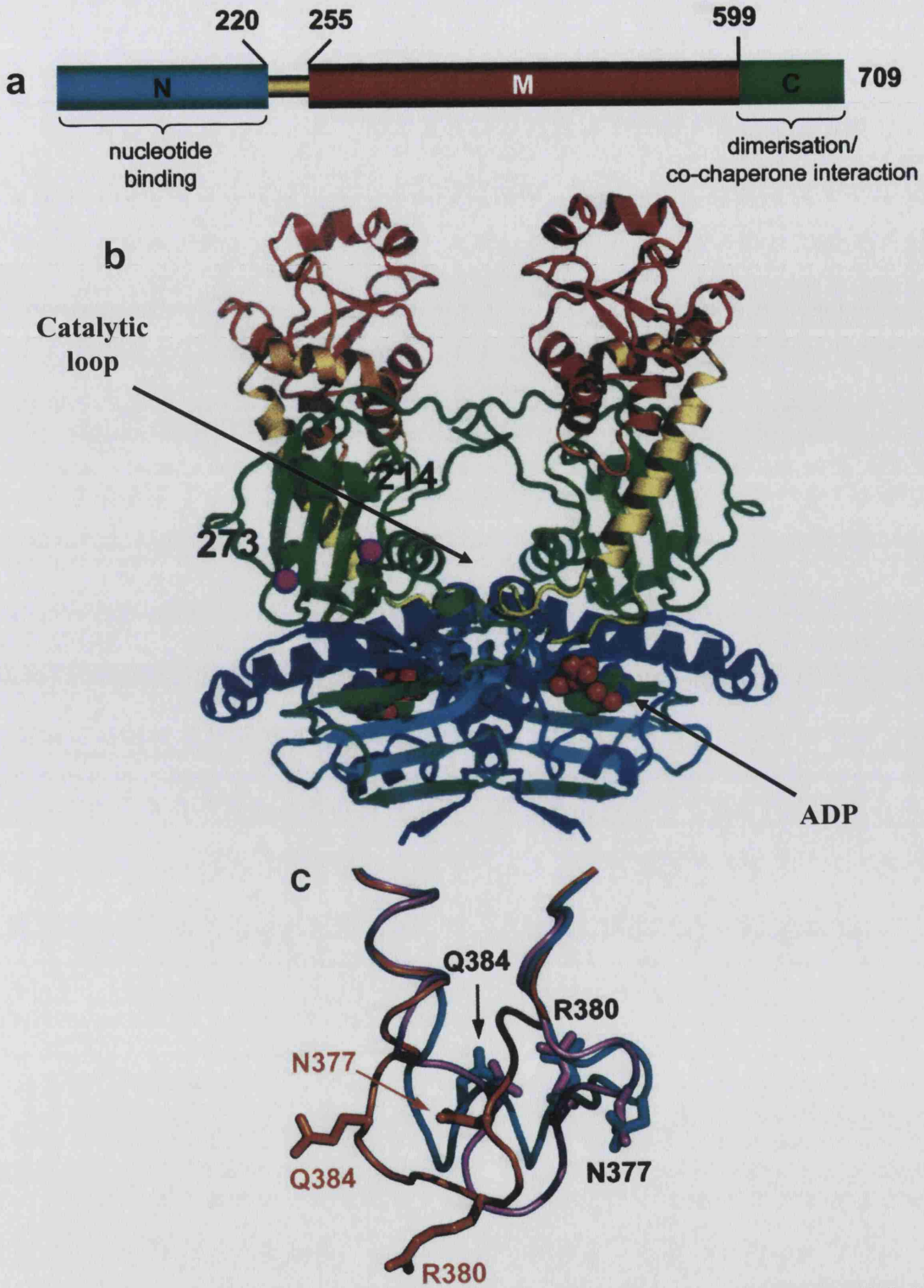

Figure 1.9. Dimerisation of Hsp90 based on the DNA GyraseB model (a) Schematic of Hsp90 with the N-terminal domain in blue, the middle region in red and C-terminal in green. **(b)** Model of the Hsp90 dimer reconstructed from solved fragment structures (middle and N-terminal domains) based on the GyrB dimer, with catalytic loop and ADP binding site highlighted. **(c)** Catalytic loop conformations from three different crystal structures of the middle domain in cyan, pink and orange. The Asn-377, Gln-384 and Arg-380 residues from the middle domain that could be involved in Hsp90 ATPase activity are highlighted. Pictures adapted from Meyer *et al.* (2003).

2000; Chadli *et al.,* 2000). The exposed surface of the closed lid could also interact with the middle segment of the same monomer, with a suggested hydrophobic patch in the middle domain, centred on Phe-349, which could participate in the inter-segment interactions (Meyer *et al.,* 2003). The efficient ATP hydrolysis in Hsp90 appears to require a series of conformational changes that together conspire to be the 'rate-limiting' step of the hydrolysis reaction. Figure 1.9 (b) is a model reconstructed from the determined structural fragments by Meyer and colleagues (2003) based on the GyrB homodimer, which are dimerised in the N-terminal domain in the presence of the nucleotide.

1.5. Kinetic studies of Hsp90 and its N-terminal domain

Studies by Weikl *et al.* (2000), have shown that the ATPase activity of Hsp90 is relatively slow *in vitro* in comparison to other ATP-hydrolysing enzymes and that its activity declines with decreasing temperature (Table 1.7). The K_M for ATP hydrolysis has been shown to decrease from 300 μM at 37 °C to 100 μM at 25 °C in full length Hsp90. The ATP molecules, although bound weakly to the N-terminal domain, are trapped during the conformational changes inside the Hsp90 dimer. It has been also shown that these changes require the presence of the middle domain of Hsp90 and at least in part the presence of the C-terminal dimerisation domain (Weikl *et al.,* 2000; Meyer *et al.,* 2003). The presence of monovalent cations such as; K^+, Na^+, Li^+, NH^{4+} and Rb^+, to a limit, increases the ATP-hydrolysing activity. The N-terminal fragment of yeast Hsp90, N(210), exhibited one-tenth of the wild-type ATPase activity (k_{cat} = 0.04 min^{-1}) at 37°C,

suggesting that regions of the Hsp90 molecule located outside of the nucleotide binding pocket are important for its ATPase activity. Similar to the full-length protein, the ATP hydrolysing activity of N(210) was enhanced in the presence of monovalent cations, Table 1.7 (Weikl *et al.*, 2000).

	k_{cat} 37°C	k_{cat} 25°C	K_M ATP Hydrolysis 37°C	K_M ATP Hydrolysis 25°C	K_d ATP 25°C	K_d ADP 25°C
Hsp90	0.35 min^{-1}	0.1 min^{-1}	300 μM[a]	100 μM[a]	500 μM[b]	150 μM[b]
N(210)	0.04 min^{-1}	-	-	-	132 μM[c]	29 μM[c]

Calculated catalytic constant (k_{cat}) for ATPase activity, a) K_M for ATP hydrolysis b) estimated dissociation constants K_d (Weikl *et al.*, 2000) c) isothermal titration calorimetry measured dissociation constants (K_d) (Prodromou *et al.*, 1997).

Table 1.7. Different kinetic values compared for Hsp90 wild type and the N-terminal domain of Hsp90. Data extracted from Weikl *et al.* (2000) and Richter *et al.* (2002).

Hsp90 binds to ADP more tightly than ATP, as shown by the K_d for ATP and ADP of 500 μM and 150 μM respectively (Table 1.7). Higher K_d values show faster binding and dissociation kinetics of the ATP, despite weak binding of the nucleotide to Hsp90 (Weikl *et al.*, 2000). This was in agreement with results of previous experiments using spin-labelled nucleotides for its weak binding (Scheibel *et al.*, 1997). Hsp90 binds ATP in a two-step mechanism, with ATP hydrolysis being the rate-limiting step of the ATPase reaction, with an apparent k_{obs} of 0.1 min^{-1} at 25°C (Weikl *et al.*, 2000). The stability and nucleotide binding properties of Hsp90 had been measured as; k_{on} 0.13 ± 0.05 S^{-1} μM^{-1}, k_{off} 2.0 ± 0.6 S^{-1} which give a calculated dissociation constant (k_{off}/k_{on}) of 15μM (Weikl *et al.*, 2000; Richter *et al.*, 2002). The ATPase activity of human Hsp90 is significantly lower than that of the yeast homologue, and it has a half-life for ATP hydrolysis of eight minutes at 37°C (McLaughlin *et al.*, 2002). McLaughlin and colleagues (2002) also

found that the ATPase activity of human Hsp90 is highly regulated by both client proteins and co-chaperone binding. The catalytic efficiency of Hsp90 is tightly regulated by intermolecular interactions mediated by N-terminal domain residues and it is thought that the dimerisation reaction itself could be the rate limiting step (Richter *et al.*, 2002).

1.6. Aims of this research

The main aims of the research described here were:

- To accomplish the backbone assignment of the Hsp90 N-terminal domain as a basis for NMR investigation.
- to characterise conformational changes in the Hsp90 N-terminal domain using the NMR backbone assignment with relaxation studies
- to sequentially assign the backbone resonance of Hsp90 N-terminal domain in complex with AMP-PNP and to map its binding site as well as to characterise it using relaxation studies
- to investigate the hypothesised 'loop open'/'loop closed' conformation for the ATPase domain using NMR data
- to investigate how mutants affect the 'ATP-lid'
- and finally to elucidate the interaction of the N-terminal domain with other nucleotides, novobiocin and the Hsp90 middle domain

These studies should provide a tool for further structural elucidation of the Hsp90 N-terminal domain, drug binding studies and mechanism of N-terminal dimerisation.

CHAPTER 2

MATERIALS AND METHODS

All chemicals were purchased either from Sigma Aldrich or BDH unless otherwise stated. Solutions were made using pure deionised water using the Elga Maxima Ultrapure water purification system. General centrifugation steps, unless stated, were performed using an ALC PK130R centrifuge (15 and 50 ml Falcon tubes) and Eppendorf 5415R (Eppendof tubes). All buffers used when dialysing the NMR samples were thermodynamically corrected for temperature (Beynon *et al.,* 1996. www.bi.umist.ac.uk/users/mjfrbn/buffers/makebuf.asp)

2.1 Transformation and purification

2.1.1 The expression system

The plasmid pRSETA vector (Invitrogen), with an insert encoding for residues 1-207 of the *Sacchromyces Cerevisiae* Hsp90 N-terminal domain plus a His-tag (6 histidines [H] and 5 other residues MRGS[HHHHHH]G from a cloning vector), which is under control of a phage T7 promoter, was kindly provided by Dr. Chris Prodromou (Structural Biology Section, Institute of Cancer Research, London, UK). Expression was carried out using the *Escherichia coli* strain BL21(DE3)pLysS (Promega-USA) host cells, which carry a chromosomal copy of the T7 RNA polymerase gene (Prodromou *et al.,* 1996). This strain also carries the DE3 bacteriophage lambda lysogen, which contains the *lacI* gene, the T7 RNA polymerase gene under control of the *lacUV5* promoter, and a small portion of the *lacZ* gene. T7 lysozyme produced from pLysS binds to T7 polymerase, inhibits the transcription and hence reduces basal levels of T7 RNA polymerase. The *lac* repressor suppresses expression of T7 RNA polymerase whereby addition of

isopropyl-β-D-thiogalactopyranoside (IPTG, Melford Laboratories Ltd.) allows expression of T7 RNA polymerase, and as a result, expression of our protein. The plasmids were stored at –20°C in 20 mM Tris buffer. The sequence of the Hsp90 N-terminal protein is shown below in the Figure 2.1.

```
                -1                9               19               29               39
                 |                |                |                |                |
MRGSHHHHHH GMASETFEFQ AEITQLMSLI INTVYSNKEI FLRELISNAS
                49               59               69               79               89
                 |                |                |                |                |
DALDKIRYKS LSDPKQLETE PDLFIRITPK PEQKVLEIRD SGIGMTKAEL
                99               109              119              129              129
                 |                |                |                |                |
INNLGTIAKS GTKAFMEALS AGADVSMIGQ FGVGFYSLFL VADRVQVISK
               149               159              169              179              189
                 |                |                |                |                |
SNDDEQYIWE SNAGGSFTVT LDEVNERIGR GTILRLFLKD DQLEYLEEKR
               199               207
                 |                |
IKEVIKRHSE FVAYPIQL
```

Figure 2.1. Single letter abbreviation of the amino acid sequence for 207 residues of the Hsp90 N-terminal domain from *S. Cerevisiae*. The first 11 residues are from the cloning vector and are not accounted for throughout this thesis.

2.1.2 Preparation of $CaCl_2$ competent cells

E. coli BL21(DE3)pLysS cells were plated out from a glycerol stock onto Luria Bertani (LB) media (10 g/L bacterial peptone, 10 g/L NaCl and 5 g/L yeast extract, pH adjusted to 7.4) and 15 g/L agar (DIFCO laboratories, USA) plates which contained 34 μg/ml chloramphenicol (CAP, Sigma) and incubated overnight at 37°C. A single colony of BL21(DE3)pLysS cells were then inoculated in 5 ml of LB with the same concentration of CAP and grown overnight at 37°C in a shaking incubator (at 200 rpm). This was then transferred to a flask containing 50 ml of fresh LB with CAP and incubated at 37°C, with shaking, until the optical

density at 600 nm (OD_{600}) reached between 0.2-0.5 absorbance units (AU). The flask was stood on ice for 20 min and centrifuged at 2500-3000 rpm for 10-15 min at 4°C, after which the pellet was re-suspended in 20-40 ml ice cold 50 mM $CaCl_2$. This was kept on ice for 20 min and once again centrifuged (at 2500 rpm for 15 min at 4°C) before re-suspending in 1 ml ice cold 50 mM $CaCl_2$ and kept on ice until required. The excess of competent cells were aliquoted in 100 µl samples with 10% v/v glycerol and stored at -80°C. General absorbance measurements during cultural growth were carried out on a Hitachi U-1800 UV/Vis spectrophotometer.

2.1.3 Transformation

1-2 µl of the plasmid DNA carrying the N-terminal domain of Hsp90, was placed in an aliquot of 100 µl of $CaCl_2$ treated competent cells in an eppendorf tube and kept on ice for 15-30 min. Heat shock was performed for 5 min in a 37°C water bath and returned on ice for 2 min. The sample was then incubated at 37°C for 1 h with 900 µl LB media without antibiotics, for recovery, and subsequently plated out on LB/agar plates with 34 µg/ml CAP and 100-150 µg/ml carbenicillin (CAB, Melford Laboratories Ltd.) before incubation overnight at 37°C.

2.1.4 Plasmid purification

The colonies picked from transformed plates were used to inoculate 5 ml LB cultures grown overnight at 37°C. The plasmid purification was carried out using the QIAprep™ Miniprep kit according to the manufactures instructions.

Following elution from the spin column by 50 µl of 10 mM Tris-HCL, pH 8.5, the DNA was stored at -20°C.

2.2 Expression of Hsp90 N-terminus in Minimal Media

The minimal medium (M9) used for the expression of isotopically enriched Hsp90 N-terminal domain contained: 6.5 g/L NaH_2PO_4; 3.0 g/L KH_2PO_4; 0.5 g/L NaCl; 1.0 g/L $(NH_4)_2SO_4$ and 2 to 4 g/L glucose which were filter sterilised and pH adjusted to 7.4. The supplements added per litre of M9 were; 2 ml 1 M $MgCl_2$; 100 µl 0.1 M $CaCl_2$; 100 µl 0.1 M $FeSO_4$ freshly made; 10 µl of the vitamin stock solution and 10 µl of the micronutrients stock. The vitamin supplements were made as a 1000 × concentrated stock solution of: 0.04 g Acetylcholine chloride, 0.05 g folic acid, pantothenic acid, 0.05 g nicotinamide, 0.1 g myo-inositol, 0.05 g pyridoxal HCl, 0.05 g thiamine HCl, 0.005 g riboflavin and 0.1 g biotin prepared in 100 ml deionised distilled water and stored at -20°C. The micronutrients were prepared as a 1000 × concentrated stock solution of: 0.0726 g Na_2MoO_4, 2.473 g H_3BO_3, 0.713 g $CoCl_2.6H_2O$, 0.25 g $CuSO_4.5H_2O$, 1.853 g $MnCl_2.4H_2O$ and 0.2876 g $ZnSO_4$ prepared in 100 ml of deionised distilled water and stored at -20°C. When uniform ^{15}N or $^{15}N/^{13}C$ labelling was carried out, the bacteria were grown in M9 using $^{15}NH_4SO_4$ (Cambridge Isotope Ltd) and $^{12}C_6$-glucose for a ^{15}N labelled sample or $^{15}NH_4SO_4$ and $^{13}C_6$-glucose (Cambridge Isotope Ltd) for a $^{15}N^{13}C$ labelled sample as the sole nitrogen and carbon source, respectively.

A single colony of the transformed *E. coli* was inoculated in LB with glucose 2 g/L, CAP and CAB antibiotics, and then incubated at 37°C with shaking at 220 rpm. Several tubes were prepared and the tube with the fastest growth was

chosen. Once the OD_{600} reached 0.6-1 AU, 50 ml of M9 with supplements, 34 μg/ml CAP, 100 μg /ml CAB and 20% glucose was inoculated with 0.5 ml of the LB culture and incubated overnight at 37°C with shaking. This initial M9 culture was spun down gently (1500 rpm 10 min) and re-suspended in fresh M9. This was used to inoculate 1 L M9 culture containing supplements, 100 μg /ml CAB, 34 μg/ml CAP, 20% glucose with the desired isotope enrichment and subsequently incubated at 220 rpm at 37°C until the OD_{600} reached 0.8- 1.0 AU. The T7 promoter was then induced by addition of IPTG to a final concentration of 0.1 mM and incubated at 37°C with shaking at 220 rpm for 8 h for the ^{15}N labelled and $^{15}N^{13}C$ labelled samples.

The cells were then harvested by centrifugation at 5000 rpm for 20 min at 4°C using a SORVALL RC5B GS3 super light rotor and the resulting pellets were stored at -20°C.

2.3 Expression of the Hsp90 N-terminus in LB media

A single colony of the transformed *E. coli* was inoculated into 400 ml of LB containing 34 μg/ml CAP and 100 μg /ml of CAB and grown overnight in a shaking incubator at 37°C. A 100 ml aliquot of the growth was then transferred to 700 ml of LB media containing the same concentration of antibiotics and grown at 37°C in a shaker incubator until the OD_{600} reached about 0.9 AU. The T7 polymerase was then induced by IPTG (final concentration of 0.1 mM). Cultures were harvested after 4 h of growth (as described for M9 growth, Section 2.2). The resulting pellets were then stored at -20°C.

2.4 Expression of the Hsp90 N-terminus in $^{2}H_2O$

Perdeuteration (>95% at Cα positions) and uniform $^{15}N/^{13}C$ isotope labelling of the polypeptide was achieved by growing the bacteria in M9 with $^{2}H_2O$ (99.9% $^{2}H_2O$, Goss Scientific Instruments) instead of H_2O and using $^{15}NH_4SO_4/^{13}C_6$-glucose as the sole nitrogen and carbon sources. A single colony of the transformed *E. coli* was inoculated into an initial flask of M9 in H_2O using $^{15}NH_4SO_4/^{13}C_6$-glucose and grown in a shaking incubator at 37°C in the presence of 34 μg/ml CAP and 100 μg /ml of CAB until the OD_{600} reached 0.5 AU. Sufficient amount of this culture was centrifuged and re-suspended in 200 ml of M9 in $^{2}H_2O$ to obtain an OD_{600} of 0.1 AU, and grown until the OD_{600} reached 0.5 AU. As a final step, sufficient amount of this culture was centrifuged and re-suspended in 2 x 500 ml of M9 in $^{2}H_2O$ to obtain an OD_{600} of 0.1 AU and grown to reach an OD_{600} of 0.8 AU before subsequent induction with IPTG at a concentration of 0.1 mM. Proper aeration and high speed shaking is crucial for bacterial growth in $^{2}H_2O$ hence flasks with grooves were used. After induction with IPTG, cells were further grown for 12 h before harvesting. Cells were harvested as described previously in Section 2.2. Hsp90 expression in *E. coli* produced a yield of ~15 mg/L of Hsp90 N-terminus which allowed for the economic ^{2}H, ^{13}C and ^{15}N labelling of the protein.

2.5 Purification of the Hsp90 N-terminus

The bacterial cell pellets were thawed on ice, re-suspended in 20 mM Tris buffer pH 8.0 and disrupted by sonication, using a *Sanyo* Soniprep 150 Ultrasonic

disintegrator, in the presence of Complete™ EDTA-free protease inhibitors cocktail (Boeringer Mannheim) while kept on ice at all times. The cell lysate was then spun at 25,000 rpm for 25 min at 4°C using a Beckman L7-65 ultra centrifuge with $70T_i$ rotor. The supernatant retained with the soluble protein was purified by loading it into a 15 ml Talon™ Metal Affinity Resin column (CLONTECH), equilibrated in 20 mM Trizma-Base at pH 8.0 containing 100 mM NaCl and 0.1 mM NaN_3 (buffer A) using a ÄKTA™ FPLC™ system (Amersham Pharmacia). The column was then washed extensively (4 column volumes) with buffer A, followed by buffer A containing 20 mM imidazole pH 8.0 and then eluted with buffer A containing 300 mM imidazole at pH 7.0. The result of running the fractions on a 12% Tricine-sodium dodecyl sulphate (Tris-Tricine SDS) polyacrylamide gel shows that the majority of the protein was eluted in buffer A containing 20 mM imidazole (shown in Figure 2.2). The protein was subsequently concentrated using an Amicon® stirred cell equipped with a YM10 membrane or Vivaspin20® sample concentrator (Vivascience, Sartorius) with an appropriate molecular cut-off.

The protein was then further purified using size exclusion chromatography columns (Hiload™ 16/60 Superdex™ 75 prep grade, Amersham Biosciences, UK). The gel-filtration column was connected to the ÄKTA™ FPLC™ and equilibrated with 20 mM Tris-HCl, 500 mM NaCl, 5mM EDTA and 0.1 mM NaN_3 adjusted to pH 8.0 and filter sterilised. The protein sample was concentrated to 1 ml and injected into the column. The protein was eluted following the absorbance at 280 nm while the FPLC was run at a constant flow rate of 1 ml/min. The fractions collected were screened by SDS- polyacrylamide gel electrophoresis (SDS-PAGE).

The His-tag proteins were finally dialysed against 2 × 1 L of 20 mM Tris buffer and 0.1 mM NaN_3 at pH 8.0 and concentrated using Vivaspin6® sample

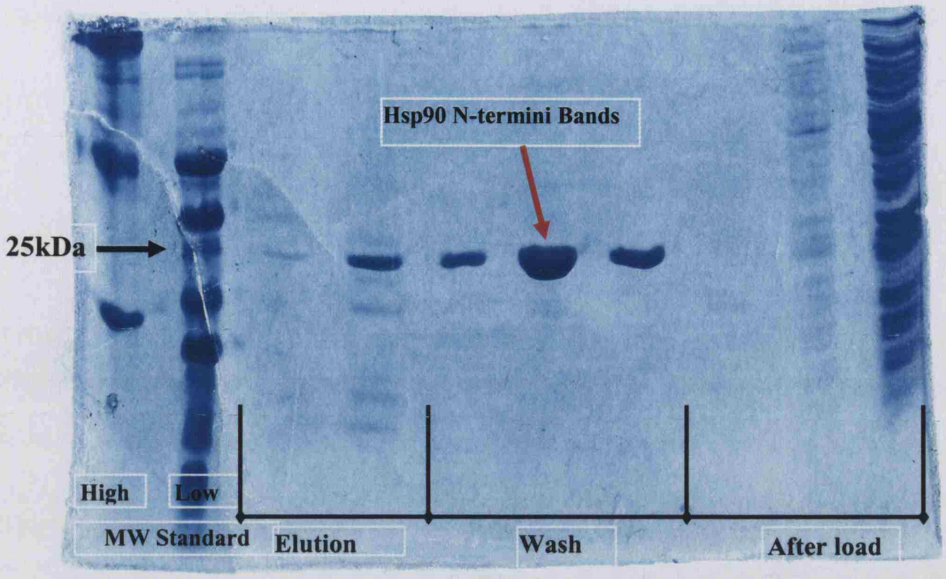

Figure 2.2. A 12% Tris-Tricine SDS PAGE gel displaying aliquots collected during purification of the Hsp90 N-terminal. The gel, stained with Coomasie brilliant blue R_{250}, was used to screen the sample taken during the purification of the Hsp90 N-terminal domain. Proteins that do not bind to the Talon column appear in the after load. The majority of the Hsp90 N-termini was collected during the wash step (Buffer A containing 20 mM imidazole). Non-specific binding proteins and the remainder of the Hsp90 N-terminal domain were collected during elution (Buffer A containing 300 mM imidazole). High and low molecular weight markers are shown on the left with the 25kDa marker band highlighted.

concentrators (Vivascience, Sartorius) with appropriate molecular weight retention to the required volume for NMR experiments. The Hsp90 N-terminal domain expression in *E.coli* that were isotopically enriched with ^{13}C and ^{15}N labelling produced a yield of ~25 mg/L of protein (for either single or double labelled samples).

2.6 Protein concentration measurements

Tris-Tricine SDS-PAGE gel electrophoresis based on the Schägger method (Schägger and von Jagow, 1987) was carried out using BioRad Mini Protean II kit equipment. The Tris-Tricine SDS-PAGE gels were made with 3% SDS, 12% acrylamide for the separating gel and 3% SDS, 4% acrylamide for the stacking gel using BioRad self-assembly gel construction kits. The 10 x concentrated anode

buffer was made using 2 M Tris with pH adjusted to 8.9. The 10 x concentrated cathode buffer contained 1 M Tris and 1M Tricine with 1% SDS w/v added after the pH was adjusting to 8.9. Following electrophoresis the bands were visualised by staining with Coomassie Brilliant Blue R_{250} and destained using a 40% methanol and 7% acetic acid solution.

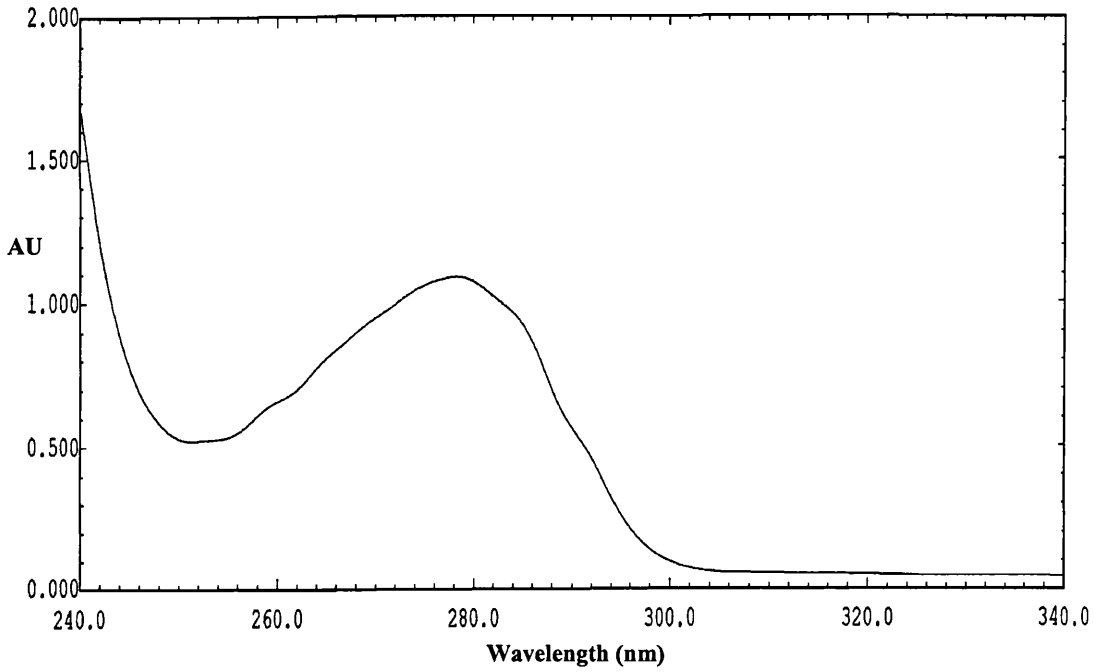

Figure 2.3 A baseline corrected UV/Vis spectrum for the purified Hsp90 N-terminal. The spectrum was recorded by scanning from 340 to 240 nm in 1 cm path length quartz cuvettes with the highest absorbance at 280 nm at about 1.1 AU. Protein concentration was calculated as 1.88 mg/ml in 20 mM Tris buffer at pH 8.0.

Protein concentrations were measured using an absorbance at 280 nm by scanning between 340 to 240 nm wavelengths using a Varian Cary 100 spectrometer with baseline correction using a blank buffer (Figure 2.3). The extinction coefficient of the Hsp90 N-terminal domain was calculated from the amino acid sequence based on the Gill and von Hippel (Gill and von Hippel, 1989) method to ε_{280}= 13370 M^{-1} cm^{-1}.

2.7 Buffer Screening

To find the optimal condition for protein solubility, small volumes of highly concentrated protein (10-15 mg/ml) were screened against four different buffers; Tris HCL, Bis(2-hydroxyethyl)aminotris-(hydroxymethyl)-methane (Bis-Tris), NaOAc and KH_2PO_4, all at a concentration of 50mM. The above buffers were prepared with various salt concentrations (no salt, 100 mM, 500 mM, and 1.0 M NaCl) and various pH (ranging from 3.0 to 9.0 all prepared at room temperature) (Table 2.1 and 2.2). The buffer screening was based on the microbatch protein crystallisation screening method (Chayen *et al.,* 1992) using Hampton 48 wells (Hampton Research). 1 µl aliquots of concentrated protein were placed in a 48 well plate and 5 µl of the above buffers were subsequently added and mixed with the protein sample. The plates were cover with mineral oil in order to prevent evaporation of the mixture and subsequently kept at room temperature.

The Hsp90 N-terminus was found to be more prone to precipitation at high salt concentration (0.5 –1 M) and at a lower pH as shown in Table 2.1 and 2.2. Precipitation of the protein happened after an hour in the presence of divalent cations ($MgCl_2$ and $CaCl_2$) especially in KH_2PO_4 and NaOAc buffers at all pH ranges and after 2 days in Tris and Bis-Tris. Comparison of Bis-Tris with Tris buffer showed a higher level of precipitation in Bis-Tris buffer. In the KH_2PO_4 buffer, the protein appeared stable at pH 7.0 in the presence of 100 and 500 mM NaCl, but any small change in the pH or addition of Mg^{2+} resulted in precipitation of the sample (Table 2.1).

The best buffer found was 20 mM Tris buffer pH 8.0, without salt, and was therefore used as our NMR buffer. The addition of 50 mM $MgCl_2$, as required for

TRIS 50mM					Potassium Phosphate 50 mM				
NaCl 0 mM					NaCl 0 mM				
6	7	8	9	pH	5	6	7	8	pH
X	X			Result	XX?	XX	XX		Result
NaCl 100 mM					NaCl 100 mM				
6	7	8	9	pH	5	6	7	8	pH
	X	?		Result	XXX	X		XX	Result
NaCl 500 mM					NaCl 500 mM				
6	7	8	9	pH	5	6	7	8	pH
		X	X	Result	XXX	XX		XX	Result
NaCl 1000 mM					NaCl 1000 mM				
6	7	8	9	pH	5	6	7	8	pH
		XX	XX	Result	XXX	XXX	X	X	Result
$CaCl_2$ 200 mM					$CaCl_2$ 200 mM				
6	7	8	9	pH	5	6	7	8	pH
XX	XX	X	XX	Result	XXX	XXX	XX?	XX	Result
$MgCl_2$ 200 mM					$MgCl_2$ 200 mM				
6	7	8	9	pH	5	6	7	8	pH
XX	XX	X	XX	Result	XXX	XXX	XX?	XX	Result
Tris buffer pKa = 8.08 at 20°C, pH range 7.0 -9.0					Phosphate buffer pKa = 7.21 at 20°C, pH range 6.3 -8.3				

Table 2.1. Phosphate and Tris buffer screening for the non-labelled Hsp90 N-terminal domain protein. 5µl of each buffer and 1µl of the protein at a concentration of about 10 -15mg/ml (protein initial buffer is 10mM Tris pH=7) were added to each well and covered with mineral oil to prevent evaporation. All experiments were conducted at room temperature. **Key: XXX**-Complete precipitation, **XX**-Moderate precipitated, **X**-Little precipitation,**?**- Precipitated after a week, **RED** occurred quickly **BLACK** occurred after 3 days.

NaOAc 50 mM					BIS-TRIS 50mM				
NaCl 0 mM					NaCl 0 mM				
3	4	5	6	pH	5	6	7	8	pH
X	XX	XXX		Result	XX		X		Result
NaCl 100 mM					NaCl 100 mM				
3	4	5	6	pH	5	6	7	8	pH
XX	XX	XXX		Result	XX	X	X?	?	Result
NaCl 500 mM					NaCl 500 mM				
3	4	5	6	pH	5	6	7	8	pH
XXX	XXX	XXX	X	Result	XXX	X	XX	XX	Result
NaCl 1000 mM					NaCl 1000 mM				
3	4	5	6	pH	5	6	7	8	pH
XXX	XXX	XXX	XX	Result	XXX	XX	X	XX	Result
$CaCl_2$ 200 mM									
3	4	5	6	pH					
XX		XXX	XX	Result					
$MgCl_2$ 200 mM					$MgCl_2$ 200 mM				
3	4	5	6	pH	5	6	7	8	pH
XX	XXX	XXX	XXX	Result	XXX	XXX	XX	XX	Result
NaOAc buffer pKa = 4.75 at 25°C, pH range 3.8 - 5.8					BIS-TRIS buffer pKa = 6.5 at 25°C, pH range 5.8-7.2				

Table 2.2. Sodium acetate and bis-tris buffer screening for the non-labelled Hsp90 N-terminal domain protein Key: **XXX**-Complete precipitation, **XX**-Moderate precipitated, **X**-Little precipitation,**?**- Precipitated after a week, **RED** occurred quickly **BLACK** occurred after a period of one week.

NMR experiments with the presence of the nucleotides caused minimal precipitation at this optimal condition. The protein at the highest working concentration of 0.8 mM continued to precipitate slowly and was found to be very sensitive to handling or change in temperature.

2.8 Acquiring nuclear magnetic resonance (NMR) spectra

NMR spectra acquired on a Varian UNITY 500 MHz and Varian UNITY plus 600 MHz proton frequency spectrometers, were carried out in the UCL/Ludwig Institute NMR laboratory, at temperatures ranging between 5°C and 35°C. The spectrometers were equipped with triple resonance Z-axis pulse field gradient (PFG) probes with four radio frequency (RF) channels for the 500 MHz and three RF channels for the 600 MHZ spectrometer. The pulse sequence used for various experiments, according to the quoted reference stated, were setup by staff members Drs Mark Pfuhl and Richard Harris. All spectra obtained at the 800 MHz proton frequency were recorded at 25°C, at the MRC Biomedical NMR centre, Mill Hill, London using a Varian INOVA spectrometer, supervised by Dr. G. Kelly.

2.8.1 Spectra recorded for single and double labelled protein samples

The experiments recorded on the ^{15}N labelled protein were ^{15}N HSQC (Bodenhausen and Ruben, 1980); ^{15}N 3D NOESY-HSQC (Ikura *et al.,* 1990a) and ^{15}N 3D TOWNY-HSQC (Kadkhodaei *et al.,* 1993). The experiments recorded on $^{15}N^{13}C$ labelled samples were ^{13}C-edited HSQC (Vuister and Bax, 1992), HNCA (Ikura *et al.,* 1990b), HN(CO)CA and HN(CACO)HA (Clubb and Wagner, 1992).

The $^{15}N^{13}C$ labelled samples were dissolved in 90% H_2O and 10% D_2O, containing 20 mM KH_2PO_4, 100 mM NaCl and 0.1 mM NaN_3 at pH* 7.0 (pH* not corrected for 10% D_2O). The concentration of the protein ranged between 0.3 – 0.8 mM. The parameters used for recording the above 3D experiments are shown in Table 2.3.a.

2.8.2 Spectra recorded for the apo and AMP-PNP bound backbone assignment using a triple labelled sample

The NMR experiments used for resonance assignment of the $^{1}H^{15}N$, ^{13}CO, $^{13}C\alpha$ and $^{13}C\beta$ nuclei were determined using a uniformly $^{2}H,^{15}N,^{13}C$-labelled Hsp90 N-terminus sample at 0.5 mM, on the Varian UNITY plus 500 MHz spectrometer in 90% H_2O and 10% D_2O containing 20 mM Tris, 0.1 mM NaN_3 pH* 8.0 (* not corrected for 10% D_2O) at 25°C. Sensitivity and resolution enhancement of the spectra was obtained by perdeuteration of the sample and hence reduction of the nuclear relaxation effects that arise for large molecules in solution. The triple resonance experiments used for sequential backbone assignment of the Hsp90 N-terminal domain were HNCA, HN(CO)CA, HN(COCA)CB, HN(CA)CB, HNCO, HN(CA)CO data sets (Yamazaki *et al.,* 1994b). ^{1}H-^{15}N HSQC and ^{15}N-edited 3D NOESY-HSQC spectra (200 ms mixing time) were recorded from a ^{2}H, ^{15}N, ^{13}C-labelled protein on a Varian INOVA 800 MHz. NOESY-HSQC and ^{15}N TOCSY-HSQC spectra were recorded for a uniformly ^{15}N-labelled sample on a UNITY plus 600 MHz to assist in assignment of $^{1}H^{\alpha}$ signals. Using these experiments an almost complete backbone $^{1}H^{N}$, $^{1}H^{\alpha}$, ^{15}N, $^{13}C\alpha$, $^{13}C\beta$ and ^{13}CO assignment for apo and AMP-PNP nucleotide bound protein was obtained. The parameters used for recording the above 3D experiments are shown in Table 2.3.b.

a) Spectra recorded on protonated sample

3D Experiment	Data set Matrix	Acquisition times (ms)	Recovery delay (s)	Transients per FID	^{13}C carrier position	^{1N}N carrier position	Total recording time (h)
HNCA	$48(t_1)\times 40(t_2)\times 256(t_3)$	$t_1(^{13}C\alpha) = 10.4$, $t_2(^{15}N) = 19.1$, $t_3(^{1}H) = 64$	1.3	24	54.7	119	80
HN(CO)CA	$56(t_1)\times 40(t_2)\times 256(t_3)$	$t_1(^{13}C\alpha_{i-1}) = 12.4$, $t_2(^{15}N) = 19.1$, $t_3(^{1}H) = 64$	1.2	24	57.1	119	80
NOESY-HSQC	$128(t_1)\times 48(t_2)\times 1024(t_3)$	$t_1(^{1}H) = 17.3$, $t_2(^{15}N) = 22.9$, $t_3(^{1}H) = 82.6$	1.3	8	-	119	85
TOWNY-HSQC	$100(t_1)\times 48(t_2)\times 512(t_3)$	$t_1(^{1}H) = 13.5$, $t_2(^{15}N) = 22.9$, $t_3(^{1}H) = 82.6$	1.3	8	-	119	85
HN(COCA)HA	$32(t_1)\times 32(t_2)\times 512(t_3)$	$t_1(^{15}N) = 15.2$, $t_2(^{1}H\alpha) = 14.5$, $t_3(^{1}H) = 64$	1.2	16	-	119	85

b) Spectra recorded on deuterated sample

3D Experiment	Data set Matrix	Acquisition times (ms)	Recovery delay (s)	Transients per FID	^{13}C carrier position	^{1N}N carrier position	Total recording time (h)
HNCA	$72(t_1)\times 32(t_2)\times 256(t_3)$	$t_1(^{13}C\alpha) = 18.8$, $t_2(^{15}N) = 18.3$, $t_3(^{1}H) = 76.8$	1.3	16	56.8	119	63
HN(CO)CA	$72(t_1)\times 32(t_2)\times 256(t_3)$	$t_1(^{13}C\alpha_{i-1})$=18.8, $t_2(^{15}N) = 18.3$, $t_3(^{1}H) = 76.8$	1.2	16	57.1	119	88
HN(CA)CB	$66(t_1)\times 32(t_2)\times 256(t_3)$	$t_1(^{13}C\beta) = 7.3$, $t_2(^{15}N) = 18.3$, $t_3(^{1}H) = 76.8$	1.3	24	-	119	89.3
HN(COCA)CB	$66(t_1)\times 32(t_2)\times 256(t_3)$	$t_1(^{13}C\beta_{(i-1)})$= 6.7, $t_2(^{15}N) = 18.3$, $t_3(^{1}H) = 76.8$	1.3	32	-	119	89.3
HNCO	$40(t_1)\times 32(t_2)\times 256(t_3)$	$t_1(^{13}CO_{(i-1)}) = 22$, $t_2(^{15}N) = 18.3$ $t_3(^{1}H) = 76.8$	1.3	8	178.3	119	17.2
HN(CA)CO	$32(t_1)\times 32(t_2)\times 512(t_3)$	$t_1(^{13}CO_{(i),(i-1)})$=17.6,$t_2(^{15}N)$=18.3,$t_3(^{1}H)$= 153	1.2	48	175.7	119	83.1

Table 2.3. 3D experiments recorded on a proton and deuterated samples. All spectra were zero filled to twice the number of points (the data set matrix) prior to Fourier transformation with forward linear prediction carried out on the t_2 dimension. **a)** Shows all spectra recorded on a protonated double labelled sample and **b)** shows all spectra recorded using a deuterated triple labelled sample.

2.9 Processing NMR data

The raw NMR data sets were processed using the NMRPipe program version 2.1 written and developed by Delaglio and colleagues (Delaglio *et al.,* 1995). Several different window functions including Gauss Broaden and sine-bell functions were used for standard manipulations of the data sets. The result was then zero-filled to at least twice the number of points and baseline corrected, zero and first order phase corrections were used if necessary. In all triple resonance 3D spectra, linear prediction of the ^{15}N indirect dimension was incorporated. The precise processing steps varied between the data sets. Spectra were visualised and inspected initially using NMRDraw version 2.1 (Delaglio *et al.,* 1995).

The processed spectra were converted into the AZARA (Boucher, 2002) format using the PIPE2AZARA command. The spectra were visualised and cross-referenced in Plot2 (Boucher, 2002). The sequential assignments for the Hsp90 N-terminal domain backbone were carried out by visual inspection using the ANSIG analysis package (Kraulis, 1989) with contour and crosspeak files generated by AZARA using the package's internal commands. All softwares were run on a SGI O2® Silicon Graphics computer or a PC with the Linux operating system.

2.10 Relaxation experiments

2.10.1 Acquiring and processing the $^{15}NT_1$, $^{15}NT_2$, $^{15}N\{^1H\}$ heteronuclear-NOE relaxation experiments

The ^{15}N T_1, T_2 and heteronuclear $\{^1H\}$-^{15}N NOE experiments were carried out on a Varian UNITY plus 600 MHz using a ^{15}N-labelled sample in 20mM Tris

and 1.0 mM azide, pH* 8.0 at 25°C. Experiments were carried out on ^{15}N labelled samples of Hsp90 wild type N-terminal with or without the presence of nucleotides. The experiments were based on published pulse sequences (Kay *et al.,* 1989a) with gradient coherence selection and sensitivity enhancement (Zhang *et al.,* 1994). The relaxation delays and pre-saturation periods are shown in Table 2.4.

The ^{15}N T_1 and ^{15}N T_2 relaxation experiments were recorded as a set of pseudo–3D HSQC experiments, i.e. a series of 2D HSQC experiments with different relaxation delay periods forming its third dimension. The relaxation spectra were processed using NMRPipe, implementing an artificial time point for each relaxation delay, and then finally converted to separate 2D NH spectra in the AZARA format for each relaxation delay using PIPE2AZARA. A ^{1}H, ^{15}N-HSQC spectrum previously recorded, processed and assigned for the Hsp90 N- terminal domain was used as reference for the 2D [^{1}H, ^{15}N]-correlation spectra in the final ANSIG session of which all the 2D NH relaxation spectra were loaded. Separate ANSIG sessions were created for different sets of $^{15}NT_1$, $^{15}NT_2$ and heteronuclear $\{^{1}H\}$-^{15}N NOE experiments. The amide crosspeaks in the 2D HSQC reference spectrum were used in the relaxation spectrum to extract the signal intensity using ANSIG. ANSIG scripts were written in-house originally by Dr Mark Pfuhl (Pfuhl *et al.,* 1999) and later edited to optimise crosspeak intensity extraction in the overlapped areas of the spectra by Dr Mark Williams. The values corresponding to the assigned crosspeaks were stored as text files for further analysis.

The $\{^{1}H\}$-^{15}N heteronuclear NOE were also recorded as a set of pseudo 3D experiments in the presence and absence of proton saturation. The data sets were processed as described previously for T_1 and T_2 spectra and signal intensity values were extracted using ANSIG in-house written scripts to text files in a similar

Sample	Experiment		Relaxation Delay Period (s) [a]										
Hsp90	^{15}N T_1	0.00819	0.03278	0.06557	0.13114	0.26228	0.52457	0.78686	1.04915	1.31144	1.57372	0.13114	0.52457
	^{15}N T_2	0.000	0.00409	0.01229	0.02049	0.02868	0.03688	0.04098	0.04508	0.012295			
	$\{^1H\}$-^{15}N NOE	0.000	2.44255	2.44255	0.000								
+AMP-PNP	^{15}N T_1	0.00819	0.01638	0.03278	0.06557	0.13114	0.26228	0.52457	0.78686	1.04915	1.31144	1.57372	0.13114
		0.52457											
	^{15}N T_2	0.000	0.00409	0.00819	0.01229	0.02049	0.02868	0.03688	0.01229	0.02868			
	$\{^1H\}$-^{15}N NOE	0.000	2.44255	2.44255	0.000								

[a] In ^{15}N T_1 and ^{15}N T_2 experiments, the time periods stated refer to the length of time permitted for relaxation in the pulse sequence. In the case of $\{^1H\}$-^{15}N NOE experiments the time stated refers to the length of the proton saturation period

Table 2.4. Delay times for ^{15}N relaxation experiments carried out on apo- Hsp90 N-terminal samples, with/without AMP-PNP. Note an extra point was collected in the ^{15}N T_1 relaxation experiment with different relaxation delay settings in the $^{15}NT_2$ experiment for the AMP-PNP bound protein.

manner to the above. The noise intensity values from T_1, T_2 and $\{^1H\}$-^{15}N NOE experiments were extracted using PLOT2 (Boucher, 2002) from a region of the spectrum unoccupied by crosspeaks.

Each $^{15}NT_1$ or $^{15}NT_2$ spectrum was obtained with 1024 and 64 complex data points collected in proton and nitrogen dimensions with spectral widths of 5570.25 and 2440.06 Hz respectively. The spectrum was recorded with 32 transients and took 38 h and 15 min for $^{15}NT_1$ and 23 h for $^{15}NT_2$ to complete. The spectra were processed using the Gauss broaden and sine-bell window functions for apodization in proton and nitrogen dimensions respectively and zero-filled to twice as number of points

The $\{^1H\}$-^{15}N heteronuclear NOE spectrum was recorded with 0 and 2.44255 delays (for proton saturation) and was repeated twice for error analysis. Each spectrum was recorded with 1024 and 64 complex data points collected in proton and nitrogen dimensions with spectral widths of 5570.25 and 2440.06 Hz accordingly. The spectrum was recorded with 40 transients, which took 22 h and 30 min to complete. The spectrum was processed using the Gauss broaden and sine-bell window functions in proton and nitrogen dimensions respectively with the FIDs zero-filled to twice the number of points and then finally Fourier transformed.

2.10.2 Calculating the R_1 and R_2 auto - relaxation rates

In order to calculate the relaxation rates, R_1 (T_1^{-1}) and R_2 (T_2^{-1}), the signal intensity values from$^{15}NT_1$ and $^{15}NT_2$ experiments and the relaxation time delays were fitted to a single exponential decay equation by the least squares regression minimisation method of Levenberg-Marquardt (Kay *et al.,* 1992; Peng and

Wagner, 1994) using Mathematica® version 4.1 for Linux (Wolfram, 2002). The output result is a text file consisting of the assigned peaks with their relaxation rate measured for each residue. A standard deviation for each experimental signal was calculated from the difference between two separate experiments with identical relaxation delay values recorded at the end of each T_1 and T_2 experiment. The errors in the relaxation rate were analysed using the Monte Carlo simulation of the errors in the individual data points.

2.10.3 Calculating the $\{^1H\}$-^{15}N heteronuclear NOE cross - relaxation rates

The $\{^1H\}$-^{15}N heteronuclear NOE experiment measures the cross-relaxation rate between ^1H and ^{15}N nuclei in the amide NH group. The $\{^1H\}$-^{15}N heteronuclear NOE value for each selected NH crosspeak was the ratio of signal intensities, from 2D $\{^1H\}$-^{15}N heteronuclear correlation spectra, with and without proton saturation. Experiments were repeated twice to validate the reproducibility of saturated and non-saturated signal intensity. For error analysis, the largest of either difference between the repeated experiments or the noise was used. All measurements were carried out using Mathematica® version 4.1 for Linux (Wolfram, 2002) from the script written in-house by Dr Mark Williams.

2.10.4 Calculating the isotropic rotational correlation time

The isotropic rotational correlation times (τ_c) were calculated from R_2/R_1 data sets, where the flexible regions (including both protein terminals), internal

mobile regions and chemical exchange contributions to R_1, R_2 and the $\{^1H\}$-^{15}N heteronuclear NOE values were filtered out (Mandel *et al.,* 1996). To estimate the error in the calculated τ_c, a Monte Carlo approach was used, using the experimental mean R_2/R_1 ratio and the standard deviation of the filtered data set to generate a simulated distribution of τ_c ratios. All the measurements and error analysis was carried using Mathematica® version 4.1.

2.11 Measuring translational diffusion coefficients using one-dimensional ^{1}H NMR

Translational diffusion coefficients, and therefore estimation of molecular weight, were measured using 1D PFG experiments (Altieri *et al.,* 1995; Dingley *et al.,* 1995) using WATERGATE for water suppression prior to acquisition. The experiments were performed at gradient strengths between 9.36 and 56.16 Gcm^{-1} (Table 2.5) at 500 MHz proton frequency at temperatures between 10 to 35°C on a sample of ^{15}N Hsp90 N-terminal domain at a concentration of 0.8 mM in 20 mM Tris, 0.1 mM azide at pH 8.0* (not corrected for D_2O effect).

The overall experiment consisted of 1D spectra at 11 gradient strengths (shown in Table 2.5) with 4096 complex data points collected for every experiment with a spectral width of 8000 Hz and 256 or 512 transients. Spectra were processed using NMRPipe and analysed using ANSIG. The data were apodized using the Exponential Window function, zero filled to twice the number of points, and finally Fourier transformed. The peak intensities were extracted from the methyl region of the 1D spectrum and converted to ASCII format using a script written-in-house by

Dr. Mark Pfuhl. Microcal™ Origin™ version 5.0 (Microcal Software, Inc) was used to analyse the data.

Pulse Field Gradients											
VNMR	4000	6000	8000	10000	12000	14000	16000	18000	20000	22000	24000
Gcm^{-1}	9.36	14.04	18.72	23.4	28.08	32.76	37.44	42.12	46.8	51.48	56.16

Table 2.5 PFG pulse values used in the diffusion experiment. The values in the first row are based on the VARIAN NMR value (500MHz machine) which are converted using Gcm^{-1}=0.00234× VNMR (personal communication with Dr. Mark Pfuhl).

2.12 Titration by NMR

Temperature titration was carried out on a ^{15}N-labelled sample for apo and AMP-PnP bound Hsp90 N-terminal domain at ~0.5 mM in 20 mM Tris buffer and pH* 8.0, for temperatures ranging from 5°C to 35°C, with 5°C intervals. A two-dimensional HSQC spectrum was recorded at each titration point, utilising PFG sensitivity enhancement (Zhang *et al.*, 1994). All the parameters used to obtain the spectra were kept consistent using the same number of transients and spectral widths throughout the experiments. After recording each set of experiments at a fixed temperature, the spectrometer transmitter for proton and nitrogen was tuned, as well as adjusting the shim, prior to recording the next step of the experiment. The results were processed as described previously in Section 2.9, with the 25°C offset for proton and nitrogen used for processing all the spectra at different temperatures. A temperature titration ranging from 10°C to 25°C with 5°C intervals, was also carried out on a ~0.4 mM ^{15}N-labelled sample in 20 mM KH_2PO_4, 30 mM NaCl at pH 7.0*. The parameters were kept similar throughout the experiments with transmitter re-calibration and the shim adjusted in between.

The spectra were processed using the same settings for the proton and nitrogen offsets as in the experiment recorded at 10°C.

The Mg^{2+} titration was carried out on 0.4 mM, ^{15}N labelled sample in 20 mM KH_2PO_4 and 30 mM NaCl at pH 7.0* with 10% D_2O. The titration steps were calculated in a way that by adding the final aliquot, the concentration of the Mg^{2+} equalled that of the protein concentration. To ensure adequate presence of the ion, another point of the titration was collected with excess of the Mg^{2+} to twice the concentration of the protein. The buffer used for preparation of the $MgCl_2$ sample was similar to the buffer used for the protein with the pH adjusted to 7.0. For each step of the titration an aliquot of 2.54 µl of the stock buffer containing 7.38 mM $MgCl_2$ was added. For each step of the titration a HSQC spectrum was recorded on a Varian spectrometer with proton frequency of 500 MHz at 25°C. The spectra were recorded using 8 transients for each FID, a delay time of 1.2 ms and a recording time of 1 h and 50 min for each HSQC spectrum. The data were processed using sine-bell function for apodization, zero filled to the nearest power of two for the complex data matrix and finally Fourier transformed.

The ATP time course titration was carried out on a 0.5 mM sample of ^{15}N-labelled Hsp90 N-terminal domain in 20 mM Tris, 5mM $MgCl_2$ and 0.1 mM azide with 10% D_2O. An aliquot of ATP was prepared in the same buffer with 5 mM $MgCl_2$ and 10% D_2O added to the sample to produce a final concentration of 10 mM ATP (20 times that of the protein concentration). The experiments were carried out using a 500 MHz proton frequency spectrometer at 25°C. The HSQC spectra were recorded as a 1024 ×128 matrix of complex data points using spectral widths of 3333 Hz and 2000 Hz in proton and nitrogen dimensions respectively using 8 transients. Each spectrum took about 20 min to record and overall 12

points were collected. The spectra were processed using Gauss broaden window function for apodization and data were zero filled to twice as number of points, Fourier transformed and finally phased.

CHAPTER 3

THE SEQUENTIAL BACKBONE ASSIGNMENT OF THE HSP90 N-TERMINAL DOMAIN

3.1 Chapter overview

In this chapter, the backbone assignment of the Hsp90 N-terminal domain and the strategies and experiments used in order to achieve this will be described. The NMR experiments recorded for assignment were initially performed on a 0.5 mM uniformly $^{1}H^{15}N^{13}C$ -labelled protein in 20 mM KH_2PO_4 and 30 mM NaCl buffer at pH 7.0* (pH uncorrected for deuterium isotope effect). The initial plan was to correlate a $^{1}H^{15}N$ amide resonance of an HSQC experiment with the following triple resonance experiments: HNCO, HN(CA)CO, HNCA, HN(CO)CA, in order to correlate intra- and inter-residue resonances of ^{13}CO, $^{13}C\alpha$ and the through-bond sequential connections. The sequential connection was followed by assignment for the residues using a 3D NOESY-HSQC experiment along with HN(COCA)HA and ^{15}N-TOWNY-HSQC experiments. Confirmation of the sequential connection using the $^{1}H\alpha$ and NOESY amide resonances was then attained. However, using this strategy, only about 60% of the intra- and inter-residue connectivity was achieved. In addition to the experimental issues there was the additional problem of instability and aggregation of the NMR sample in the KH_2PO_4 buffer at the adopted conditions that resulted in reduction in the sensitivity of the experiments. This was dealt with by buffer screening (as described in Chapter 2, Section 2.7) to achieve the most soluble condition for our protein.

In order to reduce the spectral complexity and increase the resolution and sensitivity, a $^{2}H^{15}N^{13}C$ -labelled protein was prepared by expression of the protein in D_2O media instead of H_2O. The backbone assignments of $^{1}H^{15}N$, ^{13}CO, $^{13}C\alpha$ and $^{13}C\beta$ resonances were determined from the following triple resonance experiments: HNCO, HN(CA)CO, HNCA, HN(CO)CA, HNCACB and HN(CO)CACB

(Yamazaki *et al.,* 1994b). The $^{1}H^{15}N$ amide resonances of the HSQC spectrum were picked and correlated to the intra- and inter-residue resonances of ^{13}CO, $^{13}C\alpha$ and $^{13}C\beta$ nuclei to achieve the resonance sequential connections. The resonance assignments of each residue were met, using the probabilistic method of Grzesiek and Bax (1993). The backbone assignments were confirmed through the observation of the inter-residue NOEs expected from the sequential connectivity and the known X-ray structure of the Hsp90 N-terminal domain.

As a result, 192 amide peaks out of 200 resonances in the $^{1}H^{15}N$ HSQC spectra of Hsp90 N-terminal were assigned. The recombinant protein consists of 207 residues of the Hsp90 N-terminal domain (including 5 prolines) plus the hexahistidine tag, which were not observed in the $^{1}H^{15}N$ HSQC spectra.

3.2 One-dimensional experiments

A proton ^{1}H 1D NMR experiment was conducted on the Hsp90 N-terminal domain sample. The 1D experiment is the simplest and the most sensitive experiment due to its speed of acquisition and direct detection of the proton signals. The signal arises from the protons of the protein sample resonating in a limited protein chemical shift range (about 12 ppm). The result of the ^{1}H-proton 1D experiment on a ^{1}H-^{15}N sample with 2,2-dimethyl-2-silapentane-5-sulfonate (DSS) used for referencing the spectra is shown in Figure 3.1.

From the 1D-^{1}H experiment it appears that the Hsp90 N-terminal domain protein is folded. Folded proteins have peak dispersions above 8.5 ppm and below 0.5 ppm, as well as general broad dispersions of the spectrum in the amide region. The protein's methyl and methylene groups can be observed at a range between

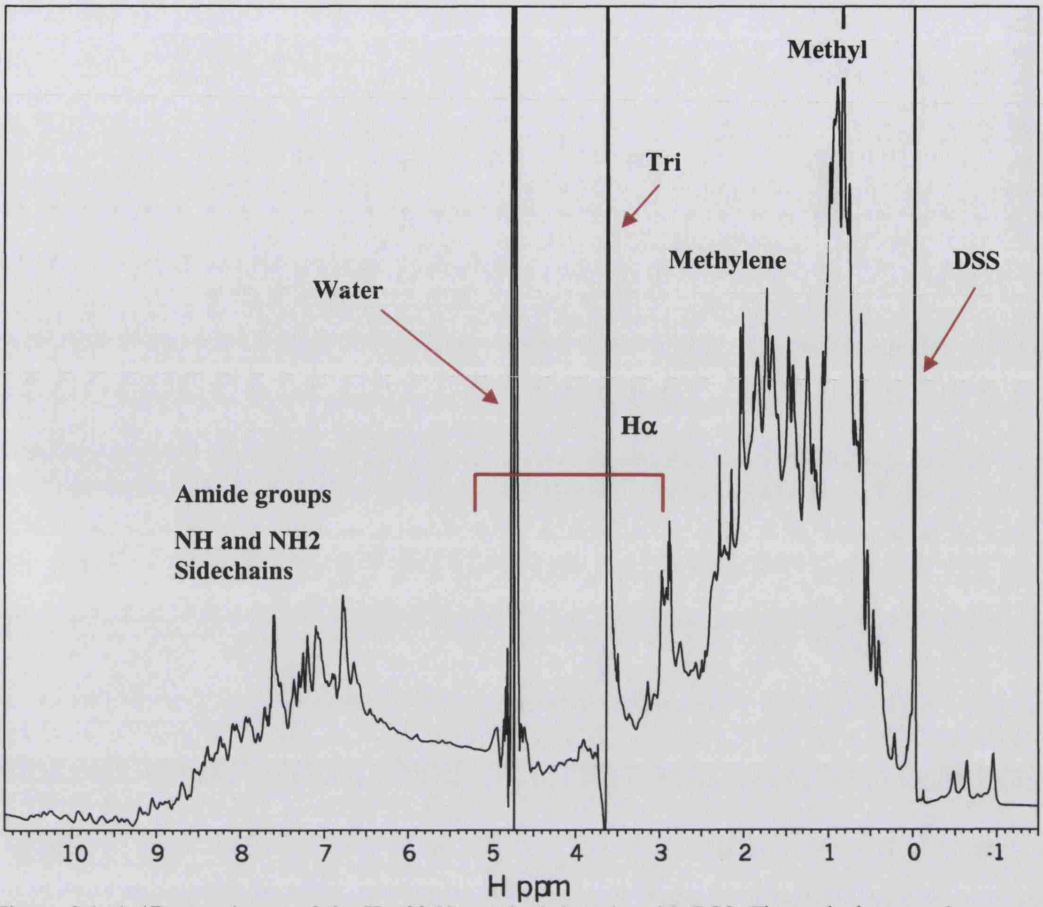

Figure 3.1. A 1D experiment of the Hsp90 N-terminal domain with DSS. The peak shown at 0 ppm was consequently used for referencing. Different regions in a 1D experiment are highlighted on the spectra.

-1 ppm to 3 ppm. The peptide Hαs are usually located in the region beginning from 3 ppm to about 5.5 ppm of the spectrum. The sharp peaks between 3.5 - 3.7 ppm are due to the Tris buffer protons and the water signal can be observed at 4.76 ppm. Due to the strong suppression of the signal from water and presence of Tris buffer, most of the Hα signals were not observed as shown in Figure 3.1. The amide region starts above 6 ppm to about 8.5 ppm with aromatic regions residing from 8.5 ppm to 9.5 ppm. The amine group on asparagine and glutamine sidechains, as well as the arginine sidechain NH and lysine NH_2, can be seen in the far end of the spectrum. The sharp peak at 0 ppm belongs to DSS, which was used for referencing the spectrum.

The chemical shift calibration was done using the methyl signal of a low concentration DSS (Wishart *et al.,* 1995). This sets the 0 ppm point of the spectrum. The position of the lock varies with different temperatures, so the position of the '0 ppm' varies accordingly. To overcome this, the 'Newoff' script, written in-house by Mark Pfhul, calibration for the 500 MHz and 600 MHz spectrometers was used to convert sequences to chemical shift according to the experimental temperature. The ^{13}C and ^{15}N chemical shift were obtained using the $^{13}C/^{1}H$ and $^{15}N/^{1}H$ frequency ratios ($^{13}C/^{1}H$=0.251449544, $^{15}N/^{1}H$=0.1013229122) (Wishart *et al.,* 1995).

3.3 Two-dimensional $^{1}H^{15}N$ heteronuclear single quantum coherence (HSQC) experiments

As the first step towards the sequential backbone assignment, one of the most useful spectra is an HSQC spectrum. The HSQC experiment is a 2D experiment that in principle gives the backbone amide resonance values for all the residues in the protein with the exception of the prolines. Prolines are not observed in the HSQC experiments due to the lack of an amide proton (Figure 3.2). As well as the amide backbone, some sidechain NH groups such as those in arginine, asparagine, glutamine and tryptophan are also observed in the spectrum (Figure 3.3). Asparagine and glutamine sidechains produce a strong doublet and one weaker doublet per residue. The sidechain crosspeaks have similar ^{15}N frequency but different ^{1}H frequency. The strong peaks belong to the NH_2 sidechain group and the weaker signals above them are from the NHD sidechain groups due to the exchange of the NH_2 protons with deuterium in the sample. All samples were

prepared with 10% D_2O consequently used for lock signal. The signals produced from exchange of the amide proton with ^2H in the NHD are less intense, hence they are seen as a weak signal above the strong signals of the sidechain amides.

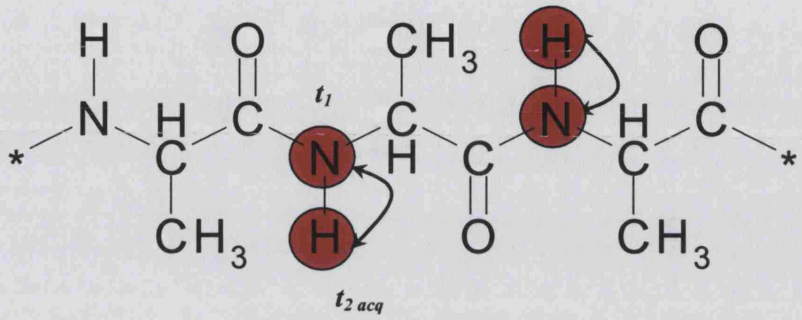

Figure 3.2. The ^1H ^{15}N-amide nuclei in a protein backbone structure (highlighted in red) recorded in the HSQC experiment. The curved arrow marks the magnetisation transfer in the HSQC experiment; t_1 and t_2 are the time periods used for recording the nitrogen and proton acquisition respectively.

Asparagine and glutamine sidechains are at the top right hand part of the spectrum. For example, two of these pairs are connected with red lines shown in Figure 3.3. There are also crosspeaks from the arginine $N_\varepsilon H_\varepsilon$ sidechain observed in the spectrum. These crosspeaks appear at an aliased nitrogen frequency in the 2D Fourier transformed HSQC spectrum and are usually located around 85-87 ppm (values from BioMagResBank). Some of these arginine sidechain crosspeaks observed in Figure 3.3 are highlighted (using green arrows). The location of these sidechain resonances varies in spectra recorded with different spectral widths. This is useful in distinguishing Hϵ sidechain crosspeaks from backbone resonances. No arginine sidechain $N_\eta H_{\eta 2}$ resonances were observed in the $^1H^{15}N$ HSQC spectrum, due to the protons being in exchange at the high pH of the sample.

The $^1H^{15}N$ HSQC spectrum of the Hsp90 N-terminal domain obtained at 800MHz is shown in Figure 3.3. The broad distribution of chemical shift resonances in the spectrum confirms a folded domain. Overall, there are about 200

backbone and 34 sidechain resonances (based on the 500 and 600 MHz spectra). In this spectrum there is a considerable overlap at the centre, which can largely be attributed to connecting loops and α-helices in its structure. The overlapping of signals at the centre of the spectrum is more prominent for the $^{1}H^{15}N$ HSQC spectra from the 500 and 600 MHz instruments compared to the 800 MHz spectrum shown in Figure 3.3. This is due to the higher magnetic field, which gives increased sensitivity, better signal to noise ratio, and hence increased dispersion of the resonances. Most of the glycines (shown by the red arrows in Figure 3.3) appear at the top of the $^{1}H^{15}N$ HSQC spectrum. These glycines are mainly in loops and turns and are not in any secondary structure. C-termini residues, such as Lys-207, can be seen as a strong peak highlighted by a blue arrow at the bottom centre of the spectrum as shown in Figure 3.3.

3.4 Sequential assignment using single- and double- labelled samples

As mentioned previously, the larger the proteins, the longer their rotational correlation time, and consequently they have a smaller T_2 relaxation time. This results in larger linewidths and increased signal overlap. As a result, conventional homonuclear 2D NMR methods do not work well for proteins larger than 20 kDa. A solution to this problem can be provided by a combination of isotopic labelling and multi-dimensional heteronuclear NMR techniques. This is because the heteronuclear couplings, $^{1}J_{CH}$ (125-160 Hz) and $^{1}J_{NH}$ (~92 Hz), are much larger than say, proton couplings $^{3}J_{HH}$ (5-12 Hz), and about 50-90% of the magnetisation can be transferred from the proton to their direct coupled heteronuclei (Clore and Gronenborn, 1993). The *J*-coupled experiments are independent of protein

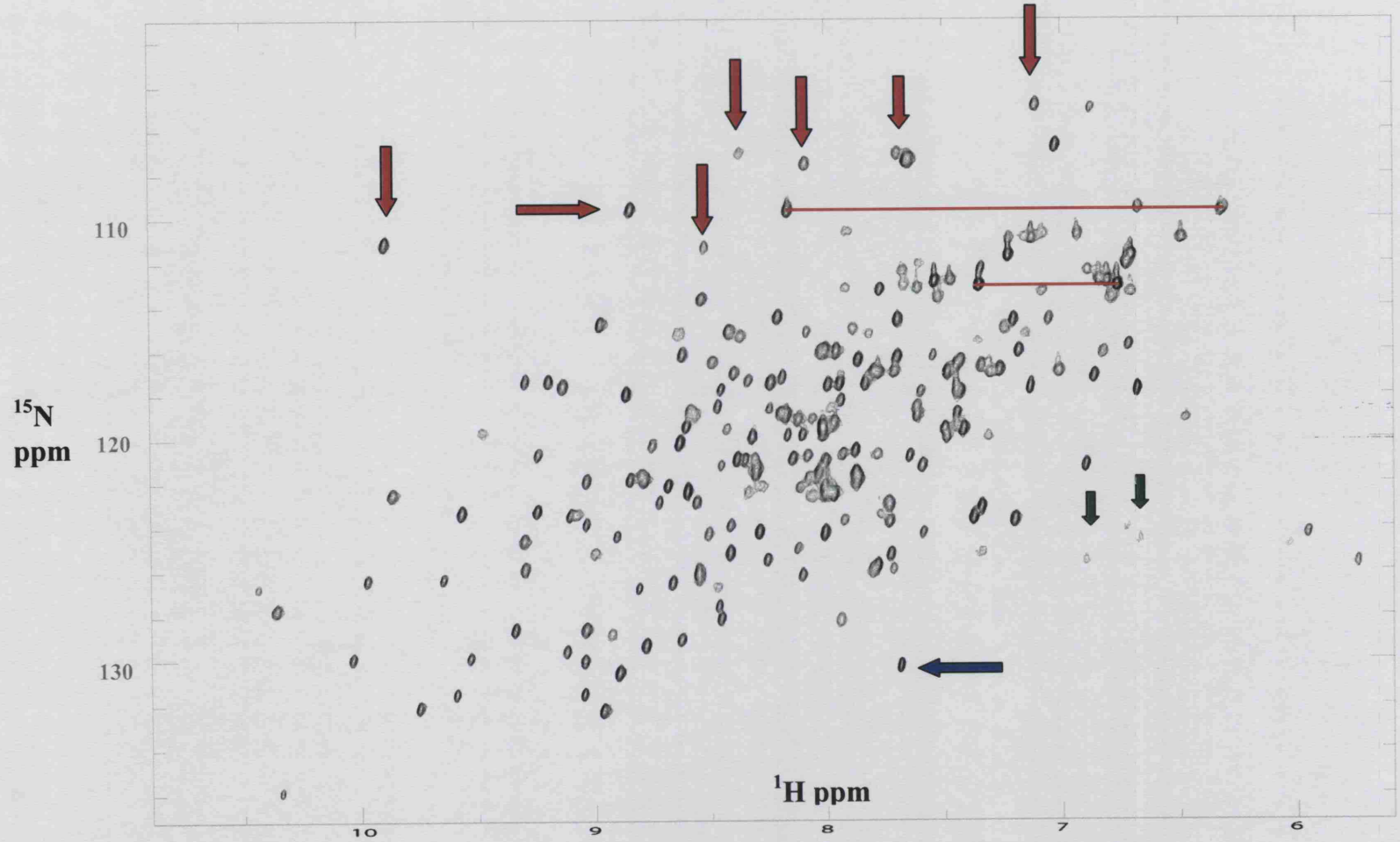

Figure 3.3 – A $^{1}H^{15}N$ HSQC spectrum of the N-terminal ATPase domain of yeast Hsp90 obtained at 800 MHz at 25°C. Red arrows point toward glycines in the spectrum. Two of the NH_2 sidechain pairs are connected with a red line and green arrows highlight two of the H_ϵ sidechains. The strong C-terminal end peak, residue Lys207, is in shown with a blue arrow.

conformation. Figure 3.4 shows a peptide segment with a summary of some of the most commonly used heteronuclear *J* couplings (in Hz) which have been used in various 3D experiments. One drawback to multidimensional experiments with double- or triple- labelling is the increased cost of protein preparation, although recent high yield expression systems have been of immense assistance. As a result, heteronuclear shift correlation experiments become highly sensitive and economical to use.

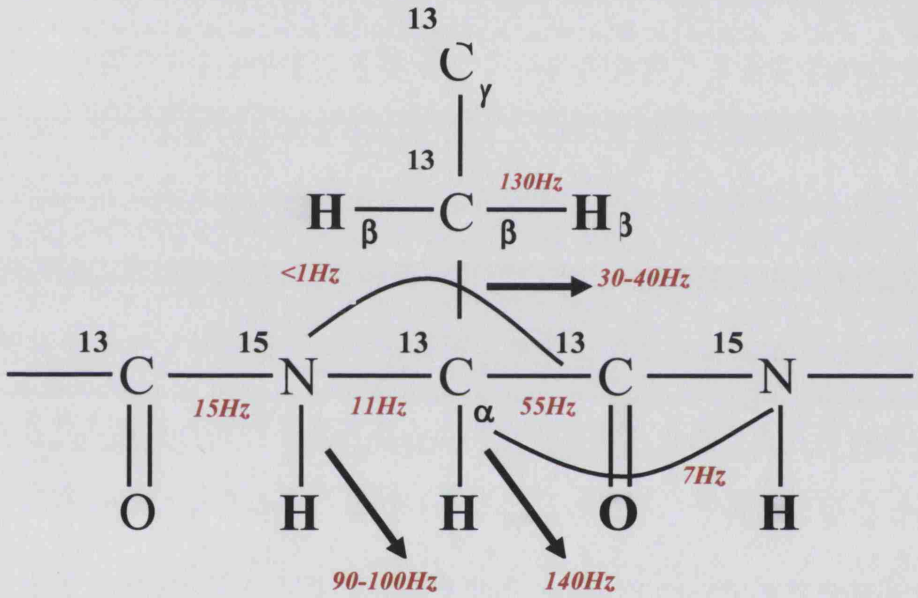

Figure 3.4. Through bond heteronuclear coupling along the polypeptide backbone chain as used in multidimensional NMR experiments. The stronger heteronuclear couplings are that of $^{1}J_{HN}$ (100 Hz) and $^{1}J_{C\alpha H\alpha}$ (140 Hz) which are mostly used in HSQC and HN(COCA)HA experiments with high sensitivity. Other most commonly used heteronuclear couplings are $^{1}J_{NC\alpha}$ (11 Hz) and $^{1}J_{C'C\alpha}$ (55 Hz) in HNCA and HN(COCA)CB experiments.

The following 3D experiments: HNCA, HN(CO)CA, HNCO and HN(CA)CO were used in order to sequentially connect the resonances. 3D, 3D TOWNY-HSQC and 3D HN(COCA)HA experiments were used to confirm the sequential connections as well as to connect the Hα resonances. A 0.5 mM $^{15}N^{13}C$-labelled sample in 20 mM KH_2PO_4 and 30 mM NaCl at pH 7.0* was used for HNCA, HN(CO)CA, HNCO, HN(CA)CO and HN(COCA)HA 3D experiments.

The HSQC, 3D NOESY-HSQC and 3D TOWNY-HSQC experiments were recorded on the same sample.

All the experiments were conducted at 600 MHz at 25°C. Due to the unique NOE pattern of each individual residue, attempts were made to use the 3D NOESY-HSQC experiments for assigning the resonances according to the protein sequence as well as using data from the crystal structure.

3.4.1 Three-dimensional HNCA

HNCA (Kay *et al.,* 1990; Ikura *et al.,* 1990b) is one of the most commonly used experiments in the backbone assignment of proteins. This experiment records the correlation of the HN amide proton and the Cα resonance of its own and the preceding residue and provides a connection between two sequential residues. Figure 3.5 (a) shows the correlation and connectivity between the nuclei that are observed in an HNCA experiment. In addition to the intra-residue correlation illustrated, the small $^{2}J_{NC\alpha}$ coupling provides some weak inter-residue peaks in the HNCA spectrum that facilitates the assignment procedure.

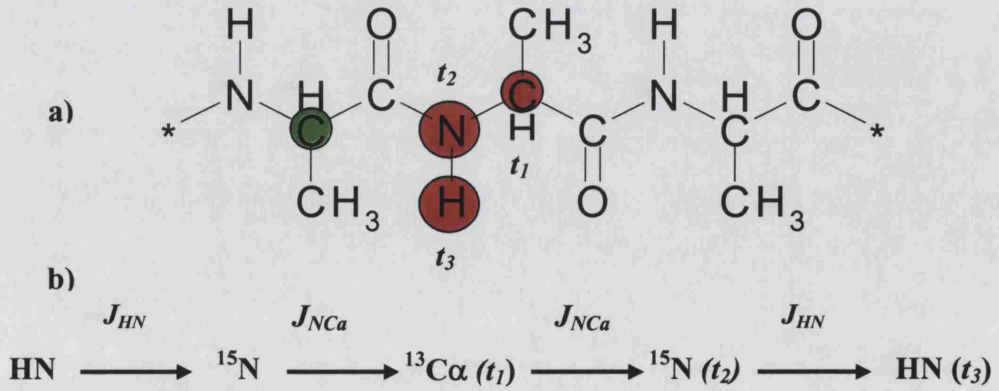

Figure 3.5. The HN amide and Cα nuclei involved in the HNCA experiment in a protein backbone (a) The red circles show nuclei belonging to residue *i* and green highlights nuclei belonging to residue *i-1* **(b)** shows the relevant coupling involved in each magnetisation transfer step

The HNCA experiment correlates the following nuclei resonances in the amino acid sequence of a protein $\{H^N_i, N^H_i, C\alpha_i, (C\alpha_{i-1})\}$. In Figure 3.5 the t_1, t_2 and t_3 denote the evolution or acquisition time in each dimension and the active coupling involved in each transfer step is indicated above the arrows. A significant limitation in this experiment is the poor resolution in the $^{13}C\alpha$ dimension. This is due mostly to the limitation in the total time that can be used for carbon evolution as a result of homonuclear carbon-carbon couplings and short transverse relaxation times (Yamazaki *et al.*, 1994a).

Another reason for the HNCA experiment being relatively insensitive is that it relies on the $^1J_{NC\alpha}$ bond coupling for magnetisation transfer which is one of the smallest one bond coupling constants (8-12 Hz). Figure 3.6 shows a HNCA spectrum from the $^{15}N^{13}C$-labelled sample using a 600 MHz instrument. The chemical shift range displayed in an HNCA experiment, shown for the $C\alpha$ resonance of different amino acids, are usually in the range 50 ppm to 70 ppm with the exception of the glycines which are about 45 ppm. In the HNCA spectrum glycine resonances were also negative which is due to the use of a constant time carbon evolution period of $1/J_{cc}$ (glycines lack a $C\beta$ atom) (Grzesiek and Bax, 1992a). Projection of the 3D HNCA experiment onto the 2D $^1H^{15}N$ plane produces a spectrum similar to that of the $^1H^{15}N$ HSQC spectrum in which asparagine and glutamine doublet sidechain crosspeaks are absent. This spectrum is useful for 3D-spectrum alignment in the nitrogen dimension and as an alternative way to identify sidechain resonances in the HSQC spectrum.

3.4.2 Three-dimensional HN(CO)CA

The HN(CO)CA experiment (Yamazaki *et al.,* 1994b; Bax and Ikura, 1991), provides an exclusive inter-residue correlation of the $\{H^{N}_{i}, N^{H}_{i}, (C\alpha_{i-1})\}$ nuclei. In this experiment magnetisation from an amide proton is transferred to its attached ^{15}N and then transfers through the ^{13}CO nucleus to the Cα of the preceding amino acid, followed by the reverse pathway for NH detection, shown in Figure 3.7 (b).

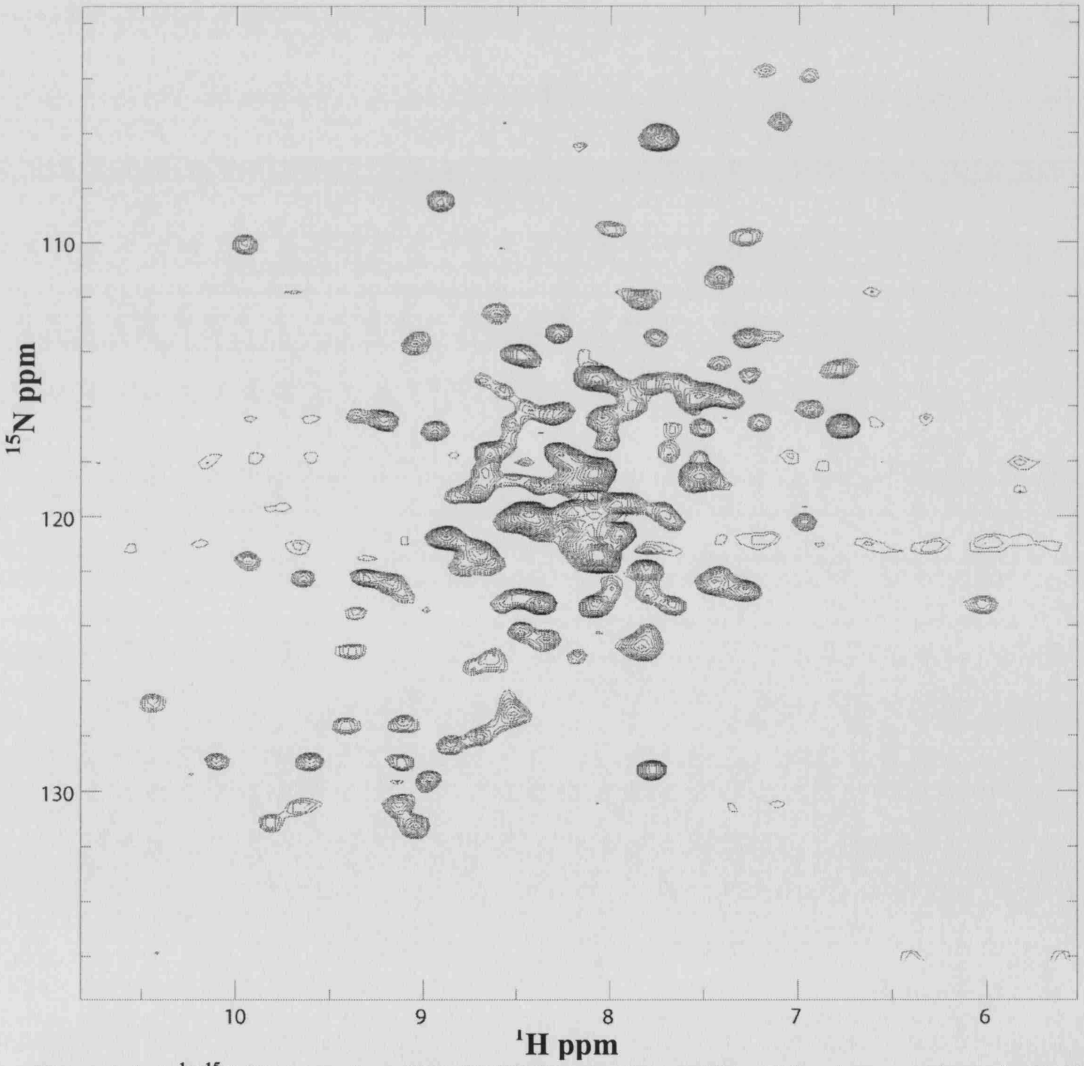

Figure 3.6. A $^{1}H^{15}N$ 2D projection of the 3D HNCA experiment. Most of the planes are shown in the 2D project.

The relatively large value of the $^{1}J_{NC'}$ (15 Hz) and $^{1}J_{C'C\alpha}$ (55 Hz) in comparison to $^{1}J_{NC\alpha}$ (11 Hz) of the HNCA experiments makes the HN(CO)CA experiment more sensitive and complementary to the HNCA. The combination of the two experiments, HNCA and HN(CO)CA is the basis for sequentially connecting the resonances. Figure 3.7 (a) shows the nuclei detected during the HN(CO)CA experiment in red and the nuclei involved in the magnetisation transfer in green.

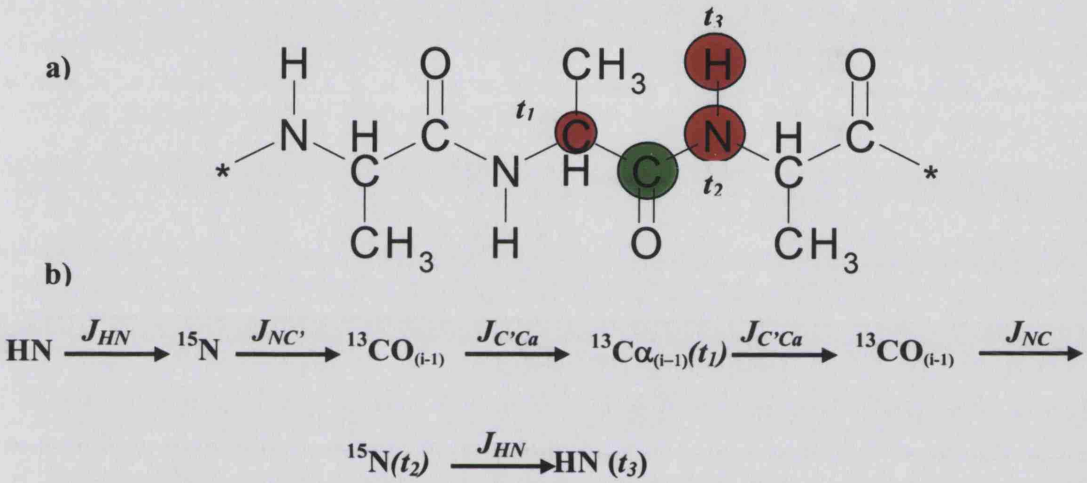

Figure 3.7 Active nuclei recorded in an HN(CO)CA experiment and those used in the magnetisation transfer. (a) active nuclei are shown in red and those used but not detected in the magnetisation transfer are in green. **(b)** Displays the direction of the magnetisation transfer, through protein backbone with the relative *J*-coupling shown above each arrow. t_1,t_2,t_3 are the evolution or acquisition times recorded for each dimension.

Figure 3.8 shows the sequential connection of the HNCA and HN(CO)CA in an ANSIG session. The HNCA experiment, here in purple, has two resonances, one strong (from Cα_i nuclei) and a second weaker resonance (from Cα_{i-1} nuclei). Each pair of the HNCA resonance is connected via vertical lines. The two HNCA chemical shifts for residue *i* and *i-1* have the same proton and nitrogen frequency, but with different ^{13}Cα frequencies. The HN(CO)CA experiment, shown in light blue, can be seen superimposed on the weak resonance of the HNCA experiment, confirming that the weaker signal belongs to the preceding residue. Moving backwards through sequence, via an HSQC experiment to the corresponding Cα of

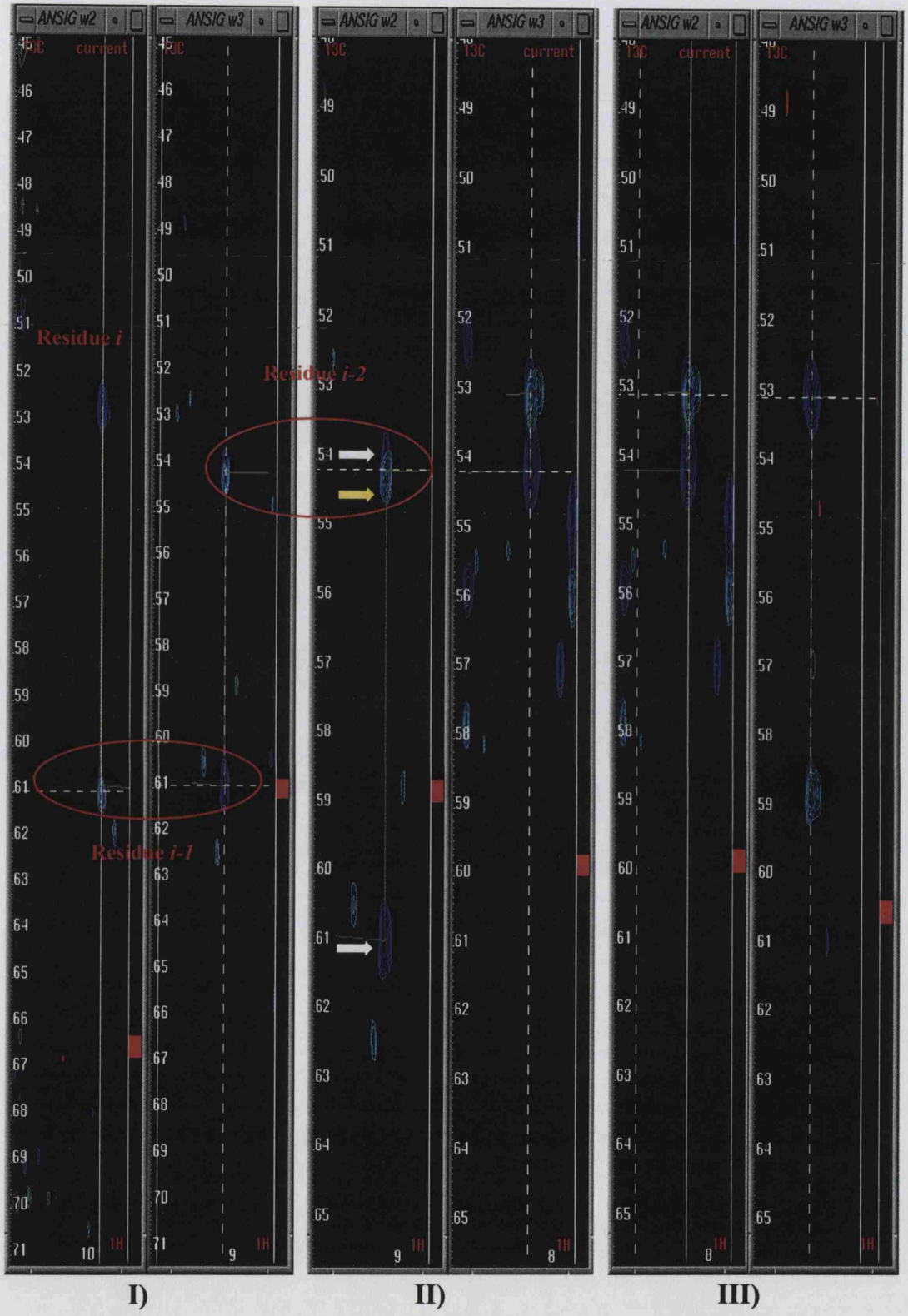

Figure 3.8 Sequential connection of the HNCA and HN(CO)CA experiments. Three different pairs of an ANSIG session (W2-W3 are paired) highlighted as I, II and III are shown here. In each strip plot intra-inter residues are sequential connected (continuous green lines) as shown in the strip plot pair (I) window. The HNCA resonances are in purple (two are indicated by white arrows) and the HN(CO)CA crosspeaks are in light blue (one of which is indicated by a yellow arrow).

the residue *i-1* and connecting it to residue *i-2,* makes the basis for sequential connection between the residues as displayed in Figure 3.8 with green lines.

3.4.3 Three-dimensional NOESY-HSQC

The 3D NOESY-HSQC experiment pulse sequence is based on a homonuclear 2D NOESY followed by a HSQC pulse sequence. The mechanism involves a $^{1}H^{1}H$ NOE step followed by a heteronuclear transfer via $^{1}J_{NH}$ heteronuclear coupling, Figure 3.9 (a.). The final spectrum is a series of 2D homonuclear experiments, whereby each one is edited by a different ^{15}N frequency. Figure 3.9 (b) shows transfer of the magnetisation through different nuclei in this experiment. First, magnetisation that has originated on the ^{1}H is transferred, by NOE cross relaxation, to the HN amide proton during the NOESY mixing period.

A HSQC experiment then transfers the magnetisation via *J* coupling from the HN amide proton to the directly bonded ^{15}N, and back to the $^{1}H^{N}$ nucleus for detection as shown in Figure 3.9. A section of the 3D NOESY-HSQC is shown in Figure 3.10. In this figure each slice displays crosspeaks between a proton and HN amide proton. Each 2D slice is spread according to the ^{15}N frequency of the amide group. The diagonal peaks belong to the amide proton resonance attached to the amide nitrogen. Other crosspeaks correspond to protons that are within the NOE range of the amide proton (less than 5 Å) that are displayed on the vertical line at the same proton frequency. Unlike 2D NOESY spectra, in which the off-diagonal peaks appear in pairs, in the 2D slices of the 3D spectrum only one of the off-diagonal signals is observed. The 3D NOESY-HSQC crosspeak patterns are characteristic of residue type and provide information about secondary and tertiary

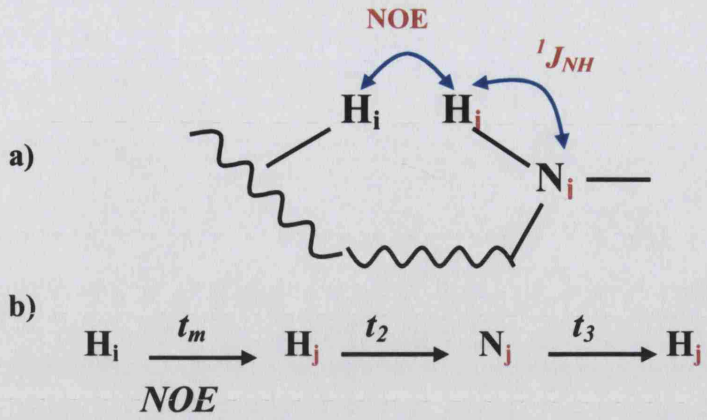

Figure 3.9. The protons detected in an NOE experiment (a) The origin and transfer of the magnetisation during the NOESY mixing time of a homonuclear $^1H^1H$ NOE experiment. A subsequent HSQC experiment transfers the magnetisation using $^1J_{NH}$ heteronuclear coupling of the H and N nuclei in the 3D NOESY HSQC. **(b)** The direction of the magnetisation transfer through different nuclei with times recorded in each dimension shown above each arrow. The mixing time (t_m), evolution time (t_2) and acquisition time (t_3) are indicated.

structure for each residue. This forms the basis for sequential assignment of the resonances. The sequential residues are found by looking for the proton amide NH-NH crosspeaks usually in different planes that are symmetrical about the diagonal in the NOESY spectrum. The resultant spectra are shown in Figure 3.10 as two sequentially connected slices in an ANSIG session.

3.4.4 Three-dimensional HN(COCA)HA

The 3D HN(COCA)HA experiment correlates the crosspeaks between the $^1H^N$ and ^{15}N nuclei of one residue with the Hα of the preceding residue $\{H^N_i, (H\alpha_{i-1})\}$. In this experiment the magnetisation is transferred through one bond couplings from $^1H^N$ through ^{15}N, ^{13}CO, $^{13}C\alpha$ nuclei to the $^1H\alpha$ and back to the H^N for detection as shown in Figure 3.11(b). This experiment is an extension to the HN(CO)CA experiment which makes use of several one-bond couplings. The nuclei that are used in this experiment are highlighted in red in Figure 3.11(a). The nuclei in green are used for magnetisation transfer and are not detected during the experiment.

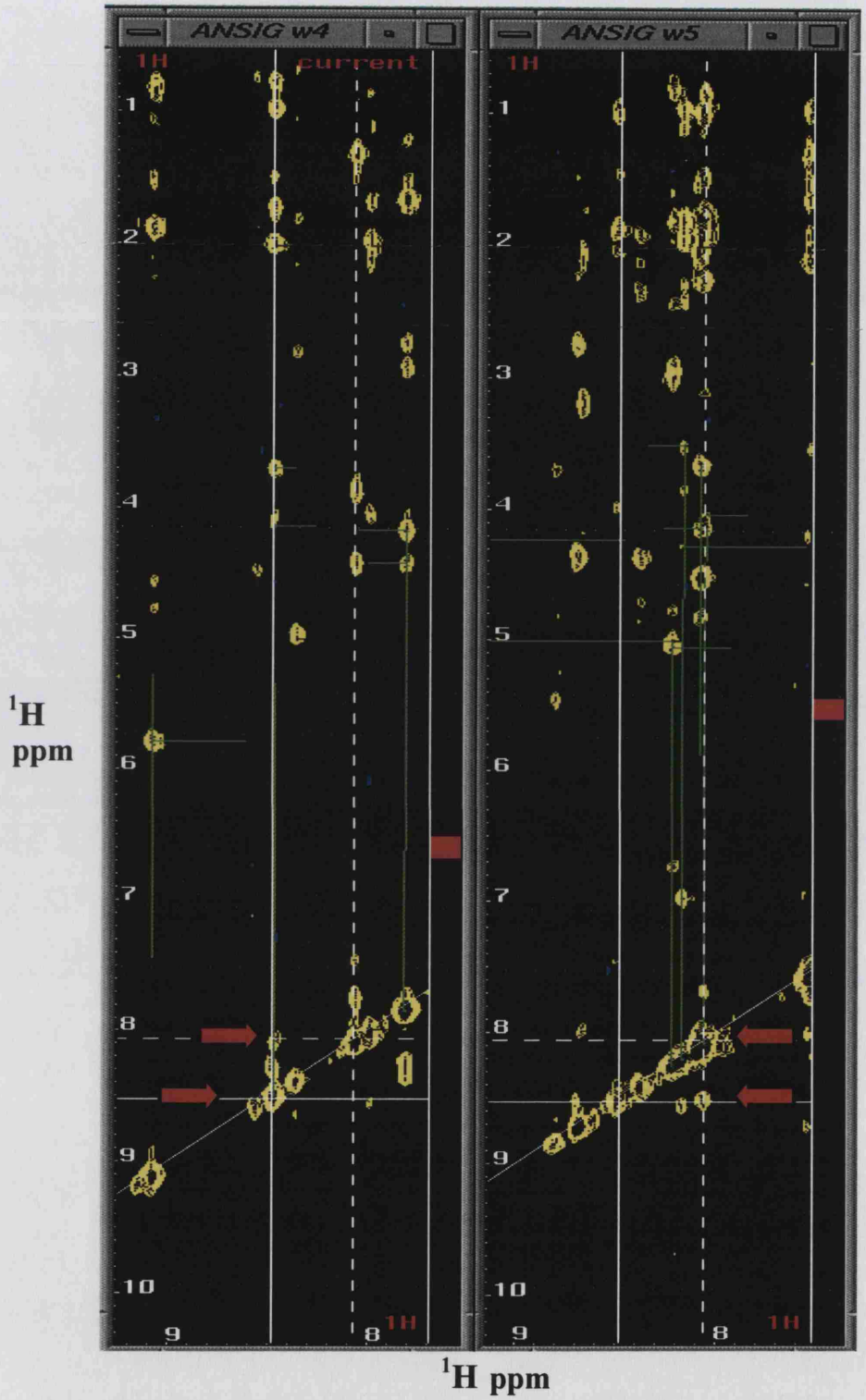

Figure 3.10. Two slices of the 3D NOESY-HSQC experiment in an ANSIG session. Diagonal crosspeaks in yellow are the ^{1}H resonance of the amide and other yellow crosspeaks belong to protons with in the NOE range of the amide proton. Red arrows highlight the corresponding sequential amide peaks in pairs.

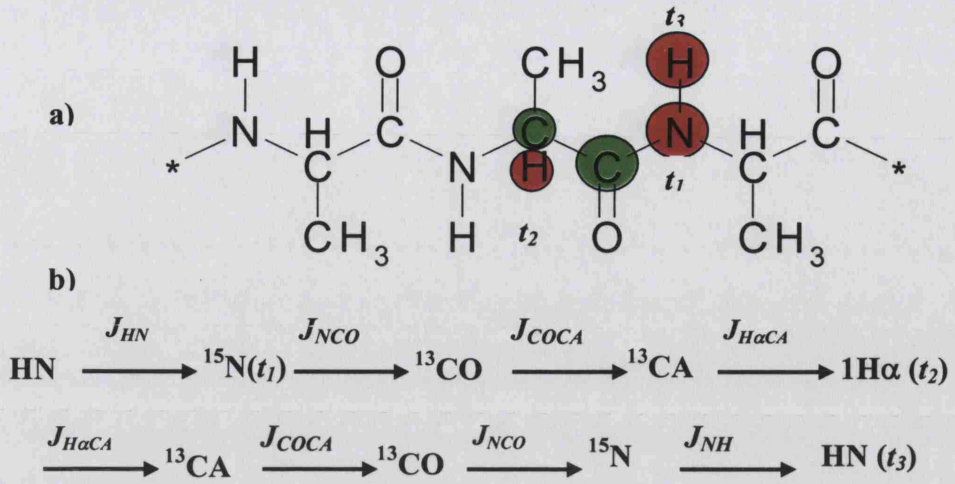

Figure 3.11 The nuclei and coupling constants involved in the HN(COCA)HA experiment (a) the nuclei involved in the HN(COCA)HA experiment (in red) and nuclei transferring the magnetisation (in green). **(b)** the direction of the magnetisation transfer in the experiment with the relative *J*-coupling shown above the arrows.

The HN(COCA)HA spectrum provides complementary information to the TOWNY-HSQC experiment for assignment of the ^{1}Hα nuclei, helping distinguish the inter/intra- residue as well as resolving the ^{1}Hα proton degeneracy ambiguity. The resultant spectrum is shown in Figure 3.12 (b) as brown crosspeaks in the spectrum. The HN(COCA)HA crosspeaks in the proton dimension of the spectrum were in doublets despite the efforts of the NMR manager to improve the pulse sequence and experimental settings, which made the assignment of the ^{1}Hα peaks too ambiguous in the crowded areas. This splitting in proton dimension could be due to a residual proton carbon coupling. Utilising the 3D NOESY-HSQC, TOWNY-HSQC and HN(COCA)HA has enabled the connection of the $H^{N}_{(i)}$ - $H^{N}_{(i+1)}$, $H^{N}_{(i)}$ - $H\alpha_{(i)}$ and $H\alpha_{(i)}$ – $H\alpha_{(i-1)}$ nuclei as shown in Figure 3.12.

3.4.5 Three-dimensional TOWNY-HSQC

This experiment correlates the HN amide crosspeaks of a residue with the ^{1}Hα and other protons of its own sidechain. The 3D ^{15}N TOWNY-HSQC is

basically a 3D ^{15}N-edited TOCSY (Total Correlation Spectroscopy) HSQC experiment in which a TOWNY pulse sequence (Kadkhodaei *et al.*, 1993) also known as a 'clean TOCSY' is used. In the TOCSY experiment cross-relaxation contributes to the magnetisation transfer during the experiment and this cross-relaxation causes artifacts observed during the mixing time. Using a TOWNY sequence is an effective way to overcome the artefacts observed.

In the 3D ^{15}N TOWNY-HSQC experiment a large number of NH-NH diagonal peaks are observed in this spectrum, which arises from NH protons along the polypeptide chain. The amide peaks are separated according to their ^{15}N frequency along 2D slices. In Figure 3.12, on the diagonal line, the crosspeak (shown in pink) recorded for the amide proton in the 3D ^{15}N TOWNY-HSQC spectrum is shown overlapping with the amide crosspeaks of the 3D ^{15}N HSQC-NOESY spectrum. Other proton resonance observed along the vertical line are from $C\alpha H_{(i)}$-$NH_{(i)}$ and sometimes $C\beta H_{(i)}$-$NH_{(i)}$ protons. This experiment is best used for assignment of the Hα resonance, when matched as a pair in combination with other experiments as shown in Figure 3.12 using red arrows. In this figure the $H\alpha_{(i)}$ resonance is connected using green vertical line to its own $NH_{(i)}$ and a horizontal green line to the $H\alpha_{(i)}$ resonance in the 3D HSQC- NOESY of NH $_{(i-1)}$.

3.5 Assignments of the double-labelled N-terminal sample and preparation for expression in D_2O

By combining all the described spectra in an ANSIG session in order to achieve the sequential assignment of the double-labelled Hsp90 N-terminal domain, only about 60% of the sequential connection of the residues was possible.

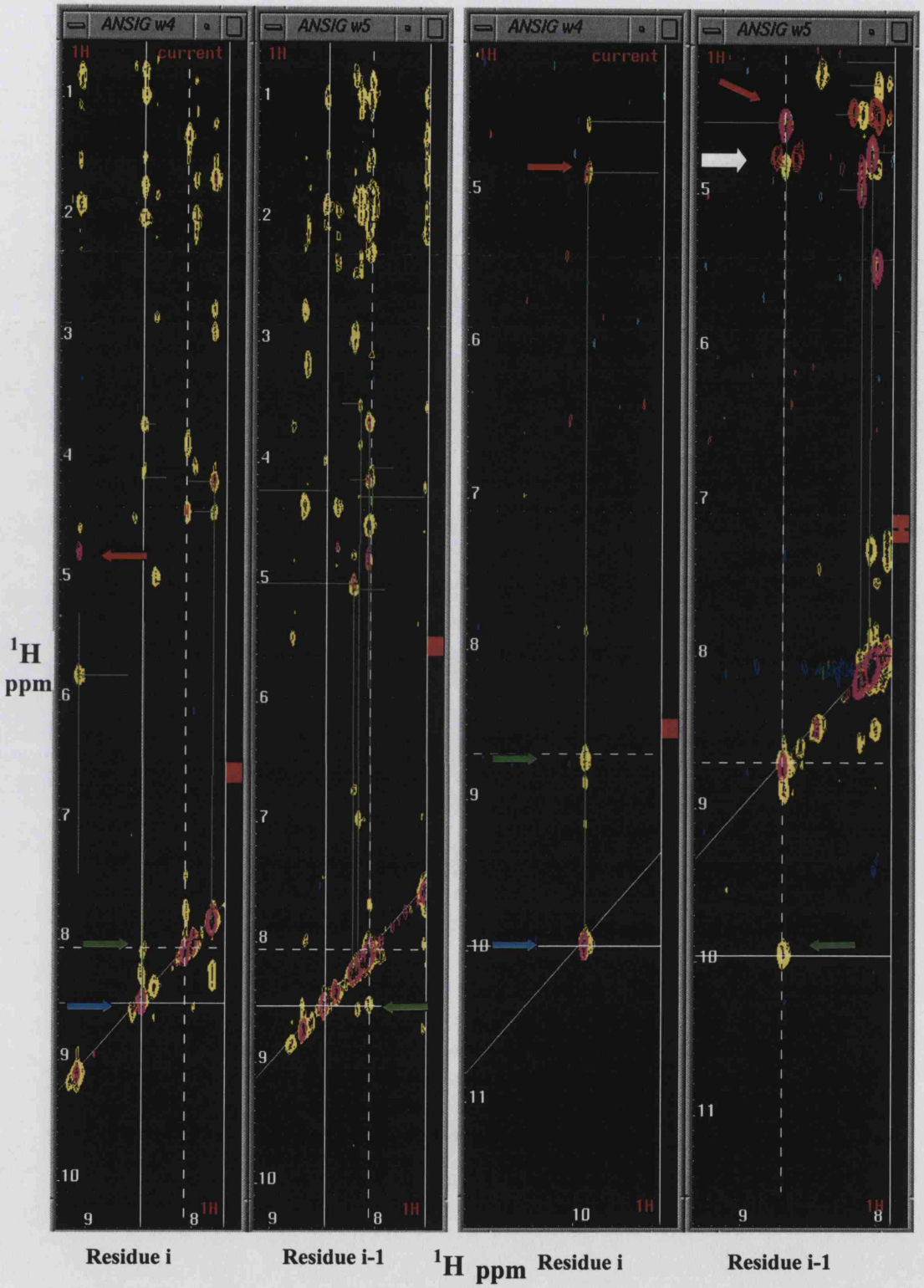

Figure 3.12. Two separate correlated window of an ANSIG session displaying the 3D ^{15}N HSQC-NOESY TOWNY-HSQC and HN(COCA)HA crosspeaks. Two pairs of slices for two different sequentially connected residues are shown. The 3D ^{15}N HSQC-NOESY crosspeaks (yellow), 3D TOWNY-HSQC (pink) and HN(COCA)HA (highlighted by a white arrow) are shown. In the first slices, amide crosspeaks for residue *i* (blue arrows) represents where crosspeaks of yellow HSQC-NOESY and pink TOWNY-HSQC overlap. The yellow vertical crosspeaks (green arrows) is from the previous or preceding amide residues. The Hα resonances are highlighted using red arrows.

The lack of resonances in some of the spectra such as the HNCA and HN(CO)CA experiments, or ambiguity in the 3D NOESY- HSQC experiments due to the resolution of the spectrum, made the sequential assignment difficult and /or too ambiguous on a 600 MHz recorded spectra to be resolved completely. The sample also showed signs of instability in the KH_2PO_4 buffer at pH 7.0*, which during the course of the experiment, resulted in aggregation and loss of the sample. The sample was also extremely sensitive to any change in the temperature. Before moving towards expressing the Hsp90 N-terminal construct in D_2O media, optimal solution conditions for our sample were resolved by buffer screening for a non labelled sample (as described in Chapter 2 section 2.7). The most suitable buffer found was 20 mM Tris buffer at pH 8.0* without salt.

3.6 Deuterium labelling strategies

To allow complete assignment of the Hsp90 N-terminal domain we adopted the strategy of deuterium labelling for our protein. Deuteration was first introduced by the groups of Crespi and Jardetzky to reduce the complexity of 1D ^1H spectra of proteins (Katz and Crespi, 1966; Crespi *et al.,* 1968; Markley *et al.,* 1968). In the mid-1980s, the same deuteration methods were used in homo- or hetero-nuclear 2D NMR spectra that effectively extended the size of proteins that could be studied by protein NMR spectroscopy (Kalbitzer *et al.,* 1985; LeMaster and Richards, 1988). Deuteration achieved this by reducing the number of observable resonances and decreasing the linewidths of the remaining resonances by eliminating the competing relaxation pathways. Finally, the combined use of perdeuteration and $^{13}C/^{15}N$ isotopic labelling with heteronuclear 3D and 4D experiments, have

increased the size of proteins which can be studied by NMR to more than 25kDa. (Bax, 1994; Clore and Gronenborn, 1994; Yamazaki *et al.,* 1994b). Because the deuteron gyromagnetic ratio (γ_D) is 6.5-fold smaller than the proton γ_H, a deuteron is 42-fold (γ^2_D / γ^2_H) less effective than a proton at causing dipolar relaxation of both the directly attached nucleus and the surrounding proton nuclei. Relaxation of non-carbonyl carbon nuclei (e.g. ^{13}C-^{1}H) is dominated by dipolar interaction with any attached proton(s) (Browne *et al.,* 1973). Relaxation of amide protons has a significant component (40%) arising from dipolar interaction with surrounding aliphatic protons (Markus *et al.,* 1994). Therefore, the incorporation of ^{2}H into $^{13}C/^{15}N$-labeled proteins dramatically increases both the carbon and HN T_2 relaxation times. The increase in these T_2 relaxation times leads to a much greater sensitivity in the key amide-detected $^{1}H/^{13}C/^{15}N$ triple-resonance correlation experiments such as HNCACB, HN(COCA)CB, HNCO and HN(CA)CO (Grzesiek and Bax, 1993; Yamazaki *et al.,* 1994b; Venters *et al.,* 1996).

A $^{1}H^{15}N$ HSQC experiment for ^{15}N labelled and $^{2}H^{15}N$ ^{13}C-labelled protein samples of the Hsp90 N-terminal domain recorded on a 500 MHz spectrometer with the same recording set-up and process options are compared in Figure 3.13. The $^{1}H^{15}N$-HSQC of the deuterated sample shows a significant narrower line width in comparison with the protonated sample and hence significantly better resolution in the deuterated spectrum. Both protein samples were approximately 98% uniformly ^{15}N labelled, and similarly 98% uniformly ^{13}C-labelled for the triple labelled sample, as well as 70% non-uniformly deuterated. $^{1}H^{13}C$ HSQC data indicates that the final $^{2}H^{15}N$ ^{13}C protein has near complete deuteration of backbone α and sidechain methylene positions (>95%), and that only the methyl groups exhibit substantial protonation as shown in Figure 3.14.

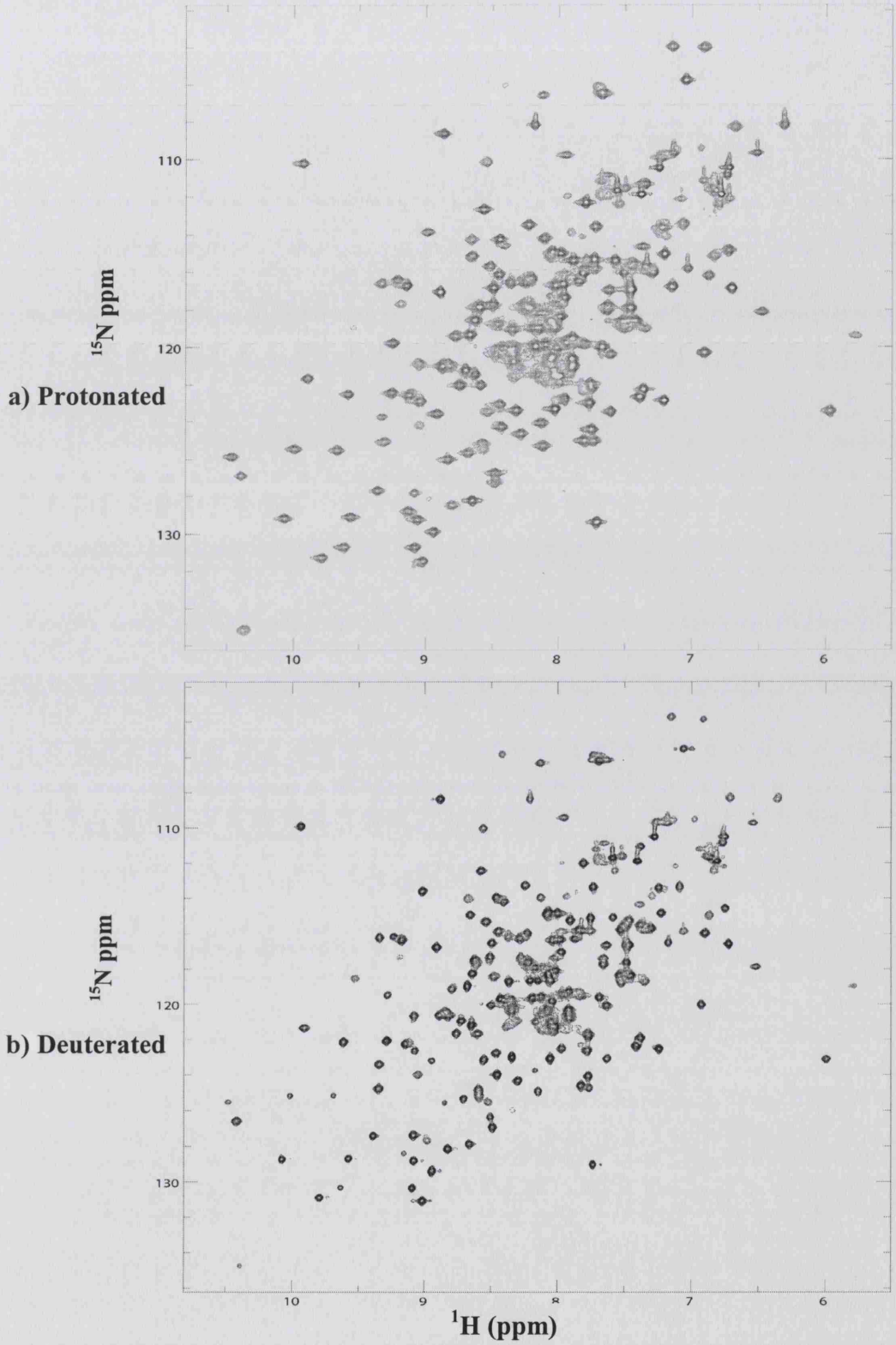

Figure 3.13 Effect of perdeuteration on the 2D $^{1}H^{15}N$ HSQC spectrum of the Hsp90 N-terminal domain. Both spectra were recorded on a 500 MHz spectrometer with similar setup and recording time. The protein in (a) is uniformly ^{15}N labelled while the deuterated protein (b) is ^{15}N, ^{13}C uniformly labelled with approximately 90% uniformly deuterated. The crosspeaks in (b) are significantly narrower in comparison to (a) with less resonance overlaps at the centre of the spectrum.

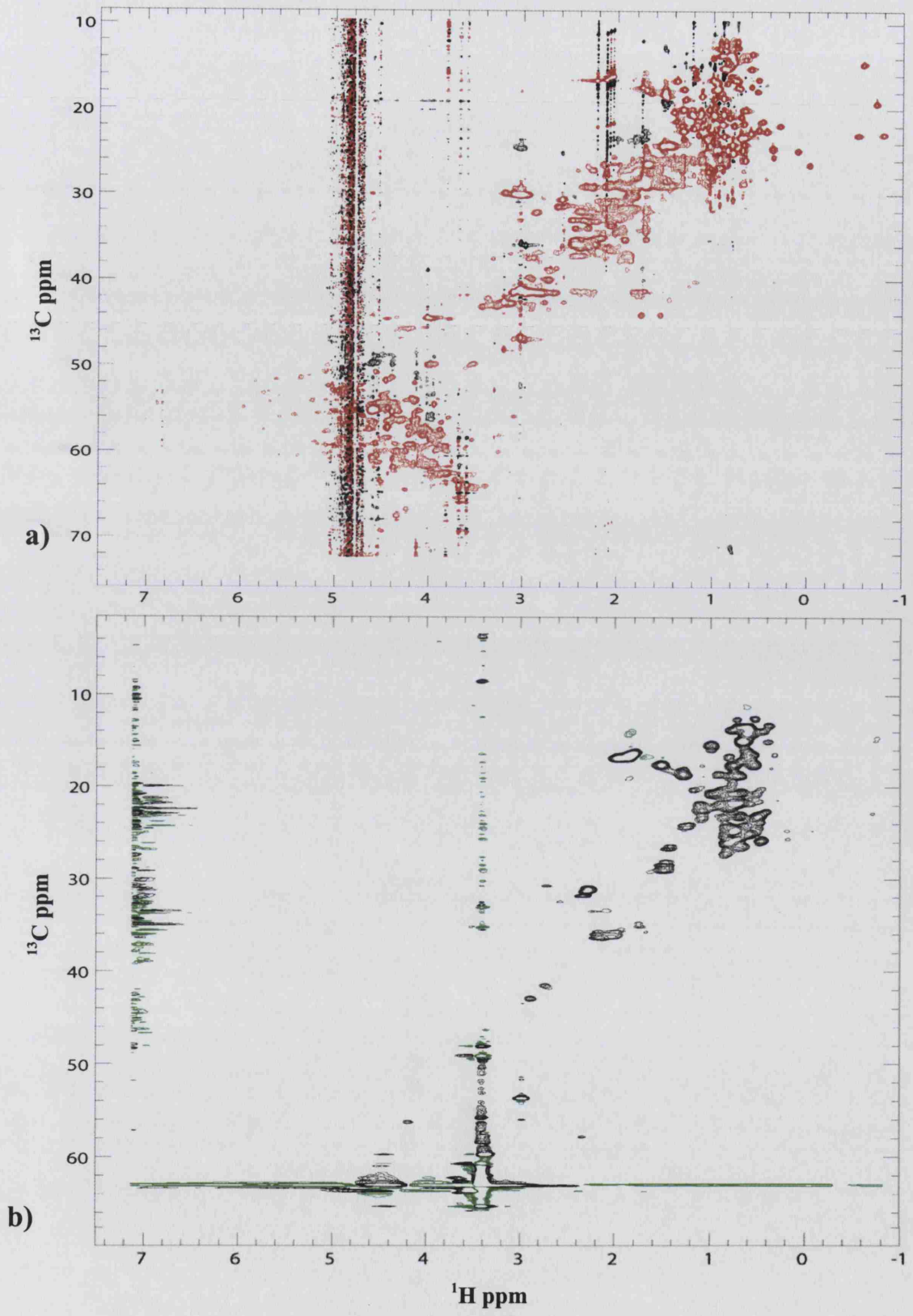

Figure 3.14 Comparison of $^{1}H^{13}C$ HSQC data from protonated (a) and deuterated (b) samples. The final ^{2}H, ^{13}C, ^{15}N protein (b) has near complete deuteration of backbone Cα and sidechain methylene positions (>95%), and only the methyl groups exhibit substantial protonation. The apparent 'broadening' is partly due to the three isotopomers (HDD, HHD, HHH), which have ^{1}H frequency differences of about 0.10-0.15 ppm.

3.7 Resonance assignment of the Hsp90 N-terminal domain using a $^{2}H^{15}N^{13}C$-labelled sample

A 0.5 mM uniformly $^{2}H^{13}C^{15}N$ labelled protein sample in 20 mM Tris buffer pH 8.0* was dissolved in 90%H_2O/10%D_2O and used to record experiments on a Varian UNITY plus 500 MHz equipped with a deuterium channel decoupler. The backbone assignments of ^{1}H, ^{15}N, ^{13}CO, $^{13}C\alpha$ and $^{13}C\beta$ resonances were determined from the following triple resonance experiments: HNCO, HN(CA)CO, HNCA, HN(CO)CA, HNCACB and HN(CO)CACB (Yamazaki *et al.,* 1994b). A $^{1}H^{15}N$HSQC used for displaying the assignment was recorded from a $^{2}H^{13}C^{15}N$-protein on a Varian INOVA 800 MHz proton frequency spectrometer.

3.7.1 A three dimensional HNCA spectrum for the $^{2}H^{15}N^{13}C$-labelled sample

This experiment was carried out in the same manner as described previously in section 3.4.1 but with some different parameters. By replacing the protons with deuteron, the dipolar interaction of the $^{1}H^{13}C$- spin pair in the protein backbone structure attenuates, for example, by a factor of approximately 15 times for molecules with a correlation time more than 10 ns (Yamazaki *et al.,* 1994a). As a result, carbon relaxation time increases which leads to improvement of the sensitivity of the experiment. The decrease in the ^{13}C line width improves the resolution of individual peaks in crowded areas and increases the signal to noise ratio of the spectra, facilitating observation of the weak resonances. Furthermore, the resolution of the $^{13}C\alpha$ nuclei is enhanced due to the longer usable evolution

time in the presence of the deuterium. The 2D ($^{13}C\alpha$, NH) projection from 3D HNCA spectra of a deuterium sample in comparison with a protonated sample is shown in Figure 3.15. There are differences in the setting of the deuterium labelled HNCA experiment in comparison to the protonated experiment, variances such as different spectral width and number of transients. Despite the differences, the resolution of the deuterated version of the HNCA experiment is substantially increased in the carbon dimension compared to the protonated spectrum as shown in Figure 3.15. Figure 3.16 shows the 2D (^{15}N, NH) projection of a 3D HNCA experiment from both a protonated and deuterated sample. The two spectra look similar to a $^{1}H^{15}N$ HSQC spectrum of the Hsp90 N-terminal sample. The deuterated spectrum has better signal to noise ratio. There are several differences in location and crosspeak intensities in between the two spectra, which could be due to the difference in the buffer and pH of the samples used.

3.7.2 A three-dimensional HN(CO)CA spectrum for the triple-labelled sample

This experiment was performed in the same manner as the HN(CO)CA experiment, described previously in Section 3.4.2. The HN(CO)CA provides the sequential connectivity in combination with the HNCA experiment. Using a deuterated sample resulted in improved sensitivity and spectral resolution in comparison with the protonated experiment by increasing the T_2 ($C\alpha$) relaxation. Figure 3.17 shows a 2D ($^{13}C\alpha$ NH) projection of the 3D HN(CO)CA experiment. The chemical shift ranges of the crosspeaks are between 42 to 67 ppm with the glycine $C\alpha$ resonance at about 45 ppm which can be seen at the top of the spectrum. Figure 3.18 shows the 2D (^{15}N,NH) projection of the 3D HN(CO)CA

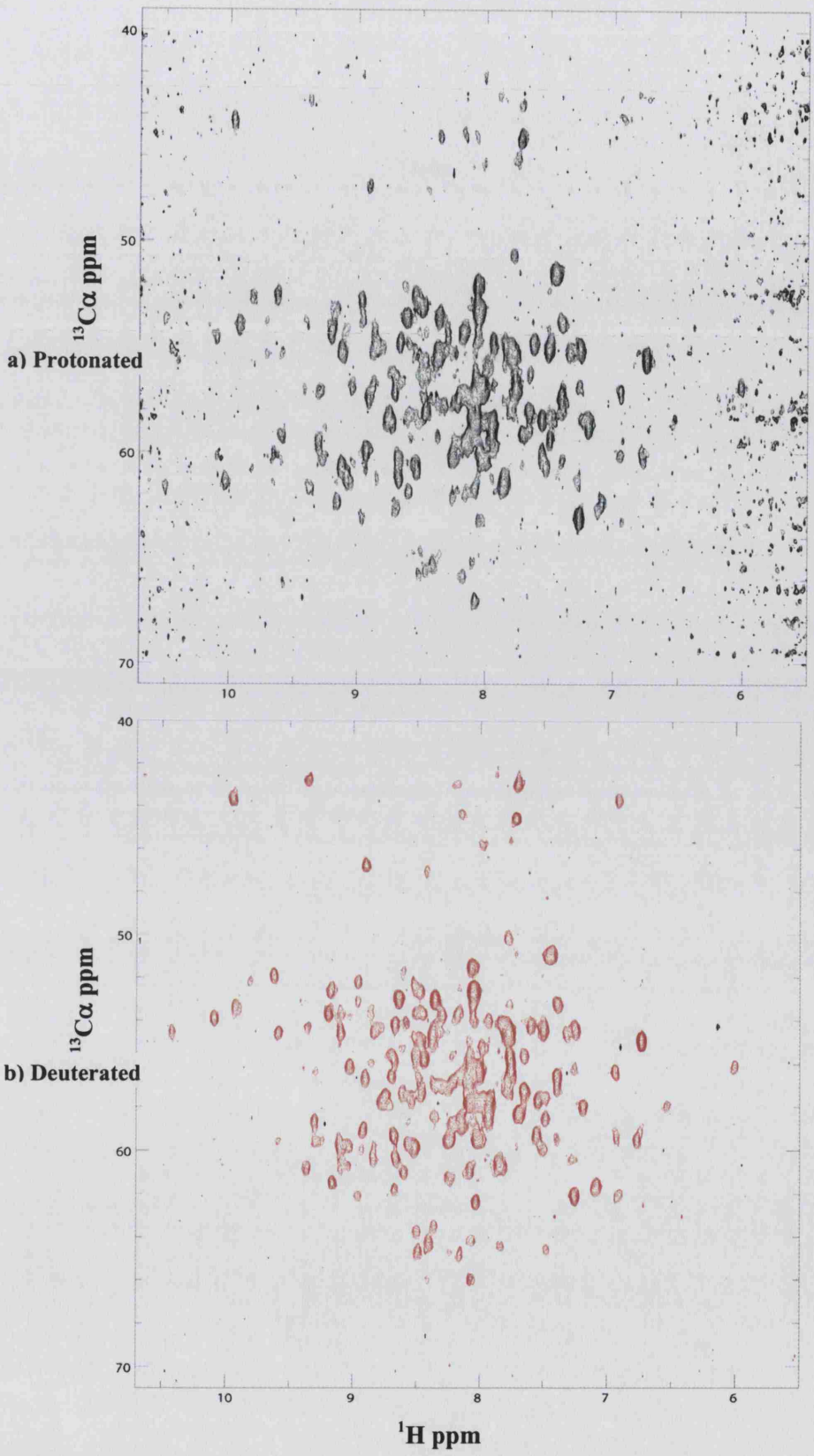

Figure 3.15. Comparison of the 2D (^{13}Cα,NH) projections from 3D HNCA spectra for a protonated (a) and deuterated (b) sample. (a) recorded at a 600MHz field strength (b) recorded at a 500MHz field strength.

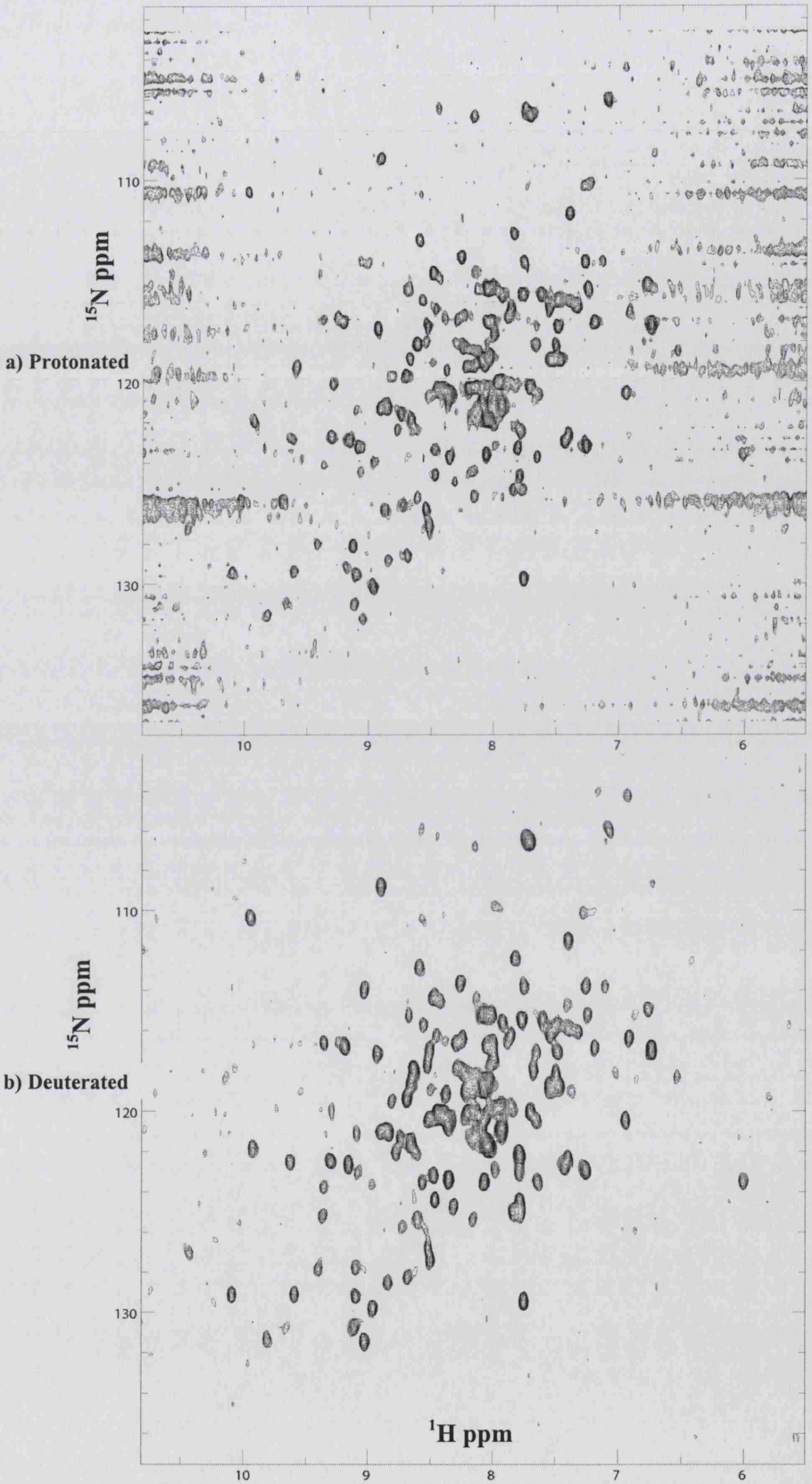

Figure 3.16. A 2D (^{15}N,NH) projection of the 3D HNCA experiment from protonated (a) and deuterated (b) samples. (a) recorded at a 600MHz field strength (b) recorded at a 500MHz field strength. The 2D projections have a similar chemical shifts dispersion as the ^{15}N ^{1}H HSQC. Not all the crosspeaks have been displayed in the deuterated sample for simplicity.

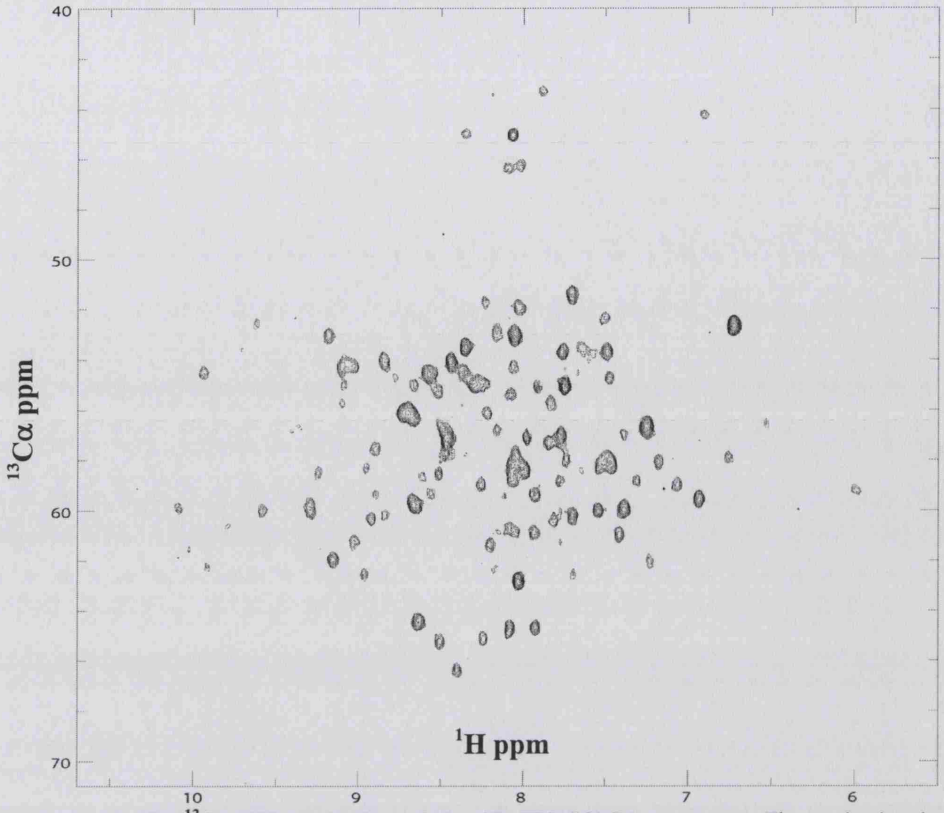

Figure 3.17. A 2D (^{13}Cα,NH) projection of the 3D HN(CO)CA spectrum. The projection is from a deuterated sample. The chemical shifts at about 45 ppm belong to the glycine residues.

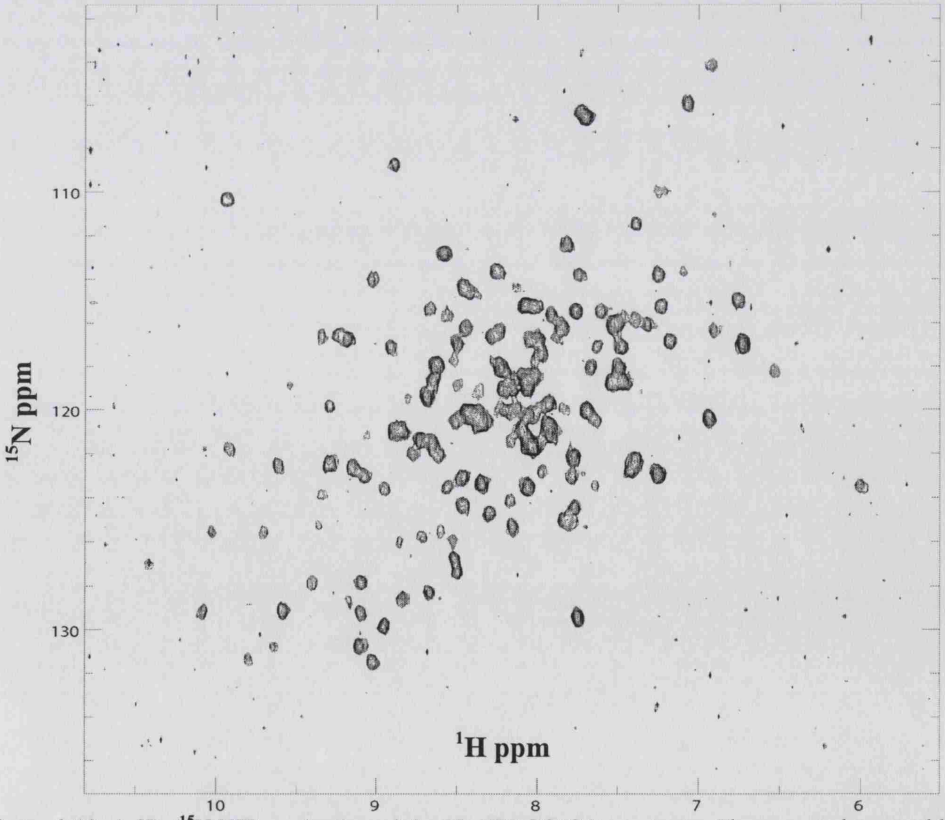

Figure 3.18. A 2D (^{15}N,NH) projection of the 3D HN(CO)CA spectrum. The crosspeaks resemble a ^{1}H^{15}N HSQC experiment without any resonances for the sidechains. The projection is from a deuterated sample. The difference in S/N ratio is due to a different number of points collected in each dimensions

experiment. This spectrum resembles the $^{1}H^{15}N$ HSQC spectrum without any resonance for the glutamine and asparagine sidechain doublets but with broader crosspeaks. This spectrum with other similar 2D projections was used in an ANSIG session to align the ^{15}N, NH crosspeaks in all 3D spectra.

3.7.3 A three-dimensional HN(CA)CB experiment

The HN(CA)CB (Yamazaki *et al.*, 1994b) experiment is a modified version of the HNCACB experiment which itself is based upon the CB(CA)NH scheme introduced by Grzesiek and Bax (Grzesiek and Bax, 1992a). The HN(CA)CB experiment provides correlations of the $^{13}C\beta$,^{15}N and H^{N} nuclei.

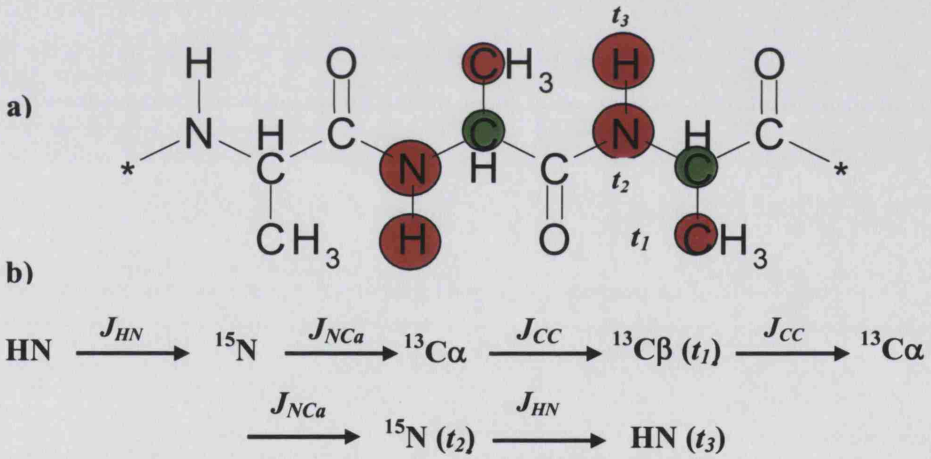

Figure 3.19. The nuclei and coupling constants involved in the HN(CA)CB experiment. (a) Detected nuclei are highlighted in red circle. Nuclei in green are used for magnetisation transfer. **(b)** Shows the direction of the magnetisation transfer. The coupling constants are shown above each arrow.

Figure 3.19 shows highlighted nuclei involved in the HN(CA)CB experiment. The red circled nuclei are directly detected and recorded during the experiment, while the nucleus in green has been used during the magnetisation transfer but not detected. Figure 3.19 (b) shows the flow of the magnetisation transfer throughout this experiment and the relative coupling involved in each step

of the magnetisation transfer as indicated above the arrows. t_1, t_2 and t_3 are the designated evolution or acquisition times. Figure 3.20 shows a 2D ($^{13}C\beta$, NH) projection of the 3D HN(CA)CB spectrum, the chemical shifts range between 15 to 75 ppm. The carbon carrier was centred at the ^{13}C region at about 42 ppm. The $^{13}C\alpha$ of the glycines are not suppressed during this experiment and hence can be observed in the spectrum, though of opposite sign to other crosspeaks (shown here in red) at the same range within other spectra, at about 45 ppm. The crosspeaks between 60 to 72 ppm belong to either serine or threonine residues. The chemical shifts around 20ppm belong to alanine residues.

Figure 3.21 shows the 2D (^{15}N, NH) projection of the 3D HN(CA)CB spectrum. This spectrum is similar to the $^{1}H^{15}N$ HSQC spectrum but comparison with Figure 3.18 of the same 2D projections of the 3D HN(CO)CA experiment shows lower signal to noise ratio and hence lower sensitivity of this experiment. The HNCA has the best signal to noise ratio in the series of experiments conducted (compare Figure 3.16 with Figures 3.19 and 3.22.)

3.7.4 A three-dimensional HN(COCA)CB experiment

The HN(COCA)CB (Yamazaki *et al.*, 1994b) experiment correlates the $^{13}C\beta_{(i-1)}$, ^{15}N and HN nuclei and assists with the intra-residue connections. Figure 3.22 (a) shows the nuclei detected in the HN(COCA)CB experiment highlighted in red, in green are the nuclei involved in the magnetisation transfer but not directly detected. Figure 3.22 (b) shows the direction of the magnetisation transfer in the 3D HN(COCA)CB experiment.

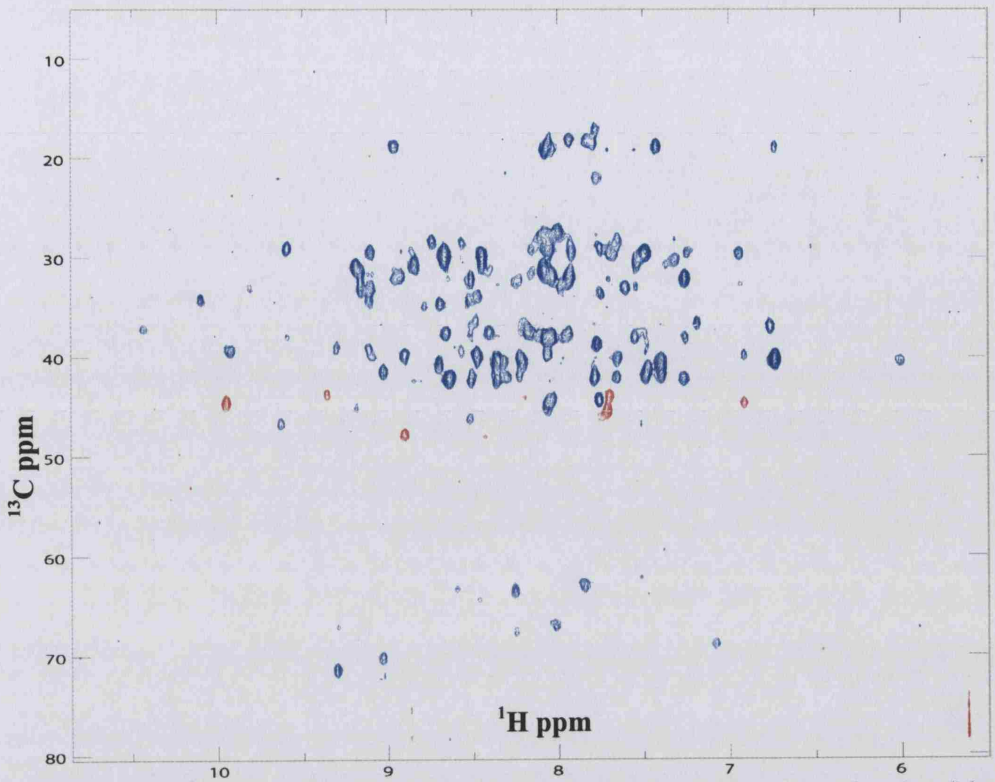

Figure 3.20. A 2D (^{13}Cβ,NH) projection of the 3D HN(CA)CB spectrum. The glycines (here in red) have an opposite sign compared to other chemical shifts. Alanine residues appear around 20 ppm while serine and threonine residue resonances can be observed between 60 to 72 ppm.

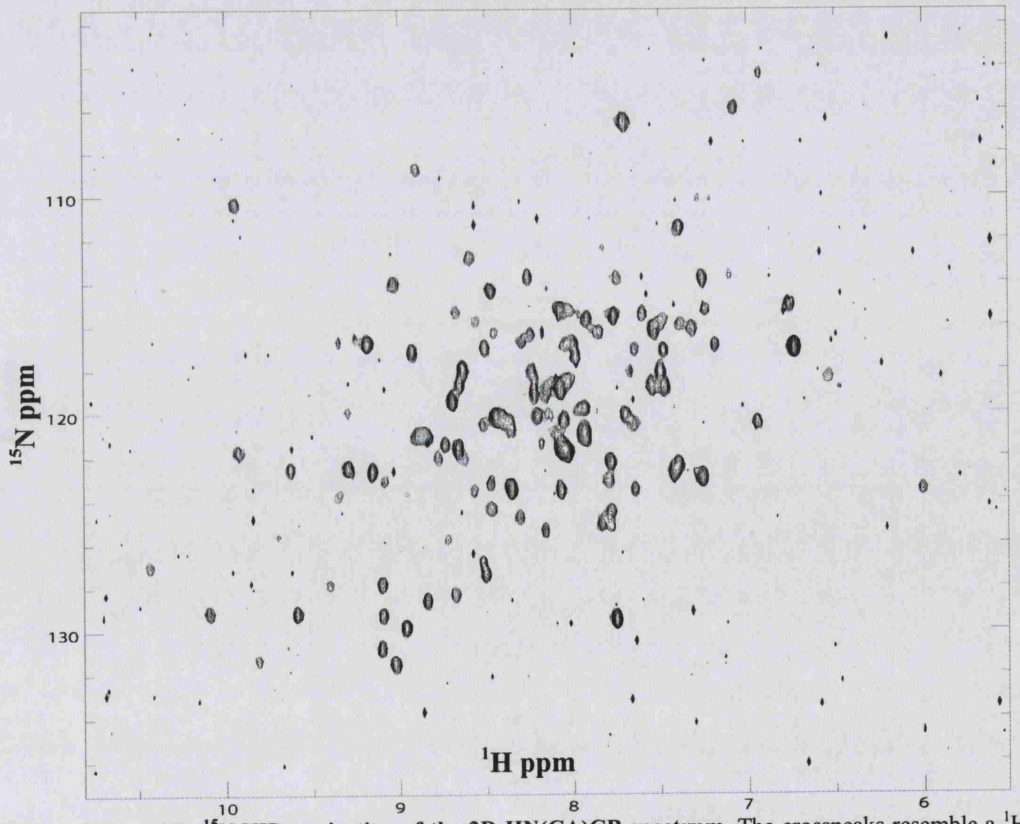

Figure 3.21. A 2D (^{15}N,NH) projection of the 3D HN(CA)CB spectrum. The crosspeaks resemble a ^{1}H^{15}N HSQC experiment without any resonances for the sidechains.

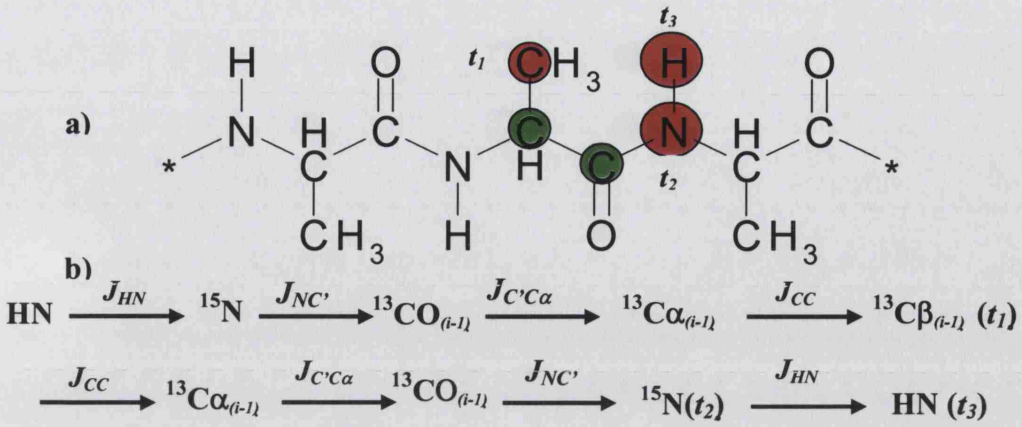

Figure 3.22. The nuclei and coupling constants involved in the HN(COCA)CB experiment. (a) The nuclei detected in this experiment are highlighted in red circles. The nuclei in green circles are used for magnetisation transfer and are not directly detected. **(b)** Shows the direction of the magnetisation transfer and coupling constants are shown above each arrow. t_1, t_2 and t_3 indicate the acquisition times.

The relative coupling involved in each step of the magnetisation transfer is indicated above the arrows, with t_1, t_2 and t_3 indicating the acquisition times. Together the HN(CA)CB and HN(COCA)CB experiments were used to assign each $C\beta_{(i)}$, $C\beta_{(i-1)}$ resonance to its amide ($HN_{(i)}$,$N_{(i)}$) resonance group as well as assignment of each residue by their specific chemical shift pattern. A 2D ($^{13}C\beta_{(i-1)}$, NH) projection of the 3D HN(CACO)CB spectrum is shown in Figure 3.23. As in the HN(CA)CB experiment, crosspeaks of opposite sign are observed for glycine residues (shown here in blue). The chemical shifts for this spectrum range between 15 to 75 ppm. As in the HN(CA)CB experiment, the serine and threonine chemical shifts are observed between 60 to 75 ppm and the alanine residues are observed around 20 ppm. The HN(COCA)CB experiment has the lowest signal to noise ratio in general, hence a greater number of transients were used in comparison to the HN(CA)CB experiment.

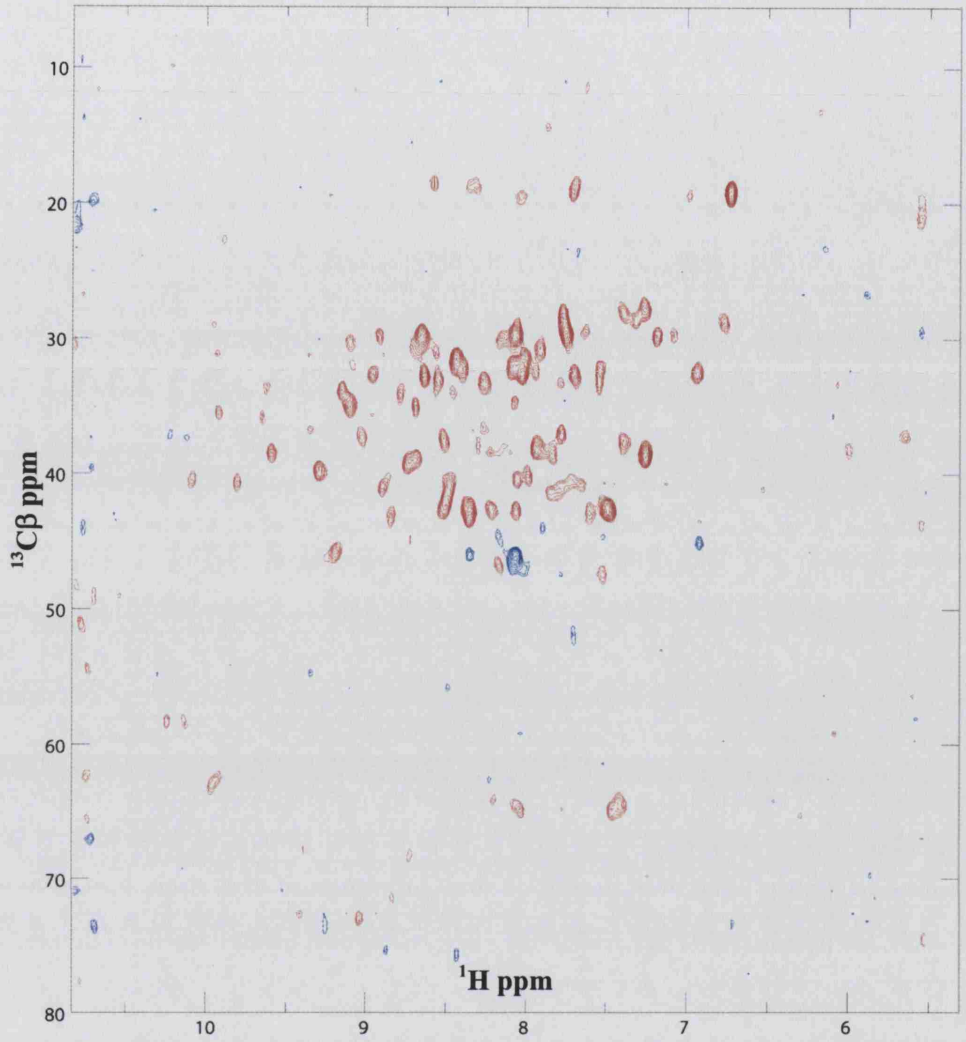

Figure 3.23 A 2D (^{13}C$\beta_{(i-1)}$,NH) projection of the 3D HN(COCA)CB spectrum. The glycines (in blue) have the opposite sign compared to other chemical shifts. Alanine residues appear around 20 ppm while serine and threonine residue resonances can be observed between 60 to 75 ppm.

3.7.5 A three-dimensional HNCO experiment

The 3D HNCO (Grzesiek and Bax, 1992b; Muhandiram and Kay, 1994) experiment is used to correlate each $^{13}CO_{(i-1)}$ resonance with amide ^{15}N and H^N nucleus resonances. The HNCO experiment affords a 3D spectrum in which ^{1}H, ^{15}N and ^{13}CO chemical shifts are displayed in three independent dimensions. The HNCO experiment is the most sensitive 3D triple resonance experiment and high quality data sets can be obtained in a relatively short time. Figure 3.24 (a) shows

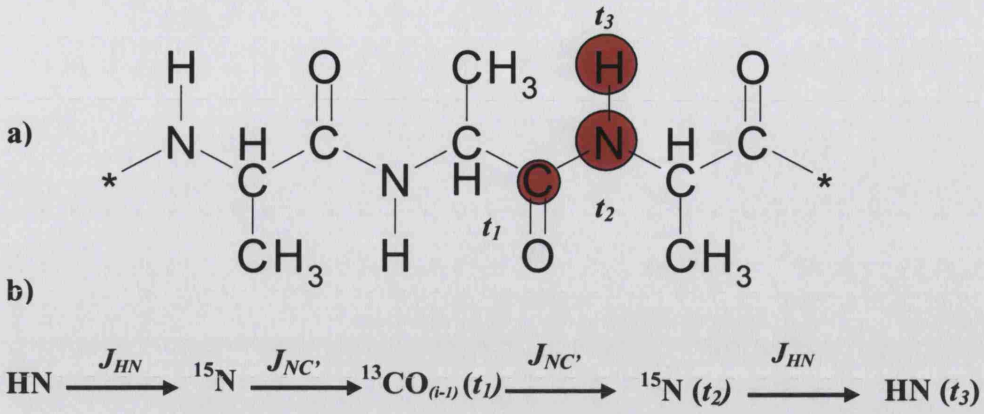

Figure 3.24. The nuclei, direction of the magnetisation transfer and coupling constants involved in the HNCO experiment. (a) Highlights the nuclei detected in this experiment in red with the t_1, t_2 and t_3 acquisition times recorded in each dimension next to its nuclei **(b)** Shows the direction of the magnetisation transfer with the relative coupling constants shown above each arrow.

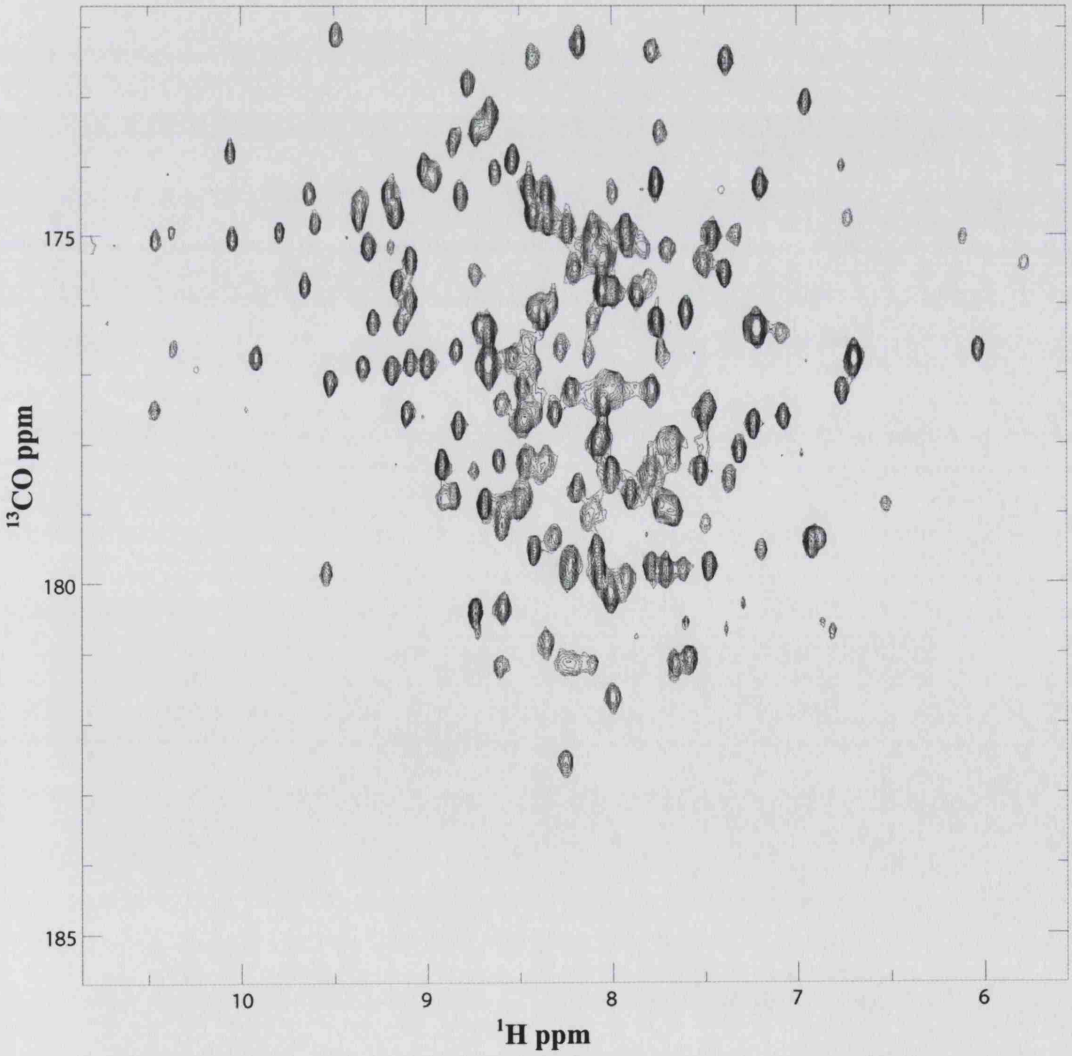

Figure 3.25 A 2D (^{13}CO$_{(i-1)}$,NH) projection of the 3D HNCO spectrum. The crosspeaks are observed between 170 to 185 ppm.

the nuclei involved in this experiment, highlighted in red, and the pathway of the magnetisation transfer in this experiment. Figure 3.25 shows a 2D $^{13}CO_{(i-1)}$, NH projection of the 3D HNCO experiment. The crosspeaks appear in the range of 170 to 185 ppm in the spectrum. The HNCO resonances, together with HN(CA)CO chemical shifts which correlate for the $^{13}CO_i$ nuclei, give an additional check point in the sequential correlation procedure to confirm a sequential connection to resolve any ambiguities in the sequential assignment procedure.

3.7.6 A three-dimensional HN(CA)CO experiment

The HN(CA)CO (Matsuo *et al.*, 1996; Clubb *et al.*, 1992) experiment correlates the $^{13}CO_i$ and $^{13}CO_{(i-1)}$ nuclei with the amide ^{15}N and H^N nuclei resonances. Figure 3.26 (a) shows the nuclei involved in the HN(CA)CO experiment. In the HN(CA)CO experiment the magnetisation is transferred from the HN proton via the ^{15}N atom and the $^{13}C\alpha$ nucleus to the $CO_{(i, i-1)}$ carbon atom and back the same way, as shown in Figure 3.26 (b). The HN(CA)CO experiment is not as sensitive as the HNCO experiment due to the fast relaxation of the $^{13}C\alpha$ coherence by the Hα proton efficient dipolar relaxation (and also the small $J_{NC\alpha}$ coupling used in the pulse sequence). Perdeuteration of the sample eliminates this effect thereby increasing the sensitivity of the experiment (Clubb *et al.*, 1992). The HNCO experiment correlated an amide proton with the CO atom of the preceding amino acid, whereas in the HN(CA)CO experiment intra- and inter-residual CO atoms are observed. Combination of the two experiments has assisted in the sequential assignment of the apo- Hsp90 N-terminal along with other experiments that will be discussed in section 3.8.

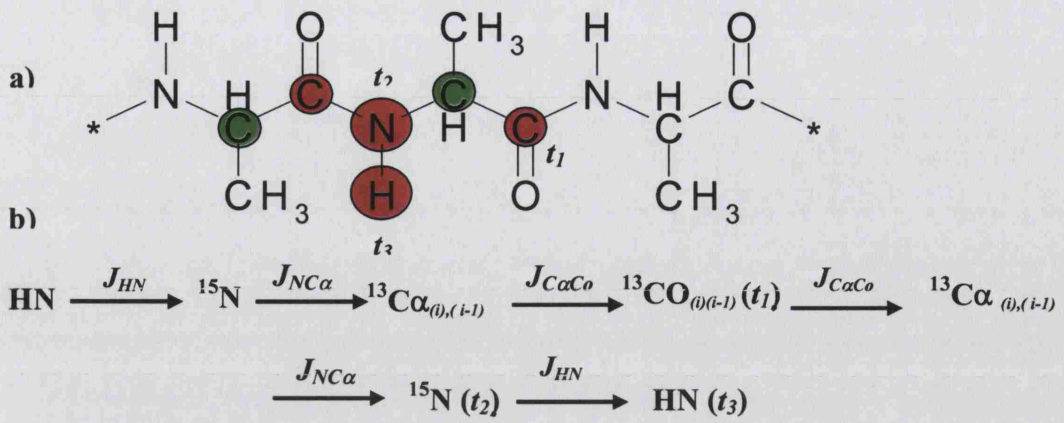

Figure 3.26. The nuclei, direction of the magnetisation transfer and the coupling constants involved in the HN(CA)CO experiment. (a) Highlights the nuclei detected in this experiment in red with the t_1, t_2 and t_3 evolution or acquisition times recorded in each dimension next to its nuclei. The $^{13}C\alpha$ nuclei in green are not detected during this experiment and act as relay **(b)** Shows the direction of the magnetisation transfer with the relative coupling constants shown above each arrow.

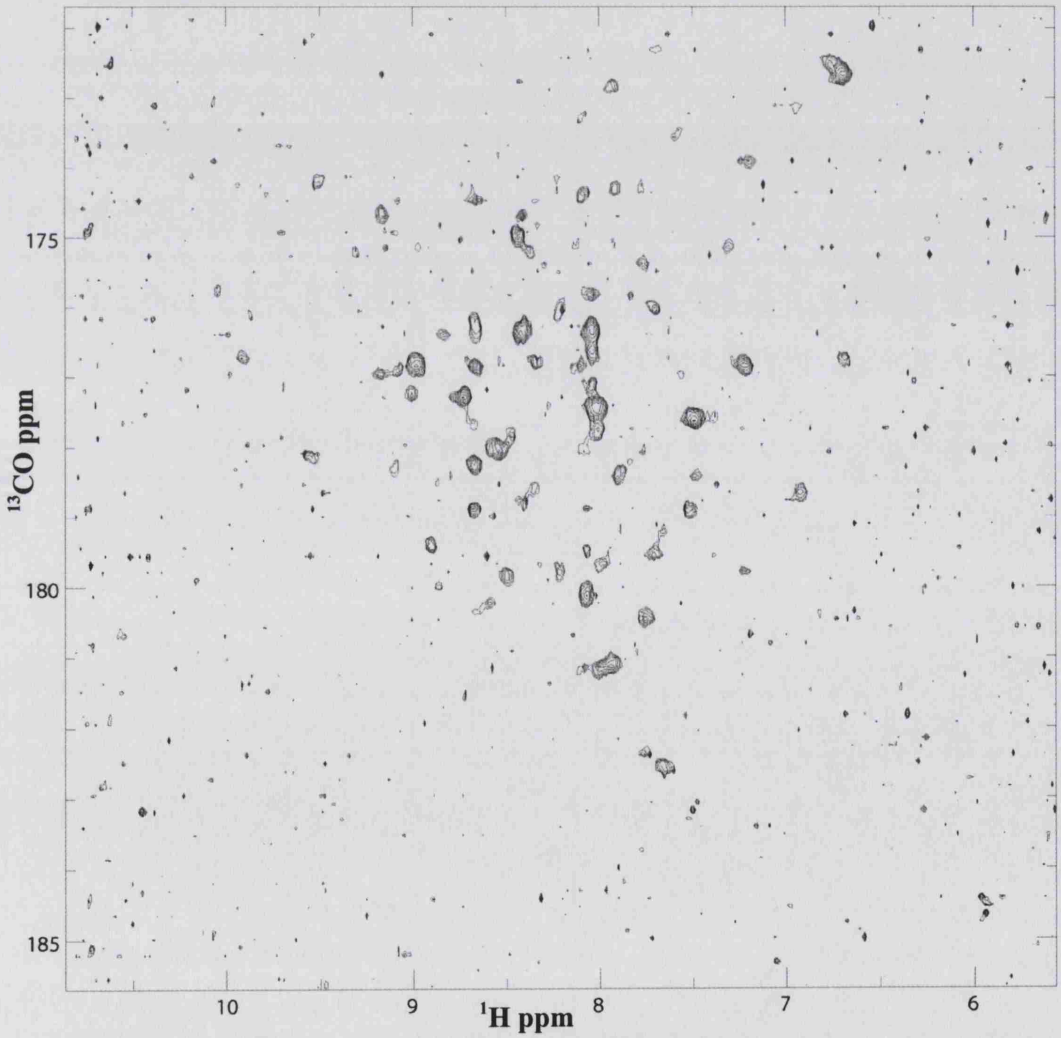

Figure 3.27. A 2D ($^{13}CO_{(i),(i-1)}$NH) projection of the 3D HN(CA)CO spectrum. The crosspeaks are observed between 170 to 185 ppm. The HN(CA)CO experiment is less sensitive than the HNCO experiment so less crosspeaks are observed in the spectrum. Not all the 2D projections are displayed

3.8 Sequential connection and assignment of the resonances

The 3D HNCA, HN(CO)CA, HN(CA)CB, HN(COCA)CB, HNCO and HN(CA)CO as well the 2D HSQC were acquired, processed using NMRPipe and converted to an AZARA file for each set of spectra (as described in Chapter 2 Section 2.9). The 2D contours were produced using the contour program from the AZARA package v2.7, written by Wayne Boucher (Boucher, 2002), from the 3D data sets. The contours created by the program can be read and loaded into an ANSIG session. The levels for contours were chosen by inspection of an NMRDraw session, where those that had the best compromise of noise level without losing any important crosspeaks were chosen.

The peaks of the spectra were initially picked automatically using the 'Peak_Find' macro in the ANSIG session and refined and adjusted later by hand. Automatic peak picking may encounter difficulties especially in areas where there are highly overlapped peaks, water artifacts or spectra with substantial noise. During the inspection, peaks picked due to noise artifacts or highly overlapped areas were removed or adjusted. Finally the contour files were loaded into an ANSIG session with the spectra for similar nuclei in the same strip plots and adjusted according to their chemical shift for similar residues (i.e. the HNCA and HN(CO)CA spectra for the $^{13}C\alpha$ nucleus were loaded into the same strip plots of the ANSIG session as shown in Figure 3.28 and the inter- intra- residue chemical shifts were aligned). Furthermore, orthogonal 2D (^{1}H,^{15}N) projections of the contour files were loaded and adjusted in the ANSIG session in a separate window. The HNCA (purple contours), HN(CO)CA (red contours), HN(CA)CB (green contours) and HN(COCA)CB (yellow contours) files were loaded in the same strip

plot pair (windows 4 and 5) of the ANSIG session with the HNCO (cyan contours) and HN(CA)CO (pink contours) contours loaded in a separate pair (windows 2 and 3).

The sequential connection starts by picking amide chemical shifts in the $^{1}H^{15}N$ HSQC spectrum (orange contours in ANSIG window 1, Figure 3.28) and correlating it to the $^{1}H^{13}C\alpha_{(i)}$ resonance for the same residue in the HNCA spectrum, before subsequently connecting it to its preceding residue $^{1}H^{13}C\alpha_{(i-1)}$ resonance using the HN(CO)CA spectrum. Note that the HNCA experiment produces two resonances for residues *(i)* and *(i-1)* and the HN(CO)CA produces only one resonance for the residue *(i-1)*. The next step was to connect the $^{13}C\alpha$ nuclei to the $^{1}H^{13}C\beta_{(i)}$ resonance from the HN(CA)CB experiment for the same residue, distinguishing it from its preceding $^{1}H^{13}C\beta_{(i-1)}$ resonance by use of the HN(COCA)CB spectrum.

A dotted horizontal line highlighted by white arrows connects the sequentially connected residues for $^{13}C\alpha$ resonances. The sequential $^{13}C\beta$ nuclei were also connected using a solid horizontal line, highlighted by red arrows. The vertical line connects the resonance belonging to the same residue (highlighted by green arrows). The $^{1}H^{13}CO$ chemical shifts of HNCO and HN(CA)CO spectra were used to sequentially connect the carbonyl chemical shifts as well as to resolve any ambiguities in connecting the sequential $^{13}C\alpha$ resonance, particularly in overlapped and crowded areas of the spectrum. The two sequential residues from the HNCO and HN(CA)CO experiments are connected using solid horizontal lines (highlighted by yellow arrows). The sequential connection moves backward through the sequence during which several resonances were missing or were too

weak to be assigned. As a result, the sequential connections are in several segments of 3 or more consecutive connected residues.

Sequential assignments of the resonances were achieved using a combination of $^{13}C\alpha$ and $^{13}C\beta$ chemical shifts based on the Grzesiek and Bax (1993) probability distribution of the chemical shifts method. The $^{13}C\alpha$ and $^{13}C\beta$ resonances are useful for identification of different amino acids due to their characteristic chemical shift ranges. Assignment was carried out by combining the individual probabilities for the $^{13}C\alpha/^{13}C\beta$ resonances corresponding to amino acid type within segments of sequentially connected residues.

A script written-in-house by Dr. Mark Pfuhl was used, based on the above method, to calculate the probability of the corresponding through bond connected resonances to different amino acid types and subsequently locating the stretch in the primary sequence of the protein (Grzesiek and Bax, 1993).

Figure 3.29 shows the assignment pathway strip plots of sequentially assigned segments of the Hsp90 N-terminal protein sequence using the plot2 program for display. The HNCA $^{13}C\alpha_{(i),(i-1)}$ resonance contours (shown in blue) and the HN(CO)CA resonance contours (shown in red) are displayed. A continuous red line shows the sequentially connected residues from Lys-139 to Glu-144. The HN(CA)CB resonance contours are displayed in black for $^{13}C\beta_{(i),(i-1)}$ nuclei and in yellow for the HN(COCA)CB resonance contours for the $^{13}C\beta_{(i-1)}$ nuclei.

A continuous black line connects the sequentially assigned residues of the $^{13}C\beta$ nuclei in Figure 3.29. For example, Ser-140 has a unique $^{13}C\beta$ chemical shift at 63.15 ppm and $^{13}C\alpha$ chemical shift of 54.81 ppm. Figure 3.30 shows strip plots of sequentially connected and assigned residues Arg-89 to Lys-195 displayed by

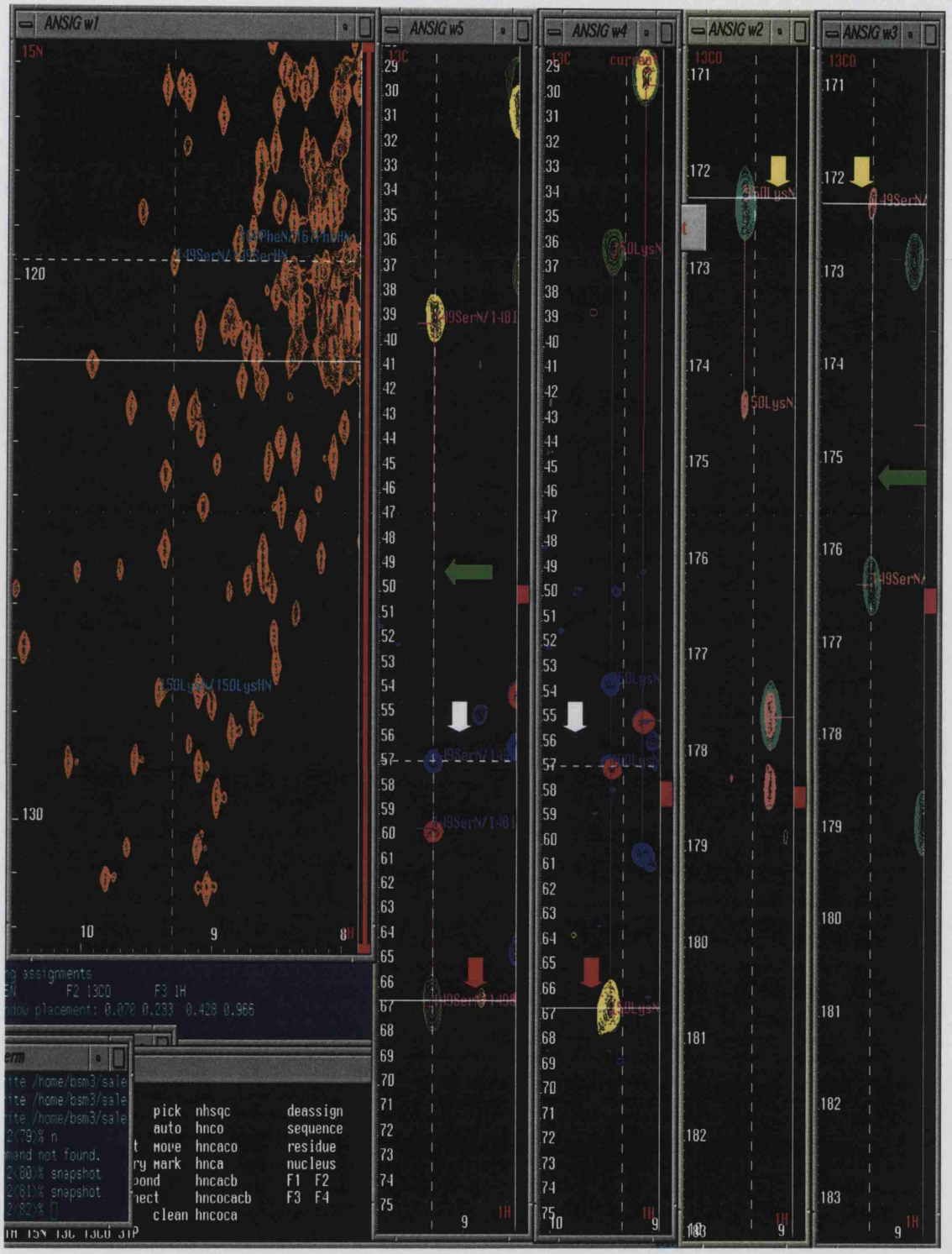

Figure 3.28 A snapshot from an ANSIG session used for sequential assignment of the apo Hsp90 N-terminal domain. This ANSIG session has six windows with HSQC resonance contours, in orange, in window 1 and all the 2D ($^{1}H^{15}N$) projections of the 3D spectra in window 6. In windows 4 and 5 the HNCA resonance contours (purple), HN(CO)CA (red), HN(CA)CB (green) and HN(COCA)CB (yellow) are loaded. Windows 2 and 3 show the HNCO and HN(CA)CO resonances in cyan and pink respectively for two sequentially connected and assigned residues

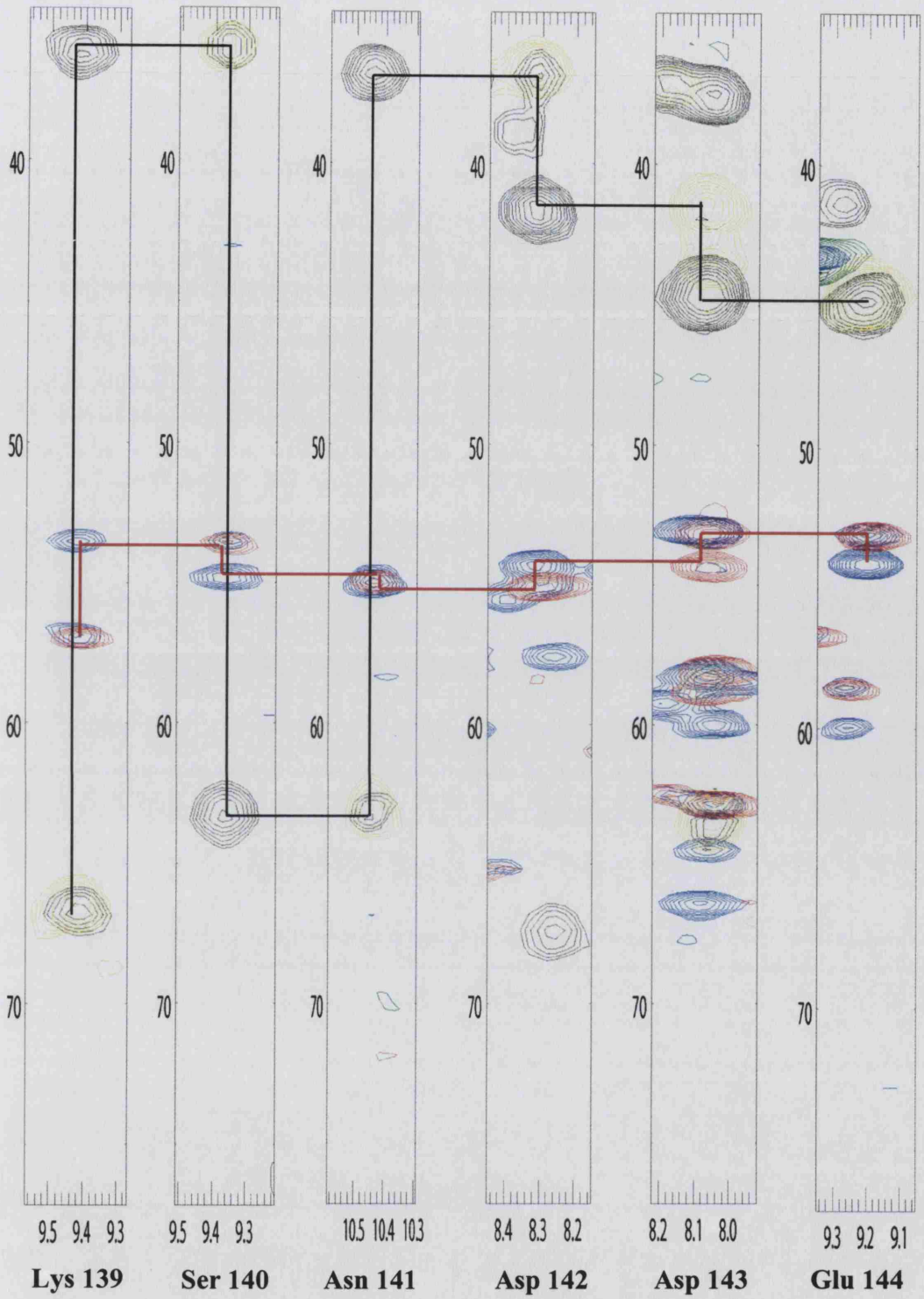

Figure 3.29 Strip plots from the 3D HNCA, HN(CO)CA, HN(CA)CB and HN(COCA)CB correlation spectra used for sequential assignment of the apo Hsp90 N-terminal. The blue crosspeaks belong to a 3D HNCA spectrum and shows the $^{13}C\alpha_{(i,\ i-1)}$ correlation. The red crosspeaks belong to a 3D HN(CO)CA spectrum showing the $^{13}C\alpha_{(i-1)}$ correlation. A red line connects the sequentially connected and assigned $^{13}C\alpha$ resonances. The black crosspeaks are from a 3D HN(CA)CB spectrum showing the $^{13}C\beta_{(i,i-1)}$ nuclei. The yellow crosspeaks are from a HN(COCA)CB spectrum for $^{13}C\beta_{(i-1)}$ correlation. The black line connects the $^{13}C\beta$ resonances.

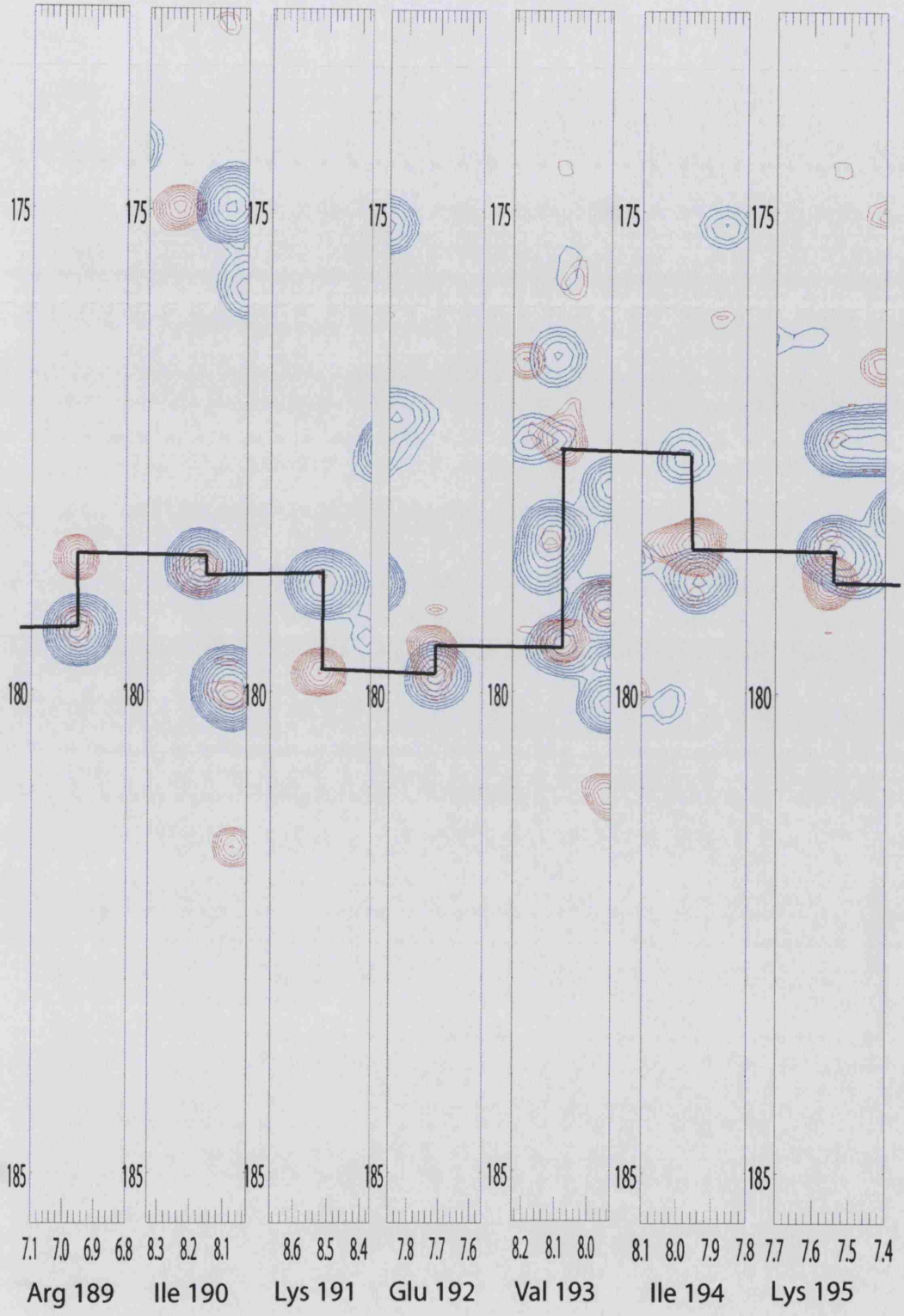

Figure 3.30 Strip plots from the 3D HNCO and HN(CA)CO correlation spectra used for sequential assignment of the apo Hsp90 N-terminal. The blue crosspeaks belong to a 3D HNCO spectrum and show the $^{13}CO_{(i-1)}$ correlation. The red crosspeaks belong to a 3D HN(CA)CO spectrum showing the $^{13}CO_{(i, i-1)}$ resonances. A black line links the sequentially connected residues. The residues arginine 189 to lysine 195 are sequentially connected and assigned as shown.

the plot2 program in the carbonyl region. The blue crosspeaks correspond to $^{13}CO_{(i-1)}$ nuclei of the 3D HNCO experiment and red crosspeaks correspond to the $^{13}CO_{(i,i-1)}$ nuclei of the 3D HN(CA)CO experiment. A black line links the sequentially connected and assigned carbonyl chemical shifts. The HNCO and HN(CA)CO experiments are most useful for resolving any ambiguities in the assignment when there are, for instance, several degeneracies in the HNCA and HN(CO)CA spectra.

$^{1}H^{15}N$ NOESY-HSQC and $^{1}H^{15}N$ TOWNY-HSQC spectra from a 800 MHz proton frequency spectrometer as well as a 3D ^{15}N NOESY-HSQC experiment from the perdeuterated sample recorded using a 600 MHz proton frequency spectrometer were used to confirm the assignments. In addition these were used to resolve any remaining ambiguities not resolved by the 3D spectra as well as to assign the $^{1}H\alpha$ resonances.

Figure 3.31 shows an assigned $^{1}H^{15}N$ HSQC spectrum recorded on an 800 MHz spectrometer. A total of 197 out of 207 residues were assigned, which constitutes approximately 95% of the Hsp90 N-terminal domain (including the 5 proline residues for which no crosspeaks were observed in the HSQC spectrum). Only one out of the six histidines from the affinity tag had a resonance observed in the HNCA and HN(CO)CA experiments. No other histidine resonances were observed either because the amides were in exchange with the solvent (assisted by the pH of the sample, pH 8.0) or were flexible on an intermediate time scale in the structure. Seventeen NH_2 sidechain resonances (34 peaks) were observed which are connected in pairs to distinguish them from amide backbone resonances. These sidechain peaks belong to eight asparagine and nine glutamine residues present in the protein sequence. Eight arginine sidechains in Figure 3.31 are highlighted with

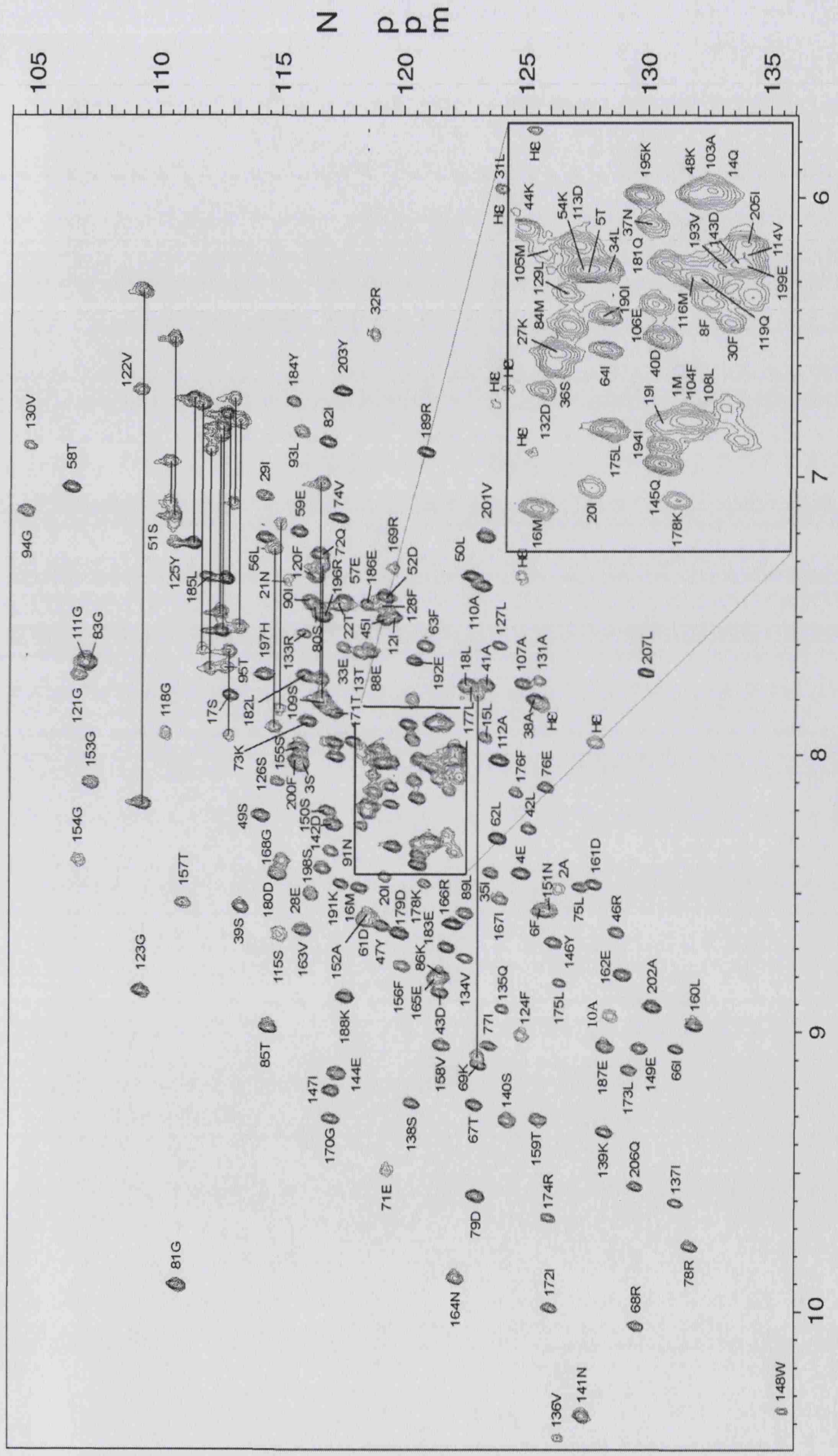

Figure 3.31. A $^{1}H^{15}N$ HSQC spectrum of Hsp90 N-terminal domain from a ^{15}N-labelled sample using 800 MHz proton frequency spectrometer recorded at 25°C.

Hε. There are twelve glycines in the protein sequence of which eleven have been assigned. The glycines are important because of the conserved G-Boxes in the Hsp90 N-terminal structure.

Table 3.1 shows the assigned residue sequence in green; the proline residues in pink and the residues not assigned are either red or not coloured. The unassigned residues 9, 23 to 26 and 97 to 99, highlighted in red, are mostly in the coil or turn structure, according to the published X-ray crystal structure (Prodromou *et al.,* 1997). The reason for the weak or unobservable resonances for these residues is either chemical exchange with the environment or the mobility of these regions (Figure 3.32). Residues 11, 100 and 101 that are not coloured are in an α-helical structure, yet have no resonance observed for them. In Figure 3.32 the assigned residues are plotted on the X-ray crystal structure of the Hsp90 N-terminal domain. The assigned residues are highlighted in green with the unassigned residues in yellow. The proposed 'ATP-lid' (residues 100 to 120) and the nucleotide-binding pocket are highlighted using red arrows and red circle respectively.

Table 3.2 shows the $^{13}C\alpha$, $^{13}C\beta$ and ^{13}CO nuclei assigned for the Hsp90 N-terminal protein sequence. Table 3.2 (a) shows the unassigned $^{13}C\alpha$ nuclei (shown in yellow) and assigned resonance (shown in green). Overall 197 $^{13}C\alpha$ atoms (95.2%) were assigned. Table 3.2 (b) shows the $^{13}C\beta$ nuclei assigned (shown in green) and the unassigned residues (in purple). The glycines (in pink) have no $^{13}C\beta$ resonance and overall 182 $^{13}C\beta$ atoms were assigned (93.24%, the glycines were included in the percentage). Finally the ^{13}CO assignment in Table 3.2(c) shows 195 ^{13}CO atoms assigned (94.2%). The unassigned residues are highlighted in blue.

MRGSHHHHHH	GMASETFEFQ	AEITQLMSLI	INTVYSNKEI	FLRELISNAS
DALDKIRYKS	LSDPKQLETE	PDLF IRITPK	PEQKVLEIRD	SGIGMTKAEL
INNLGTIAKS	GTKAFMEALS	AGADVSMIGQ	FGVGFYSLFL	VADRVQVISK
SNDDEQYIWE	SNAGGSFTVT	LDEVNERIGR	GTILRLFLKD	DQLEYLEEKR
IKEVIKRHSE	FVAYPIQL			

Table 3.1. The Hsp90 N-terminal domain residues assigned in the $^{1}H^{15}N$ HSQC spectrum. The dotted area at beginning of the sequence is where the six-histidine residues from the construct are located. Pink highlighted prolines don't have any chemical shifts in the spectrum. The red highlighted residues are in the coil or turn structure and are not assigned. The residues not coloured are in an α-helical structure and not assigned.

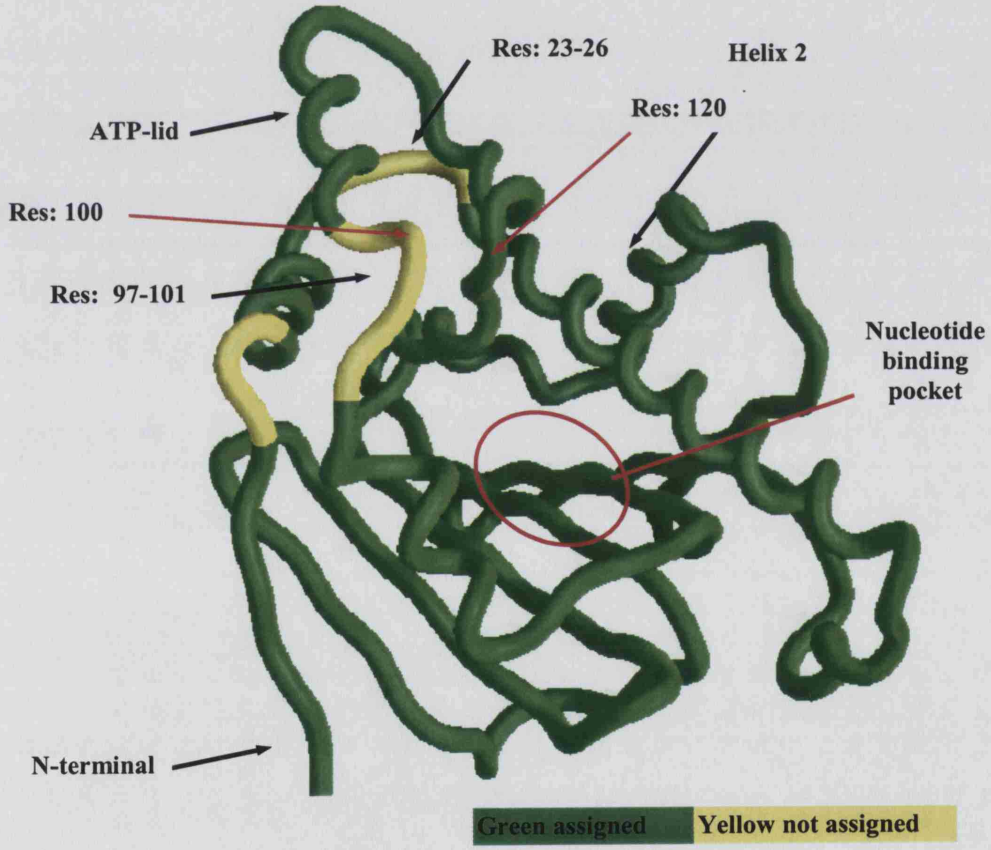

Figure 3.32. Assigned residues plotted on the X-ray crystal structure of the Hsp90 N-terminal domain. Residues assigned are shown in green with the unassigned residues in yellow.

Table 3.2 Residues assigned for the (a) $^{13}C\alpha$ nuclei (b) $^{13}C\beta$ nuclei and (c) ^{13}CO nuclei. The yellow residues (in a) pink residues (in b) and blue residues (in c) were not assigned due to lack of resonance. The residues MRGSHHHHHH are part of the construct with six histidines and generally no correlations were observed for them. Glycine residues have no $^{13}C\beta$ correlation.

Table 3.3 shows the chemical shift of the amide resonances. The $^{13}C\alpha$, $^{13}C\beta$ and ^{13}CO nuclei, assigned to the 207 residues are displayed in Tables 3.4, 3.5 and 3.6. Table 3.7 shows the Hα nuclei assigned for 141 out of 207 residues.

No.	Res.	Nuc.	CS	No.	Res	Nuc.	CS	No.	Res.	Nuc.	CS	No.	Res.	Nuc.	CS
0	Gly	N	109.98	36	Ser	N	117.52	69	Lys	N	122.16	105	Met	N	117.28
		HN	8.38			HN	8.21			HN	9.12			HN	8.00
1	Met	N	119.99	37	Asn	N	119.34	71	Glu	N	118.47	106	Glu	N	119.50
		HN	8.31			HN	7.94			HN	9.50			HN	8.10
2	Ala	N	125.44	38	Ala	N	124.52	72	Gln	N	115.60	107	Ala	N	123.98
		HN	8.50			HN	7.80			HN	7.28			HN	7.75
3	Ser	N	114.84	39	Ser	N	112.37	73	Lys	N	115.14	108	Leu	N	120.32
		HN	8.06			HN	8.56			HN	7.88			HN	8.32
4	Glu	N	123.90	40	Asp	N	119.56	74	Val	N	116.42	109	Ser	N	115.74
		HN	8.43			HN	8.17			HN	7.15			HN	7.82
5	Thr	N	118.32	41	Ala	N	122.53	75	Leu	N	126.27	110	Ala	N	122.27
		HN	8.04			HN	7.76			HN	8.48			HN	7.39
6	Phe	N	124.75	42	Leu	N	124.25	76	Glu	N	124.82	111	Gly	N	106.04
		HN	8.58			HN	8.28			HN	8.12			HN	7.68
7	Glu	N	118.63	43	Asp	N	120.54	77	Ile	N	122.55	112	Ala	N	122.99
		HN	8.34			HN	8.87			HN	9.05			HN	8.03
8	Phe	N	120.47	44	Lys	N	116.96	78	Arg	N	130.80	113	Asp	N	118.03
		HN	8.10			HN	7.95			HN	9.77			HN	8.00
10	Ala	N	127.88	45	Ile	N	118.27	79	Asp	N	122.05	114	Val	N	121.28
		HN	9.00			HN	7.51			HN	9.59			HN	8.02
12	Ile	N	118.64	46	Arg	N	127.79	80	Ser	N	115.47	115	Ser	N	113.92
		HN	7.50			HN	8.65			HN	7.47			HN	8.66
13	Thr	N	117.32	47	Tyr	N	118.17	81	Gly	N	109.84	116	Met	N	120.21
		HN	7.64			HN	8.62			HN	9.91			HN	8.05
14	Gln	N	120.73	48	Lys	N	120.26	82	Ile	N	115.89	117	Ile	N	119.42
		HN	7.90			HN	7.90			HN	6.88			HN	7.81
15	Leu	N	122.42	49	Ser	N	113.18	83	Gly	N	106.09	118	Gly	N	109.35
		HN	7.95			HN	8.22			HN	7.67			HN	7.93
16	Met	N	117.26	50	Leu	N	121.84	84	Met	N	117.84	119	Gln	N	120.40
		HN	8.49			HN	7.36			HN	8.15			HN	8.06
17	Ser	N	111.93	51	Ser	N	109.62	85	Thr	N	113.52	120	Phe	N	115.41
		HN	7.79			HN	7.17			HN	9.00			HN	7.36
18	Leu	N	121.56	52	Asp	N	118.30	86	Lys	N	120.57	121	Gly	N	105.79
		HN	7.76			HN	7.43			HN	8.80			HN	7.71
19	Ile	N	119.68	54	Lys	N	118.15	87	Ala	N	116.27	122	Val	N	108.21
		HN	8.34			HN	8.05			HN	8.02			HN	6.69
20	Ile	N	118.36	55	Gln	N	116.27	88	Glu	N	117.64	123	Gly	N	108.29
		HN	8.46			HN	7.96			HN	7.64			HN	8.86
21	Asn	N	114.26	56	Leu	N	113.32	89	Leu	N	121.59	124	Phe	N	123.91
		HN	7.36			HN	7.22			HN	8.58			HN	9.03
22	Thr	N	116.46	57	Glu	N	116.57	90	Ile	N	115.17	125	Tyr	N	109.61
		HN	7.47			HN	7.45			HN	7.44			HN	7.24
27	Lys	N	117.59	58	Thr	N	105.44	91	Asn	N	116.09	126	Ser	N	113.86
		HN	8.19			HN	7.04			HN	8.36			HN	8.11
28	Glu	N	115.24	59	Glu	N	114.74	92	Asn	N	117.27	127	Leu	N	122.99
		HN	8.52			HN	7.20			HN	9.17			HN	7.61
29	Ile	N	113.24	61	Asp	N	117.42	93	Leu	N	114.86	128	Phe	N	118.16
		HN	7.07			HN	8.60			HN	6.84			HN	7.47
30	Phe	N	120.92	62	Leu	N	122.90	94	Gly	N	103.62	129	Leu	N	117.85
		HN	8.14			HN	8.32			HN	7.13			HN	8.08
31	Leu	N	123.03	63	Phe	N	119.99	95	Thr	N	111.65	130	Val	N	103.77
		HN	5.97			HN	7.61			HN	7.68			HN	6.89
32	Arg	N	117.80	64	Ile	N	118.58	96	Ile	N	120.85	131	Ala	N	124.64
		HN	6.50			HN	8.19			HN	8.30			HN	7.74
33	Glu	N	116.56	65	Arg	N	128.66	102	Lys	N	121.32	132	Asp	N	117.28
		HN	7.61			HN	10.06			HN	8.09			HN	8.26
34	Leu	N	118.56	66	Ile	N	130.25	103	Ala	N	120.53	133	Arg	N	114.98
		HN	8.03			HN	9.08			HN	7.90			HN	7.56
35	Ile	N	122.69	67	Thr	N	122.00	104	Phe	N	120.07	134	Val	N	121.58
		HN	8.44			HN	9.26			HN	8.33			HN	8.74

No.	Res.	Nuc.	CS	No.	Res	Nuc.	CS	No.	Res.	Nuc.	CS	No.	Res.	Nuc.	CS
135	Gln	N	123.12	154	Gly	N	105.76	173	Leu	N	128.33	192	Glu	N	119.54
		HN	8.93			HN	8.40			HN	9.13			HN	7.67
136	Val	N	125.44	155	Ser	N	114.78	174	Arg	N	125.09	193	Val	N	120.85
		HN	10.46			HN	7.98			HN	9.67			HN	8.03
137	Ile	N	130.25	156	Phe	N	119.05	175	Leu	N	125.49	194	Ile	N	119.73
		HN	9.61			HN	8.77			HN	8.83			HN	8.37
138	Ser	N	119.40	157	Thr	N	109.94	176	Phe	N	123.66	195	Lys	N	119.23
		HN	9.26			HN	8.54			HN	8.15			HN	7.89
139	Lys	N	127.34	158	Val	N	120.60	177	Leu	N	121.77	196	Arg	N	115.68
		HN	9.37			HN	9.06			HN	7.75			HN	7.50
140	Ser	N	123.32	159	Thr	N	124.69	178	Lys	N	119.97	197	His	N	113.27
		HN	9.32			HN	9.33			HN	8.48			HN	7.71
141	Asn	N	126.51	160	Leu	N	130.99	179	Asp	N	118.88	198	Ser	N	115.77
		HN	10.40			HN	9.00			HN	8.66			HN	8.42
142	Asp	N	116.16	161	Asp	N	126.85	180	Asp	N	113.86	199	Glu	N	121.12
		HN	8.26			HN	8.47			HN	8.44			HN	8.01
143	Asp	N	121.06	162	Glu	N	128.07	181	Gln	N	119.75	200	Phe	N	114.69
		HN	8.03			HN	8.81			HN	8.02			HN	8.03
144	Glu	N	116.28	163	Val	N	114.85	182	Leu	N	115.00	201	Val	N	122.45
		HN	9.15			HN	8.64			HN	7.73			HN	7.22
145	Gln	N	119.63	164	Asn	N	121.27	183	Glu	N	120.86	202	Ala	N	129.31
		HN	8.41			HN	9.89			HN	8.70			HN	8.93
146	Tyr	N	125.26	165	Glu	N	120.36	184	Tyr	N	114.48	203	Tyr	N	116.48
		HN	8.69			HN	8.82			HN	6.72			HN	6.70
147	Ile	N	116.08	166	Arg	N	121.08	185	Leu		110.98	205	Ile	N	121.21
		HN	9.21			HN	8.63				7.36			HN	7.99
148	Trp	N	134.64	167	Ile	N	123.08	186	Glu	N	117.56	206	Gln	N	128.63
		HN	10.37			HN	8.53			HN	7.46			HN	9.56
149	Glu	N	128.75	168	Gly	N	114.11	187	Glu	N	127.30	207	Leu	N	128.96
		HN	9.06			HN	8.38			HN	9.06			HN	7.72
150	Ser	N	115.91	169	Arg	N	118.63	188	Lys	N	116.68	206	Gln	N	128.63
		HN	8.21			HN	7.33			HN	8.89			HN	9.56
151	Asn	N	125.07	170	Gly	N	116.14	189	Arg	N	119.94	207	Leu	N	128.96
		HN	8.57			HN	9.32			HN	6.91			HN	7.72
152	Ala	N	117.58	171	Thr	N	116.20	190	Ile	N	118.55				
		HN	8.59			HN	7.85			HN	8.13				
153	Gly	N	106.24	172	Ile	N	125.08	191	Lys	N	116.45				
		HN	8.11			HN	9.99			HN	8.47				

Table 3.3 Chemical shifts derived from the $^{1}H^{15}N$ HSQC experiment. The (No) indicates the residue number with its three letter abbreviation amino acid (Res) and the amide H and HN chemical shift for each residue. Totally 191 amides were assigned out of 207 residues including 5 prolines, which results in 94% of the N_i/NH_i atoms assigned. Res. stands for residue and CS the abbreviation for chemical shifts.

No	Res	Cα		No	Res	Cα		No	Res	Cα		No	Res	Cα
-1	His	56.30		12	Ile	63.76		28	Glu	57.99		40	Asp	57.28
0	Gly	45.01		13	Thr	66.38		29	Ile	62.40		41	Ala	54.97
1	Met	55.09		14	Gln	58.52		30	Phe	59.23		42	Leu	57.53
2	Ala	52.32		15	Leu	58.02		31	Leu	56.57		43	Asp	57.12
3	Ser	57.78		16	Met	60.47		32	Arg	58.37		44	Lys	59.98
4	Glu	55.42		17	Ser	61.27		33	Glu	57.60		45	Ile	59.65
5	Thr	61.40		18	Leu	57.73		34	Leu	57.32		46	Arg	59.82
6	Phe	55.67		19	Ile	64.00		35	Ile	65.16		47	Tyr	60.89
7	Glu	55.18		20	Ile	64.24		36	Ser	61.79		48	Lys	59.03
8	Phe	59.35		21	Asn	53.74		37	Asn	55.66		49	Ser	60.02
10	Ala	55.88		26	Asn	51.75		38	Ala	54.56		50	Leu	57.13
11	Glu	60.05		27	Lys	59.30		39	Ser	61.48		51	Ser	58.24

No	Res	Cα	No	Res	Cα	No	Res	Cα	No	Res	Cα
52	Asp	51.42	92	Asn	55.05	135	Gln	53.68	173	Leu	53.52
53	Pro	64.72	93	Leu	54.40	136	Val	61.26	174	Arg	55.01
54	Lys	58.28	94	Gly	46.72	137	Ile	59.65	175	Leu	54.34
55	Gln	56.86	95	Thr	63.45	138	Ser	56.85	176	Phe	57.01
56	Leu	54.73	96	Ile	61.39	139	Lys	53.53	177	Leu	55.29
57	Glu	59.01	102	Lys	59.40	140	Ser	54.81	178	Lys	56.08
58	Thr	62.09	103	Ala	54.49	141	Asn	55.03	179	Asp	57.04
59	Glu	55.02	104	Phe	58.90	142	Asp	54.29	180	Asp	53.05
60	Pro	64.48	105	Met	59.39	143	Asp	53.09	181	Gln	53.70
61	Asp	53.50	106	Glu	58.89	144	Glu	54.12	182	Leu	56.09
62	Leu	53.49	107	Ala	54.72	145	Gln	56.19	183	Glu	57.91
63	Phe	56.13	108	Leu	57.33	146	Tyr	58.47	184	Tyr	59.97
64	Ile	59.97	109	Ser	60.98	147	Ile	59.96	185	Leu	53.68
65	Arg	54.32	110	Ala	51.40	148	Trp	55.65	186	Glu	55.00
66	Ile	60.13	111	Gly	45.05	149	Glu	54.99	187	Glu	60.43
67	Thr	59.10	112	Ala	51.95	150	Ser	57.57	188	Lys	59.54
68	Pro	62.01	113	Asp	53.13	151	Asn	52.17	189	Arg	56.86
69	Lys	53.02	114	Val	64.55	152	Ala	53.28	190	Ile	65.32
70	Pro	65.63	115	Ser	60.67	153	Gly	44.90	191	Lys	60.21
71	Glu	58.84	116	Met	56.12	154	Gly	46.15	192	Glu	58.83
72	Gln	55.11	117	Ile	64.94	155	Ser	56.65	193	Val	66.39
73	Lys	58.06	118	Gly	46.37	156	Phe	54.93	194	Ile	64.70
74	Val	58.53	119	Gln	56.95	157	Thr	58.99	195	Lys	58.28
75	Leu	52.89	120	Phe	57.71	158	Val	61.41	196	Arg	58.05
76	Glu	54.00	121	Gly	46.05	159	Thr	61.29	197	His	57.10
77	Ile	60.63	122	Val	59.38	160	Leu	56.60	198	Ser	57.91
78	Arg	52.56	123	Gly	47.26	161	Asp	54.20	199	Glu	58.28
79	Asp	52.36	124	Phe	60.98	162	Glu	54.99	200	Phe	56.62
80	Ser	54.50	125	Tyr	60.78	163	Val	62.32	201	Val	62.62
81	Gly	44.22	126	Ser	61.62	164	Asn	53.92	202	Ala	52.66
82	Ile	62.56	127	Leu	57.81	165	Glu	56.39	203	Tyr	55.43
83	Gly	43.46	128	Phe	60.42	166	Arg	54.62	204	Pro	62.84
84	Met	54.25	129	Leu	57.18	167	Ile	60.17	205	Ile	59.99
85	Thr	60.26	130	Val	60.01	168	Gly	47.49	206	Gln	55.04
86	Lys	60.87	131	Ala	50.62	169	Arg	56.67	207	Leu	56.59
87	Ala	54.47	132	Asp	53.88	170	Gly	43.29			
90	Ile	65.11	133	Arg	54.69	171	Thr	61.46			
91	Asn	55.55	134	Val	58.29	172	Ile	61.08			

Table 3.4 The ^{13}Cα nucleus chemical shifts from HNCA and HN(CO)CA experiments. The (No) indicates the residue number and (Res) shows the three-letter abbreviation amino acid code while (Cα) indicates the ^{13}Cα nuclei chemical shifts. Totally 195 resonances were assigned out of 207 residues that resulted in 94.2% of the ^{13}Cα atoms assigned.

No	Res	Cβ	No	Res	Cβ	No	Res	Cβ	No	Res	Cβ
-1	His	30.16	47	Tyr	37.13	91	Asn	39.15	145	Gln	29.48
0	Gly	30.97	48	Lys	32.33	92	Asn	30.59	146	Tyr	45.36
1	Met	32.27	49	Ser	63.07	93	Leu	38.50	147	Ile	41.40
2	Ala	18.43	50	Leu	40.26	102	Lys	31.59	148	Trp	34.31
3	Ser	64.46	51	Ser	63.60	103	Ala	17.58	149	Glu	32.74
4	Glu	33.55	52	Asp	40.84	104	Phe	37.65	150	Ser	67.32
5	Thr	69.57	53	Pro	31.22	105	Met	31.65	151	Asn	38.25
6	Phe	42.44	54	Lys	30.57	106	Glu	28.37	152	Ala	16.29
7	Glu	30.46	55	Gln	26.86	107	Ala	16.72	155	Ser	66.52
8	Phe	40.43	56	Leu	41.85	108	Leu	40.48	156	Phe	40.71
11	Glu	28.97	57	Glu	28.97	109	Ser	62.58	157	Thr	71.92
12	Ile	37.53	58	Thr	68.45	110	Ala	18.27	158	Val	34.56
13	Thr	67.48	59	Glu	28.92	112	Ala	18.66	159	Thr	71.71
14	Gln	27.39	60	Pro	31.79	113	Asp	43.66	160	Leu	41.03
15	Leu	39.97	61	Asp	41.84	114	Val	31.77	161	Asp	42.11
16	Met	32.27	62	Leu	39.84	115	Ser	62.46	162	Glu	30.20
17	Ser	62.44	63	Phe	41.37	116	Met	32.09	163	Val	34.33
18	Leu	41.16	64	Ile	39.41	117	Ile	36.54	164	Asn	38.88
19	Ile	36.63	65	Arg	33.82	119	Gln	27.17	165	Glu	28.86
20	Ile	37.45	66	Ile	38.53	120	Phe	39.61	166	Arg	29.98
21	Asn	40.17	67	Thr	70.77	122	Val	30.23	167	Ile	38.99
26	Asn	37.38	68	Pro	32.81	124	Phe	39.80	169	Arg	30.44
27	Lys	31.63	69	Lys	31.17	125	Tyr	36.98	171	Thr	72.10
28	Glu	28.09	70	Pro	31.31	126	Ser	62.48	172	Ile	41.08
29	Ile	37.43	71	Glu	27.71	127	Leu	39.63	173	Leu	42.01
30	Phe	37.03	72	Gln	29.78	128	Phe	36.85	174	Arg	30.66
31	Leu	39.89	73	Lys	28.83	129	Leu	42.47	175	Leu	41.81
32	Arg	28.58	74	Val	36.20	130	Val	32.58	176	Phe	36.10
33	Glu	27.81	75	Leu	45.76	131	Ala	21.53	177	Leu	41.92
34	Leu	39.26	76	Glu	31.19	132	Asp	41.82	178	Lys	34.00
35	Ile	35.75	77	Ile	39.49	133	Arg	32.61	179	Asp	40.27
36	Ser	62.23	78	Arg	32.56	134	Val	34.44	180	Asp	39.14
37	Asn	37.61	79	Asp	46.41	135	Gln	30.58	181	Gln	27.23
38	Ala	17.68	80	Ser	61.74	136	Val	32.03	182	Leu	38.17
39	Ser	62.79	82	Ile	39.46	137	Ile	39.03	183	Glu	27.84
40	Asp	40.15	84	Met	36.26	138	Ser	66.67	184	Tyr	36.45
41	Ala	18.07	85	Thr	69.86	139	Lys	36.15	185	Leu	41.37
42	Leu	40.04	86	Lys	30.59	140	Ser	63.15	186	Glu	29.20
43	Asp	39.19	87	Ala	17.57	141	Asn	36.71	187	Glu	28.85
44	Lys	32.40	88	Glu	29.23	142	Asp	41.56	188	Lys	31.39
45	Ile	37.61	89	Leu	41.48	143	Asp	44.71	189	Arg	29.05
46	Arg	29.22	90	Ile	38.51	144	Glu	30.58	190	Ile	37.26

No	Res	Cβ	No	Res	Cβ	No	Res	Cβ	No	Res	Cβ
191	Lys	31.73	195	Lys	31.18	199	Glu	28.89	203	Tyr	39.71
192	Glu	28.92	196	Arg	30.08	200	Phe	37.54	205	Ile	37.45
193	Val	30.88	197	His	33.20	201	Val	31.68	206	Gln	28.66
194	Ile	37.02	198	Ser	63.43	202	Ala	18.23	207	Leu	43.74

Table 3.5 The ^{13}Cβ nucleus chemical shifts from HN(CA)CB and HN(COCA)CB experiments. Totally 182 resonances were assigned out of 207 residues including 11 glycines which resulted in 93.24% of the ^{13}Cβ atoms assigned.

No	Res	Co	No	Res	Co	No	Res	Co	No	Res	Co
-1	His	176.60	38	Ala	179.15	71	Glu	178.11	109	Ser	175.19
0	Gly	174.79	39	Ser	177.25	72	Gln	175.03	110	Ala	178.12
1	Met	176.77	40	Asp	178.89	73	Lys	174.31	111	Gly	175.47
2	Ala	178.01	41	Ala	182.52	74	Val	173.90	112	Ala	175.84
3	Ser	174.36	42	Leu	178.74	75	Leu	175.25	113	Asp	177.91
4	Glu	174.97	43	Asp	179.88	76	Glu	176.78	114	Val	176.18
5	Thr	173.22	44	Lys	181.11	77	Ile	175.01	115	Ser	176.50
6	Phe	174.39	45	Ile	176.90	78	Arg	174.35	116	Met	177.14
7	Glu	178.68	46	His	179.83	79	Asp	177.35	117	Ile	176.09
8	Phe	177.23	47	Tyr	180.13	80	Ser	174.61	118	Gly	178.38
11	Glu	179.19	48	Lys	179.58	81	Gly	172.95	119	Gln	177.34
12	Ile	178.47	49	Ser	175.57	82	Ile	174.78	120	Phe	176.64
13	Thr	177.88	50	Leu	179.50	83	Gly	172.81	121	Gly	175.56
14	Gln	179.08	51	Ser	175.00	84	Met	176.17	122	Val	176.27
15	Leu	178.91	52	Asp	174.05	85	Thr	174.46	123	Gly	176.08
16	Met	177.80	53	Pro	179.96	86	Lys	178.43	124	Phe	175.39
17	Ser	177.14	54	Lys	180.13	87	Ala	181.22	125	Tyr	177.23
18	Leu	181.01	55	Gln	177.67	88	Glu	179.29	126	Ser	176.42
19	Ile	178.32	56	Leu	179.75	89	Leu	178.71	127	Leu	178.00
20	Ile	177.74	57	Glu	177.62	90	Ile	179.40	128	Phe	176.13
21	Asn	176.19	58	Thr	176.35	91	Asn	177.57	129	Leu	179.49
26	Asn	175.60	59	Glu	173.04	92	Asn	177.40	130	Val	173.42
27	Lys	177.29	60	Pro	176.80	93	Leu	178.75	131	Ala	175.81
28	Glu	176.47	61	Asp	176.10	94	Gly	174.95	132	Asp	176.16
29	Ile	177.38	62	Leu	175.21	95	Thr	175.41	133	Arg	173.49
30	Phe	176.59	63	Phe	172.25	101	Thr	176.72	134	Val	174.10
31	Leu	178.80	64	Ile	175.04	102	Lys	179.17	135	Gln	175.13
32	Arg	179.78	65	Arg	175.71	103	Ala	181.05	136	Val	174.91
33	Glu	180.04	66	Ile	175.17	104	Phe	176.99	137	Ile	176.32
34	Leu	181.61	67	Thr	173.32	105	Met	180.04	138	Ser	172.29
35	Ile	178.29	68	Pro	176.87	106	Glu	179.95	139	Lys	174.41
36	Ser	177.58	69	Lys	176.26	107	Ala	181.69	140	Ser	177.33
37	Asn	178.56	70	Pro	179.89	108	Leu	181.80	141	Asn	177.49

No	Res	Co	No	Res	Co	No	Res	Co	No	Res	Co
142	Asp	175.30	159	Thr	174.06	176	Phe	175.70	193	Val	179.46
143	Asp	174.64	160	Leu	177.17	177	Leu	178.28	194	Ile	178.83
144	Glu	174.67	161	Asp	177.74	178	Lys	178.89	195	Lys	178.47
145	Gln	176.28	162	Glu	176.85	179	Asp	177.64	196	Arg	178.87
146	Tyr	174.43	163	Val	176.77	180	Asp	177.85	197	His	177.78
147	Ile	176.56	164	Asn	176.65	181	Gln	176.23	198	Ser	175.78
148	Trp	176.12	165	Glu	176.24	182	Leu	180.42	199	Glu	177.43
149	Glu	174.84	166	Arg	178.30	183	Glu	177.25	200	Phe	176.26
150	Ser	173.99	167	Ile	176.88	184	Tyr	172.40	201	Val	176.80
151	Asn	175.59	168	Gly	174.99	185	Leu	177.51	202	Ala	176.71
152	Ala	177.20	169	Arg	174.75	186	Glu	177.59	203	Tyr	172.50
153	Gly	175.86	170	Gly	172.48	187	Glu	178.34	204	Pro	175.70
154	Gly	175.07	171	Thr	173.75	188	Lys	179.37	205	Ile	177.09
155	Ser	172.84	172	Ile	175.24	189	Arg	178.61	206	Gln	174.21
156	Phe	173.44	173	Leu	175.64	190	Ile	178.86	207	Leu	182.36
157	Thr	175.38	174	Arg	173.65	191	Lys	179.79			
158	Val	176.79	175	Leu	175.50	192	Glu	179.56			

Table 3.6 The ^{13}CO nucleus chemical shifts from HNCO and HN(CA)CO experiments. In total 195 resonances were assigned out of 207 residues which resulted in 94.2% of the atoms assigned.

No.	Res.	Hα	No.	Res.	Hα	No.	Res.	Hα	No.	Res.	Hα
0	Gly	3.97	36	Ser	4.26	59	Glu	4.61	91	Asn	4.58
1	Met	4.55	37	Asn	4.38	61	Asp	4.94	93	Leu	4.21
2	Ala	4.45	38	Ala	4.14	62	Leu	4.26	96	Ile	4.49
3	Ser	4.96	40	Asp	4.41	63	Phe	4.99	103	Ala	4.19
4	Glu	4.49	41	Ala	4.16	64	Ile	4.96	106	Glu	3.94
6	Phe	4.36	42	Leu	3.87	65	Arg	5.60	107	Ala	4.16
7	Glu	4.65	44	Lys	4.16	66	Ile	5.09	109	Ser	4.25
14	Gln	3.99	45	Ile	4.53	67	Thr	4.90	110	Ala	4.55
17	Ser	4.10	46	Arg	3.91	69	Lys	5.02	112	Ala	4.39
18	Leu	4.13	47	Tyr	4.35	71	Glu	4.22	113	Asp	4.82
19	Ile	3.63	48	Lys	4.07	72	Gln	4.51	116	Met	4.58
20	Ile	3.97	49	Ser	4.35	73	Lys	3.55	119	Gln	4.10
22	Thr	4.35	50	Leu	4.16	74	Val	5.12	120	Phe	4.56
28	Glu	4.11	51	Ser	4.64	75	Leu	4.71	122	Val	4.99
29	Ile	3.58	52	Asp	5.10	76	Glu	5.76	126	Ser	4.58
31	Leu	3.10	54	Lys	4.11	77	Ile	4.73	128	Phe	5.01
32	Arg	3.64	55	Gln	3.79	78	Arg	5.85	129	Leu	4.32
33	Glu	4.02	56	Leu	4.26	79	Asp	5.63	130	Val	4.58
34	Leu	4.13	57	Glu	3.89	84	Met	4.93	131	Ala	5.08
35	Ile	3.67	58	Thr	3.95	88	Glu	3.84	132	Asp	4.95

No.	Res.	Hα	No.	Res.	Hα	No.	Res.	Hα	No.	Res.	Hα
133	Arg	5.10	150	Ser	4.84	172	Ile	4.55	190	Ile	3.50
134	Val	5.76	151	Asn	5.37	173	Leu	4.94	191	Lys	3.83
135	Gln	5.69	152	Ala	3.96	174	Arg	4.52	192	Glu	4.06
136	Val	4.93	155	Ser	5.43	175	Leu	4.48	194	Ile	3.64
137	Ile	5.22	156	Phe	5.24	176	Phe	4.62	195	Lys	3.97
138	Ser	5.58	157	Thr	5.65	177	Leu	4.39	196	Arg	4.02
139	Lys	4.86	158	Val	5.58	178	Lys	4.31	197	His	4.93
140	Ser	4.99	159	Thr	5.08	179	Asp	4.35	199	Glu	3.87
141	Asn	4.43	161	Asp	4.46	180	Asp	4.88	200	Phe	4.67
143	Asp	5.07	162	Glu	4.74	181	Gln	5.00	201	Val	4.02
144	Glu	4.49	163	Val	4.51	182	Leu	4.08	202	Ala	4.14
145	Gln	5.17	164	Asn	4.85	184	Tyr	4.23	205	Ile	4.71
146	Tyr	5.07	165	Glu	4.16	185	Leu	4.41	206	Gln	4.46
147	Ile	5.19	166	Arg	4.45	186	Glu	4.36	207	Leu	4.74
148	Trp	5.96	167	Ile	4.21	188	Lys	3.97			
149	Glu	5.70	171	Thr	5.38	189	Arg	4.26			

Table 3.7 The ^{1}Hα nucleus chemical shifts from the $^{1}H^{15}N$ HSQC NOESY, 3D TOWNY-HSQC and HN(COCA)HA experiments. The (No) indicates the residue number and (Res) shows the three letter abbreviation amino acid code. In total 141 resonances were assigned out of 207 residues. Several crosspeaks were missing due to chemical exchange or were too ambiguous to be assigned.

3.9 Secondary structure prediction using nuclei chemical shifts

The deviation of ^{13}Cα, ^{13}Cβ and ^{13}CO chemical shifts from random coil values for the Hsp90 N-terminal domain were used to predict the secondary structure using the chemical shift index (CSI) program (Wishart and Sykes, 1994). The mean random coil values were corrected for deuterium isotope shift effect using methods of Gardner (Gardner *et al.*, 1997) and Venters (Venters *et al.*, 1996). Replacement of proton with deuterium causes an upfield change in the chemical shift of the nearby ^{15}N and ^{13}C nuclei mainly by the through-bond mechanism (Hansen, 1988). The deuterium effect has a wider range of shifts for the Cβ position than that observed for the Cα position due to differences in the sidechain

structures and presence of specifically protonated sites in certain amino acids. Therefore it was necessary to modify the random coil values in the CSI program to incorporate the above effect. In contrast, the deuteration effect on NH and ^{13}CO chemical shifts are insignificant (Gardner *et al.,* 1997). Figure 3.33 shows the consensus secondary structure prediction output of the CSI program (version 2.0) using the 13Cα, $^{13}C\beta$, ^{13}CO and $^{1}H\alpha$ chemical shifts of the Hsp90 N-terminal domain. In this figure a consensus output index of 1 indicates a β-sheet structure while an index number of –1 identifies the regions that have an α-helical structure. An index number of 0 indicates a random coil region in the structure. Detail and separate prediction of the secondary structure from $^{13}C\alpha$, $^{13}C\beta$, ^{13}CO and $^{1}H\alpha$ nuclei in comparison to the X-ray crystal structure are shown in Table 3.8.

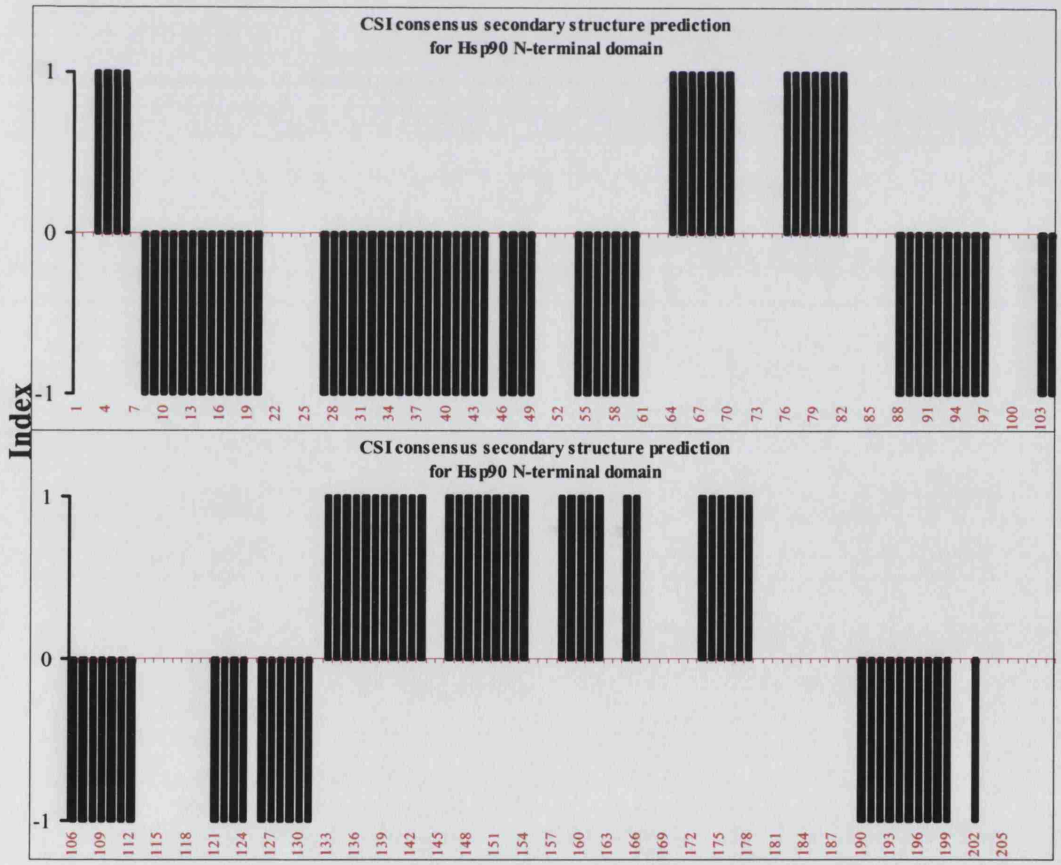

Figure 3.33. The graphic CSI output for consensus secondary structure prediction for the Hsp90 N-terminal domain. On the vertical line, index numbers 1 indicate β-sheets whereas –1 indicate an α-helical structure, the predicted random coil regions have an index number of 0.

Table 3.8 shows that the secondary structures predicted by CSI have a similar structure to that of the X-ray crystal structure. The minor difference observed between the predicted solution and the X-ray crystal secondary structure are mostly in the lengths of some of the secondary structures, or are within the error range of the program. The differences are highlighted in Table 3.8. There is also a predicted gap in the second helix where residue Ile-45 close to the end of the structure has been predicted as coil (highlighted in bold red in Table 3.8). This could be due to flexibility in this part of the second helix that needs further investigation using dynamic studies that will follow in the next chapter.

apo						apo	apo	apo						apo	apo
Res	AA	Hα	Cα	CO	Cβ	Cons	Cry	Res	AA	Hα	Cα	CO	Cβ	Cons	Cry
1	M	C	C	C	C	C	C	39	S	H	H	H	C	H	H
2	A	B	C	C	C	C	C	40	D	H	H	H	C	H	H
3	S	B	C	C	B	B	C	41	A	H	H	H	C	H	H
4	E	B	C	B	B	B	B	42	L	H	H	H	C	H	H
5	T	B	B	B	B	B	B	43	D	H	H	H	C	H	H
6	F	C	B	B	B	B	B	44	K	H	H	H	C	H	H
7	E	C	B	H	B	C	B	45	I	C	C	H	C	C	H
8	F	H	H	H	B	H	C	46	R	H	H	H	C	H	H
9	Q	H	H	H	C	H	C	47	Y	H	H	H	C	H	H
10	A	H	H	H	C	H	H	48	K	H	H	H	B	H	H
11	E	H	H	H	C	H	H	49	S	H	H	H	B	H	H
12	I	H	H	H	C	H	H	50	L	C	H	H	B	C	H
13	T	H	H	H	C	H	H	51	S	C	C	H	B	C	T
14	Q	H	H	H	C	H	H	52	D	C	C	C	B	C	T
15	L	H	H	H	C	H	H	53	P	C	C	C	C	C	H
16	M	H	H	H	C	H	H	54	K	H	C	H	C	H	H
17	S	H	H	H	C	H	H	55	Q	H	C	H	C	H	H
18	L	H	H	H	C	H	H	56	L	H	C	H	C	H	H
19	I	C	H	H	C	H	H	57	E	H	C	H	C	H	H
20	I	C	H	H	C	H	H	56	L	H	C	H	C	H	H
21	N	C	C	H	C	C	T	57	E	H	C	H	C	H	H
22	T	C	C	C	C	C	C	58	T	H	C	H	C	H	T
23	V	C	C	C	C	C	C	59	E	C	C	B	C	C	C
24	Y	C	C	C	C	C	C	60	P	C	C	B	C	C	C
25	S	C	C	C	C	C	S	61	D	C	C	B	C	C	C
26	N	C	C	C	C	C	C	62	L	B	B	B	C	B	C
27	K	H	H	C	C	H	T	63	F	B	B	B	B	B	C
28	E	H	H	C	C	H	T	64	I	B	B	B	B	B	B
29	I	H	H	C	C	H	H	65	R	B	B	B	B	B	B
30	F	H	H	H	C	H	H	66	I	B	B	B	B	B	B
31	L	H	H	H	C	H	H	67	T	B	B	B	B	B	B
32	R	H	H	H	C	H	H	68	P	B	B	C	C	B	B
33	E	H	H	H	C	H	H	69	K	C	C	C	C	C	B
34	L	H	H	H	C	H	H	70	P	C	C	C	C	C	H
35	I	H	H	H	C	H	H	71	E	C	C	C	C	C	H
36	S	H	H	H	C	H	H	72	Q	C	C	B	C	C	H
37	N	H	H	H	C	H	H	73	K	C	C	B	C	C	T
38	A	H	H	H	C	H	H	74	V	B	B	B	B	B	B

apo						apo	apo
Res	AA	Hα	Cα	CO	Cβ	Cons	Cry
75	L	B	B	B	B	B	B
76	E	B	B	C	B	B	B
77	I	B	B	C	B	B	B
78	R	B	B	C	B	B	B
79	D	B	B	C	B	B	B
80	S	B	B	C	C	B	C
81	G	C	C	B	C	C	S
82	I	C	C	B	C	C	C
83	G	C	B	B	C	C	C
84	M	C	B	B	C	C	C
85	T	C	B	B	C	C	C
86	K	H	H	H	C	H	H
87	A	H	H	H	C	H	H
88	E	H	H	H	C	H	H
89	L	H	H	H	B	H	H
90	I	H	H	H	B	H	H
91	N	H	H	H	B	H	H
92	N	H	H	H	C	H	H
93	L	H	H	H	C	H	T
94	G	H	H	H	C	H	T
95	T	H	H	C	C	H	T
96	I	C	C	C	C	C	S
97	A	C	C	C	C	C	C
98	K	C	C	C	C	C	C
99	S	C	C	C	C	C	T
100	G	C	C	C	C	C	T
101	T	H	H	H	C	H	H
102	K	H	H	H	C	H	H
103	A	H	H	H	C	H	H
104	F	H	H	H	C	H	H
105	M	H	H	H	C	H	H
106	E	H	H	H	C	H	H
107	A	H	H	H	C	H	H
108	L	H	H	H	C	H	H
109	S	H	H	H	C	H	H
110	A	C	C	H	C	C	H
111	G	C	C	H	C	C	T
112	A	C	C	C	C	C	C
113	D	C	C	C	C	C	C
114	V	C	H	C	C	C	H
115	S	C	H	C	C	C	H
116	M	C	H	C	C	C	H
117	I	C	H	C	C	C	T
118	G	C	H	H	C	H	G
119	Q	C	H	H	C	H	G
120	F	C	H	H	C	H	H
121	G	C	H	H	C	H	T
122	V	C	C	C	C	C	T
123	G	H	H	H	C	H	H
124	F	H	H	H	C	H	H
125	Y	H	H	H	C	H	H
126	S	H	H	H	C	H	H
127	L	H	H	H	C	H	H
128	F	B	H	H	C	H	H
129	L	B	H	H	B	C	H
130	V	B	B	B	B	B	T
131	A	B	B	B	B	B	B
132	D	B	B	B	B	B	S
133	R	B	B	B	B	B	B
134	V	B	B	B	B	B	B
135	Q	B	B	B	B	B	B
136	V	B	B	B	B	B	B

apo						apo	apo
Res	AA	Hα	Cα	CO	Cβ	Cons	Cry
137	I	B	B	B	B	B	B
138	S	B	B	B	B	B	B
139	K	B	B	B	B	B	B
140	S	B	B	C	B	B	C
141	N	C	C	C	C	C	T
142	D	C	C	B	B	C	T
143	D	B	C	B	B	B	S
144	E	B	C	B	B	B	C
145	Q	B	C	B	B	B	C
146	Y	B	C	C	B	B	B
147	I	B	B	C	B	B	B
148	W	B	B	C	B	B	B
149	E	B	B	C	B	B	B
150	S	B	B	C	B	B	B
151	N	B	B	C	C	B	C
152	A	C	C	C	C	C	S
153	G	C	C	C	C	C	S
154	G	C	C	C	C	C	S
155	S	B	B	C	B	B	B
156	F	B	B	C	B	B	B
157	T	B	B	C	B	B	B
158	V	B	B	C	B	B	B
159	T	B	B	C	B	B	B
160	L	C	C	C	B	C	B
161	D	C	C	C	B	C	C
162	E	B	C	C	B	B	C
163	V	B	C	C	B	B	S
164	N	B	C	C	C	C	S
165	E	C	C	C	C	C	C
166	R	C	C	C	C	C	C
167	I	C	C	C	C	C	C
168	G	C	C	C	C	C	S
169	R	C	C	B	B	C	S
170	G	B	B	B	B	B	B
171	T	B	B	B	B	B	B
172	I	B	B	B	B	B	B
173	L	B	B	B	B	B	B
174	R	B	C	B	B	B	B
175	L	B	C	B	B	B	B
176	F	B	C	C	C	C	B
177	L	C	C	C	C	C	B
178	K	C	C	C	C	C	C
179	D	C	C	C	C	C	T
180	D	C	C	C	C	C	T
181	Q	C	C	C	C	C	T
182	L	C	C	C	C	C	H
183	E	C	C	C	C	C	H
184	Y	C	C	C	C	C	H
185	L	C	C	C	C	C	S
186	E	C	C	H	C	C	S
187	E	H	H	H	C	H	H
188	K	H	H	H	C	H	H
189	R	H	H	H	C	H	H
190	I	H	H	H	C	H	H
191	K	H	H	H	C	H	H
192	E	H	H	H	C	H	H
193	V	H	H	H	C	H	H
194	I	H	H	H	C	H	H
195	K	H	H	H	B	H	H
196	R	H	H	H	B	H	H
197	H	C	H	H	B	C	H
198	S	C	H	H	B	C	C

apo						apo	apo	apo						apo	apo
Res	**AA**	**Hα**	**Cα**	**CO**	**Cβ**	**Cons**	**Cry**	**Res**	**AA**	**Hα**	**Cα**	**CO**	**Cβ**	**Cons**	**Cry**
199	E	C	H	H	C	H	S	**204**	**P**	C	C	C	C	C	C
200	**F**	C	C	C	C	C	C	**205**	**I**	C	C	C	C	C	B
201	**V**	C	C	C	C	C	C	**206**	**Q**	C	C	C	C	C	B
202	**A**	C	C	C	C	C	S	**207**	**L**	C	C	C	C	C	B
203	**Y**	C	C	C	C	C	S								

Table 3.8. The secondary structure prediction of the apo- Hsp90 N-terminal domain using CSI, version 2, compared to the secondary structure from X-ray crystal studies. The differences in the solution and the crystal structure are highlighted in red where the difference is in an α-helix, and in blue where the difference is in β-sheet predicted instead of a random coil. Key: Res: residue number, AA: amino acid , C; coil, H: helix ,B: β-sheet.

Combining dynamic studies with the backbone assignment will give us a better understanding of the protein structure in solution as well as a means to investigate and compare effects when nucleotides or drugs are added to the protein.

3.10 Chapter summary

The main findings of this section were as follows:

- The 3D experiments recorded using a triple-labelled sample proved to be advantageous over the double-labelled sample spectra in achieving backbone assignment despite being recorded at a lower magnetic field (500 MHz compared to 600 MHz for double labelled spectra).
- Implementing the optimal buffer condition made it possible to have a higher sample concentration hence improving the spectral resolution, sensitivity and stability of the protein sample.
- The sequential backbone assignment of the Hsp90 N-terminal domain is the necessary step to solve the solution structure of the Hsp90 N-terminal domain.
- The backbone assignments provided the basis for studying nucleotide, drug or other domains interacting with the protein in a fast and reliable way.

- The chemical shifts extracted from the nuclei were used for secondary structure prediction using CSI, and the majority of the X-ray crystal structure of the Hsp90 N-terminal domain was verified in the solution form.
- The sequential assignment has been published (Journal of Biomolecular NMR (2002) **23:** 327-328) and deposited in the BioMagResBank under accession code 5355.

CHAPTER 4

DYNAMIC STUDIES OF THE APO- HSP90 N-TERMINAL DOMAIN USING RELAXATION EXPERIMENTS

4.1 Chapter overview

Information on a protein's dynamics can be obtained using a series of methods known as relaxation experiments. The relaxation experiments make it possible to investigate dynamic processes, from picoseconds to nanoseconds, such as re-orientation of bond vectors, and local motions which contribute to the longitudinal (R_1) and transverse (R_2) relaxation, and to that of the heteronuclear cross-relaxation, of a NMR signal. The backbone dynamic characterisation and rotational diffusion of a protein are commonly investigated using amide ^{15}N-auto and ^{15}N-cross relaxation rates extracted from $^{15}NT_1$, $^{15}NT_2$ and heteronuclear $\{^1H\}^{15}N$ NOE experiments. From nuclear spin relaxation rates, molecular motions of a protein such as molecular tumbling, segmental motion and conformational exchange can be analysed and identified. The R_2 and R_1 values extracted from relaxation data are sensitive to different motional frequencies. Therefore, by measuring both R_2 and R_1 values, it is possible to obtain dynamic information over a large range of motional regimes.

In order to investigate the dynamics of the Hsp90 N-terminal domain, a series of relaxation experiments were conducted on a ^{15}N labelled sample. All the experiments were recorded as pseudo-3D HSQC experiments, which have been described earlier in chapter 2, section 2.10. The R_1, R_2 and heteronuclear NOE values were extracted from their respective spectra, plotted, analysed and finally the isotropic rotational correlation time for the Hsp90 N-terminal domain was calculated from the combined results. A series of NMR based diffusion experiments were also carried out in a range of temperatures between 10°C to 35°C on the same sample, in order to estimate its translational diffusion constant and to

calculate its molecular weight. Relaxation pulse sequences and their detailed mechanism require substantial background knowledge, which is beyond the scope of this thesis and has thus not been described in this chapter.

4.2 Analysis of the $^{15}NT_1$ and $^{15}NT_2$

The longitudinal (also known as spin-lattice) relaxation time constant, T_1, describes the time scale required for the recovery of the Boltzmann equilibrium magnetisation (Freeman, 1997). Following a 90° or 180° pulse the excited population of the nuclei relax back to equilibrium by exchanging energy with the surroundings (the lattice). The usual range of T_1 relaxation time constants is about 100 ms to 100 s, but in some cases can take as long as hours or days to reach equilibrium. The longitudinal relaxation rate constant, R_1 ($R_1=1/T_1$) is also often quoted for dynamic studies of a protein.

The T_1 pulse sequence yields signals that decay to zero with an increase in the relaxation delays (See Table 2.3, Chapter 2, for relaxation delays). The signal intensities extracted from crosspeaks of the 2D amide correlation spectrum, were fitted against the incremented relaxation using this equation (Kay *et al.*, 1989b).

$$A(t) = A_0 \exp\left(\frac{-t}{T_i}\right) \qquad \textbf{Equation 4.1}$$

In Equation 4.1 $A(t)$ stands for signal intensity at time (t), A_0 for its initial value, t is the relaxation time delay and T_i is the relaxation time constant where i=1 or 2. The result of the $^{15}NT_1$ relaxation experiment as R_1 (in s^{-1}), on a per residue basis, is shown in Figure 4.1. Only the assigned peaks are shown in Figure 4.1 and the missing residues are left blank. Interpretations of the results together with other relaxation experiments with regard to the structure of the Hsp90 N-terminal are

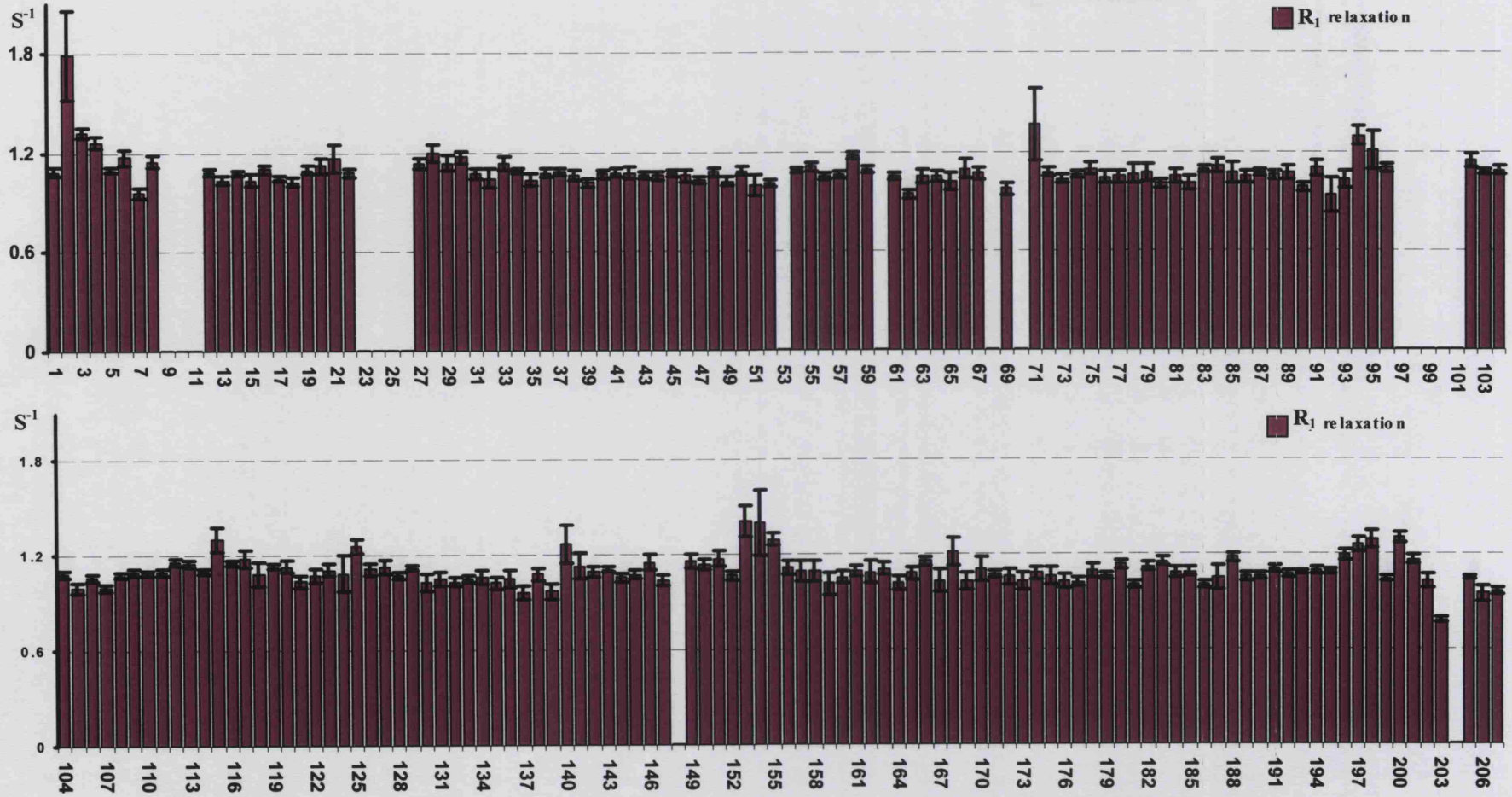

Figure 4.1 Backbone NH ^{15}N R_1 relaxation of $^{1}H^{15}N$-labelled Hsp90 N-terminal at 25°C recorded at 600 MHz. Error bars indicate the standard deviation for each residue.

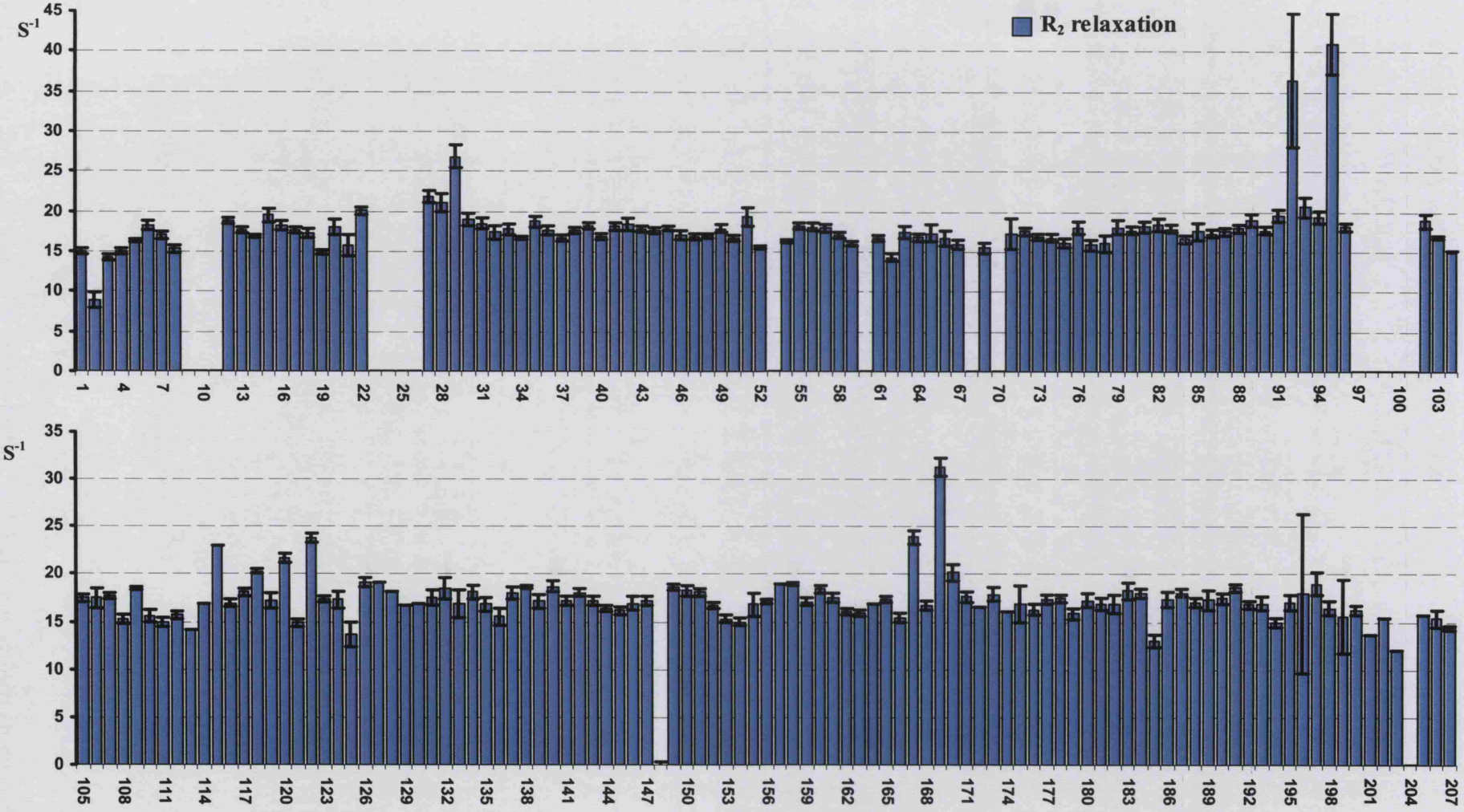

Figure 4.2 Backbone NH ^{15}N R_2 relaxation of $^{1}H^{15}N$-labelled Hsp90 N-terminal at 25°C recorded at 600 MHz. Error bars indicate the standard deviation for each residue. The unassigned residues are left as blanks. The T_2 values are in ms.

described in Section 4.3.

The transverse (also known as the spin-spin) relaxation time constant, T_2, takes into account the decay of coherence of the nuclear spins. The range of the T_2 value is wide and can be in the range of several seconds, for small molecules, to milliseconds for larger proteins. Like the T_1 experiment, the T_2 pulse sequences yields signals that decay to zero as the relaxation delay increases. The decay curve was fitted using Equation 4.1 with two parameters. The R_2 rate measurements must be interpreted with caution due to the effect of chemical exchange on the relaxation rates. As the ^{15}N magnetisation is kept in the transverse plane during the relaxation period, any nucleus exchanging between two chemical environments will relax faster and give rise to an additional contribution to the measured R_2 value. The $^{15}NT_2$ relaxation experiments are, in general, more sensitive than the $^{15}NT_1$ experiment. The results for the $^{15}NT_2$ relaxation as R_2 values (in s^{-1}) for each assigned residue is shown in Figure 4.2 with unassigned peaks left blank.

4.3 Analysis of the $\{^1H\}$-^{15}N heteronuclear NOE

The steady-state heteronuclear $\{^1H\}$-^{15}N NOE relaxation experiment describes the cross-relaxation rate between ^1H and ^{15}N nuclei in the protein backbone amide group. The enhancement of the ^{15}N magnetisation (reduced in practice due to the negative gyromagnetic ratio of ^{15}N) transpires during saturation of the proton bonded to nitrogen. The NOE values extracted from the experiment are the ^{15}N signal intensities recorded with saturation (I_{sat}) and without saturation (I_{unsat}) of the proton.

The sensitivity of the $\{^1H\}$-^{15}N heteronuclear NOE experiment is notably lower than that of the $^{15}NT_1$ and $^{15}NT_2$ experiments. This is because the initial

magnetisation is derived from the ^{15}N spins instead of the protons. Additionally, in contrast to the $^{15}NT_1$ and $^{15}NT_2$ experiments, it is necessary to wait for a longer period in order to ensure that cross-relaxation does not prevent the ^{15}N spin magnetisation from attaining its equilibrium value prior to the application of the initial ^{15}N spin pulse (Clore and Gronenborn, 1993). The consequence of this lower sensitivity is increased uncertainly in the measured values.

The heteronuclear NOE value is a useful indicator for the rate of a particular NH group's local motion. As a result, the heteronuclear NOE value with a (I_{sat}/I_{unsat}) ratio lower than the mean rate indicates that the NH group is undergoing a larger amplitude motion than average (Stone *et al.,* 1993). The (I_{sat}/I_{unsat}) ratios extracted from the $^{1}H^{15}N$ heteronuclear NOE relaxation experiment for the Hsp90 N-terminal are shown in Figure 4.3. The low NOE values (higher mobility) are mostly in the loop regions and also at the two ends of the protein.

In Figure 4.4, the $^{1}H^{15}N$ heteronuclear-NOE values are plotted on the X-ray crystal structure of the Hsp90 N-terminal domain and displayed as worm representation. The more mobile regions (below median value) are highlighted in darker red, the median value (0.76) and areas close to it are in white, whereas less mobile regions or values above the median are in blue. The median value was chosen because it was less affected by high and low data values. The red regions also include residues that have not been assigned due to apparent conformational exchange.

Generally where there is a secondary structure there tends to be less mobility than average, while in loop and turn areas it is the opposite. Regions with higher mobility than average include the two termini of the protein, and residues 1 to 5 and 197 to 207, due to inherent flexibility of these two ends. Residues 96, 102

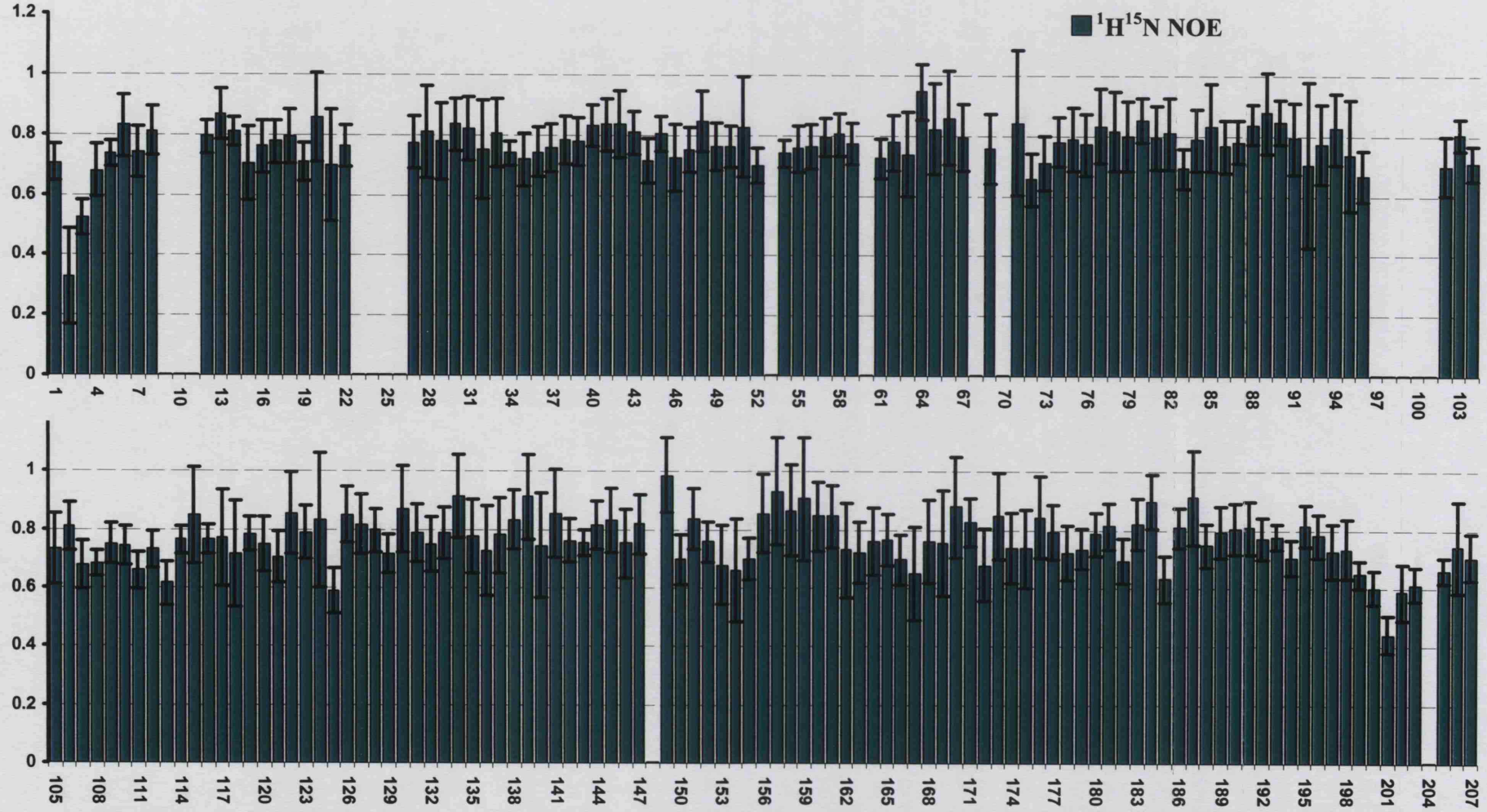

Figure 4.3 Backbone NH $^{1}H^{15}N$ heteronuclear NOE relaxation of $^{1}H^{15}N$-labelled Hsp90 N-terminal at 25°C recorded at 600 MHz. Error bars indicate the standard deviation for each residue. The unassigned residues are left as blanks.

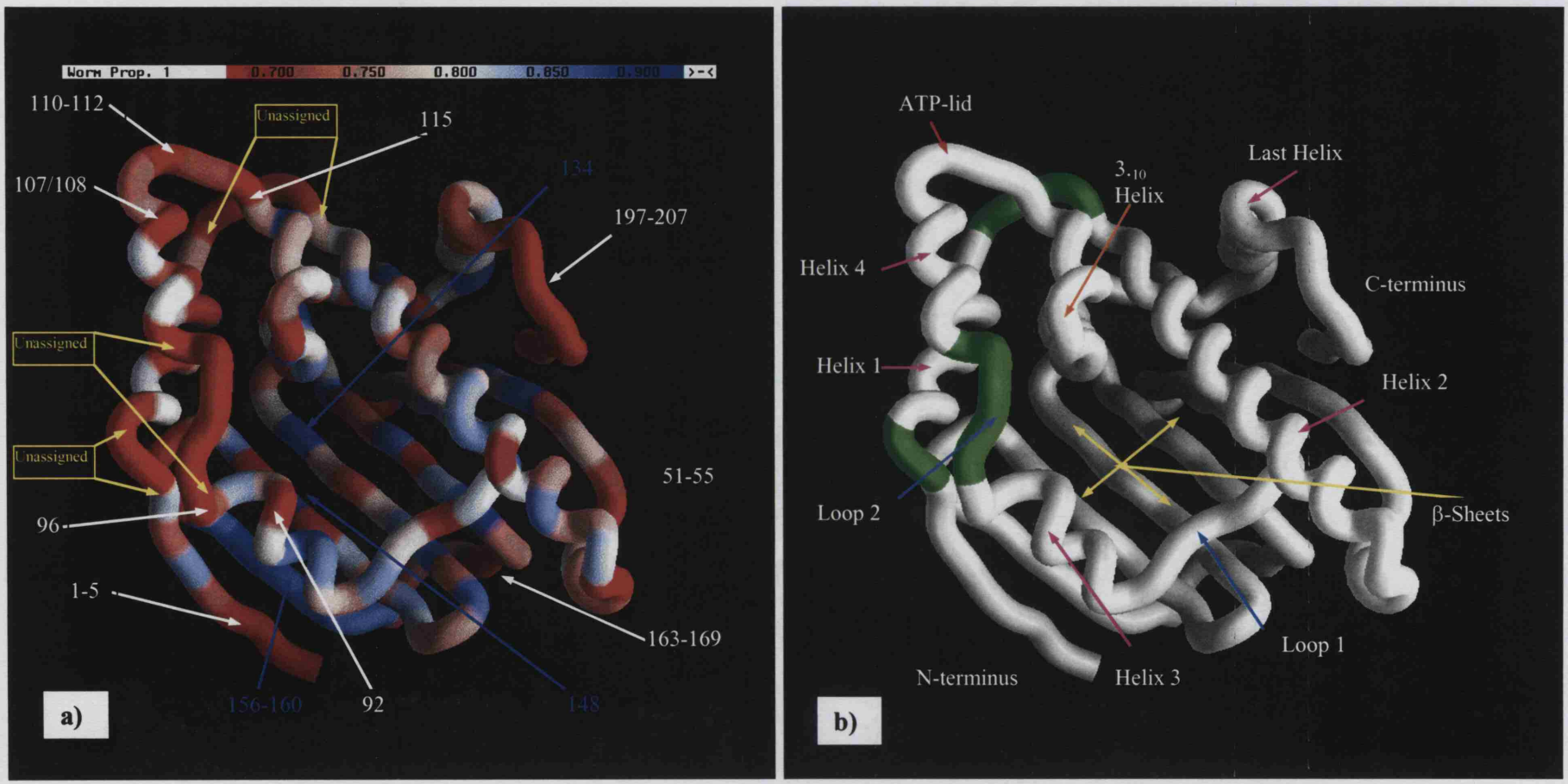

Figure 4.4. The $^{1}H^{15}N$ Heteronuclear NOE values mapped on the X –ray crystal structure of the Hsp90 N-terminal domain. (a) Heteronuclear NOE values in red show the more mobile region (below 0.8) and in blue the least mobile (above 0.8) from the median NOE value (0.76). The unassigned residues are also displayed in red but separated using yellow arrows. **(b)** The unassigned residues in the Hsp90 N-terminal domain structure in worm representation are in green with different secondary structures highlighted.

to 115 which make part of the loop region proposed by Prodromou *et al.,* (1997) as 'ATP-lid' (100-120) also have higher mobility. The residues 97 to 101 in the 'lid' have not been assigned which could be due to intermediate exchange with its environment. Finally, residues 163 to 169 which are in a loop and turn structure have a higher mobility than average. This region according to the solved crystal structure has a kinked shape which could be due to its packing in the crystal structure. Residues with less mobility than average are mostly located in the β-sheets making the bottom of the nucleotide binding pocket, from which some of the residues are highlighted in Figure 4.4.

4.4 Calculation of the isotropic correlation time (τ_c) of the Hsp90 N-terminal domain.

The rotational correlation time, τ_c, is the time taken for a typical molecule to rotate through 1 radian (Freeman, 1997). The τ_c of a protein in solution, is affected by the viscosity of the solution, η_w, and the temperature of the sample, T, as described here by the Stokes-Einstein equation (Equation 4.2), where r is the hydrodynamic radius of the molecule and k the Boltzmann constant. Increasing the viscosity of the solution, for example, or a decrease in temperature, will increase the correlation time of the protein. Through this equation the τ_c can be used to estimate the apparent molecular weight of a protein at 25°C, MW $\approx 2\tau_c$, in water.

$$\tau_c = \frac{4\pi\eta_w r^3}{3kT} \qquad \textbf{Equation 4.2}$$

The calculation of the isotropic rotational correlation time and analysis of the local relaxation of the Hsp90 N-terminal domain was carried out according to

the Lipari and Szabo model-free approach (Lipari and Szabo, 1982a; Lipari and Szabo, 1982b). In this approach it was necessary to exclude those residues which undergo chemical exchange (the residues with short T_2 values) and residues with rapid local motion (the residues with low heteronuclear NOE values). Application of these filters makes it possible to assume that the extracted value represents only the tumbling rate of the protein with minimum effect from the local motion on the final correlation time. Only amide groups with I_{sat}/I_{unsat} values greater than a cut off value (NOE > 0.65) were permitted in the final calculation. As a result, 11 out of 189 residues were filtered out mostly from flexible ends of the sequence using the applied filter on the $\{^1H\}$-^{15}N heteronuclear NOE values. The residues 2, 3, 113, 125, 167, 185, 199, 200, 201, 202 and 203 that predominantly belong to the flexible end or beginning of the sequence were omitted from the final calculation. In the next step a statistical filter shown in Equation 4.3 was applied in order to exclude residues with $^{15}N R_2/R_1$ values significantly different from the sample mean value. In Equation 4.3, (R_1) and (R_2) are the average ^{15}N longitudinal and ^{15}N transverse relaxation rates respectively, $R_{1,i}$ and $R_{2,i}$ are individual amide relaxation rates and SD is the overall standard deviation value for ^{15}N R_2/R_1 (Tjandra *et al.*, 1995).

$$\left(\frac{\langle R_1 \rangle - R_{1,i}}{(R_1)} - \frac{\langle R_2 \rangle - R_{2,i}}{\langle R_2 \rangle} \right) > 1.5 \times SD \qquad \textbf{Equation 4.3}$$

By applying this filter another five residues, residues 29, 92, 95, 122 and 169 were omitted. The average values for R_1, R_2 and $\{^1H\}$-^{15}N heteronuclear NOE before and after filtering was applied, are shown with their errors in Table 4.1. The

isotropic rotational correlation time was estimated based on equations taken from Mandel *et al.,* (1996) and the scripts were written by Dr. Mark Pfuhl.

As a result, an average isotropic rotational correlation time (τ_c) of 12.5 ns was calculated from data of 173 residues. A standard deviation of +/- 0.269897 ns was estimated using a Monte Carlo analysis to produce a Gaussian distribution for the estimation of the uncertainty in determining the τ_c (Figure 4.5) arising from uncertainty in the experimental R_2/R_1. The MW of the protein can be estimated from τ_c to be about 25±0.54kDa, which is the approximate size for the Hsp90 N-terminal domain.

The relaxation rate ratios of R_2/R_1 can give information about the orientation of the secondary structures in the protein since it is independent of internal mobility. The ratio values are usually in the same range for the structured regions and vary in the loop and non-structured segments. Figure 4.6 shows a plot of the R_2/R_1 ratio against the sequence of the protein with the residues in a secondary structure highlighted. High ratio values such as those of residues 92, 95, 168 and 170 most probably have proton exchange. No significant variation versus protein sequence could be observed in the R2/R1 rations and overall seems constant apart from few spurious signals, which could be due to error in experimental measurements.

	R_1 (s^{-1})	SD[a] (±)	R_2 (s^{-1})	SD (±)	NOE	SD
Before filter [b]	1.09311	0.0966236	17.6097	3.08224	0.766839	0.0810397
After filter [c]	1.08831	0.0759104	17.3874	1.338905	0.77669	0.0615408

a) Standard deviation; b) Average values from all 189 cross peaks; c) Average data selected using a NOE and $\langle R_2/R_1 \rangle$ filter (173 crosspeaks)

Table 4.1 Average values for R_1, R_2 and heteronuclear NOE before and after application of the filter to calculate the isotopic rotational correlation time.

Distribution of τ_c values from fits to individual experimental R_2/R_1 values

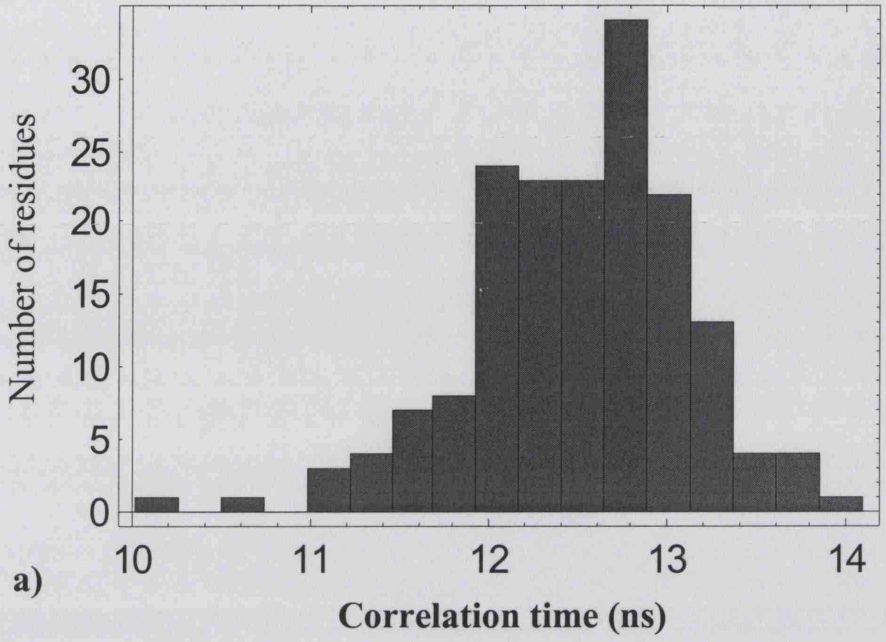

Distribution of average τ_c values from the Monte Carlo calculation

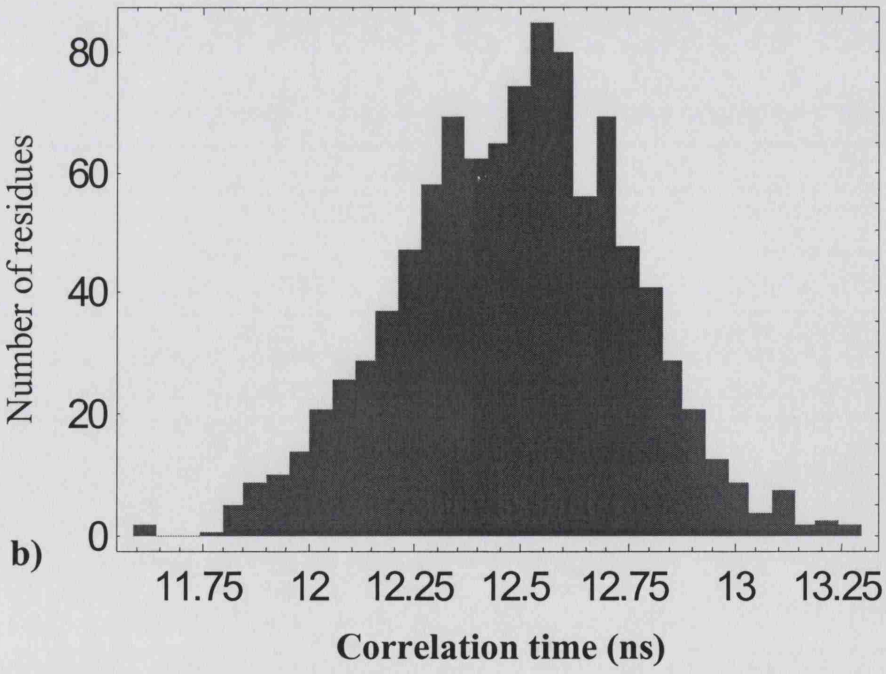

Figure 4.5 Estimation of the correlation time (a) Distributions of individual residues times (τ_C) of selected residues. **(b)** Monte Carlo analysis of the average τ_C

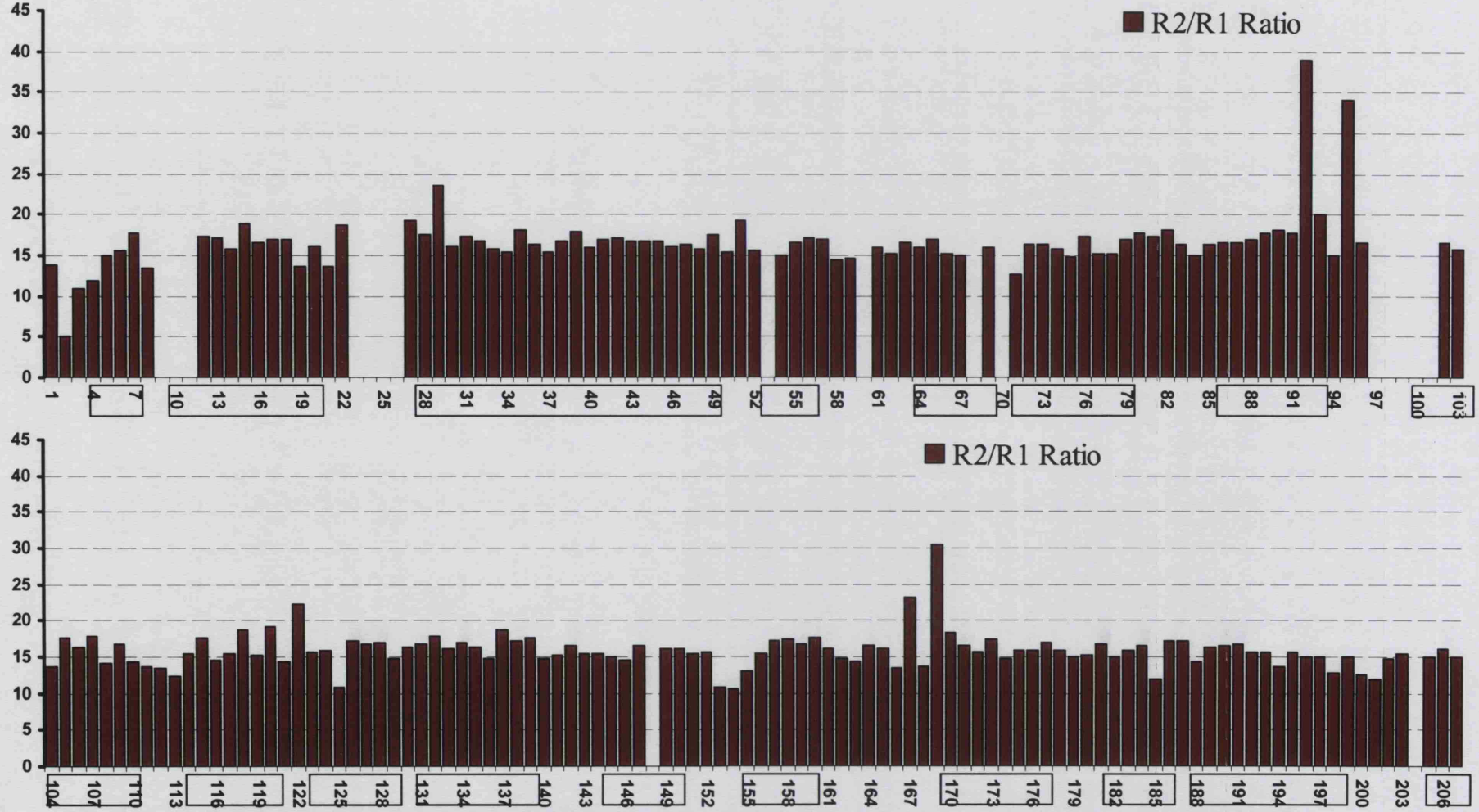

Figure 4.6 Backbone NH ^{15}N R_2/R_1 ratios of the ^{1}H^{15}N-labelled Hsp90 N-terminal at 25°C recorded at 600 MHz. Boxes show where there is a secondary structure.

4.5 Measurement of the translational diffusion coefficient

There have been reports suggesting a heat induced dimerisation in the N-terminal domain of the Hsp90 full length protein (Yonehara *et al.,* 1996; Maruya *et al.,* 1999) that could be investigated using diffusion experiments within the limits of NMR experiments.

Macromolecular self-diffusion is described as random translational motion in the absence of a concentration gradient. The coefficient of this motion is known as the translational diffusion coefficient, Ds, which is the average of the square distance travelled per molecule per unit of time. From D_S, molecular size and other hydrodynamic properties of a molecule can be inferred. The state of self-association of a protein can be obtained directly from its diffusion coefficient or via the relationship between its mass and diffusion coefficient.

A PFG NMR method, based on a spin-echo pulse sequence (Altieri *et al.,* 1995; Dingley *et al.,* 1995) repeated with successively increasing gradient strengths as described in Chapter 2, Section 2.11 can be used to determine the translational diffusion coefficient. These NMR diffusion experiments were carried out to investigate the dimerisation state of the protein in solution in a range of temperatures from 10 to 35°C.

Figure 4.7 shows an example of a series of 1D signal decay experiments recorded at different PFG pulses displayed next to the spectrum recorded at 25°C. The amplitudes (peak intensities [R(τ)]) are attenuated in each spectrum due to translational diffusion, which are related to D_s by Equation 4.4.

$$R(\tau) = R(0)\exp(-(\gamma_H \sigma G)^2(\Delta - {}^{\sigma}/_{3})D_s) \qquad \textbf{Equation 4.4}$$

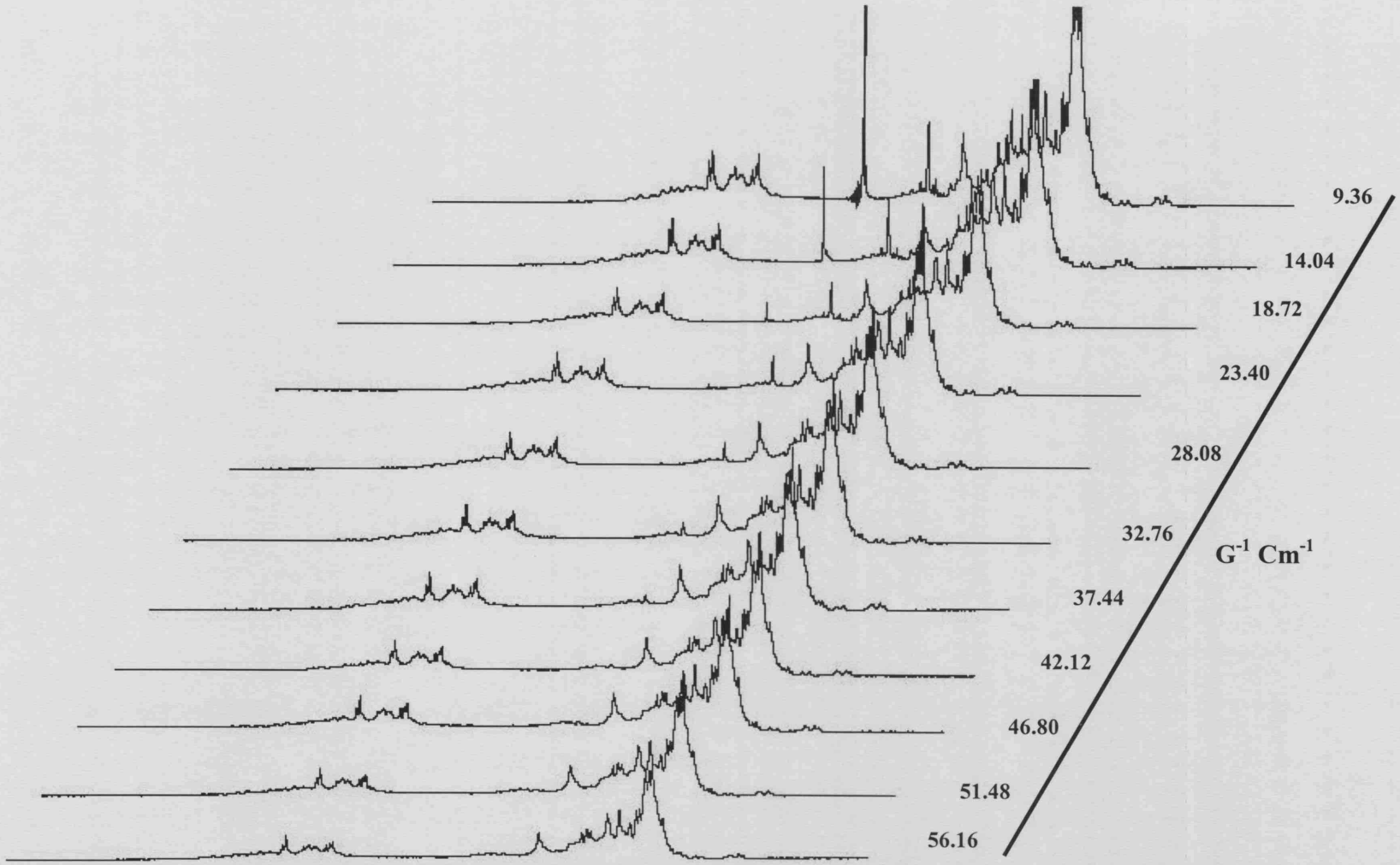

Figure 4.7 Example of signal decay in a 1D diffusion experiment with increasing gradient strength, from a ^{1}H Hsp90 N-terminal domain sample. The sample was in 20 mM Tris buffer at pH 8.0 and the spectrum was recorded at 500 MHz, at 25°C. The gradient strength level (G^{-1} Cm^{-1}) at each 1D spectrum is displayed at the right hand side of the spectrum

In this Equation the $R(\tau)$ is the signal strength at time τ, R_0 is the reference signal at time zero, γ_H is the proton gyromagnetic ratio and G is the gradient strength (G/cm) (Dingley *et al.,* 1995). The experiments were conducted so that the PFG duration, σ, was set to 5 ms, the diffusion delay, Δ, was set at 40 ms and G set as shown in Table 2.4, Chapter 2. Best fit to the data was achieved using a three-parameter fit of Equation 4.5 in which R_∞, is normalised signal intensity at the infinite time and R_0 at zero time. In Equation 4.5 the x, $[x=\gamma_H^2\sigma^2(\Delta - {}^{\sigma}/_3)]$ is a constant while D_S is found through a nonlinear least square fitting of an exponential on the data (Dingley *et al.,* 1995). The nonlinear regression method was carried out on the peak intensity with direct weighting against the result using Origin™.

$$R = R_\infty + R_0\exp(-G^2D_Sx) \qquad \textbf{Equation 4.5}$$

By setting the R_∞ to zero, a two-parameter fit was also tested against the data and compared with the above method (results are shown in Table 4.2 and Figure 4.8). The result of the exponential fit of peak intensities versus gradient square, with a three parameter fit (in blue) compared to two parameter fit (in red) are shown in Figure 4.8. The result of the fit, performed on data sets carried out at 20°C, yielded a translational diffusion coefficient of about 9.3453×10^{-7} cm^2s^{-1}. The result for the same data sets using a two parameter fit gave a translational diffusion coefficient of $7.092\times10^{-7}cm^2s^{-1}$. The three-parameter fit complied better with our data. The three-parameter method using Equation 4.5 was therefore used throughout this chapter for all of the diffusion experiments carried out at different temperatures.

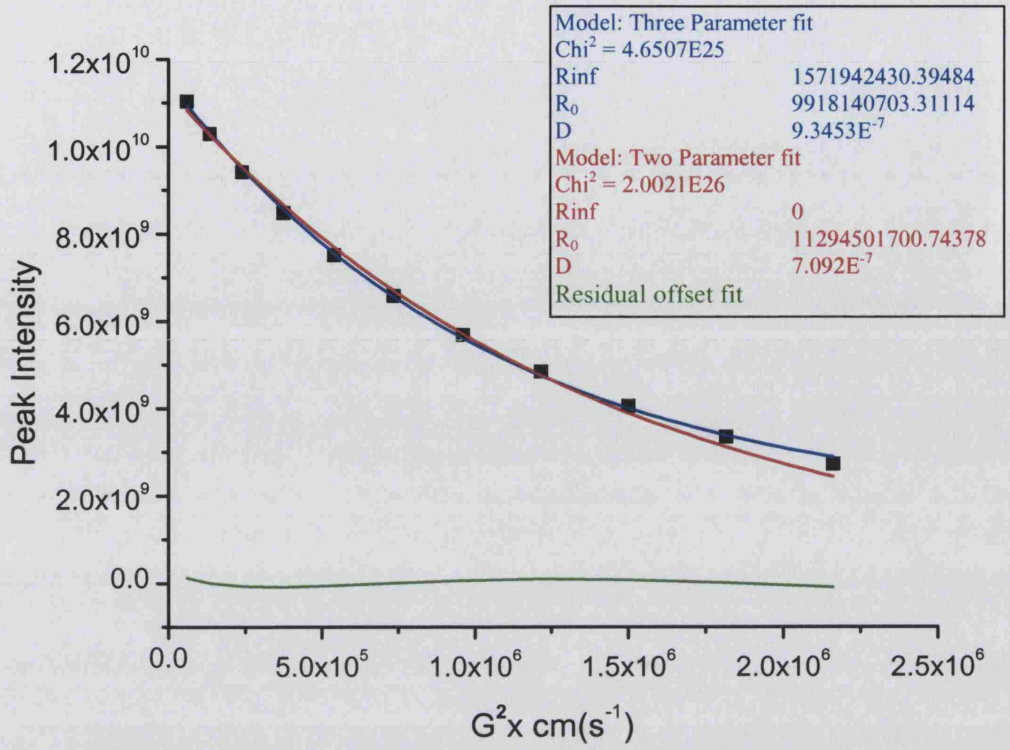

Figure 4.8. Comparison of two parameter (red line) with three parameter (blue line) data fitting using Equation 4.5. The green line represents the residual offset for the 3-parameter fit.

No. of Parameters fitted	Ds (cm^2s^{-1})	Chi$^{2\,a}$
Three	9.3453×10^{-7}	4.6507×10^{25}
Two	7.092×10^{-7}	2.0021×10^{26}
a) Chi-square		

Table 4.2 Estimation of diffusion coefficients from a three and two parameter fit using Equation 4.5.

The molecular weight for the protein at 20°C was estimated using the linear fit from various protein molecular weights against their $1/D_s^3$ at 20°C, adapted from Creighton (1992), are shown in Figure 4.9. From this figure the molecular weight of the Hsp90 N-terminal domain at 20°C was estimated to be 24.36 ± 3.049 kDa. In order to extract the molecular weight for the proteins at temperatures other than that of 20°C Equation 4.6 was used. Equation 4.6 shows the relationship between molecular weight and D_S (m^2s^{-1}), where k is the Boltzmann constant ($J\,k^{-1}$), T is the temperature (K), η is the viscosity of the solution ($kg\,m^{-1}s^{-1}$), N_A is Avogadro's

number (mol^{-1}); ν_2 is the partial specific volume of the molecule ($m^3\ kg^{-1}$), σ_1 the fractional amount of water bound to the molecule (g H_2O per g diffusant), and ν_1, is the partial specific volume of solvent water ($m^3\ kg^{-1}$). The Perrin factor, F, is related to the shape of the molecule, which in turn is related to the frictional coefficient of the protein, which itself is related to temperature and D_S.

$$MW = \left[\frac{kT}{6\pi\eta F D_s}\right]^3 \left[\frac{4\pi N_A}{3[\nu_2 + \sigma_1\nu_1]}\right] \qquad \textbf{Equation 4.6}$$

In order to estimate the molecular weight at different temperatures, F and the second part of the Equation 4.6 was presumed constant and only changes in temperature and viscosity were considered. The estimated molecular weight for the protein at 20°C was used to replace the constant parameters in the first section of Equation 4.6. The variation in water viscosity as temperature changes is plotted in Figure 4.10. Data for water viscosity at different temperatures was adapted from Cho *et al.*, (1999) and extrapolated using a second order exponential decay fit using Origin™. Based on the measured Ds, temperature and viscosity as the only variable in equation 4.6 molecular weight for the protein at different temperature was calculated. The results for D_S calculated at temperatures ranging from 10°C to 35°C are shown in Figure 4.11 and Table 4.3.

Temperature	$D_S \times 10^{-7} cm^2\ s^{-1}$	MW estimate kDa ±3	Viscosity g $cm^{-1}\ s^{-1}$
35°C	17.006	30.9	0.74
30°C	11.380	23.0	0.80
25°C	9.7519	22.9	0.92
20°C	9.3479	24.4	1.0
15°C	9.4535	29.0	1.16
10°C	9.4457	33.2	1.30

Table 4.3. The Ds for the Hsp90 N-terminal at different temperatures with estimated molecular weight.
Data were extracted from Figures 4.10 and 4.11

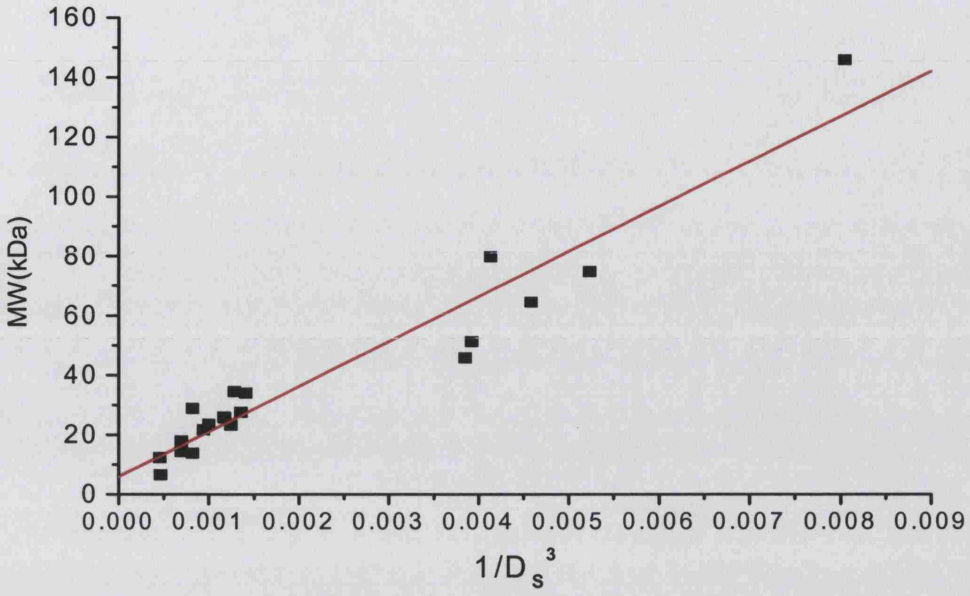

Figure 4.9 A linear fit of molecular weight versus the reciprocal of their translational diffusion coefficient to the 3rd power ($1/D_S^3$). Data was adapted from Creighton (1992) carried out at 20°C.

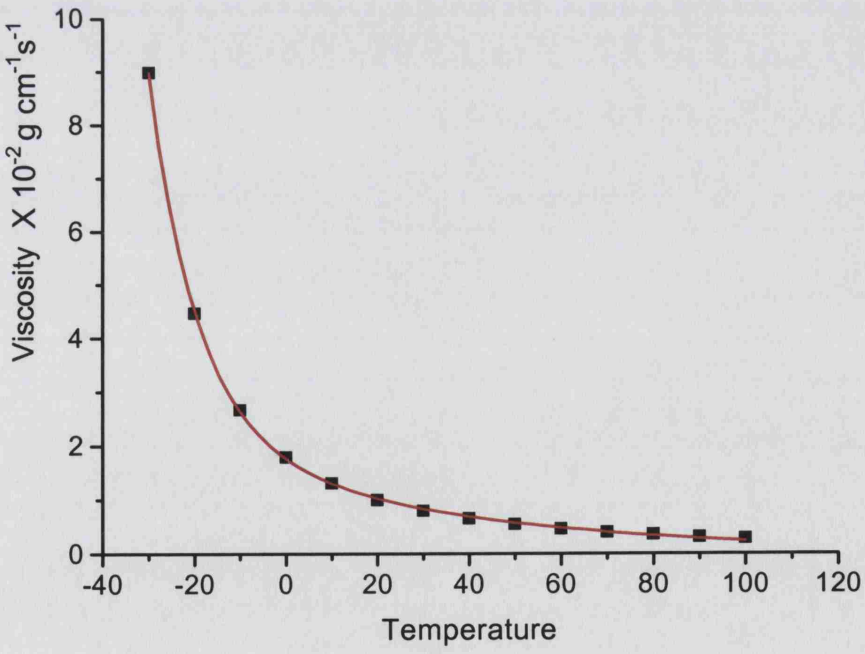

Figure 4.10. The change in water viscosity at different temperatures (°C). Data were adapted from Cho *et al.* (1999) and extrapolated using a second order exponential decay fit.

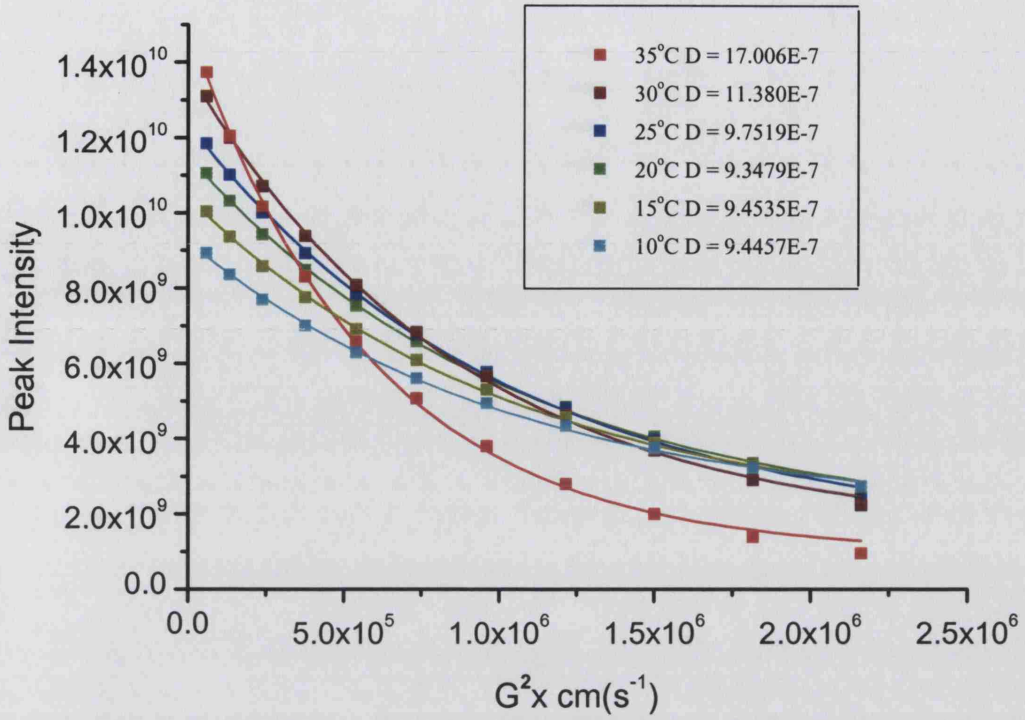

Figure 4.11. NMR diffusion experiments carried out at temperatures ranging from 10°C to 35°C using a three-parameter fit of Equation 4.4

The D_S at temperatures 10°C to 25°C is more or less in the same range, and starts to increase at 30°C and almost doubles at 35°C. This could be due to further reduction in water viscosity as temperature increases, which results in faster macromolecule diffusion. (Variations possibly due to changes in protein hydration or changes in its hydrodynamic properties).

The estimated molecular weight also decreases from 10°C to 25°C and starts to increase from 30°C to 35°C (Table 4.3). The variation seen could be due to several reasons, such as protein hydration and changes in the shape of the protein as the temperature changes. As a result, it could be suggested that only one species of the protein can be seen, or another possibility is a partial aggregation of the protein at different temperatures.

4.6 Temperature titration

The temperature titration was carried out on ^{15}N-labelled, N-terminal domain of Hsp90 in 20 mM Tris buffer at pH 8.0* (25°C). The pKa for Tris buffer was 8.06 with a temperature coefficient of –0.028 per °C which gave about a 0.3 difference in pH for every 10 °C change in temperature. A series of $^{1}H^{15}N$ HSQC spectra were recorded, each at different temperatures, ranging from 5°C to 35°C with 5°C intervals as shown in Figures 4.12 and 4.13.

It has long been known that the chemical shifts of amide proton resonances shift as the temperature increases (Ohnishi and Urry, 1969). The main reason for this is thought to be related to the changes in the hydrogen bonds present in the protein and with water. The amide chemical shifts are strongly affected by their local environment. As the temperature of the sample rises, the magnitude of thermal fluctuations in the protein increases, which results in the expansion of the average inter-atomic distances (Baxter and Williamson, 1997). Average hydrogen bond lengths increase as temperature rises, resulting in a reduction in its downfield shift effect of the carboxyl group on the amide, in the hydrogen bond. As a result, most amide protons experience an upfield shift in their resonance frequencies (Cierpicki and Otlewski, 2001; Baxter and Williamson, 1997). Most proton chemical shifts display linear temperature dependence. The protons which exhibit a curved temperature dependence indicate that at least two conformational species exist in that region of the protein that are in fast exchange over the temperature range studied (Baxter and Williamson, 1997). Generally, interpreting the result of the temperature shifts is complicated due to complexity of the protein structures and various internal and external forces involved. The upfield movement in the

proton shift is greater for inter-molecular hydrogen bonds (such as bonds to bulk water) than for intra-molecular hydrogen bonds, and hence the chemical shift of amide protons hydrogen bonded to water will shift upfield further with temperature than internally hydrogen-bonded amides (Cierpicki and Otlewski, 2001). This will affect mostly residues on the surface of the structure, which are in contact with solvent.

Figure 4.12 shows the temperature titration for the Hsp90 N-terminal domain, beginning at 10°C in dark blue with 5°C increments to 35°C shown in red. We see that, some peaks are stronger and more dispersed at lower temperatures (highlighted as yellow arrows) while for most resonances it is the opposite case as they are stronger and well dispersed (as shown using red arrows). As the temperature increases, the density of most liquids is reduced and the tumbling rate of the protein increases, which results in a decrease in protein correlation time (Equation 4.2, Section 4.4). Figure 4.13 shows the superposition of a temperature titration for the Hsp90 N-terminal domain from 5°C (in black) to 35°C (in red) for comparison.

Most of the protons have an upfield shift as the temperature increases while in the nitrogen dimension these can be either upfield, downfield, or even show no change as the temperature increases. Most resonances display a linear change as temperatures increase. One of the arginine or glutamine NH_2 sidechain crosspeak pairs (highlighted using a red arrow) in Figure 4.13 has a curved shape in comparison to the other, which is linear, suggesting presence of two different species for the sidechain protons during the temperature titration. There are, however, resonances that do not change as much as others during the titration, of which residues Thr-159 and Leu-160 are examples. This could be because of strong

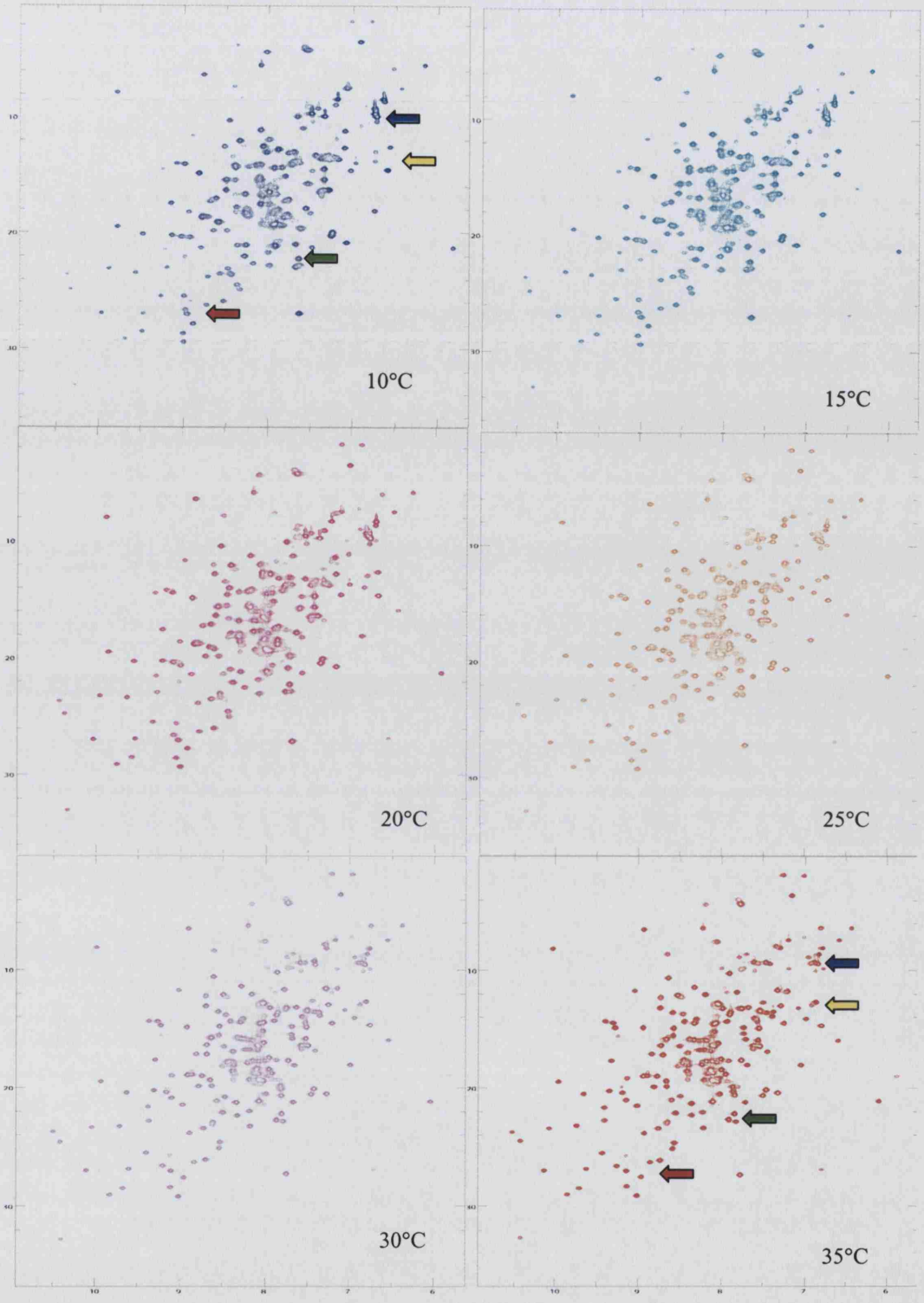

Figure 4.12. Temperature titration spectra from 10°C to 35°C for the Hsp90 N-terminal domain. The titration begins with 10°C (from top left in dark blue) to 35°C (bottom left at in red). The arrows point to the regions that are affected during the temperature titration.

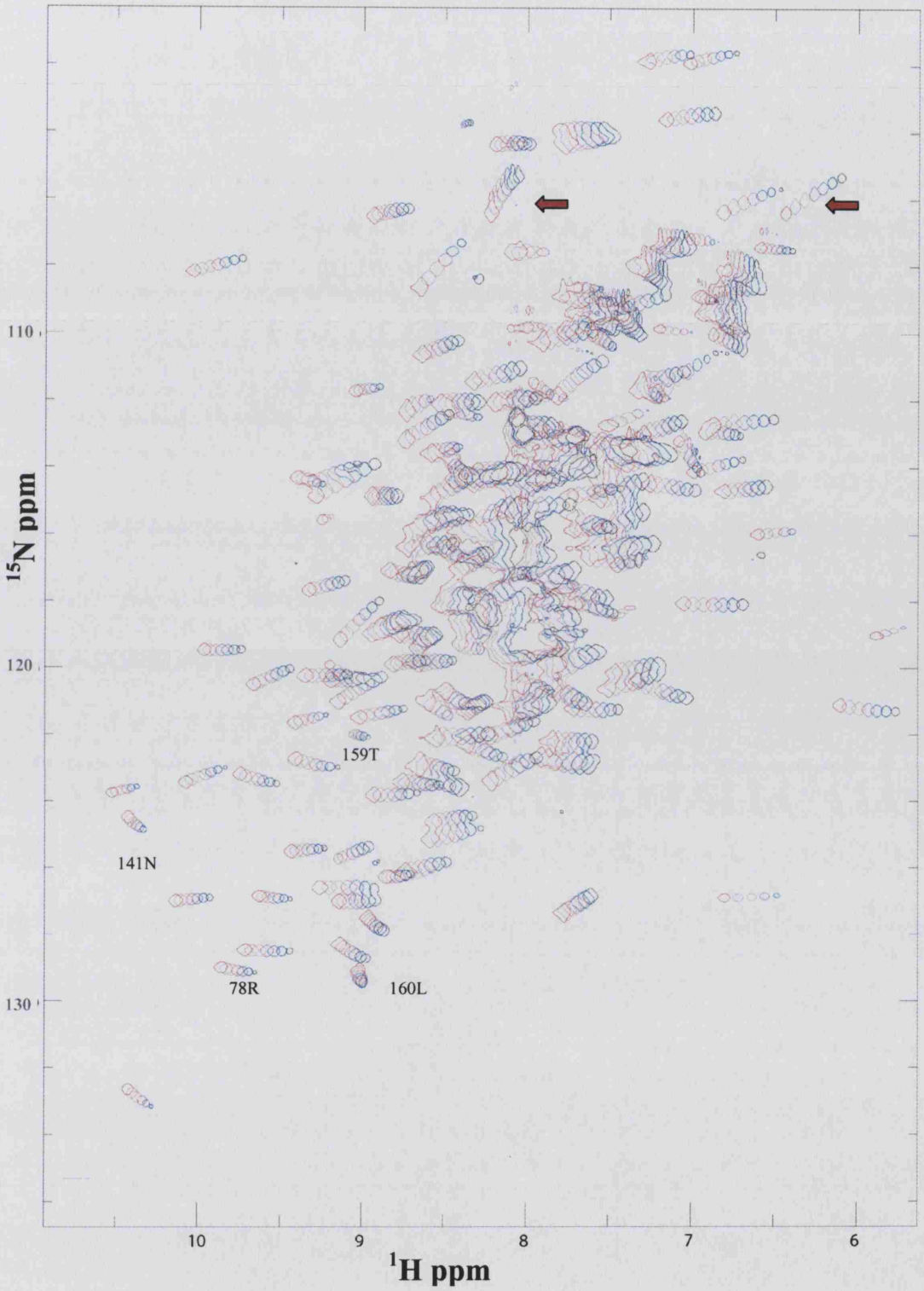

Figure 4.13. Superposition of the temperature titration from 5°C to 35°C for the Hsp90 N-terminal domain. The red arrows point to the curved shape titration of a side chain crosspeak in comparison to its pair, which has a different pattern to it.

intra-molecular hydrogen bonds, which makes them less susceptible to temperature change or other hydrogen bond acceptors in the surrounding structure. For most of the crosspeaks at the centre of the spectrum, resonance intensity remains almost unchanged during the varying temperatures. This could be due to the structure of the helices, where most residues are hydrogen bonded (short and long) e.g Arg-189, and their motion is less affected by change in the temperature. Most of the residues in β-sheets and β-turns are located at the bottom left corner of the spectra with short temperature shifts either upfield or downfield in the nitrogen dimension, showing an increase in their peak intensity as temperature rises. Residue Arg-78, in a β-sheet, and residue Asn–141, in a β-turn, show this effect (as highlighted in Figure 4.12). In the β-sheet the short hydrogen bonds are dominant, while 3_{10} helices and β-turns have longer hydrogen bonds. For α-helices, both short and long hydrogen bonds are observed and the temperature shift is also dependent upon packing of the helix, polar and non-polar groups, which can cause curvature in the helix structure.

4.7 Chapter summary

The main findings of this section were as follows:

- The R_2/R_1 relaxation rates plotted on the X-ray crystal structure of the Hsp90 N-terminal domain showed a uniformed value for the secondary structures suggesting an overall isotropic motion for the protein. Residues that were possibly in exchange were highlighted.
- The heteronuclear NOE values show the local motion in the secondary structure of the protein that highlights several regions of interest in the protein. For example, parts of the 'ATP-lid' were observed which could be essential for nucleotide and drug binding.
- Using the relaxation experiment, τ_c of the protein was calculated as 12.5 ns which is in good agreement with the anticipated tumbling rate of a 25 kDa monomeric protein at 20°C.
- Diffusion experiments showed that the Hsp90 N-terminal domain is predominantly monomer in solution and has an apparent temperature dependence aggregation.
- Finally temperature titrations were presented as reference points for the resonance recorded at different temperatures as well as indicating its effect on the chemical shifts.

CHAPTER 5

NUCLEOTIDE BINDING STUDIES

5.1 Chapter overview

Hsp90 has been found by crystallography to bind ADP and AMP-PNP in a Mg^{2+} dependent manner. In all the X-ray crystal structures solved to date for the yeast Hsp90 N-terminal domain with nucleotide, only one conformation was observed with no difference between the ADP and ATP bound structures. Also no electron density was observed for the γ-phosphate of the ATP bound to the protein. In this chapter the effects of nucleotides binding to the N-terminal domain of Hsp90 has been investigated using NMR. Initially ATP was titrated in the presence of Mg^{2+} in a ^{15}N-labelled sample to investigate its ATPase activity in KH_2PO_4 buffer, pH 7.0* at 10°C. The shifts in the HSQC resonances were compared to those of the ADP bound form. Due to instability of the sample in KH_2PO_4 buffer and possible interaction of the phosphate ions with nucleotide, a buffer optimisation was carried out (details in Chapter 2). This resulted in the usage of 20 mM Tris buffer, in which the protein had better solubility, for all other experiments. To study the ATPase activity of the N-terminal domain in Tris buffer compared to that in phosphate buffer, a time course titration was carried out on a ^{15}N-labelled sample at 25°C, which showed clear ATPase activity for the protein. In order to observe and study the effect of nucleotide binding to the protein, particularly ATP, the backbone assignment of AMP-PNP, a non-hydrolysable analogue of ATP, bound to the N-terminal domain of Hsp90 in the presence of Mg^{2+} was chosen as a model. The sequential backbone assignment of the protein in the presence of AMP-PNP was compared to the apo- assignments and the differences were analysed. A secondary structure prediction was carried out, using the CSI program (version 2.0), and the data was compared to the known crystal

structure of the Hsp90- N-terminal domain and the secondary structure predicted by the apo- sample. Dynamic studies were carried out using a ^{15}N-labelled sample at 25°C in the presence of 5 mM AMP-PNP and 10 mM Mg^{2+} on a 600 MHz proton frequency spectrometer. The relaxation and dynamics results were also compared to the apo- relaxation data to elucidate the effect of the AMP-PNP on the protein.

5.2. Titration of Mg^{2+}

It is known that Mg^{2+} is essential to the ATPase activity of the Hsp90 N-terminal domain and interacts with oxygens of α and β phosphates of ADP (Prodromou *et al.*, 1997). Prodromou *et al.* (1997) also reported the sidechain amide oxygen of Asn-37 to interact with Mg^{2+}, which with three water molecules and the oxygens of the phosphates, makes an approximate octahedral coordination centred for the ion. Gly-123 is the other residue which has a through water connection with the ion. The Mg^{2+} ion is also present in all GHKL superfamily proteins, where structures have been solved with nucleotide, which suggests occupancy of Mg^{2+} in the pocket is essential in this motif (Hu *et al.*, 2003).

The initial step with the binding studies was to investigate whether the N-terminal domain of Hsp90 alone was able to bind Mg^{2+}, hence a stock sample of $MgCl_2$ (pH 7.0) in phosphate buffer with 10% D_2O was prepared. Mg^{2+} was added in a 6-step titration to reach a final concentration of 0.8 mM (two-fold excess) ensuring sufficient presence of ion for binding to the protein, even for a weak binding constant. The results of these $Mg2^{+}$ titrations are shown in Figure 5.1, the spectrum in blue is the first point in the titration followed by additional aliquots of

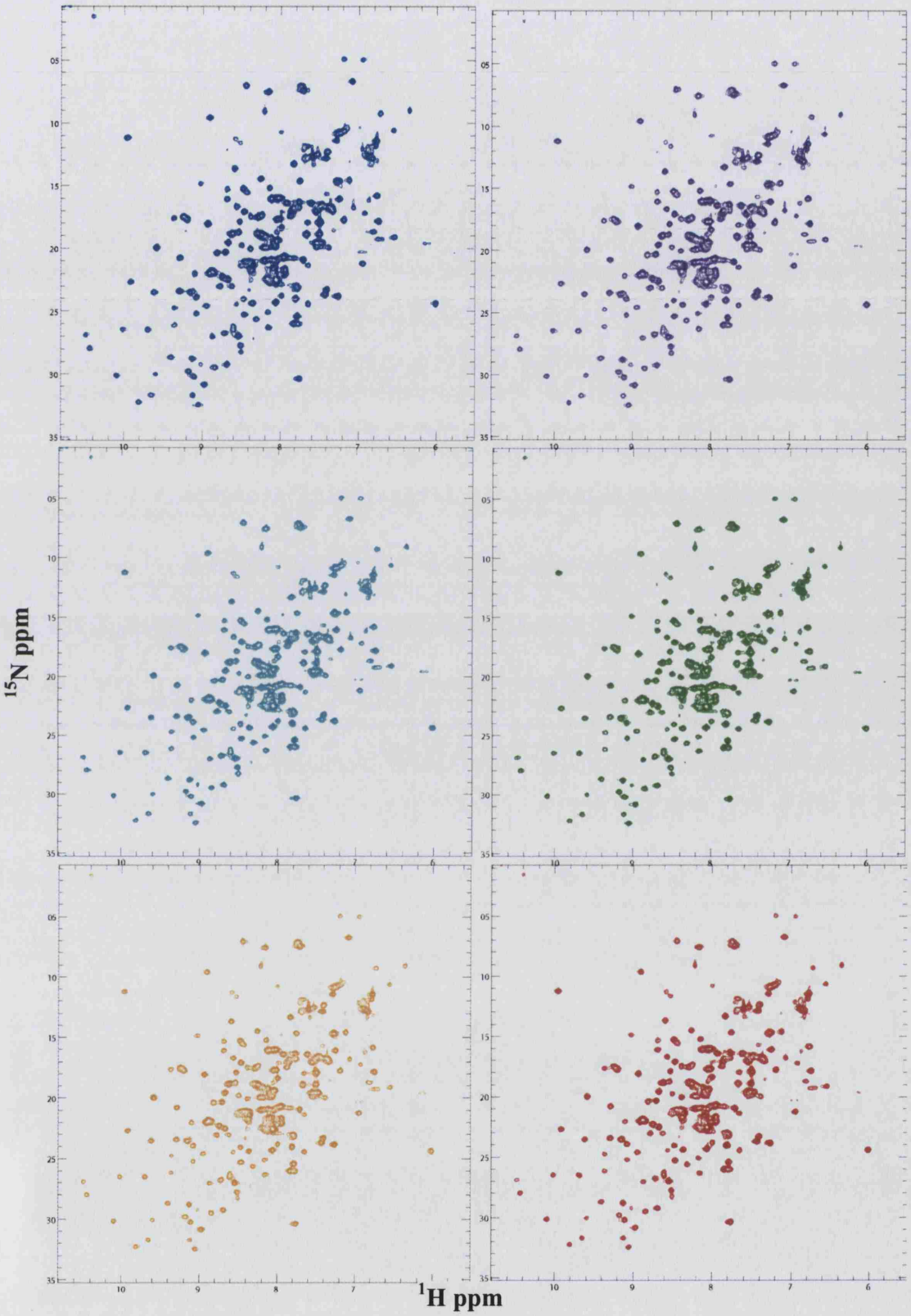

Figure 5.1. The $^{1}H^{15}N$ HSQC spectra recorded during different steps of Mg^{2+} titration. No difference was observed during the titration in comparison to the spectrum without Mg^{2+}. The spectrum in blue is the first titration point, following left to right, with the final titration point in red (bottom right).

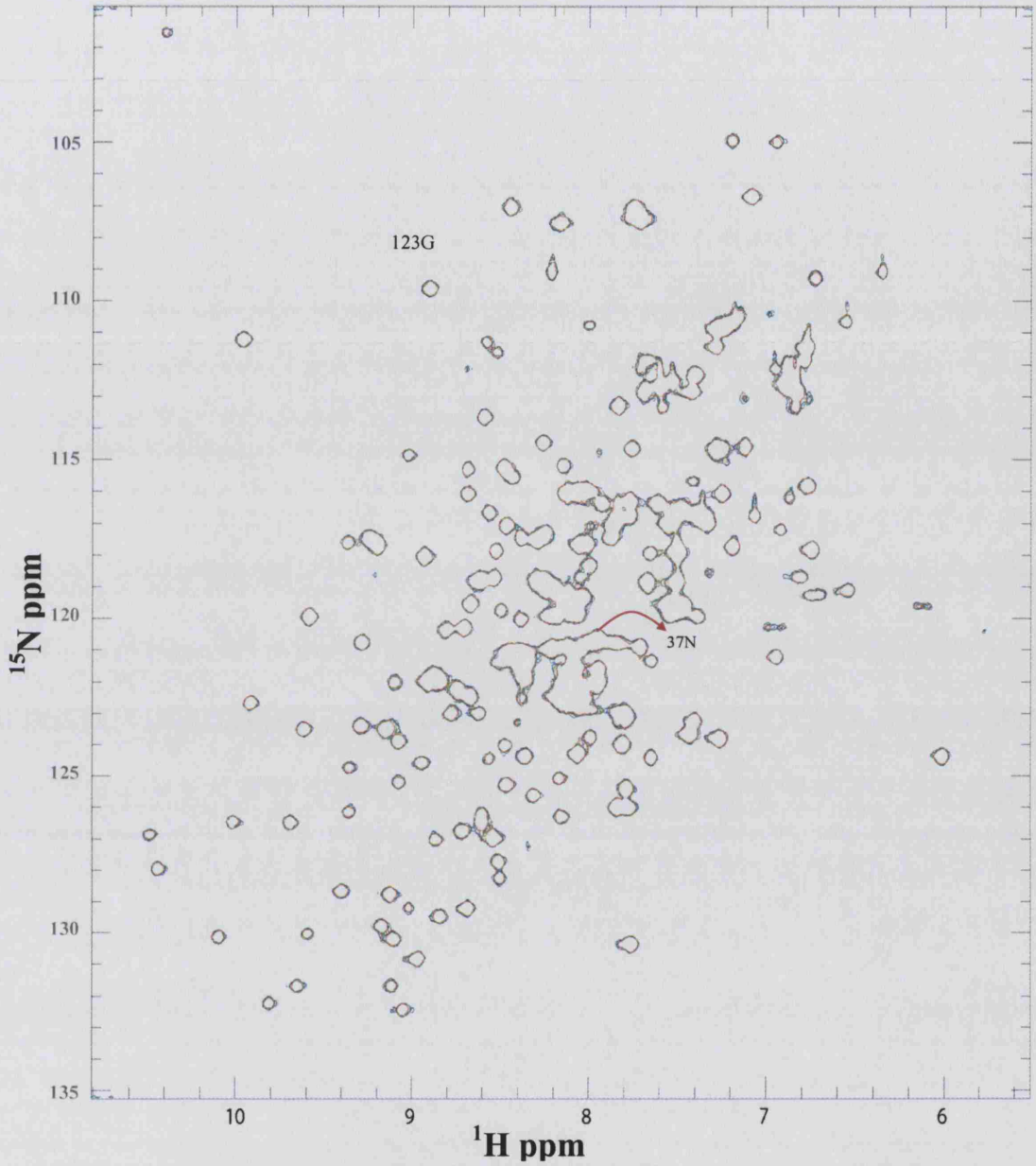

Figure 5.2. The result of overlapping the HSQC spectra from the Mg^{2+} titration. Residues Gly-123 and Asn-37 are highlighted. No difference during the titrations of Mg^{2+} were observed and exhibits that Mg^{2+} by itself does not bind to the N-terminal domain of Hsp90.

2.54 µl of $MgCl_2$ buffer (from left to right) in each step with the final spectrum shown in red. Figure 5.2 shows the superimposition of the titration point with the crosspeaks of interest highlighted. No significant difference was observed for the spectra in the presence and absence of Mg^{2+}, confirming that Mg^{2+}, even in the presence of phosphate, doesn't bind to the protein. Neither of the two residues

(Asn-37 or Gly-123) showed any change in their chemical shifts during the titration.

5.3 Comparison of apo- and ADP/ATP bound spectra in phosphate buffer

In order to investigate nucleotide binding, 0.4 mM ADP with 5 mM $MgCl_2$, prepared in a similar buffer as the protein sample (20 mM KH_2PO_4, 30 mM NaCl at pH 7.0) with 10% D_2O was added to a 0.35 mM sample of ^{15}N-labelled, N-terminal domain of Hsp90. A $^{1}H^{15}N$ HSQC was recorded for the sample at 10°C and the resultant spectrum is shown in Figure 5.3 (a) (in red) and compared with a HSQC spectrum of an apo- sample (in blue). A considerable number of crosspeaks were shifted as a result of ADP binding to the protein, with some of the differences being larger than others, from which Gly 81, 83, 94, 121 and 123 are predominant, easy to detect and all involved in nucleotide binding according to the X-ray crystal structure (Prodromuo *et al.,* 1997).

Figure 5.3 (b) shows the consequential spectrum of the ATP titration in KH_2PO_4 buffer at 10°C (red), compared to the ADP bound protein (blue) in a similar buffer recorded at the same temperature. There are about 20-25 crosspeak differences between the two spectra, again predominantly around the conserved glycine region located at top of the spectrum. In Figure 5.3 (b) the ATP chemical shift can be seen with quite broad peaks in comparison to the apo- or the ADP bound spectra (as highlighted with yellow arrows). These broad crosspeaks belong to a single residue where the chemical shift of its amide resonance in apo-, ATP and possibly ADP are observed in the same spectrum. Broad crosspeaks indicate

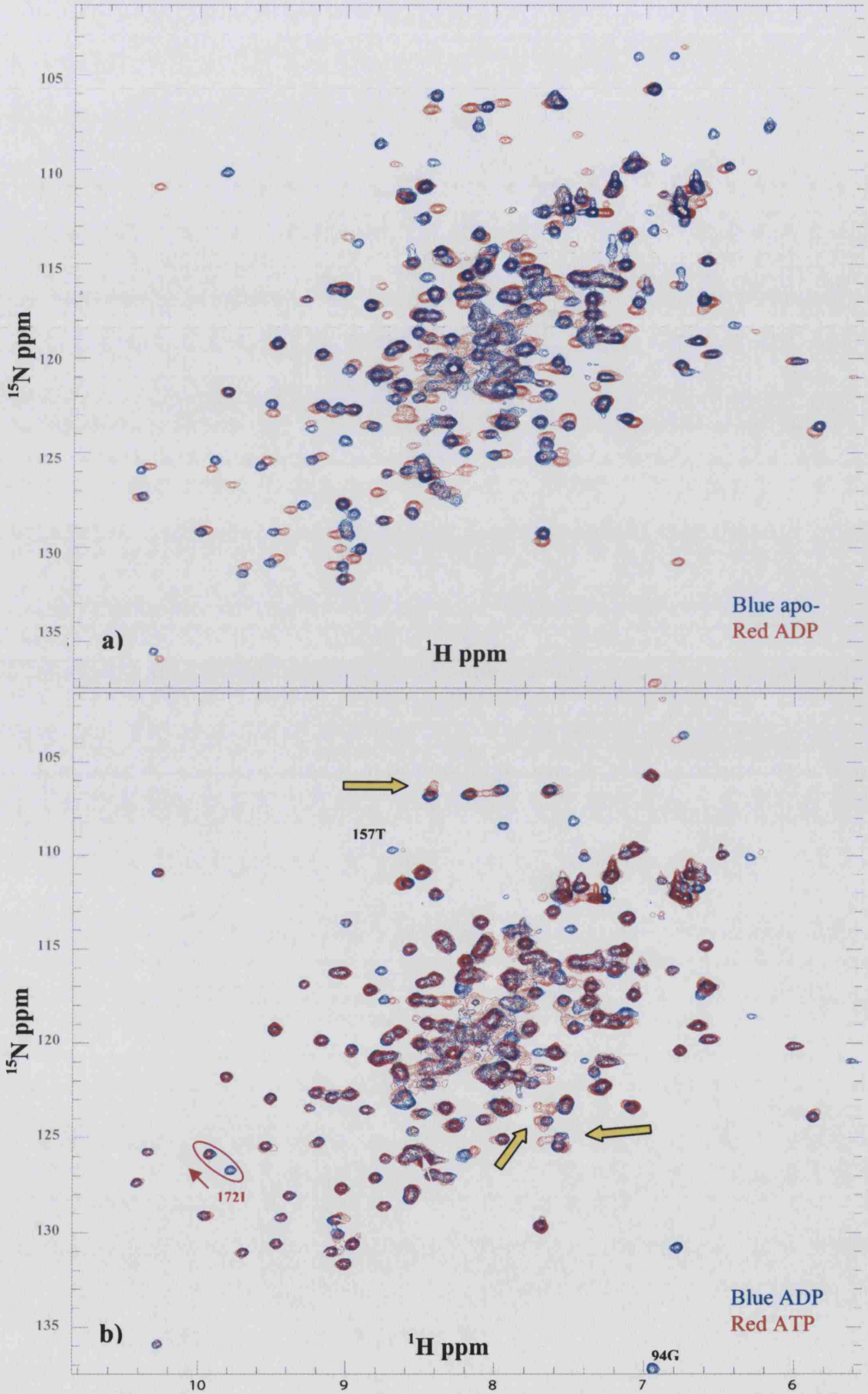

Figure 5.3. Comparison of apo-, ADP and ATP spectra in phosphate buffer. Experiments were carried out at 10°C. **(a)** Compares the spectrum of apo- Hsp90 N-terminal domain (blue) with the ADP bound (red) spectrum. **(b)** Compares the spectrum of ADP bound (red) with the ATP bound spectrum. Yellow arrows highlight the broad crosspeaks (in conformational exchange) observed in the spectrum.

conformational exchange taking place for these residues. The presence of conformational exchange makes it difficult to compare accurately the difference between the ATP and ADP bound spectra, however, despite this there are residues that have different resonance in the two spectra. As an example, residue Ile-172 is the residue close to Thr-171, which according to the X-ray crystal structure has a through water interaction with adenine of the nucleotide. The amide of residue Ile-172 is toward the nucleotide binding pocket and the reason for its lack of the signal in the ATP bound spectrum could be due to this location. The glycine residues at the top of spectrum are other examples of residues with broad crosspeaks that are most likely in conformational exchange and have different chemical shifts for the ATP and ADP bound spectra. Presence of phosphate in the buffer is not desirable due to its possible interaction with nucleotide phosphates and/or any effect it might have on protein ATPase activity in this buffer. Therefore results presented from this point onward were carried out in Tris buffer.

5.4. ATP time course titration in Tris buffer

It has been previously shown that Hsp90 has weak ATPase activity which can be reduced further by lowering the temperature (Weikl *et al.,* 2000). This weak binding and activity questioned its capability of binding nucleotides (Jakob *et al.,* 1996) until it was finally verified that Hsp90 binds nucleotide when the X-ray crystal structure of the N-terminal domain with ADP was solved by Prodromou *et al.,* (1997). Weikl *et al.,* (2000) also showed that the N-terminal fragment of yeast Hsp90 had one tenth ATPase activity of the full length protein (data measured at 37°C). In order to study the ATPase activity of the protein, an ATP time course of the protein's HSQC was carried out as described in Chapter 2, Section 2.12.

Figure 5.4 shows seven out of twelve points of the ATP time course titration. The first spectrum in black is the apo- spectra, recorded prior to adding ATP. The blue spectrum in Figure 5.4 is the first HSQC spectrum recorded after 20 min which shows the ATP bound population fingerprint with the Hsp90 N-terminal domain. As time passes, further chemical shift was observed in the HSQC spectra at later time point titrations, indicating that ATP was being used and hydrolysed to ADP. A clear ATPase activity for the protein was observed at 25°C with the second set of shifts in the crosspeaks indicating that the population was possibly changing toward a more ADP bound form.

Figure 5.5 shows the superimposition of the ATP time course titration for comparison. Here the two different sets of populations are highlighted with the apo- spectrum crosspeaks in black. Moving from one population to another (apo-, ATP bound and ADP) occurs in slow exchange and crosspeaks begin to disappear and reappear at another location, with no intermediate crosspeaks observed during experiment. There are some crosspeaks that are broader, observed at different stages of titration. The broad crosspeaks are indicative of a possible conformational exchange for residues involved in nucleotide binding or are affected as a consequence of this binding. Crosspeaks with clearly two different populations observed in Figure 5.5 are residues Gly-94, Gly-111, Thr-157, Ile-172.

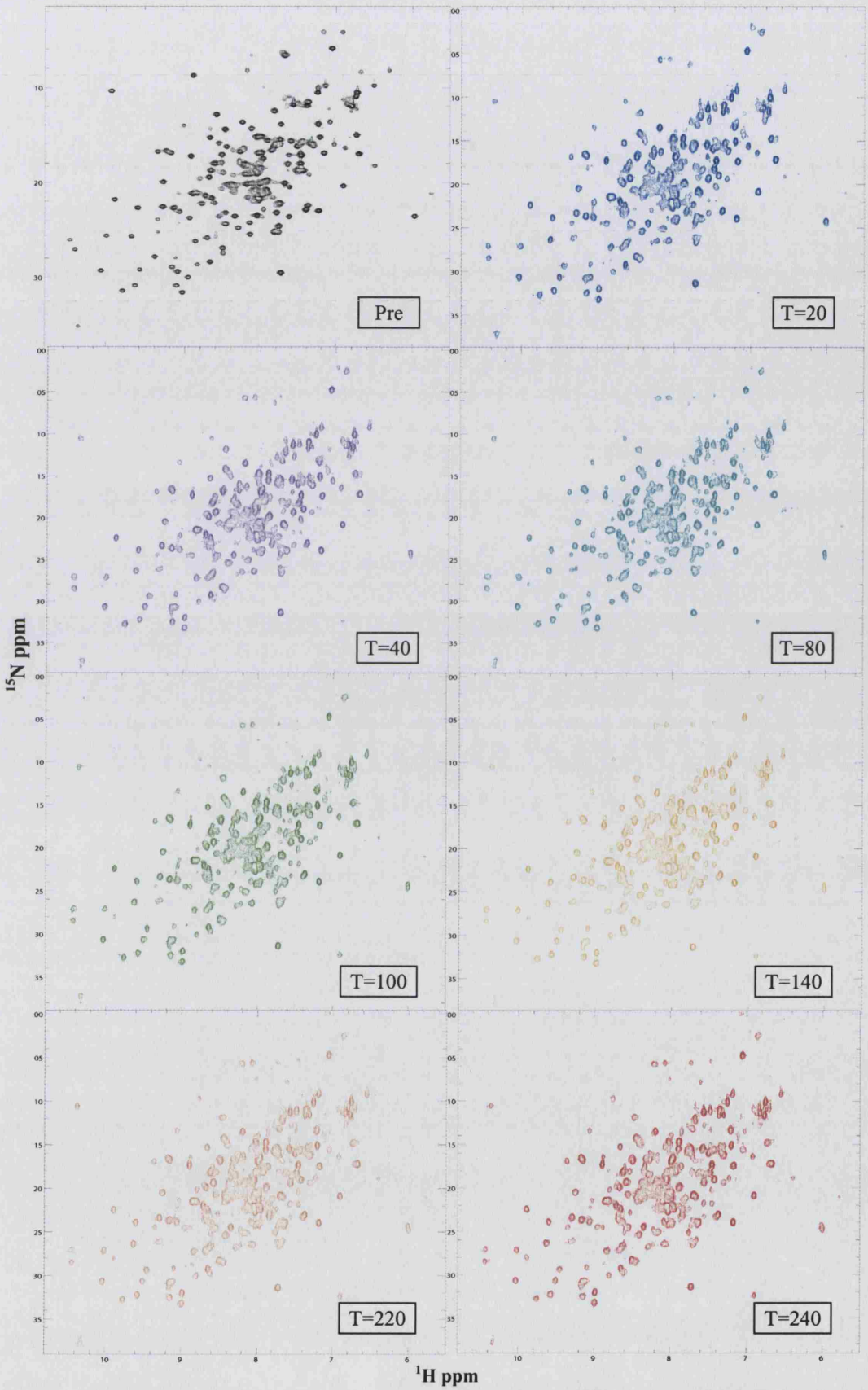

Figure 5.4. Seven out of twelve ATP time course titration points recorded as a series of HSQC spectra. The titration points are from left to right. The 1st spectra (pre) was recorded prior to conducting the experiments

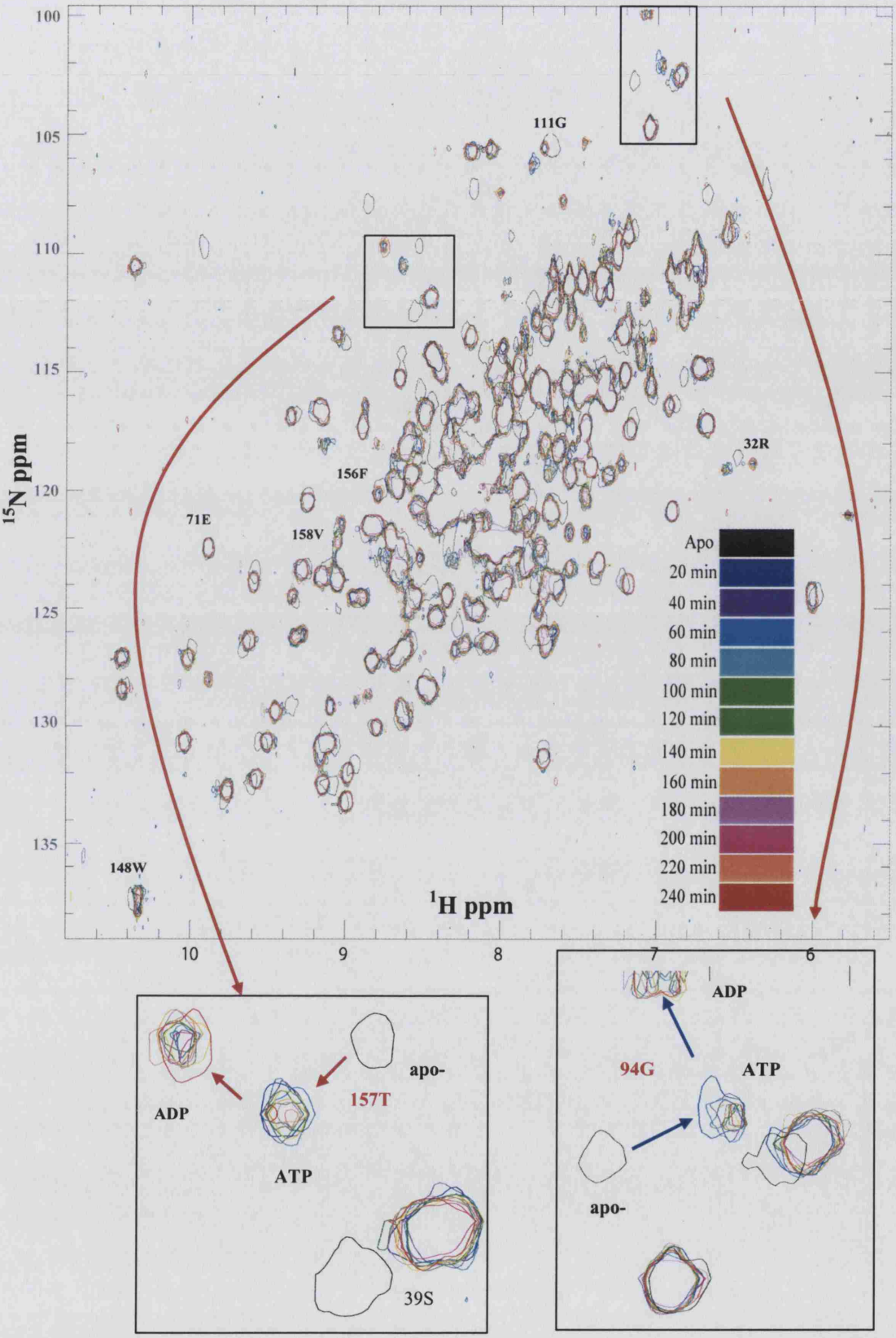

Figure 5.5. Superimposition of all twelve ATP time course titration points using a ^{15}N-labelled sample of the Hsp90 N-terminal domain. Arrows indicated movement from one population (apo-) to another (ATP or ADP).

5.5. Nucleotide bound spectra in Tris buffer recorded at 25°C

The optimised buffer condition significantly improved the stability of the sample, especially in the presence of nucleotides. Figure 5.6 shows a spectrum of the Hsp90 N-terminal domain bound with AMP-PNP (in blue) and ADP (in black) recorded on a 600 MHz proton frequency spectrometer using a ^{15}N-labelled sample in 20 mM Tris. Some of the differences between the two spectra are highlighted using coloured arrows. The glycine residues at the top of the spectra in the AMP-PNP bound spectrum have a different position in comparison to the ADP bound spectrum. Figure 5.7 shows the superimposition of the AMP-PNP bound spectrum to that of the ADP bound. Overall, about 50 crosspeaks are in different positions between the two spectra suggesting a possible different conformation between the AMP-PNP and the ADP bound protein. Residues Leu-93, Gly-94, Ala-107, Ala-110 and Gly-111 are some examples and happen to be located at the 'ATP-lid'. Other residues affected are Leu-31, Arg-32, Asn-37, Ala-38, Ala-41 and Leu-42 which are all located in the second long helix that comprises one side of the nucleotide binding pocket and according to the X-ray crystal structure are involved with the nucleotide interaction. Other residues that have different conformations and are easy to identify are Trp-148, Thr-157, Thr-159 and Asp-161. Residue Trp-148 is located in the pocket and the crosspeak highlighted (using a dark purple arrow) in Figure 5.6 is its side-chain crosspeak (from ADP bound assignments by Mark Williams, data not shown) which is only observed when ADP is present. The three other residues previously mentioned are all located in the sixth β-strand. All this suggests a possible different conformation of the Hsp90 N-terminal domain between the AMP-PNP and ADP bound structures.

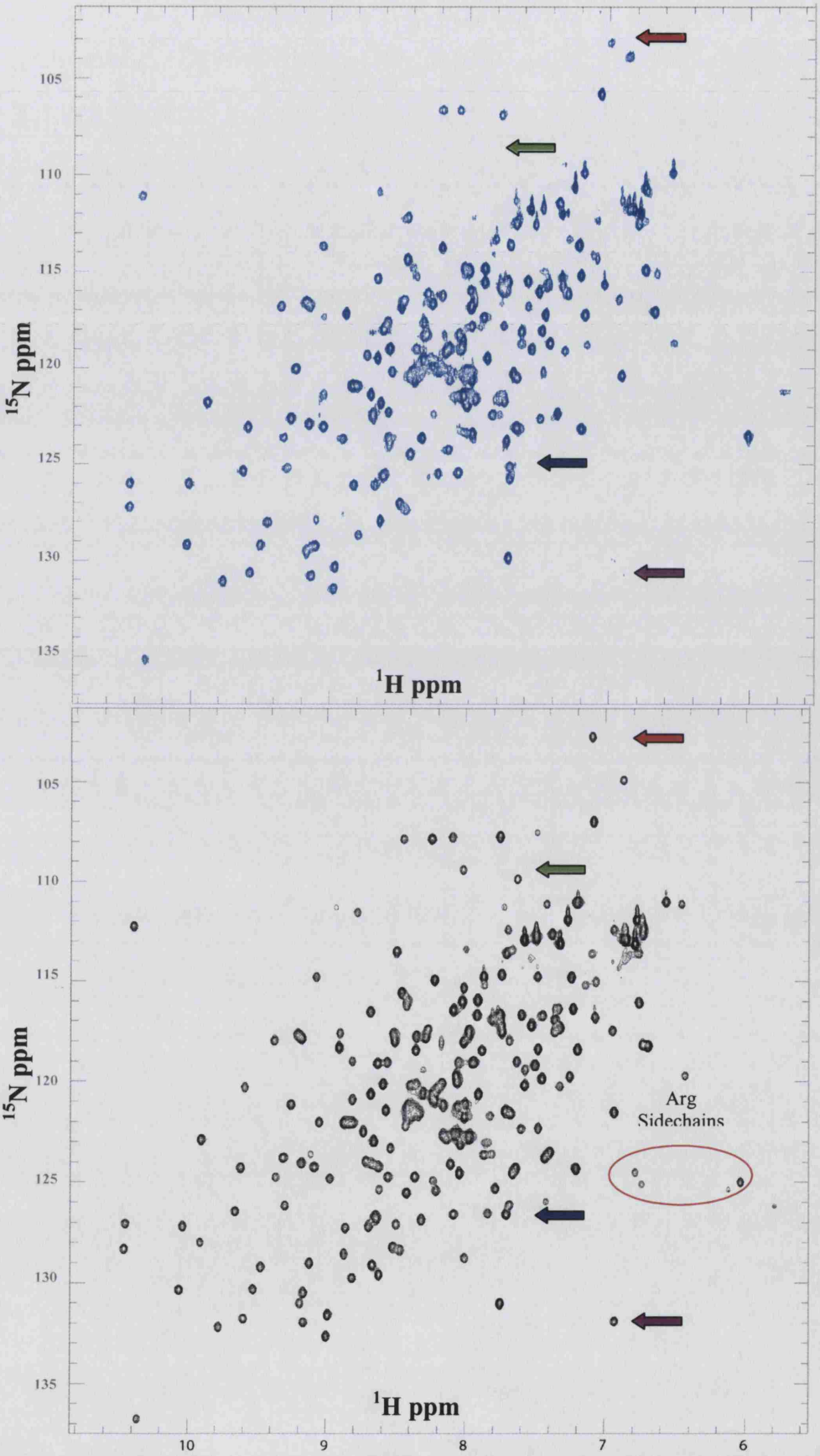

Figure 5.6. Comparison of the AMP-PNP bound (in blue) with the ADP bound spectrum (in black). Some differences between the two spectra are highlighted using arrows and a red circle for the Arg sidechains.

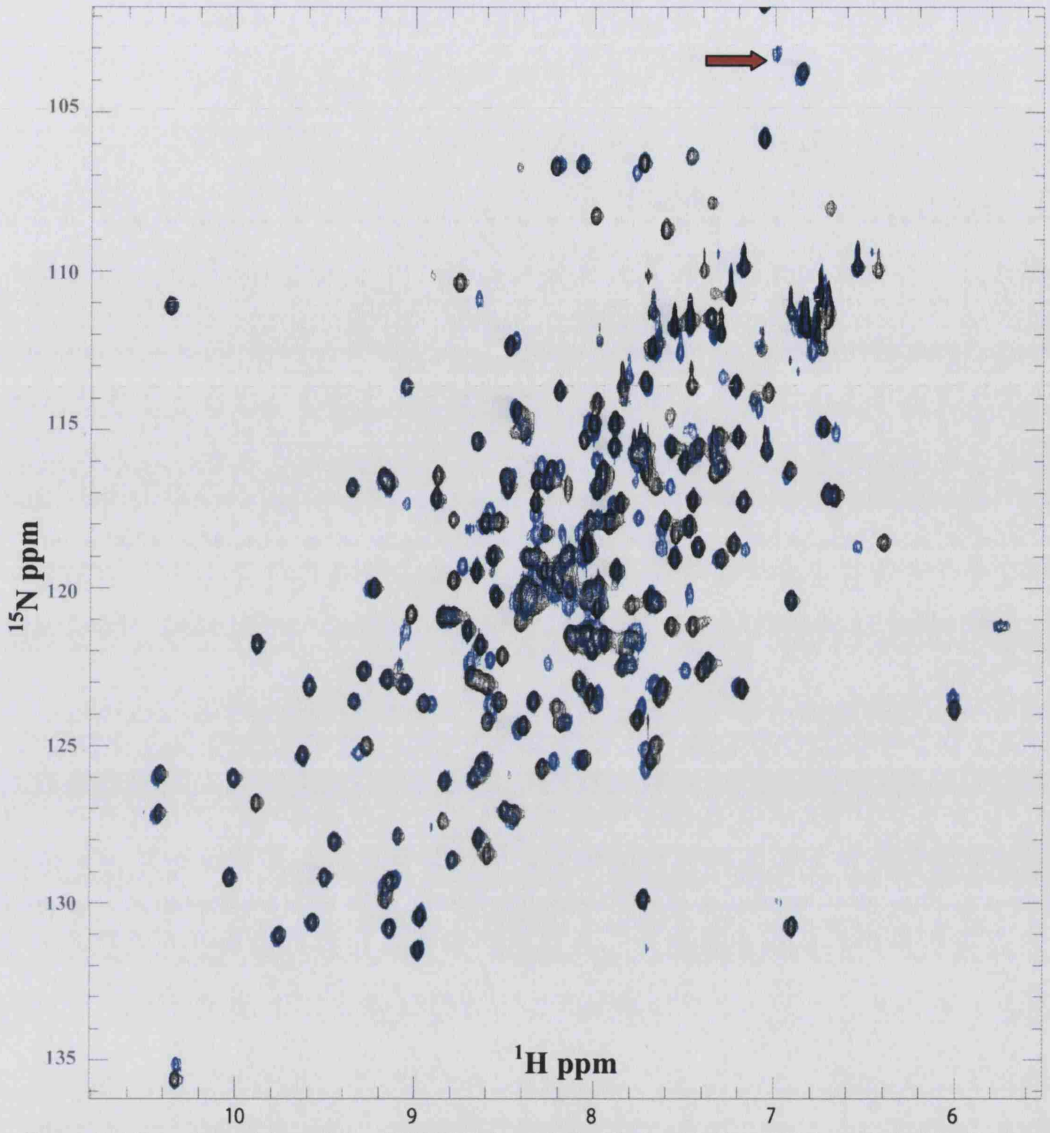

Figure 5.7 Superimposition of the AMP-PNP bound (in blue) with the ADP bound (in black) spectra. Gly-94 is highlighted by a red arrow.

The difference observed in HSQC chemical shift patterns recorded could also be due to the nucleotide contact with NH of the protein.

Since no intermediate peaks were observed for AMP-PNP and ADP bound spectra, and only two populations of bound and unbound were seen, it was concluded that the binding event of the protein and the ligand was in the slow exchange regime. That is, that the off rate for AMP-PNP is smaller than the difference in resonance frequency of the two states. This result complies with

previous observation for weak binding of the ATP as well as weak ATPase activity (Prodromou *et al.*, 2000); (Weikl *et al.*, 2000).

Comparison of the AMP-PNP bound spectra to that of ATP bound suggests that it could be a good model for studying the possible conformational change, as the binding of AMP-PNP shows a similar pattern to that of the initial point of the ATP time course titration shown in Figure 5.5. The Gly-94 residue highlighted in Figure 5.7 has the same chemical shift location as shown from earlier recorded time points. The difference between the ATP (black) and AMP-PNP bound (red) spectra are compared in Figure 5.8. An accurate comparison is difficult due to problems when acquiring an ATP bound spectrum of Hsp90 N-terminal domain, mostly due to its ATPase activity that results in presence of various conformations of apo- ATP/ADP observed in the same spectrum. There are about 20 chemical shift differences observed between the two spectra. This difference could be due to the residues in the apo- or ADP conformations in the ATP bound spectrum as highlighted using blue arrows in Figure 5.8. Some of the differences can be seen in Figure 5.9 when the ADP bound resonances (in red) are compared to the ATP bound resonance (in black.). About 30 different crosspeak differences were observed between the ATP and ADP bound spectra in the Figure 5.9.

5.6. The backbone assignment of the Hsp90 N-terminal domain bound to AMP-PNP

Due to the slow exchange and the large differences in chemical shifts for many residues in the nucleotide bound spectra, simply moving an assignment from an apo-spectra crosspeak to the closest AMP-PNP crosspeak was not sufficient

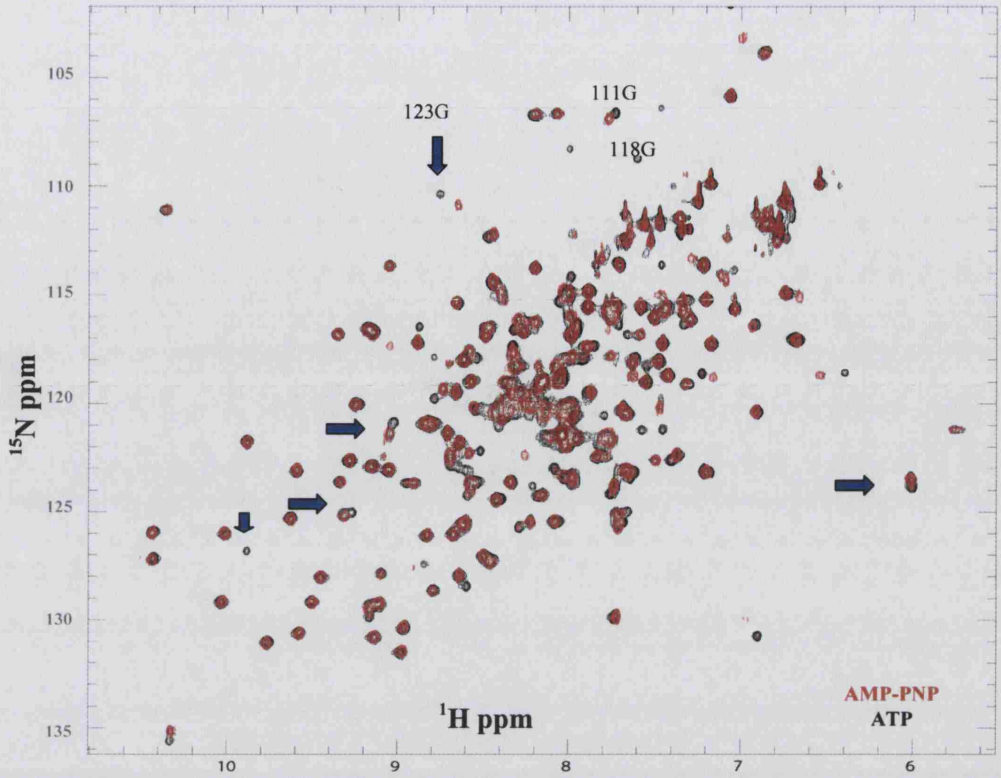

Figure 5.8. Comparison of the AMP-PNP bound (in red) to the ATP bound spectrum (in black) carried out on the N-terminal domain of Hsp90 at 25°C. There are differences between the two spectra, which could be due to presence of ADP as a result of ATPase activity of the protein.

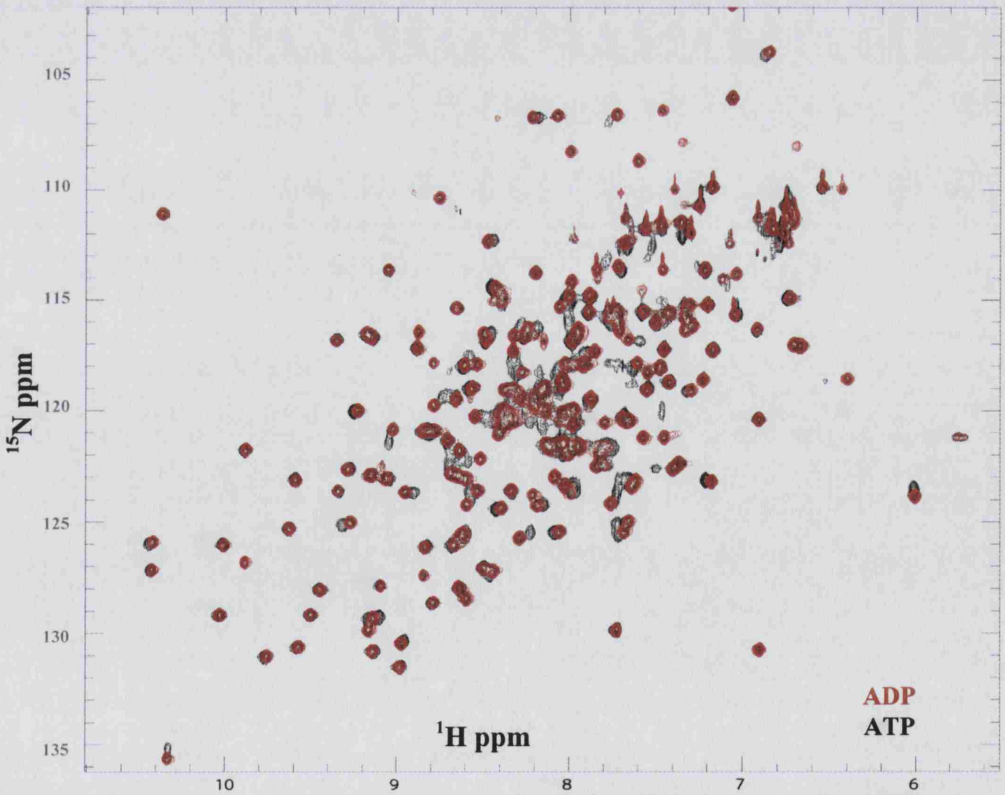

Figure 5.9. Comparison of the ADP bound spectrum (red) with the ATP bound spectrum (black). There are about 30 crosspeak differences between the two spectra, mainly due to conformation exchange and ATPase activity of the ATP bound spectrum.

especially in the crowded area of spectrum. Therefore, backbone assignment was carried out for the AMP-PNP bound protein, as mentioned previously for the apo-form. The same $^{2}H^{15}N^{13}C$ labelled sample of the Hsp90 N-terminal domain used in the apo- backbone assignment at pH 6.9 (pH changed due to added AMP-PNP) was used for recording the spectra. An aliquot of AMP-PNP in the same buffer as the sample was added until a final concentration of 5 mM for AMP-PNP and Mg^{2+} was reached. The spectra recorded for the backbone assignments of $^{1}H^{15}N$, ^{13}CO, $^{13}C\alpha$ and $^{13}C\beta$ resonances were from the following triple resonance experiments: HSQC, HNCO, HN(CA)CO, HNCA, HN(CO)CA, HNCACB and HN(CO)CACB. The resonance assignment was carried out by correlating intra- and inter-residue resonances of ^{13}CO, $^{13}C\alpha$ and $^{13}C\beta$ shifts, which were then assigned using the probabilistic method of Grzesiek and Bax (1993). The same experimental settings used for the apo- sample were used for the AMP-PNP bound sample. A $^{1}H^{15}N$ HSQC was used for displaying the assignment and was recorded from a $^{1}H^{15}N$ labelled protein on a Varian INOVA 800 MHz spectrometer. To assist the assignment, 3D ^{15}N HSQC-NOESY and 3D ^{15}N TOWNY-HSQC spectra were recorded using a Varian INOVA spectrometer with an 800 MHz proton frequency from ^{15}N-labelled and $^{2}H^{15}N^{13}C$ labelled samples in 20 mM Tris.

Due to the pH of the sample and presence of Mg^{2+}, protein precipitation occurred which was problematic during long hours of spectra recording and resulted in loss of sensitivity in the spectra. The 3D HNCA and 3D HNCO experiments have the strongest signal due to sensitivity of the experiment, even at a low protein concentration, as shown in Figures 5.10 and 5.15. In contrast the HN(CA)CB spectrum was the least sensitive experiment, hence the resonances

were weak with half as many crosspeaks, compared to the same experiment for the apo- sample as shown in Figure 5.11.

The 2D ^{15}N projection of the HNCA and HN(CA)CB are shown in Figures 5.12 and 5.13. These two spectra resemble the chemical shift pattern of an HSQC spectrum, although the side-chain resonances of glutamine and asparagine, usually observed at the top right-hand side of the spectrum as a doublet, were not observed. The ^{15}N,NH projections were used for aligning the spectra in the ^{15}N dimension frequency, as well as during the assignment, to correlate a resonance to its preceding sequentially connected residues which were located in the same plane. During the assignment most of the crosspeaks in the HNCA and HN(CO)CA experiment were assigned, while not as many HN(CA)CB and HN(CO)CACB crosspeaks were observed.

The 3D HNCO experiment was the most sensitive and together with the HN(CA)CO data were used to assign the ^{13}CO nuclei. Figure 5.14 shows the 2D ($^{13}CO_{(i),(i-1)}$,NH) projection of the 3D HNCO experiment and Figure 5.15 its 2D (^{15}N,NH) projection. The 2D ($^{13}CO_{(i-1)}$,NH) projection of the 3D HN(CA)CO is shown in Figure 5.16. This experiment is not as sensitive as the 3D HNCO experiment and not as many resonances as expected were observed. The 3D HN(CO)CA experiment 2D projection in (^{15}N,NH) is shown in Figure 5.17.

In collecting all the above spectra for backbone assignment, a total of 182 amide resonances of the $^{1}H^{15}N$ HSQC spectrum were assigned out of the 207 residues, excluding 5 prolines that constitutes 88% of the sequence. Also 32 side-chain crosspeaks belonging to glutamine and asparagine were observed and connected as 16 doublets. Seven arginine side-chain crosspeaks were also recognised in the $^{1}H^{15}N$ HSQC spectra, highlighted as Hε, in Figure 5.18. (All the

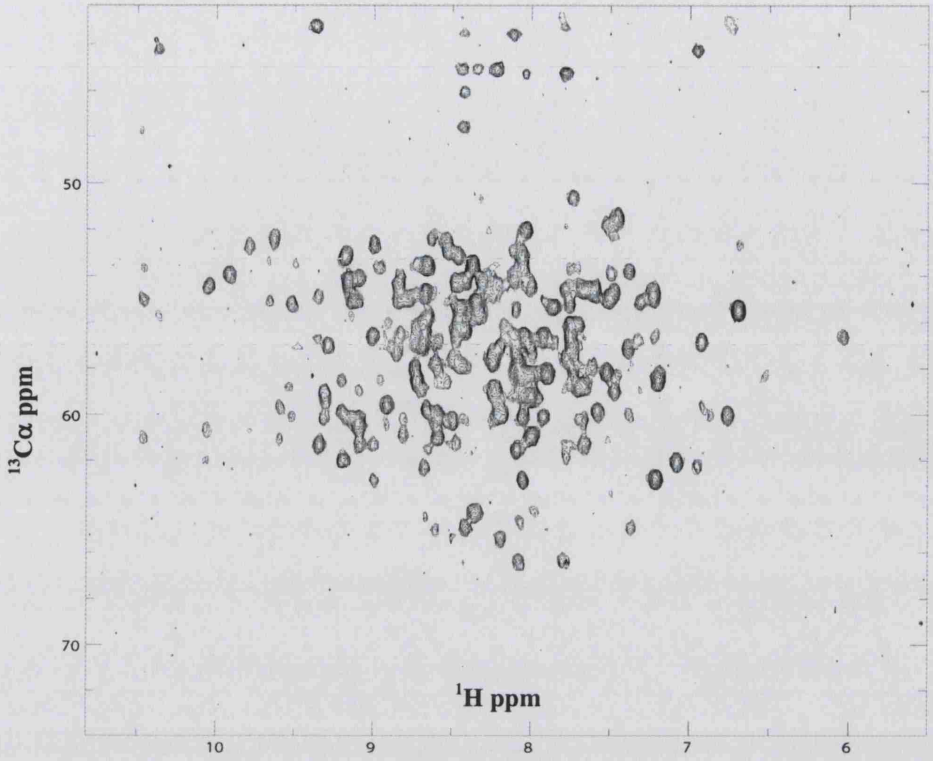

Figure 5.10 The 2D (^{13}Cα,NH) projections from 3D HNCA spectra for a deuterated sample. The projection does not include the entire 2D layers for simplicity.

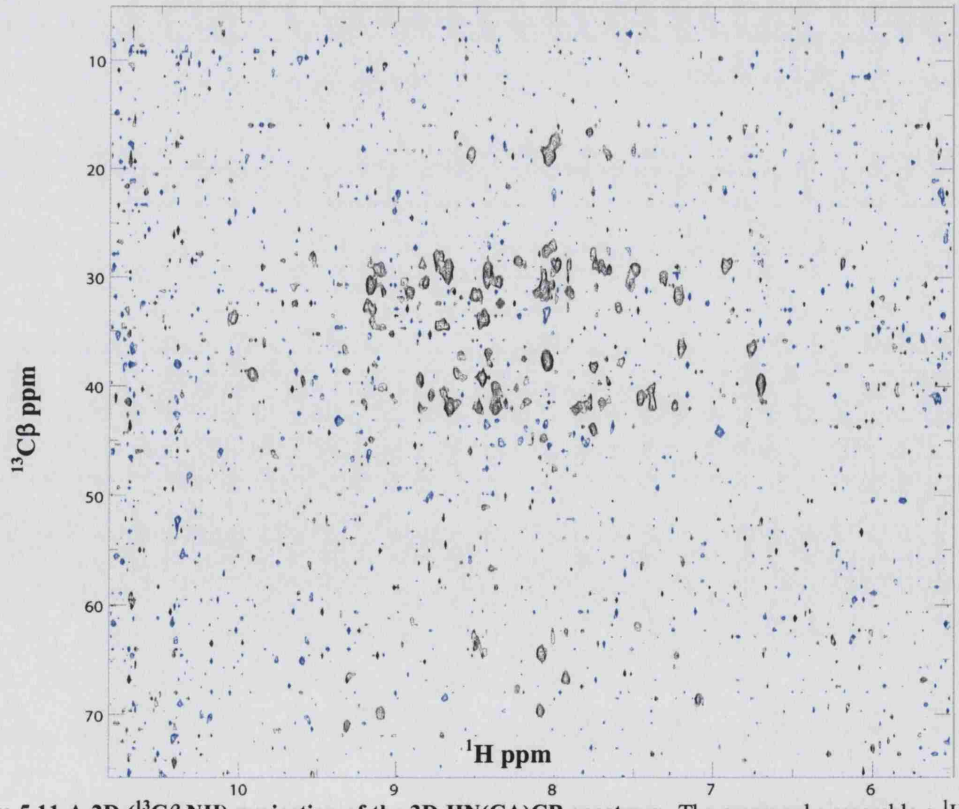

Figure 5.11 A 2D (^{13}Cβ,NH) projection of the 3D HN(CA)CB spectrum. The crosspeaks resemble a ^{1}H^{15}N HSQC experiment without any resonances for the side-chains.

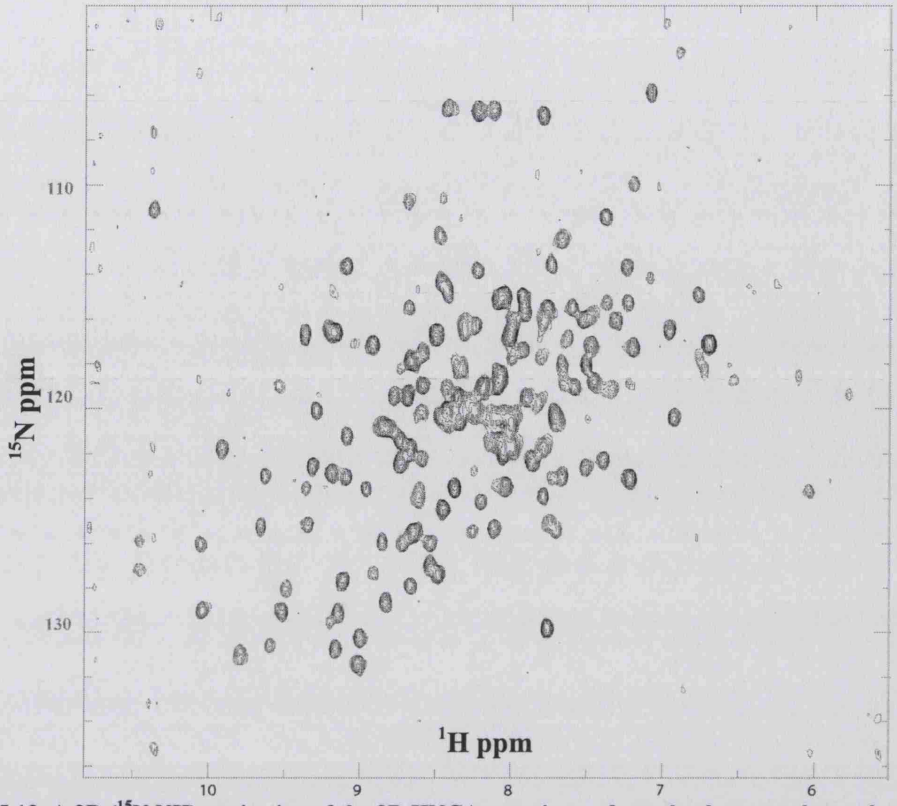

Figure 5.12. A 2D (^{15}N,NH) projection of the 3D HNCA experiment from the deuterated samples. The 2D projections have similar chemical shifts dispersion as the ^{15}N ^{1}H HSQC.

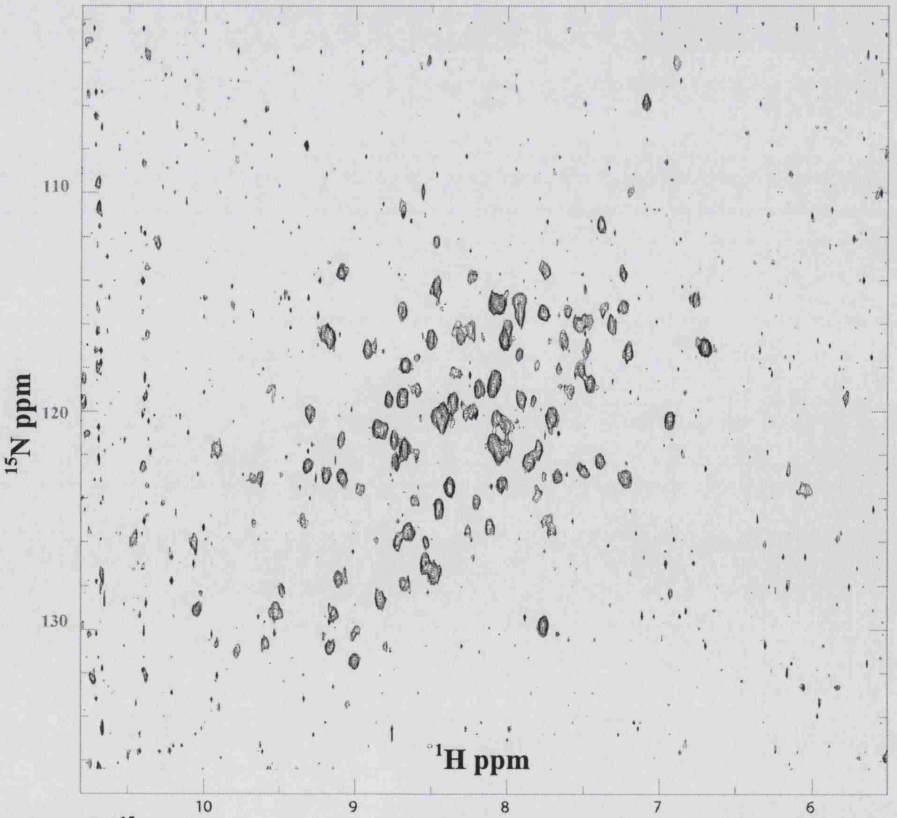

Figure 5.13. A 2D (^{15}N,NH) projection of the 3D HN(CA)CB spectrum. The crosspeaks resemble a ^{1}H^{15}N HSQC experiment without any resonances for the side-chains.

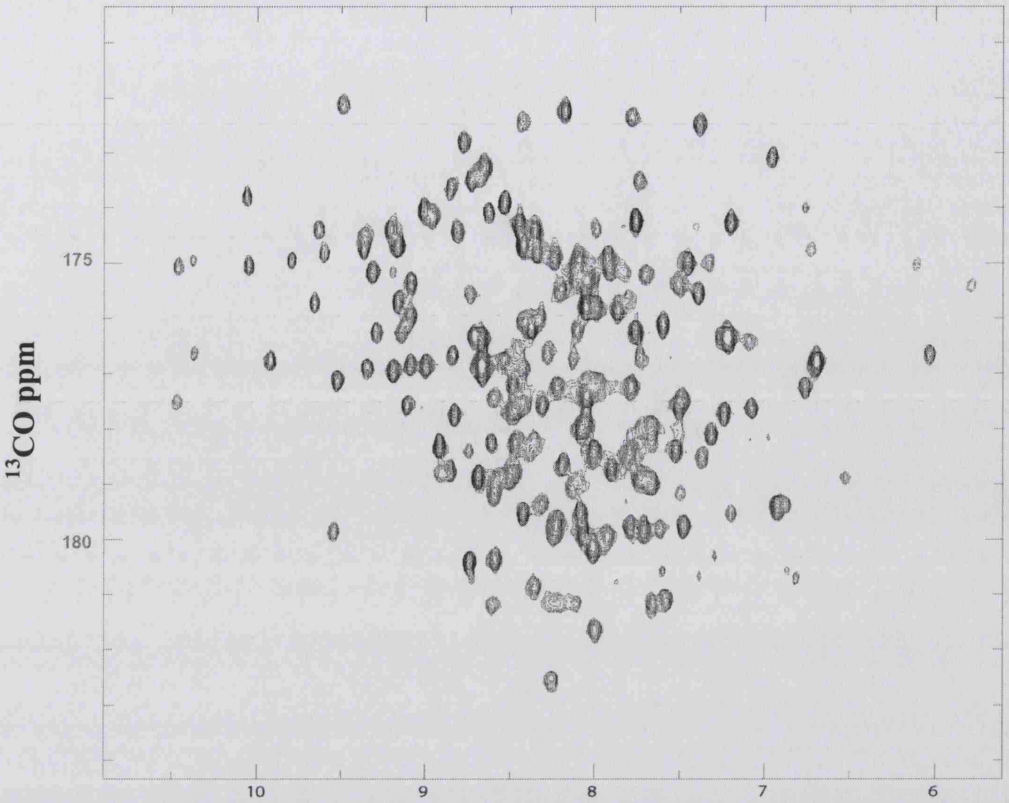

Figure 5.14 A 2D ($^{13}CO_{(i-1)}$,NH) projection of the 3D HNCO spectrum from an AMP-PNP bound sample. The crosspeaks are observed between 170 to 185 ppm.

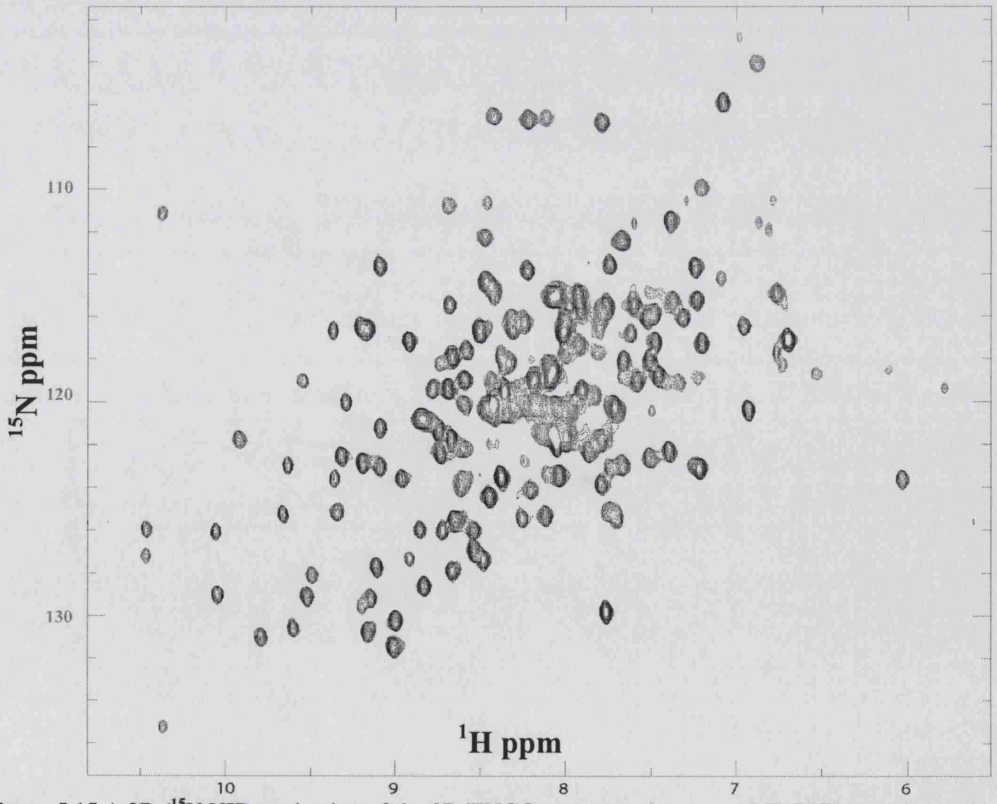

Figure 5.15 A 2D (^{15}N,NH) projection of the 3D HNCO spectrum from an AMP-PNP bound sample. The crosspeaks resemble an HSQC experiment.

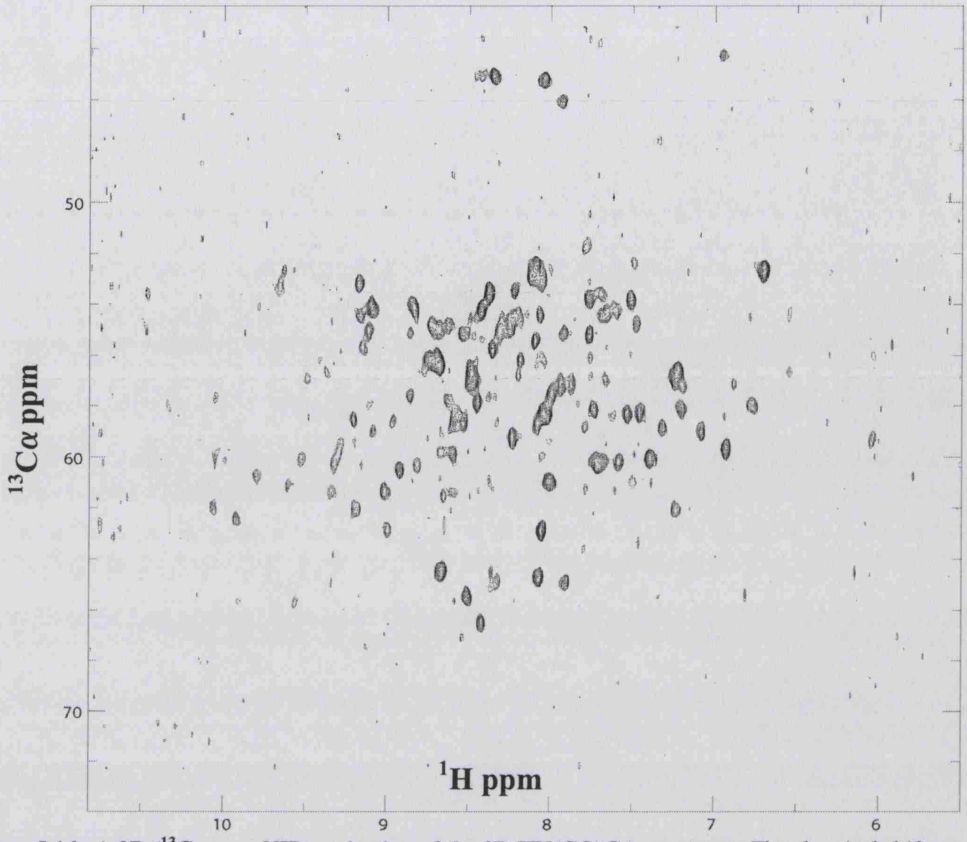

Figure 5.16. A 2D ($^{13}C\alpha_{(i),(i-1)}$,NH) projection of the 3D HN(CO)CA spectrum. The chemical shifts at about 45 ppm belong to the glycine residues.

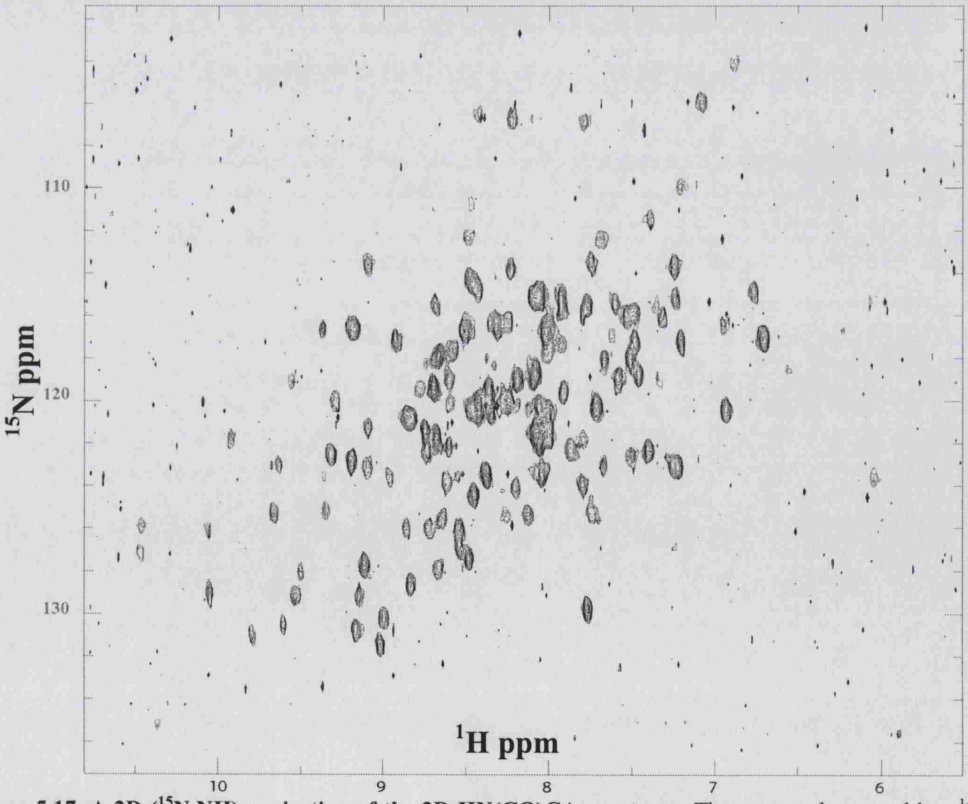

Figure 5.17. A 2D (^{15}N,NH) projection of the 3D HN(CO)CA spectrum. The crosspeaks resemble a $^{1}H^{15}N$ HSQC experiment without any resonances for the side-chains.

side-chains chemical shifts are based on the 800 MHz proton frequency spectrum.)

Figure 5.18 shows the backbone assignment of the Hsp90 N-terminal domain displayed using a $^{1}H^{15}N$ HSQC spectrum recorded on an 800 MHz proton frequency spectrometer. There are several differences between the 500 MHz proton frequency spectrum and that of the 800 MHz spectrum used here to display the assignment. Several crosspeaks were not present in the 800 MHz spectra possibly due to the existing problem with the water-gate suppression (according to the NMR manager) only used in recording the 800 MHz spectra. As a result, many crosspeaks that are in exchange with solvent were not present in the spectrum. Two of these resonances (represented with red crosses in Figure 5.18) belong to residues Gly-170 and Asn-92 that were assigned using the 500 MHz proton frequency spectra but were absent in the 800 MHz spectrum. A comparison of the 500 MHz proton frequency spectrum with that of 800 MHz spectrum, both recorded using the same triple labelled sample is shown in Figure 5.19. Some of these absent crosspeaks are highlighted using blue arrows. Other crosspeaks that were not assigned, either had no resonance in other spectra recorded for backbone assignment, or belonged to a side-chain. Some of the crosspeaks in the 800 MHz spectrum were quite broad and had very weak signals indicating possible conformational exchange for these residues (highlighted by black arrows in Figure 5.19).

Comparison of the apo- and ADP bound spectra to that of the AMP-PNP bound spectrum confirmed this idea. Some weak crosspeaks in the AMP-PNP bound spectrum could be observed as strong signals in the apo- form, suggesting presence of an apo- conformation population in the AMP-PNP complex. An example is seen in residue Thr-157 (highlighted using a yellow arrow),

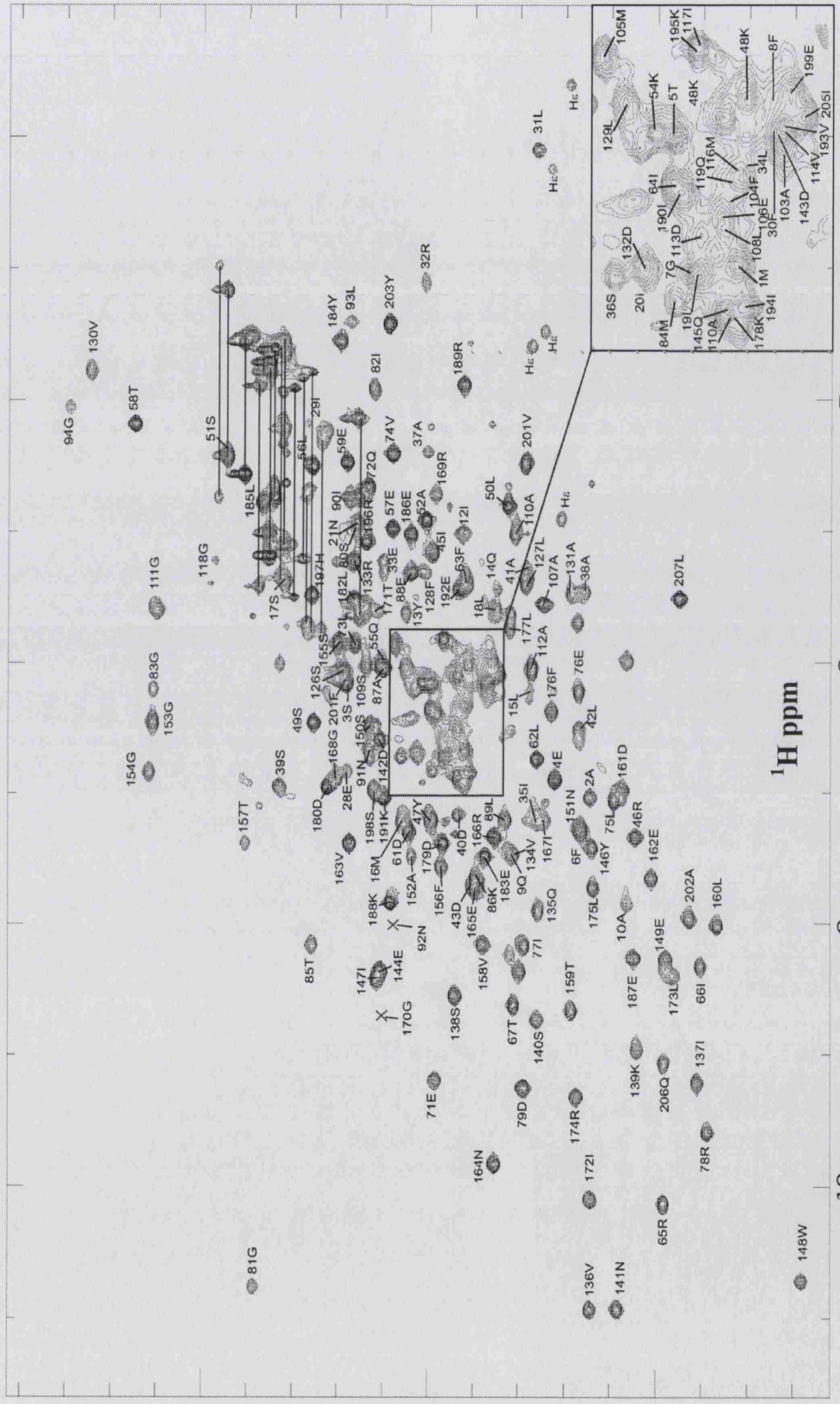

Figure 5.18. The sequential backbone assignment of the AMP-PNP bound Hsp90 N-terminal domain displayed using an 800 MHz proton frequency spectrum.

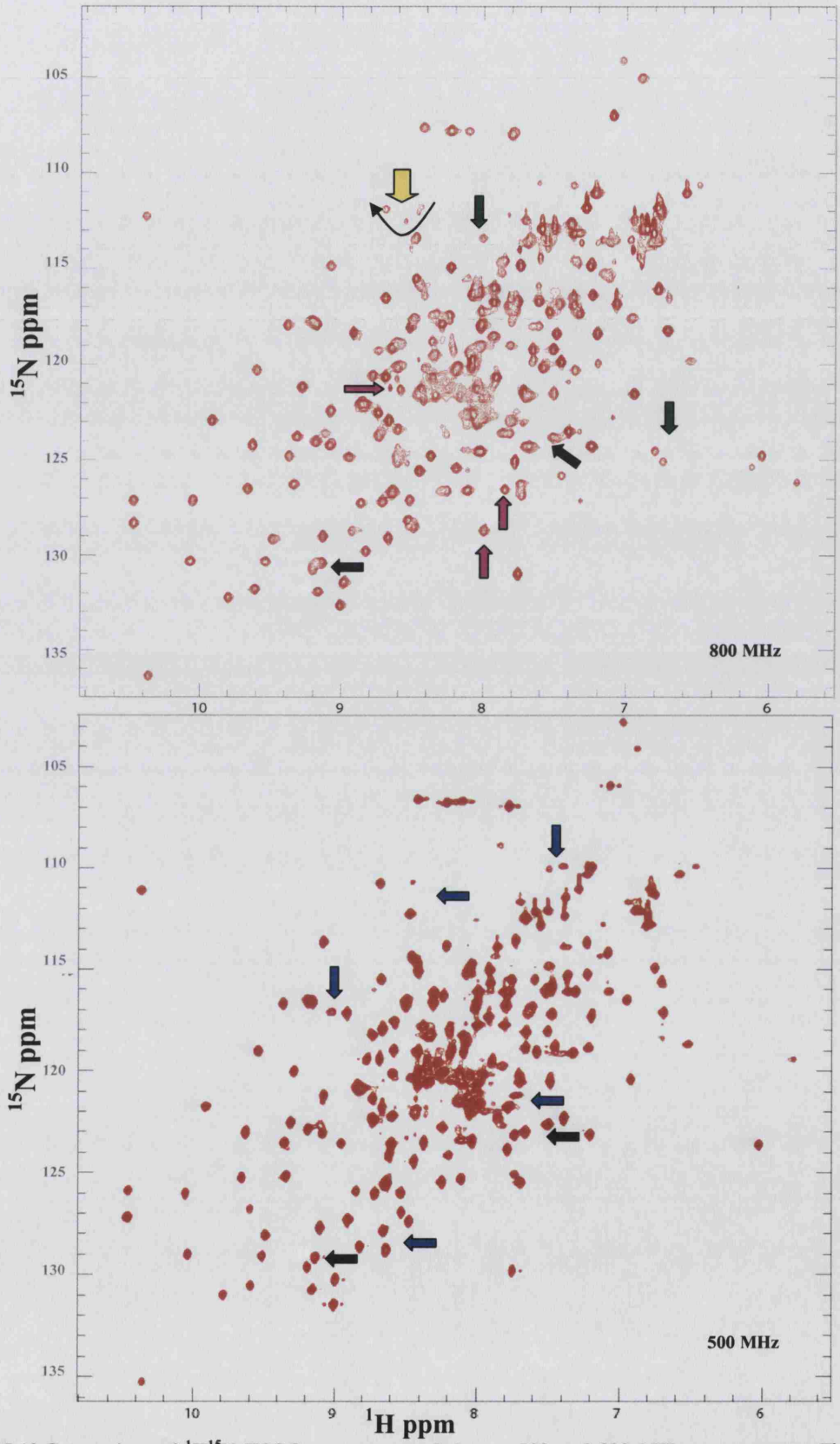

Figure 5.19.Comparison of $^{1}H^{15}N$ HSQC spectra recorded on a 500 and 800 MHz spectrometer. The same sample from the Hsp90 N-terminal domain with AMP-PNP was used. The arrows highlight the differences observed between the two spectra (refer to the text for details).

where its apo- and ADP bound resonance is shown as a weak signal close to the crosspeak for the AMP-PNP bound resonance in the spectrum. There are also crosspeaks present in the 800 MHz spectrum that have no equivalent in the 500 MHz spectrum (Figure 5.19). Some of these resonances belong to the arginine sidechain that are highlighted using dark green arrows. There were a number of crosspeaks (highlighted by pink arrows), especially at the centre of the spectrum, that had broad and weak signals, for which assignment was not possible using the 3D scalar coupling experiments (e.g. HNCA, HN(CO)CA). Also the 3D NOESY-HSQC and 3D TOWNY-HSQC experiments recorded using the 800 MHz spectrometer produced no signal for these residues (possibly due to strong water suppression used in the pulse sequence of the 800 MHz based experiments. Comparison of Figure 5.6 (in blue) which is an AMP-PNP bound spectrum recorded at 600 MHz using a ^{15}N-labelled sample, with that of Figure 5.19 shows less crosspeaks present than the 500 MHz spectrum, but more resonances than the 800 MHz. This suggests that a higher magnetic field, in this case does not produce a better spectrum, nor does it increase the resolution of the spectra for the protein and in fact less crosspeaks can be seen at higher magnetic fields. These unexpected problems and lack of ^{13}Cβ signals for several residues, made the assignment of the AMP-PNP bound spectra less successful than the apo- assignments since using a higher magnetic field was not advantageous. Also all the 3D ^{15}N HSQC-NOESY and ^{15}N HSQC –TOWNY spectra recorded on a 800 MHz machine could not assist with the assignment since the same field sensitive residues were missing.

Table 5.1 shows the amide residues that have been assigned in the ^{1}H^{15}N HSQC spectrum in green, non-assigned residues in yellow and prolines, which have no resonance in the HSQC spectrum, in pink. The first set of unassigned

residues (dotted) is from the construct, including the six histidines, from the his-tag bound to the N-terminal of the protein. The unassigned residues from Hsp90 N-terminal domain were Glu-11, Thr-22, Val-23, Tyr-24, Ser-25, Asn-26, Thr-95, Ile-96, Ala-97, Lys-98, Ser-99, Gly-100, Thr-101, Val-114, Ser-115, Phe-120, Gly-121, Val-122, Gly-123, Phe-124, Tyr-125.

MRGSHHHHHH	GMASETFEFQ	AEITQLMSLI	INTVYSNKEI	FLRELISNAS
DALDKIRYKS	LSDPKQLETE	PDLF IRITPK	PEQKVLEIRD	SGIGMTKAEL
INNLGTIAKS	GTKAFMEALS	AGADVSMIGQ	FGVGFYSLFL	VADRVQVISK
SNDDEQYIWE	SNAGGSFTVT	LDEVNERIGR	GTILRLFLKD	DQLEYLEEKR
IKEVIKRHSE	FVAYPIQL	**HN nuclei**		

Table 5.1. The Hsp90 N-terminal AMP-PNP bound residues assigned in the $^{1}H^{15}N$ HSQC spectrum. The dotted area at the beginning of the sequence is where the six-histidine residues from the construct are located. Pink highlights prolines that don't have any chemical shifts in the spectrum. The yellow residues are not assigned.

Other nuclei such as $^{13}C\alpha$, $^{13}C\beta$ and ^{13}CO that were assigned to their residues for the AMP-PNP bound Hsp90 N-terminal protein are shown in Table 5.2. Table 5.2 (a) shows the unassigned $^{13}C\alpha$ nuclei (in yellow) and assigned resonances (in green). Overall 180 residues out of 207 (86.96%) from $^{13}C\alpha$ atoms were assigned. Table 5.2 (b) shows the $^{13}C\beta$ nuclei assigned (in green) and the unassigned residues (in purple). The glycines (in red) have no $^{13}C\beta$ resonance and overall 177 $^{13}C\beta$ atoms were assigned (85.5%) including 11 glycines. Finally the ^{13}CO assignments are shown in Table 5.2 (c) where 179 ^{13}CO atoms (86.5%) were assigned. The unassigned residues are highlighted in blue. Some additional unassigned residues compared to the apo- assignments are; Met-16, Asn-91, Phe- and 104. Table 5.3 shows the amide resonance assignments from a $^{1}H^{15}N$ HSQC

experiment for H and HN nuclei. The $^{13}C\alpha$, $^{13}C\beta$ and ^{13}CO nuclei, assigned to the 207 residues are displayed in Tables 5.4, 5.5 and 5.6 that follow.

MRGSHHHHHH	GMASETFEFQ	AEITQLMSLI	INTVYSNKEI	FLRELISNAS
DALDKIRYKS	LSDPKQLETE	PDLF IRITPK	PEQKVLEIRD	SGIGMTKAEL
INNLGTIAKS	GTKAFMEALS	AGADVSMIGQ	FGVGFYSLFL	VADRVQVISK
SNDDEQYIWE	SNAGGSFTVT	LDEVNERIGR	GTILRLFLKD	DQLEYLEEKR
IKEVIKRHSE	FVAYPIQL	**a) $^{13}C\alpha$ nuclei**		

MRGSHHHHHH	GMASETFEFQ	AEITQLMSLI	INTVYSNKEI	FLRELISNAS
DALDKIRYKS	LSDPKQLETE	PDLF IRITPK	PEQKVLEIRD	SGIGMTKAEL
INNLGTIAKS	GTKAFMEALS	AGADVSMIGQ	FGVGFYSLFL	VADRVQVISK
SNDDEQYIWE	SNAGGSFTVT	LDEVNERIGR	GTILRLFLKD	DQLEYLEEKR
IKEVIKRHSE	FVAYPIQL	**b) $^{13}C\beta$ nuclei**		

MRGSHHHHHH	GMASETFEFQ	AEITQLMSLI	INTVYSNKEI	FLRELISNAS
DALDKIRYKS	LSDPKQLETE	PDLF IRITPK	PEQKVLEIRD	SGIGMTKAEL
INNLGTIAKS	GTKAFMEALS	AGADVSMIGQ	FGVGFYSLFL	VADRVQVISK
SNDDEQYIWE	SNAGGSFTVT	LDEVNERIGR	GTILRLFLKD	DQLEYLEEKR
IKEVIKRHSE	FVAYPIQL	**c) ^{13}CO nuclei**		

Table 5.2 Residues assigned for the (a) $^{13}C\alpha$ nuclei (b) $^{13}C\beta$ nuclei and (c) ^{13}CO nuclei in the Hsp90 N-terminal domain with bound AMP-PNP. The yellow residues (in a) purple residues (in b) and blue residues (in c) were not assigned due to lack of resonance. Prolines are in pink and glycines are highlighted in red. The residues MRGSHHHHHH are part of the construct with six histidines and generally no correlation were observed for them. Glycine residues have no $^{13}C\beta$ correlation.

No.	Res.	Nuc.	CS	No.	Res	Nuc.	CS	No.	Res.	Nuc.	CS	No.	Res.	Nuc.	CS
0	Gly	N	110.71	35	Ile	N	123.53	66	Ile	N	130.73	104	Phe	N	120.39
	Gly	HN	8.46		Ile	HN	8.61		Ile	HN	9.17		Phe	HN	8.20
1	Met	N	120.53	36	Ser	N	117.77	67	Thr	N	122.53	105	Met	N	117.73
	Met	HN	8.34		Ser	HN	8.38		Thr	HN	9.32		Met	HN	8.00
2	Ala	N	126.01	37	Asn	N	118.86	69	Lys	N	122.87	106	Glu	N	120.00
	Ala	HN	8.54		Asn	HN	7.22		Lys	HN	9.20		Glu	HN	8.23
3	Ser	N	115.10	38	Ala	N	125.47	71	Glu	N	119.03	107	Ala	N	123.86
	Ser	HN	8.08		Ala	HN	7.70		Glu	HN	9.55		Ala	HN	7.79
4	Glu	N	124.44	39	Ser	N	112.27	72	Gln	N	116.08	108	Leu	N	120.11
	Glu	HN	8.45		Ser	HN	8.48		Gln	HN	7.32		Leu	HN	8.25
5	Thr	N	118.94	40	Asp	N	120.12	73	Lys	N	115.67	109	Ser	N	116.09
	Thr	HN	8.10		Asp	HN	8.60		Lys	HN	7.91		Ser	HN	8.00
6	Phe	N	125.58	41	Ala	N	122.95	74	Val	N	117.29	110	Ala	N	122.62
	Phe	HN	8.65		Ala	HN	7.66		Val	HN	7.20		Ala	HN	7.51
7	Glu	N	119.46	42	Leu	N	125.45	75	Leu	N	126.95	111	Gly	N	106.94
	Glu	HN	8.36		Leu	HN	8.25		Leu	HN	8.54		Gly	HN	7.79
8	Phe	N	121.09	43	Asp	N	120.78	76	Glu	N	125.29	112	Ala	N	123.43
	Phe	HN	8.01		Asp	HN	8.86		Glu	HN	8.11		Ala	HN	8.03
9	Gln	N	122.35	44	Lys	N	117.33	77	Ile	N	123.03	113	Asp	N	119.59
	Gln	HN	8.75		Lys	HN	7.92		Ile	HN	9.09		Asp	HN	8.28
10	Ala	N	127.29	45	Ile	N	119.05	78	Arg	N	130.99	116	Met	N	120.22
	Ala	HN	8.91		Ile	HN	7.59		Arg	HN	9.79		Met	HN	8.12
12	Ile	N	120.53	46	Arg	N	127.85	79	Asp	N	123.00	117	Ile	N	119.70
	Ile	HN	7.49		Arg	HN	8.67		Asp	HN	9.64		Ile	HN	7.85
13	Thr	N	117.70	47	Tyr	N	118.95	80	Ser	N	115.87	118	Gly	N	108.87
	Thr	HN	7.81		Tyr	HN	8.59		Ser	HN	7.48		Gly	HN	7.85
14	Gln	N	121.20	48	Lys	N	120.60	81	Gly	N	111.10	119	Gln	N	120.57
	Gln	HN	7.74		Lys	HN	8.00		Gly	HN	10.38		Gln	HN	8.10
15	Leu	N	123.42	49	Ser	N	113.82	82	Ile	N	116.49	126	Ser	N	114.78
	Leu	HN	8.12		Ser	HN	8.22		Ile	HN	6.96		Ser	HN	8.04
16	Met	N	117.54	50	Leu	N	122.29	83	Gly	N	106.69	127	Leu	N	123.15
	Met	HN	8.59		Leu	HN	7.39		Gly	HN	8.12		Leu	HN	7.74
17	Ser	N	112.47	51	Ser	N	109.94	84	Met	N	119.07	128	Phe	N	118.84
	Ser	HN	7.67		Ser	HN	7.20		Met	HN	8.43		Phe	HN	7.66
18	Leu	N	121.76	52	Asp	N	118.77	85	Thr	N	113.65	129	Leu	N	118.25
	Leu	HN	7.79		Asp	HN	7.46		Thr	HN	9.09		Leu	HN	8.11
19	Ile	N	119.83	54	Lys	N	118.53	86	Lys	N	120.84	130	Val	N	104.08
	Ile	HN	8.36		Lys	HN	8.07		Lys	HN	8.81		Val	HN	6.89
20	Ile	N	118.28	55	Gln	N	116.88	87	Ala	N	116.62	131	Ala	N	125.06
	Ile	HN	8.35		Gln	HN	8.01		Ala	HN	8.01		Ala	HN	7.74
21	Asn	N	114.81	56	Leu	N	113.66	88	Glu	N	118.08	132	Asp	N	118.15
	Asn	HN	7.51		Leu	HN	7.24		Glu	HN	7.66		Asp	HN	8.33
27	Lys	N	117.93	57	Glu	N	117.18	89	Leu	N	122.17	133	Arg	N	115.47
	Lys	HN	8.20		Glu	HN	7.48		Leu	HN	8.60		Arg	HN	7.60
28	Glu	N	115.05	58	Thr	N	105.89	90	Ile	N	115.27	134	Val	N	122.37
	Glu	HN	8.42		Thr	HN	7.08		Ile	HN	7.37		Val	HN	8.74
29	Ile	N	114.15	59	Glu	N	115.24	91	Asn	N	116.10	135	Gln	N	123.57
	Ile	HN	7.09		Glu	HN	7.23		Asn	HN	8.31		Gln	HN	8.96
30	Phe	N	121.23	61	Asp	N	117.91	92	Asn	N	117.09	136	Val	N	125.87
	Phe	HN	8.06		Asp	HN	8.67		Asn	HN	9.03		Val	HN	10.47
31	Leu	N	123.61	62	Leu	N	123.51	93	Leu	N	115.59	137	Ile	N	130.53
	Leu	HN	6.03		Leu	HN	8.38		Leu	HN	6.72		Ile	HN	9.60
32	Arg	N	118.67	63	Phe	N	120.51	94	Gly	N	102.77	138	Ser	N	120.02
	Arg	HN	6.53		Phe	HN	7.71		Gly	HN	6.99		Ser	HN	9.29
33	Glu	N	116.80	64	Ile	N	118.92	102	Lys	N	122.12	139	Lys	N	128.04
	Glu	HN	7.62		Ile	HN	8.18		Lys	HN	8.45		Lys	HN	9.49
34	Leu	N	120.73	65	Arg	N	129.00	103	Ala	N	121.49	140	Ser	N	123.51
	Leu	HN	8.10		Arg	HN	10.04		Ala	HN	8.14		Ser	HN	9.36

No.	Res.	Nuc.	CS	No.	Res	Nuc.	CS	No.	Res.	Nuc.	CS	No.	Res.	Nuc.	CS
141	Asn	N	127.16	158	Val	N	121.22	176	Phe	N	124.13	193	Val	N	121.57
	Asn	HN	10.47		Val	HN	9.09		Phe	HN	8.20		Val	HN	8.08
142	Asp	N	116.63	159	Thr	N	125.17	177	Leu	N	122.30	194	Ile	N	120.67
	Asp	HN	8.31		Thr	HN	9.35		Leu	HN	7.86		Ile	HN	8.42
143	Asp	N	121.49	160	Leu	N	131.44	178	Lys	N	120.34	195	Lys	N	119.46
	Asp	HN	8.07		Leu	HN	9.01		Lys	HN	8.47		Lys	HN	7.90
144	Glu	N	116.61	161	Asp	N	127.37	179	Asp	N	119.40	196	Arg	N	116.03
	Glu	HN	9.17		Asp	HN	8.48		Asp	HN	8.69		Arg	HN	7.52
145	Gln	N	120.08	162	Glu	N	128.59	180	Asp	N	114.33	197	His	N	113.53
	Gln	HN	8.42		Glu	HN	8.83		Asp	HN	8.47		His	HN	7.74
146	Tyr	N	125.98	163	Val	N	115.46	181	Gln	N	120.23	198	Ser	N	116.47
	Tyr	HN	8.72		Val	HN	8.68		Gln	HN	8.06		Ser	HN	8.50
147	Ile	N	116.49	164	Asn	N	121.76	182	Leu	N	115.53	199	Glu	N	121.61
	Ile	HN	9.21		Asn	HN	9.92		Leu	HN	7.76		Glu	HN	7.99
148	Trp	N	135.24	165	Glu	N	120.76	183	Glu	N	121.37	200	Phe	N	115.00
	Trp	HN	10.37		Glu	HN	8.84		Glu	HN	8.74		Phe	HN	8.05
149	Glu	N	129.14	166	Arg	N	121.76	184	Tyr	N	114.91	201	Val	N	123.10
	Glu	HN	9.15		Arg	HN	8.67		Tyr	HN	6.76		Val	HN	7.21
150	Ser	N	116.28	167	Ile	N	124.04	185	Leu	N	111.42	202	Ala	N	130.22
	Ser	HN	8.24		Ile	HN	8.62		Leu	HN	7.39		Ala	HN	9.01
151	Asn	N	125.50	168	Gly	N	114.64	186	Glu	N	118.04	203	Tyr	N	117.09
	Asn	HN	8.63		Gly	HN	8.43		Glu	HN	7.51		Tyr	HN	6.70
152	Ala	N	118.24	169	Arg	N	119.10	187	Glu	N	127.70	205	Ile	N	121.99
	Ala	HN	8.74		Arg	HN	7.33		Glu	HN	9.11		Ile	HN	8.06
153	Gly	N	106.74	170	Gly	N	116.68	188	Lys	N	117.17	206	Gln	N	129.06
	Gly	HN	8.22		Gly	HN	9.37		Lys	HN	8.92		Gln	HN	9.52
154	Gly	N	106.58	171	Thr	N	116.11	189	Arg	N	120.41	207	Leu	N	129.78
	Gly	HN	8.43		Thr	HN	7.79		Arg	HN	6.93		Leu	HN	7.76
155	Ser	N	114.99	172	Ile	N	126.00	190	Ile	N	119.16				
	Ser	HN	7.93		Ile	HN	10.06		Ile	HN	8.20				
156	Phe	N	119.40	173	Leu	N	129.64	191	Lys	N	116.76				
	Phe	HN	8.78		Leu	HN	9.20		Lys	HN	8.51				
157	Thr	N	110.75	174	Arg	N	125.26	192	Glu	N	120.20				
	Thr	HN	8.69		Arg	HN	9.66		Glu	HN	7.71				

Table 5.3 Chemical shifts derived from the $^{1}H^{15}N$ HSQC experiment of the AMP-PNP bound Hsp90 N-terminal domain. The (No) indicates the residue number with its three-letter abbreviated for the amino acid (Res) and the amide H and HN chemical shift for each residue. Totally 186 amides were assigned out of 207 residues including 5 prolines, which resulted in 89.85% of the amides assigned. The CS abbreviation stands for chemical shifts.

No	Res	Cα	No	Res	Cα	No	Res	Cα	No	Res	Cα
0	Gly	44.98	12	Ile	63.56	28	Glu	57.84	39	Ser	61.41
1	Met	55.22	13	Thr	66.42	29	Ile	62.13	40	Asp	56.89
2	Ala	52.50	14	Gln	58.56	30	Phe	59.27	41	Ala	54.74
3	Ser	57.84	15	Leu	58.32	31	Leu	56.65	42	Leu	57.61
4	Glu	55.46	16	Met	60.22	32	Arg	58.32	43	Asp	57.13
5	Thr	61.42	17	Ser	61.42	33	Glu	57.84	44	Lys	60.22
6	Phe	55.70	18	Leu	57.60	34	Leu	57.60	45	Ile	59.82
7	Glu	55.22	19	Ile	64.27	35	Ile	64.99	46	Arg	59.75
8	Phe	59.27	20	Ile	64.21	36	Ser	61.65	47	Tyr	60.94
9	Gln	56.89	21	Asn	54.03	37	Asn	54.40	48	Lys	59.27
10	Ala	55.94	27	Lys	58.80	38	Ala	54.51	49	Ser	59.99

No	Res	Cα	No	Res	Cα	No	Res	Cα	No	Res	Cα
50	Leu	57.13	90	Ile	64.99	140	Ser	54.98	175	Leu	54.39
51	Ser	58.32	91	Asn	55.70	141	Asn	55.03	176	Phe	56.89
52	Asp	51.41	92	Asn	54.98	142	Asp	54.51	177	Leu	55.22
54	Lys	58.32	93	Leu	54.03	143	Asp	53.02	178	Lys	56.17
55	Gln	56.89	94	Gly	47.12	144	Glu	54.27	179	Asp	57.13
56	Leu	54.74	102	Lys	59.27	145	Gln	56.17	180	Asp	53.08
57	Glu	59.03	103	Ala	54.51	146	Tyr	58.56	181	Gln	53.79
58	Thr	62.13	104	Phe	59.28	147	Ile	59.75	182	Leu	56.17
59	Glu	54.98	105	Met	59.27	148	Trp	55.70	183	Glu	58.08
61	Asp	53.58	106	Glu	58.79	149	Glu	54.98	184	Tyr	59.99
62	Leu	53.55	107	Ala	54.51	150	Ser	57.84	185	Leu	53.79
63	Phe	56.17	108	Leu	57.36	151	Asn	52.36	186	Glu	54.98
64	Ile	59.99	109	Ser	60.94	152	Ala	53.55	187	Glu	60.46
65	Arg	54.51	110	Ala	51.89	153	Gly	44.98	188	Lys	59.51
66	Ile	60.22	111	Gly	45.22	154	Gly	46.17	189	Arg	56.89
67	Thr	59.03	112	Ala	52.12	155	Ser	56.64	190	Ile	65.46
71	Glu	58.80	113	Asp	54.03	156	Phe	54.98	191	Lys	60.22
72	Gln	55.22	116	Met	56.29	157	Thr	59.03	192	Glu	58.80
73	Lys	58.08	117	Ile	64.92	158	Val	61.42	193	Val	66.42
74	Val	58.56	118	Gly	46.10	159	Thr	61.18	194	Ile	64.99
75	Leu	52.84	119	Gln	56.65	160	Leu	56.65	195	Lys	58.32
76	Glu	54.03	126	Ser	61.41	161	Asp	54.27	196	Arg	58.08
77	Ile	60.70	127	Leu	57.89	162	Glu	54.98	197	His	57.13
78	Arg	52.60	128	Phe	60.46	163	Val	62.37	198	Ser	57.60
79	Asp	52.36	129	Leu	57.13	164	Asn	54.03	199	Glu	58.32
80	Ser	54.74	130	Val	59.99	165	Glu	56.41	200	Phe	56.65
81	Gly	44.26	131	Ala	50.70	166	Arg	54.75	201	Val	62.84
82	Ile	62.37	132	Asp	54.25	167	Ile	60.22	202	Ala	52.60
83	Gly	43.55	133	Arg	54.74	168	Gly	47.60	203	Tyr	55.46
84	Met	54.27	134	Val	58.56	169	Arg	56.65	205	Ile	59.98
85	Thr	60.22	135	Gln	53.55	170	Gly	43.31	206	Gln	55.22
86	Lys	60.94	136	Val	61.10	171	Thr	61.88	207	Leu	56.65
87	Ala	54.51	137	Ile	59.61	172	Ile	60.70			
88	Glu	58.80	138	Ser	57.03	173	Leu	53.32			
89	Leu	57.84	139	Lys	53.55	174	Arg	55.22			

Table 5.4 The $^{13}C\alpha$ nucleus chemical shifts from HNCA and HN(CO)CA experiments in the AMP-PNP bound Hsp90 N-terminal domain. The (No) indicates the residue number and (Res) shows the three-letter abbreviation for the amino acid while (Cα) indicates the $^{13}C\alpha$ nuclei chemical shifts. Totally 181 resonances were assigned out of 207 residues that resulted in 87.44% of the $^{13}C\alpha$ atoms assigned.

No.	Res.	Cβ	No.	Res.	Cβ	No.	Res.	Cβ	No.	Res.	Cβ
1	Met	32.40	48	Lys	31.84	107	Ala	16.58	159	Thr	71.81
2	Ala	18.59	49	Ser	62.91	108	Leu	40.31	160	Leu	40.88
3	Ser	64.61	50	Leu	40.31	109	Ser	62.91	161	Asp	42.01
4	Glu	33.53	51	Ser	63.48	110	Ala	18.28	162	Glu	30.14
5	Thr	69.69	52	Asp	40.88	112	Ala	18.84	163	Val	34.66
6	Phe	42.01	54	Lys	30.71	113	Asp	42.57	164	Asn	39.18
7	Glu	30.14	55	Gln	26.76	116	Met	32.29	165	Glu	29.01
8	Phe	40.31	56	Leu	42.01	117	Ile	36.54	166	Arg	30.14
9	Gln	27.34	57	Glu	29.01	122	Val	30.68	167	Ile	39.18
10	Ala	18.27	58	Thr	68.56	126	Ser	64.60	169	Arg	30.71
13	Thr	67.47	59	Glu	29.01	127	Leu	39.75	171	Thr	71.39
14	Gln	27.88	61	Asp	42.01	128	Phe	36.93	172	Ile	40.88
15	Leu	40.31	62	Leu	39.75	129	Leu	42.57	173	Leu	42.01
16	Met	31.88	63	Phe	41.44	130	Val	32.42	174	Arg	30.71
17	Ser	62.67	64	Ile	39.18	131	Ala	21.10	175	Leu	41.98
18	Leu	41.44	65	Arg	34.10	132	Asp	42.01	176	Phe	36.36
19	Ile	36.92	67	Thr	70.83	133	Arg	32.40	177	Leu	42.01
20	Ile	37.49	71	Glu	27.88	134	Val	34.66	178	Lys	34.10
21	Asn	40.31	72	Gln	29.80	135	Gln	30.71	179	Asp	40.31
27	Lys	31.81	73	Lys	29.01	136	Val	31.84	180	Asp	39.18
28	Glu	28.44	74	Val	36.36	137	Ile	39.18	181	Gln	27.31
29	Ile	37.44	75	Leu	45.96	138	Ser	66.31	182	Leu	38.05
30	Phe	36.92	76	Glu	31.27	139	Lys	35.79	183	Glu	27.88
31	Leu	39.75	77	Ile	39.74	140	Ser	62.91	184	Tyr	36.36
32	Arg	28.45	78	Arg	32.40	141	Asn	36.92	185	Leu	41.44
33	Glu	27.88	79	Asp	46.53	142	Asp	41.44	186	Glu	29.14
34	Leu	39.21	80	Ser	61.78	143	Asp	44.83	187	Glu	29.01
35	Ile	35.79	82	Ile	39.75	144	Glu	30.71	188	Lys	31.27
36	Ser	62.39	84	Met	36.92	145	Gln	29.58	189	Arg	29.01
37	Asn	36.94	85	Thr	69.69	146	Tyr	45.40	190	Ile	37.49
38	Ala	18.28	86	Lys	30.71	147	Ile	41.44	191	Lys	31.84
39	Ser	62.91	87	Ala	17.71	148	Trp	34.66	192	Glu	29.01
40	Asp	39.75	88	Glu	29.58	149	Glu	32.97	193	Val	31.27
41	Ala	18.84	89	Leu	41.44	150	Ser	67.43	194	Ile	36.92
42	Leu	40.31	90	Ile	38.62	151	Asn	38.62	195	Lys	31.27
43	Asp	39.18	91	Asn	39.18	152	Ala	16.58	196	Arg	30.14
44	Lys	32.97	103	Ala	17.71	155	Ser	66.87	197	His	33.53
45	Ile	38.05	104	Phe	38.05	156	Phe	40.88	198	Ser	63.48
46	Arg	29.58	105	Met	31.86	157	Thr	71.96	199	Glu	29.01
47	Tyr	36.92	106	Glu	28.45	158	Val	34.66	200	Phe	37.49

201	Val	31.84		203	Tyr	39.75		206	Gln	28.45	
202	Ala	18.27		205	Ile	37.49		207	Leu	43.70	

Table 5.5 The $^{13}C\beta$ nucleus chemical shifts from HN(CA)CB and HN(CO)CACB experiments. The (No) indicates the residue number and (Res) shows the three letter abbreviation for the amino acid. In total 177 resonances were assigned out of 207 residues including 11 glycines, which resulted in 85.5% of the $^{13}C\beta$ atoms assignments.

No.	Res.	Co	No.	Res.	Co	No.	Res.	Co	No.	Res.	Co
0	Gly	174.81	46	Arg	180.35	92	Asn	176.94	147	Ile	176.62
1	Met	176.84	47	Tyr	180.24	93	Leu	178.08	148	Trp	176.28
2	Ala	178.09	48	Lys	179.67	102	Lys	179.10	149	Glu	174.92
3	Ser	174.35	49	Ser	175.60	103	Ala	181.14	150	Ser	174.13
4	Glu	175.03	50	Leu	179.56	104	Phe	177.18	151	Asn	175.49
5	Thr	173.22	51	Ser	175.03	105	Met	179.90	152	Ala	177.29
6	Phe	174.47	52	Asp	174.13	106	Glu	179.78	153	Gly	176.05
7	Glu	178.54	54	Lys	180.12	107	Ala	181.25	154	Gly	175.03
8	Phe	178.43	55	Gln	177.75	108	Leu	181.71	155	Ser	172.87
9	Gln	178.81	56	Leu	179.78	109	Ser	175.37	156	Phe	173.45
10	Ala	180.80	57	Glu	177.63	110	Ala	178.43	157	Thr	175.37
12	Ile	178.55	58	Thr	176.39	111	Gly	175.37	158	Val	176.96
13	Thr	177.97	59	Glu	173.07	112	Ala	176.62	159	Thr	174.13
14	Gln	178.99	61	Asp	176.16	113	Asp	177.97	160	Leu	177.18
15	Leu	178.99	62	Leu	175.26	116	Met	177.10	161	Asp	177.75
16	Met	177.97	63	Phe	172.32	117	Ile	176.08	162	Glu	176.84
17	Ser	177.29	64	Ile	175.03	118	Gly	178.35	163	Val	176.73
18	Leu	180.91	65	Arg	175.71	119	Gln	177.13	164	Asn	176.69
19	Ile	178.20	66	Ile	175.18	125	Tyr	177.97	165	Glu	176.39
20	Ile	177.97	71	Glu	178.09	126	Ser	176.68	166	Arg	178.31
21	Asn	176.28	72	Gln	175.15	127	Leu	178.20	167	Ile	176.96
27	Lys	177.52	73	Lys	174.35	128	Phe	176.28	168	Gly	175.03
28	Glu	176.45	74	Val	173.90	129	Leu	179.33	169	Arg	174.81
29	Ile	177.41	75	Leu	175.26	130	Val	173.45	170	Gly	172.43
30	Phe	176.65	76	Glu	176.84	131	Ala	175.94	171	Thr	173.79
31	Leu	178.92	77	Ile	175.03	132	Asp	176.05	172	Ile	175.15
32	Arg	179.84	78	Arg	174.47	133	Arg	173.56	173	Leu	175.72
33	Glu	181.14	79	Asp	177.52	134	Val	174.24	174	Arg	173.68
34	Leu	181.23	80	Ser	174.98	135	Gln	175.03	175	Leu	175.49
35	Ile	178.43	81	Gly	173.11	136	Val	174.92	176	Phe	175.94
36	Ser	176.49	82	Ile	175.15	137	Ile	176.28	177	Leu	178.31
37	Asn	178.89	83	Gly	172.43	138	Ser	172.21	178	Lys	178.88
38	Ala	178.80	84	Met	176.05	139	Lys	174.47	179	Asp	177.63
39	Ser	177.45	85	Thr	174.47	140	Ser	177.52	180	Asp	177.86
40	Asp	178.99	86	Lys	178.43	141	Asn	177.63	181	Gln	176.28
41	Ala	182.61	87	Ala	181.25	142	Asp	175.37	182	Leu	180.46
42	Leu	178.77	88	Glu	179.22	143	Asp	174.69	183	Glu	177.30
43	Asp	179.90	89	Leu	178.54	144	Glu	174.69	185	Leu	177.61
44	Lys	181.14	90	Ile	179.33	145	Gln	176.28	186	Glu	177.63
45	Ile	177.07	91	Asn	177.52	146	Tyr	174.35	187	Glu	178.31

No.	Res.	Co	No.	Res.	Co	No.	Res.	Co	No.	Res.	Co
188	Lys	179.44	193	Val	179.56	198	Ser	175.82	203	Tyr	172.66
189	Arg	178.65	194	Ile	178.77	199	Glu	177.41	205	Ile	177.18
190	Ile	178.88	195	Lys	178.43	200	Phe	176.39	206	Gln	174.24
191	Lys	179.90	196	Arg	178.88	201	Val	176.83	207	Leu	182.39
192	Glu	179.55	197	His	177.75	202	Ala	176.85			

Table 5.6 The ^{13}CO nucleus chemical shifts from HNCO and HN(CA)CO experiments of the AMP-PNP bound Hsp90 N-terminal domain. The (No) indicates the residue number and (Res) shows the three-letter abbreviation for the amino acid. In total 179 resonances were assigned out of 207 residues which resulted in 86.5% of the ^{13}CO atoms assigned.

Residue		ADP/ATP Interaction
Glu-33	sidechain	Through water interaction to oxygen in α-phosphate and Mg^{2+}
Leu-34	carbonyl	Through water hydrogen bond to adenine N6
Asn-37	sidechain	Through water interaction N7 adenine
Asn-37	sidechain	Direct hydrogen bond to α-phosphate
Asn-37	sidechain	Direct and through water interaction with Mg^{2+}
Asp-40	sidechain	Through water interaction to oxygen in β-phosphate
Ala-41	sidechain	van der Waals contact
Lys-44	sidechain	Binds through water to O2' and O3' oxygens of the ribose sugar
Asp-79	sidechain	Direct hydrogen bond to adenine N6
Asp-79	sidechain	Through water interaction with adenine N1
Gly-83	amide	Through water interaction adenine N1
Met-84	sidechain	van der Waals contact to adenine
Asn-92	sidechain	Through water N3 adenine O2'of ribose
Asn-92	sidechain	Direct hydrogen bond to O2'of ribose
Lys-98	sidechain	Hydrogen bond /ion pair to β phosphate and water molecules
Gly-118	H	Through water interaction to oxygen in β-phosphate and Mg^{2+}
Gly-121	H	Through water interaction to oxygen in α-phosphate
Gly-123	amide	Through water interaction to oxygen in β-phosphate and Mg^{2+}
Phe-124	amide	Hydrogen bond to oxygen in α phosphate
Thr-171	sidechain	Through water interaction with adenine N1

Table 5.7. Residues involved in the nucleotide binding in the yeast Hsp90 N-terminal domain. Details of the ADP interacting molecules are shown. Data extracted from (Prodromou *et al.*, 1997). For figures to assist the above table refer to Chapter 1, Figures 1.3 and 1.5.

5.7 Consensus chemical shift differences of the apo- and AMP-PNP bound spectra

The HN nuclei chemical shifts were extracted from the HSQC spectra of the apo- and AMP-PNP bound Hsp90 N-terminal domain. Consensus chemical shift differences between the Hsp90 N-terminal domain in complex with AMP-PNP and the Hsp90 N-terminal domain alone were calculated as the normalized weighted averaged chemical shift differences for the amides ($\Delta\delta HN = \{[\Delta\delta H^2 + (\Delta\delta N/5)^2\}/2\}^{1/2}$) as described in Shao *et al,* (2003) and are shown in Figure 5.20.

The ΔδHN mostly show changes in the local environment of the residues, such as hydrogen bonding and ring-current shifts. The regions mostly affected by nucleotide binding (above the median value of 0.08 ppm, green line, shown in Figure 5.20) are as follows; residues 4 to 21 which make the first β-strand and the first α-helical secondary structure with the maximum ΔδHN value observed for residues 12 to 15; residues 28 to 49 which include the second helix that makes one side of the nucleotide-binding pocket with maximum ΔδHN shifts observed for residues 34 to 38 and 40 to 42, which are mainly involved in drug and nucleotide binding. The next region is the first loop of the nucleotide binding pocket, residues 81 to 85, which have a relatively high ΔδHN. Many of these residues are also involved in nucleotide, direct or water mediated interactions (Table 5.7). Part of the third helix, residues 92 to 94, constructing one side of the nucleotide-binding pocket also have high ΔδHN shifts. This helix, together with the second nucleotide loop, is involved in trapping GM with a conformational change observed for this region in the human Hsp90 N-terminal domain (Stebbins *et al.,* 1997). The proposed 'ATP-lid'(residues 100 to 121) begins with a large ΔδHN value at residue

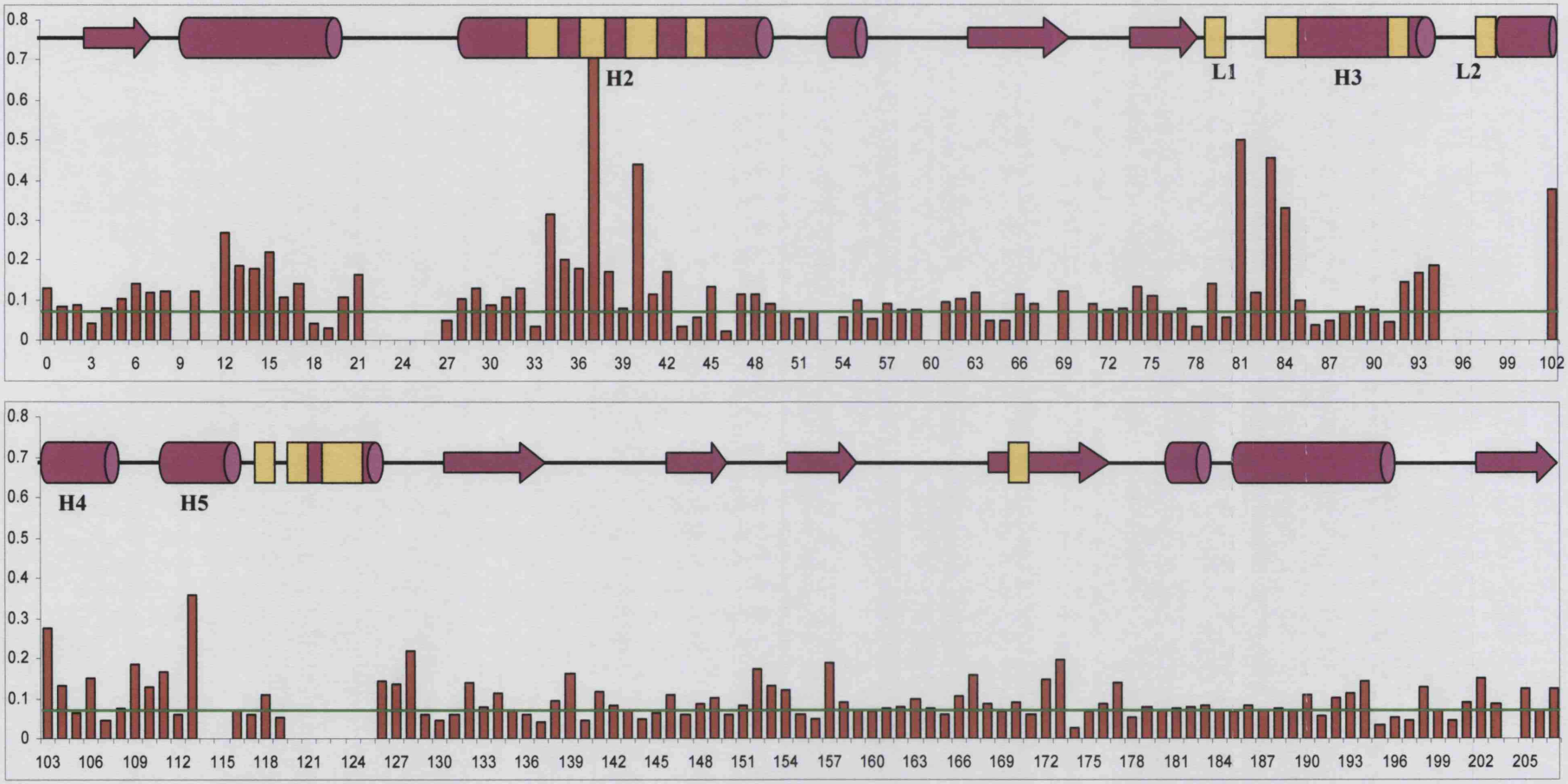

Figure 5.20 The ΔδHN of the apo- and AMP-PNP bound Hsp90 N-terminal domain extracted from the HSQC experiments. The secondary structures corresponding to the ΔδHN are shown above the graph with some regions highlighted. The green line shows the median value of 0.08 ppm. The yellow boxes highlights where the nucleotide or drugs bind to the protein.

102 but further in the sequence the shift difference is reduced until residue 108, which has the lowest shift value in this region. From residue 108 onward there begins an increase in the ΔδHN shifts, with residue 113 showing the highest shift difference among all residues in the lid. The level of chemical shift differences in this region was not sufficiently uniform to suggest a conformational change in the entire 'ATP-lid', however, there are regions in and around this lid that appear to be affected by nucleotide binding. Residues 114, 115 and 120 to 124 have not been assigned in the AMP-PNP bound spectra. The only residues assigned in this region are residues 116 to 119 for which medium ΔδHN shift (around the median values) differences were observed. The unassigned peaks were broad and weak, indicating a possible intermediate or conformational exchange. Using a higher magnetic field did not improve the quality of the spectra in this region and resulted in complete disappearance of the some resonance (refer to Figures 5.18 and 5.19). Finally, other regions affected by nucleotide binding are residues 125 to 128 in the second 3_{10} helix connected to the 'ATP-lid' which are involved in nucleotide and drug binding to this domain. Several sections of the β-sheets, which form the bottom of the nucleotide-binding pocket in the X-ray crystal structure, are strongly affected by binding, as shown by the moderate shifts in residues 138, 139, 151 to 154, 157 and 172 and 173. There are residues with medium shift that are outside the nucleotide binding pocket, such as residues 192 to 194, 198, 201 to 203 located on the last helix of the structure, adjacent to the second helix. These shifts could be a secondary effect in the local environment due to conformational change occurring in the second helix.

The average backbone carbon nuclei chemical shift difference $\Delta\delta^{13}C$ were calculated using the $^{13}C\alpha$, $^{13}C\beta$ and ^{13}CO chemical shift differences ($\Delta\delta^{13}C\alpha$,

$\Delta\delta^{13}C\beta$ and $\Delta\delta^{13}CO$) between the apo- and the AMP-PMP bound spectra extracted from HNCA, HN(CO)CA, HNCACB, HN(CO)CACB, HNCO and HN(CA)CO experiments. The results of the $\Delta\delta^{13}C$ are shown in Figure 5.21, with the median value of 0.095 ppm drawn as a green line. The $\Delta\delta^{13}C$ are an indication of a conformational change in the secondary structure of the protein. Areas with a $\Delta\delta^{13}C$ value above the median, similar to the ΔδHN shifts, are residues 6 to 8, 12 to 21, 33 to 42, 82 to 84 and 92 to 113 with large $\Delta\delta^{13}C$ of 0.4 ppm and above observed for residues 8, 33, 36, 37, 41, 93, 94 and 113. There are, however, some differences observed compared to the ΔδHN shifts. For example, residues 44 to 48 (from which Lys 44 interacts with the nucleotide) and residue 80 have a ΔδHN value below the median (Figure 5.20) in contrast to a $\Delta\delta^{13}C$ value above median. Other residues with similar differences are residues 125, 126, 148, 150 and 171 to 173.

Residues 131 to 135, which make part of the fourth β-strand, show a moderate level of $\Delta\delta^{13}C$ and ΔδHN shifts around the median value. These residues are not involved in nucleotide binding and the shift observed for this region could be due to the conformational change taking place in the neighbouring 3_{10} helix. Residue Tyr-125 is a pH sensitive residue (data not shown) and is located in the second 3_{10} helix close to residue Phe-124 and Gly-123 which are involved in interacting with the nucleotide phosphate group through their backbone amides (Table 5.7). The high $\Delta\delta^{13}C$ chemical shift difference observed for Tyr-125 could highlight the importance of this helix in interacting with the nucleotide by providing a hydrophobic patch and possibly undergoing a conformational change (helix-coil transition) upon nucleotide binding, as was suggested in the Hsp90 N-terminal domain human homolog (Stebbins *et al.*, 1997).

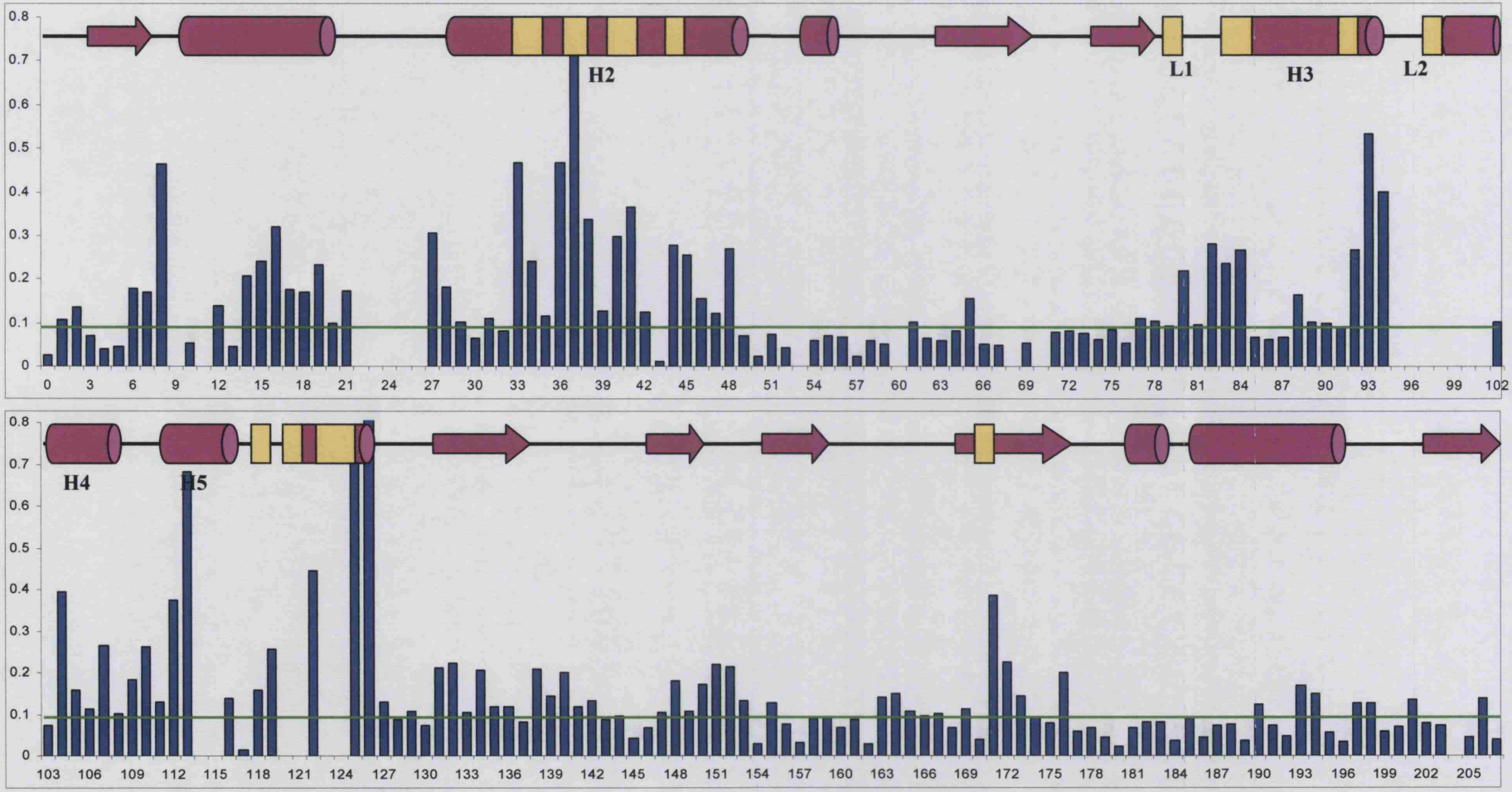

Figure 5.21.a The $\Delta\delta^{13}C$ of the apo- and AMP-PNP bound Hsp90 N-terminal domain averaged from $\Delta\delta^{13}C\alpha$, $\Delta\delta^{13}C\beta$ and $\Delta\delta^{13}CO$. The secondary structures corresponding to the $\Delta\delta^{13}C$ are shown above the graph with some regions highlighted. The green line shows the median value of 0.095 ppm. The yellow boxes highlights where the nucleotide or drugs bind to the protein.

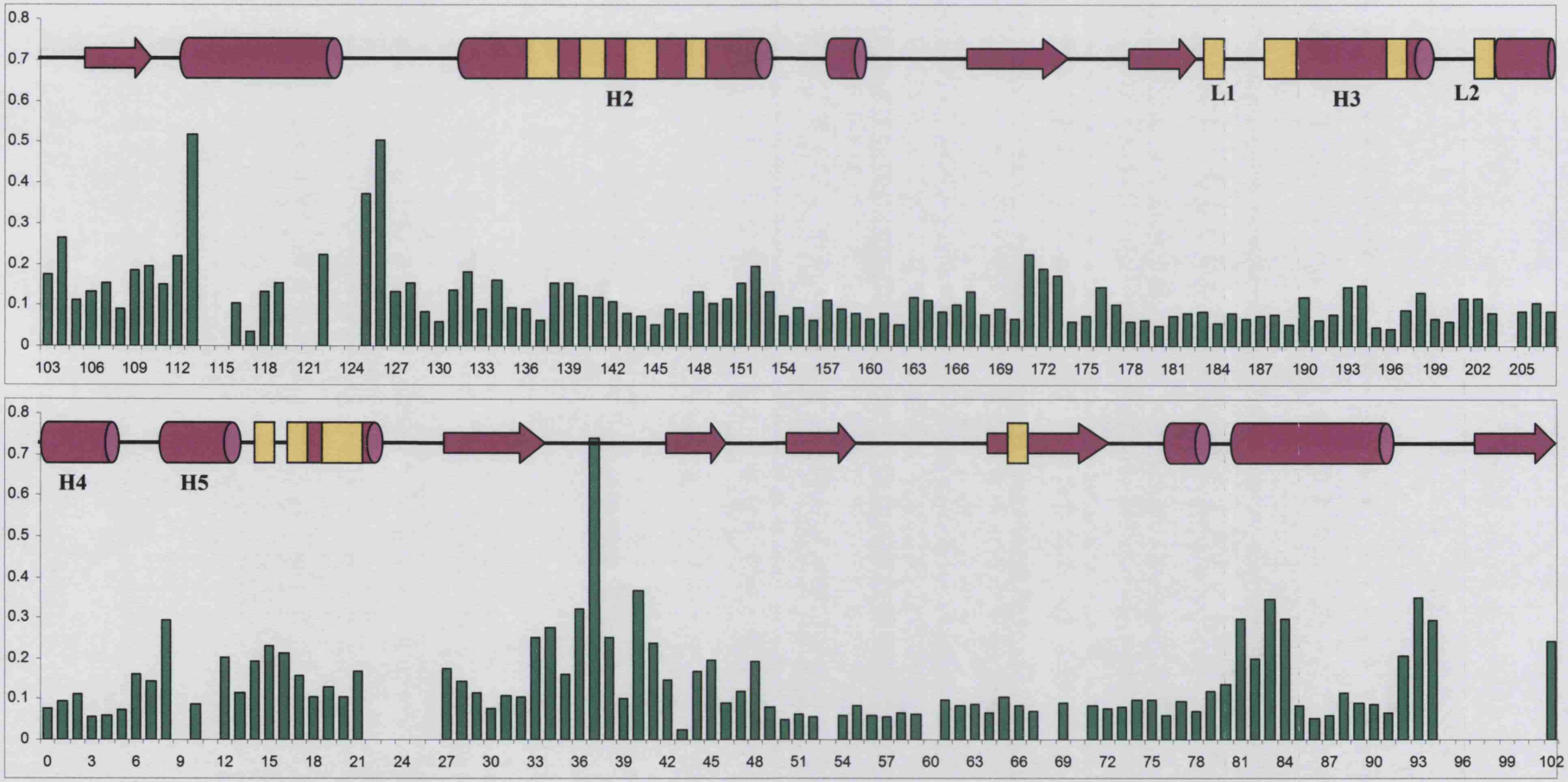

Figure 5.21.b The averaged total sum of the $\Delta\delta^{13}C$ and $\Delta\delta HN$ for the apo- and AMP-PNP bound Hsp90 N-terminal domain. The secondary structures corresponding to the total chemical shift differences are shown above the graph with some regions highlighted. The yellow boxes highlights where the nucleotide or drugs bind to the protein.

Residues Phe-120 to Phe-124, from which Gly-121, 123 and Phe-124 make the conserved G2 box (previously shown in Figure 1.7, Chapter 1) as well as residues Thr-95 to Thr-101 were not assigned (highlighted as a large yellow region in Figure 5.21). The area equivalent to residues 95 to 106 in the human Hsp90 N-terminal domain has been shown to interact with GM and produces a small conformational change upon drug binding (Stebbins *et al.,* 1997). The possible movement of this region could explain why residues 95 to 101 have not been assigned in the AMP-PNP spectra and no resonance was observed, indicating intermediate exchange for these resonances. These residues are surface proteins that have inherent flexibility. The above observation suggests that the mobile loop remains flexible in the presence of AMP-PNP. Residues 9 and 11, located on the loop connected to the first helix may interact with residues 95 to 101. This could explain the lack of signal for both regions in the apo- and AMP-PNP bound spectra. The importance of this region (residues 9 to 11) was confirmed when the first 24 residues were deleted in a construct made by Richter *et al.* (2002), which resulted in loss of N-terminal domain dimerisation and severely affected ATPase activity. This could be due either to their involvement in dimerisation as suggested by Richter *et al.* (2002) or its possible interaction with the 95 to 101 loop region. Further investigation needs to be conducted as to whether or not this movement is essential for catalysis, or is perhaps a location for the interaction of the ATPase regulatory proteins. It is possible that this flexibility is necessary to allow access for the nucleotides to be buried in the deep active site or that this loop is perhaps acting as molecular trap door.

5.8 Secondary structure prediction using chemical shifts

In order to investigate possible structural changes associated with binding of the AMP-PNP to the Hsp90 N-terminal domain, secondary structure predicted using the CSI program was carried out for $^{13}C\alpha$, $^{13}C\beta$ and ^{13}CO nuclei chemical shifts. The results of the prediction from the AMP-PNP bound spectra compared to that of apo- and X-ray crystal secondary structures are shown in Table 5.8 and summarized in Figure 5.22. The secondary structure differences for the apo- and AMP-PNP bound structures are highlighted in red where a helix, and in blue where β-sheets, were predicted differently in Table 5.8. Residues highlighted in green indicate differences between the AMP-PNP predicted structure and the X-ray crystal structure. In addition the differences are also plotted on the worm representation of the X-ray crystal structure of the Hsp90 N-terminal domain shown in Figure 5.23.

Most of the secondary structure predicted from the chemical shifts is similar to that of the X-ray crystal structure with minor differences observed mostly in the length of secondary structures. For example, residues 8 and 9 are predicted as helix (in contrast to coil in the X-ray crystal structure) increasing the length of the first helix. Also, residues 62 and 63 are predicted as β-strand, which resulted in an increase in the length of the second β-strand.

The regions that have been predicted differently in the AMP-PNP bound solution structure compared to the apo- form are residues 83 to 85, 93 to 95, 118-119, 143 to 146 and 162-163, highlighted in Figure 5.22 with blue circles. Residues 83 to 85 have a coil structure in the apo- form while a β-sheet structure has been predicted for the same region in the AMP-PNP bound. This could possibly indicate

apo						Amp			apo	Amp	apo	apo						Amp			apo	Amp	apo
Res	AA	Hα	Cα	CO	Cβ	Cα	CO	Cβ	Cons	Cons	Cry	Res	AA	Hα	Cα	CO	Cβ	Cα	CO	Cβ	Cons	Cons	Cry
1	M	C	C	C	C	C	C	C	C	C	C	36	S	H	H	H	C	H	H	C	H	H	H
2	A	B	C	C	C	C	C	C	C	C	C	37	N	H	H	H	C	H	H	C	H	H	H
3	S	B	C	C	B	C	C	B	B	C	C	38	A	H	H	H	C	H	H	C	H	H	H
4	E	B	C	B	B	B	B	B	B	B	B	39	S	H	H	H	C	H	H	C	H	H	H
5	T	B	B	B	B	B	B	B	B	B	B	40	D	H	H	H	C	H	H	C	H	H	H
6	F	C	B	B	B	B	B	B	B	B	B	41	A	H	H	H	C	H	H	C	H	H	H
7	E	C	B	H	B	B	H	B	C	C	B	42	L	H	H	H	C	H	H	C	H	H	H
8	F	H	H	H	B	H	H	B	H	C	C	43	D	H	H	H	C	H	H	C	H	H	H
9	Q	H	H	H	C	H	H	C	H	H	C	44	K	H	H	H	C	H	H	C	H	H	H
10	A	H	H	H	C	H	H	C	H	H	H	45	I	C	C	H	C	C	H	C	C	C	H
11	E	H	H	H	C	H	H	C	H	H	H	46	R	H	H	H	C	H	H	C	H	H	H
12	I	H	H	H	C	H	H	C	H	H	H	47	Y	H	H	H	C	H	H	C	H	H	H
13	T	H	H	H	C	H	H	C	H	H	H	48	K	H	H	H	B	H	H	C	H	H	H
14	Q	H	H	H	C	H	H	C	H	H	H	49	S	H	H	H	B	H	H	C	H	H	H
15	L	H	H	H	C	H	H	C	H	H	H	50	L	C	H	H	B	H	H	C	C	H	H
16	M	H	H	H	C	H	H	C	H	H	H	51	S	C	C	H	B	C	H	C	C	C	T
17	S	H	H	H	C	H	H	C	H	H	H	52	D	C	C	C	B	C	C	C	C	C	T
18	L	H	H	H	C	H	H	C	H	H	H	53	P	C	C	C	C	C	C	C	C	C	H
19	I	C	H	H	C	H	H	C	H	H	H	54	K	H	C	H	C	C	H	C	H	C	H
20	I	C	H	H	C	H	H	C	H	H	H	55	Q	H	C	H	C	C	H	C	H	C	H
21	N	C	C	H	C	H	H	C	C	H	T	56	L	H	C	H	C	C	H	C	H	C	H
22	T	C	C	C	C	C	C	C	C	C	C	57	E	H	C	H	C	C	H	C	H	C	H
23	V	C	C	C	C	C	C	C	C	C	C	58	T	H	C	H	C	C	H	C	H	C	T
24	Y	C	C	C	C	C	C	C	C	C	C	59	E	C	C	B	C	C	B	C	C	C	C
25	S	C	C	C	C	C	C	C	C	C	S	60	P	C	C	B	C	C	B	C	C	C	C
26	N	C	C	C	C	C	C	C	C	C	C	61	D	C	C	B	C	C	B	C	C	C	C
27	K	H	H	C	C	H	C	C	H	C	T	62	L	B	B	B	C	B	B	C	B	C	C
28	E	H	H	C	C	H	H	C	H	H	T	63	F	B	B	B	B	B	B	B	B	B	C
29	I	H	H	C	C	H	H	C	H	H	H	64	I	B	B	B	B	B	B	B	B	B	B
30	F	H	H	H	C	H	H	C	H	H	H	65	R	B	B	B	B	B	B	B	B	B	B
31	L	H	H	H	C	H	H	C	H	H	H	66	I	B	B	B	B	B	B	B	B	B	B
32	R	H	H	H	C	H	H	C	H	H	H	67	T	B	B	B	B	B	B	B	B	B	B
33	E	H	H	H	C	H	H	C	H	H	H	68	P	B	B	C	C	B	C	C	B	C	B
34	L	H	H	H	C	H	H	C	H	H	H	69	K	C	C	C	C	C	C	C	C	C	B
35	I	H	H	H	C	H	H	C	H	H	H	70	P	C	C	C	C	C	C	C	C	C	G

apo						Amp			apo	Amp	apo
Res	AA	Hα	Cα	CO	Cβ	Cα	CO	Cβ	Cons	Cons	Cry
71	E	C	C	C	C	C	C	C	C	C	G
72	Q	C	C	B	C	C	B	C	C	C	G
73	K	C	C	B	C	C	B	C	C	C	T
74	V	B	B	B	B	B	B	B	B	B	B
75	L	B	B	B	B	B	B	B	B	B	B
76	E	B	B	C	B	B	C	B	B	B	B
77	I	B	B	C	B	B	C	B	B	B	B
78	R	B	B	C	B	B	C	B	B	B	B
79	D	B	B	C	B	B	C	B	B	B	B
80	S	B	B	C	C	B	C	C	B	C	C
81	G	C	C	B	C	C	C	C	C	C	S
82	I	C	C	B	C	C	C	B	C	C	C
83	G	C	B	B	C	B	C	B	C	B	C
84	M	C	B	B	C	B	C	B	C	B	C
85	T	C	B	B	C	B	C	B	C	B	C
86	K	H	H	H	C	H	H	C	H	H	H
87	A	H	H	H	C	H	H	C	H	H	H
88	E	H	H	H	C	H	H	C	H	H	H
89	L	H	H	H	B	H	H	C	H	H	H
90	I	H	H	H	B	H	H	C	H	H	H
91	N	H	H	H	B	H	H	C	H	H	H
92	N	H	H	H	C	H	H	C	H	H	H
93	L	H	H	H	C	C	H	C	H	C	T
94	G	H	H	H	C	C	H	C	H	C	T
95	T	H	H	C	C	C	C	C	H	C	T
96	I	C	C	C	C	C	C	C	C	C	S
97	A	C	C	C	C	C	C	C	C	C	C
98	K	C	C	C	C	C	C	C	C	C	C
99	S	C	C	C	C	C	C	C	C	C	T
100	G	C	C	C	C	C	C	C	C	C	T
101	T	H	H	H	C	C	C	C	H	C	H
102	K	H	H	H	C	H	H	C	H	H	H
103	A	H	H	H	C	H	H	C	H	H	H
104	F	H	H	H	C	H	H	C	H	H	H
105	M	H	H	H	C	H	H	C	H	H	H
106	E	H	H	H	C	H	H	C	H	H	H

apo						Amp			apo	Amp	apo
Res	AA	Hα	Cα	CO	Cβ	Cα	CO	Cβ	Cons	Cons	Cry
107	A	H	H	H	C	H	H	C	H	H	H
108	L	H	H	H	C	H	H	C	H	H	H
109	S	H	H	H	C	H	H	C	H	H	H
110	A	C	C	H	C	H	H	C	C	H	H
111	G	C	C	H	C	C	H	C	C	C	T
112	A	C	C	C	C	C	H	B	C	C	C
113	D	C	C	C	C	C	C	B	C	C	C
114	V	C	H	C	C	C	C	B	C	C	G
115	S	C	H	C	C	C	C	C	C	C	G
116	M	C	H	C	C	C	C	C	C	C	G
117	I	C	H	C	C	C	C	C	C	C	T
118	G	C	H	H	C	C	C	C	H	C	G
119	Q	C	H	H	C	C	C	C	H	C	G
120	F	C	H	H	C	C	C	C	H	C	G
121	G	C	H	H	C	C	C	C	H	C	T
122	V	C	C	C	C	C	C	C	C	C	T
123	G	H	H	H	C	C	C	C	H	C	G
124	F	H	H	H	C	C	C	C	H	C	G
125	Y	H	H	H	C	H	H	C	H	H	G
126	S	H	H	H	C	H	H	C	H	H	G
127	L	H	H	H	C	H	H	C	H	H	G
128	F	B	H	H	C	H	H	C	H	H	G
129	L	B	H	H	B	H	H	B	C	C	G
130	V	B	B	B	B	B	B	B	B	B	T
131	A	B	B	B	B	B	B	B	B	B	B
132	D	B	B	B	B	B	B	B	B	B	S
133	R	B	B	B	B	B	B	B	B	B	B
134	V	B	B	B	B	B	B	B	B	B	B
135	Q	B	B	B	B	B	B	B	B	B	B
136	V	B	B	B	B	B	B	B	B	B	B
137	I	B	B	B	B	B	B	B	B	B	B
138	S	B	B	B	B	B	B	B	B	B	B
139	K	B	B	B	B	B	B	B	B	B	B
140	S	B	B	C	B	B	C	B	B	B	C
141	N	C	C	C	C	C	C	C	C	C	T
142	D	C	C	B	B	C	B	B	C	C	T

apo						Amp			apo	Amp	apo	apo						Amp			apo	Amp	apo
Res	AA	Hα	Cα	CO	Cβ	Cα	CO	Cβ	Cons	Cons	Cry	Res	AA	Hα	Cα	CO	Cβ	Cα	CO	Cβ	Cons	Cons	Cry
143	D	B	C	B	B	C	B	B	B	C	S	176	F	B	C	C	C	C	C	C	C	C	B
144	E	B	C	B	B	C	B	B	B	C	C	177	L	C	C	C	C	C	C	C	C	C	B
145	Q	B	C	B	B	C	B	B	B	C	C	178	K	C	C	C	C	C	C	C	C	C	C
146	Y	B	C	C	B	C	C	B	B	C	B	179	D	C	C	C	C	C	C	C	C	C	T
147	I	B	B	C	B	B	C	B	B	B	B	180	D	C	C	C	C	C	C	C	C	C	T
148	W	B	B	C	B	B	C	B	B	B	B	181	Q	C	C	C	C	C	C	C	C	C	T
149	E	B	B	C	B	B	C	B	B	B	B	182	L	C	C	C	C	C	C	C	C	C	G
150	S	B	B	C	B	B	C	B	B	B	B	183	E	C	C	C	C	C	C	C	C	C	G
151	N	B	B	C	C	B	C	C	B	C	C	184	Y	C	C	C	C	C	C	C	C	C	G
152	A	C	C	C	C	C	C	C	C	C	S	185	L	C	C	C	C	C	H	C	C	C	S
153	G	C	C	C	C	C	C	C	C	C	S	186	E	C	C	H	C	C	H	C	C	C	S
154	G	C	C	C	C	C	C	C	C	C	S	187	E	H	H	H	C	H	H	C	H	H	H
155	S	B	B	C	B	B	C	B	B	B	B	188	K	H	H	H	C	H	H	C	H	H	H
156	F	B	B	C	B	B	C	B	B	B	B	189	R	H	H	H	C	H	H	C	H	H	H
157	T	B	B	C	B	B	C	B	B	B	B	190	I	H	H	H	C	H	H	C	H	H	H
158	V	B	B	C	B	B	C	B	B	B	B	191	K	H	H	H	C	H	H	C	H	H	H
159	T	B	B	C	B	B	C	B	B	B	B	192	E	H	H	H	C	H	H	C	H	H	H
160	L	C	C	C	B	C	C	B	C	C	B	193	V	H	H	H	C	H	H	C	H	H	H
161	D	C	C	C	B	C	C	B	C	C	C	194	I	H	H	H	C	H	H	C	H	H	H
162	E	B	C	C	B	C	C	B	B	C	C	195	K	H	H	H	B	H	H	C	H	H	H
163	V	B	C	C	B	C	C	B	B	C	S	196	R	H	H	H	B	H	H	B	H	C	H
164	N	B	C	C	C	C	C	B	C	C	S	197	H	C	H	H	B	H	H	B	C	C	H
165	E	C	C	C	C	C	C	B	C	C	C	198	S	C	H	H	B	H	H	B	C	C	C
166	R	C	C	C	C	C	C	B	C	C	C	199	E	C	H	H	C	H	H	C	H	H	S
167	I	C	C	C	C	C	C	B	C	C	C	200	F	C	C	C	C	C	H	C	C	C	C
168	G	C	C	C	C	C	C	C	C	C	S	201	V	C	C	C	C	C	C	C	C	C	C
169	R	C	C	B	B	C	B	B	C	C	S	202	A	C	C	C	C	C	C	C	C	C	S
170	G	B	B	B	B	B	B	B	B	B	B	203	Y	C	C	C	C	C	C	C	C	C	S
171	T	B	B	B	B	B	B	B	B	B	B	204	P	C	C	C	C	C	C	C	C	C	C
172	I	B	B	B	B	B	B	B	B	B	B	205	I	C	C	C	C	C	C	C	C	C	B
173	L	B	B	B	B	B	B	B	B	B	B	206	Q	C	C	C	C	C	C	C	C	C	B
174	R	B	C	B	B	B	B	B	B	B	B	207	L	C	C	C	C	C	C	C	C	C	B
175	L	B	C	B	B	C	B	B	B	C	B												

Table 5.8 The secondary structure prediction of the apo- and AMP-PNP bound Hsp90 N-terminal domain using CSI, version 2, compared to the secondary structure from X-ray crystal studies. Key: **Res:** residue number, **AA:** amino acid, C: coil, H: Helix, B: β-sheet. Red were helix and blue were β-strand was predicted. Green highlighted the differences between the X-crystal and the AMP-PNP bound in solution secondary structures.

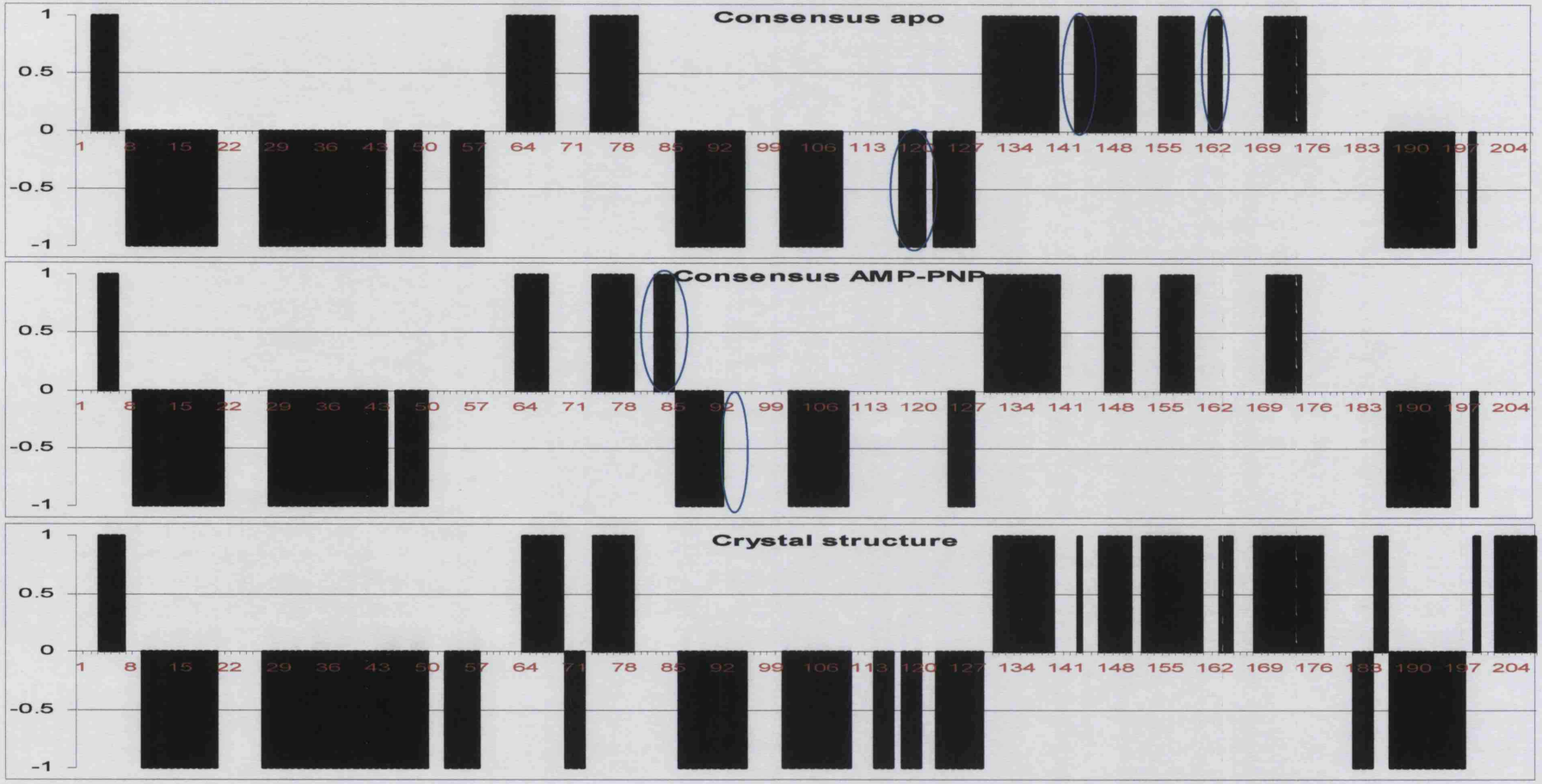

Figure 5.22 Graphical representation of the CSI secondary structure prediction from apo- and AMP-PNP bound Hsp90 N-terminal domain compared to the X-ray crystal structure. The β-sheets have a score of 1, α-helices -1 and coils 0 value plotted against the sequence number. The blue circles highlight the difference between apo- and AMP-PNP bounds.

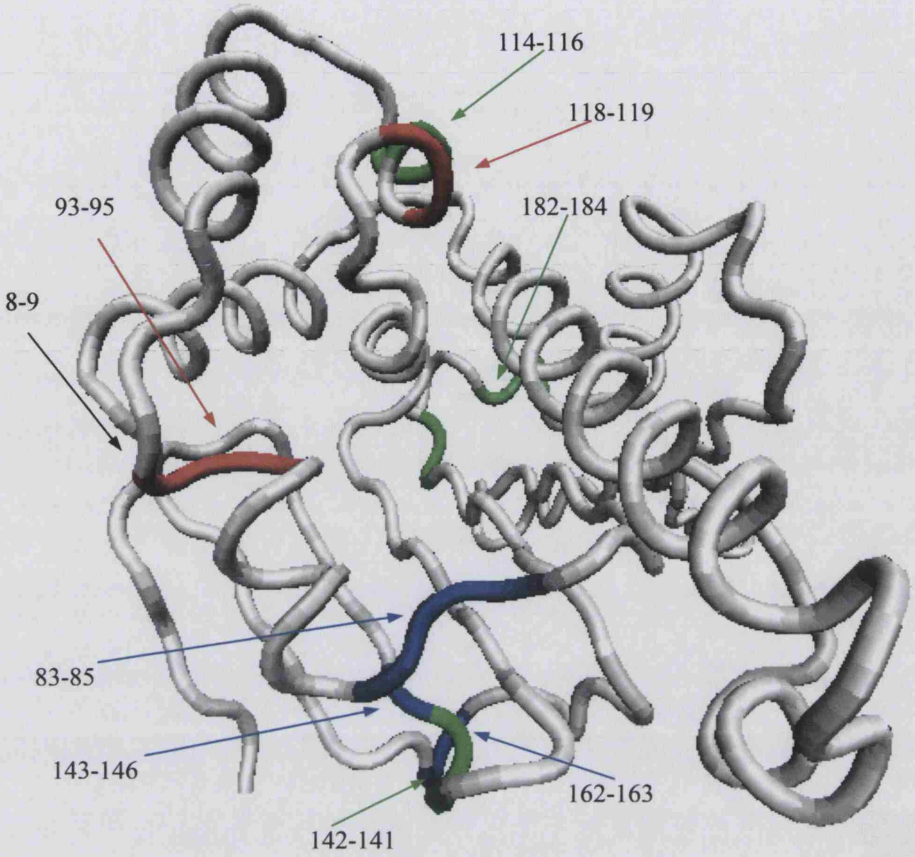

Figure 5.23 Residues predicted different using chemical shifts from apo- and AMP-PNP bound forms highlighted on the X-ray crystal structure of the Hsp90 N-terminal domain. Areas predicted different as helix are in red, β-sheets in blue between apo- and the AMP-PNP bound. Secondary structures difference from the crystal structure and the solution AMP-PNP bound structure are in green.

reduced mobility in this region in the presence of nucleotide. In contrast, residues 93 to 95 were predicted as helix in the apo- form while the same region is predicted as random coil in the AMP-PNP bound form, which could indicate an increase in the mobility of this region. Residues 118 and 119 in the apo- form have been predicted as 3_{10} helix, similar to the X-ray crystal structure, while the same region has been predicted as random coil in the AMP-PNP bound predicted structure. Other regions that have been predicted differently belong to residues 143 to 145, 162 and 163 predicted as β-strands instead of coil. Differences between the X-ray crystal structure and the AMP-PNP bound solution structure are minor and similar

to differences found in the apo- form. Residues 68 to 72, 114 to 116, 141-142, 176-177 and 182 to184 that are structured in the crystal form are predicted as coil in the solution structures. The differences are shown in Table 5.8 and are also highlighted in green in Figure 5.23. These regions, which are mostly away from the nucleotide binding pocket, show a small chemical shift difference in the nucleotide bound form, Figures 5.20 and 5.21. Finally, the last 10 residues in the protein have also been predicted less structured in solution, which is predictable for C-terminal residues of a protein which are more flexible in solution.

5.9 Relaxation studies of the AMP-PNP bound Hsp90 N-terminal domain

The $^{15}NT_1$, $^{15}NT_2$ and heteronuclear $\{^1H\}^{15}N$ NOE experiments were carried out on the AMP-PNP bound Hsp90 N-terminal domain in 20 mM Tris buffer, pH 8.0* at 25°C. The $^{15}NT_1$ and $^{15}NT_2$ relaxation experiments were recorded using a $^1H^{15}N$ labelled sample of Hsp90 N-terminal. The $^{15}NT_1$ and $^{15}NT_2$ spectra were recorded using 13 and 9 relaxation delay times (including two repeated time points for error analysis) respectively. The $^{15}NT_1$, $^{15}NT_2$ and $\{^1H\}^{15}N$ NOE experiments were recorded and processed as mentioned previously for the apo- sample in Chapter 2.

Results of the $^{15}NR_1$, $^{15}NR_2$ and $\{^1H\}^{15}N$ heteronuclear NOE are shown in Figures 5.24, 5.25 and 5.26 respectively. The difference in the relaxation rates of R_1, R_2 and H-NOE between the apo- and AMP-PNP bound Hsp90 N-terminal domain (ΔR_1, ΔR_2 and ΔNOE) are shown in Figure 5.27. The residues with a

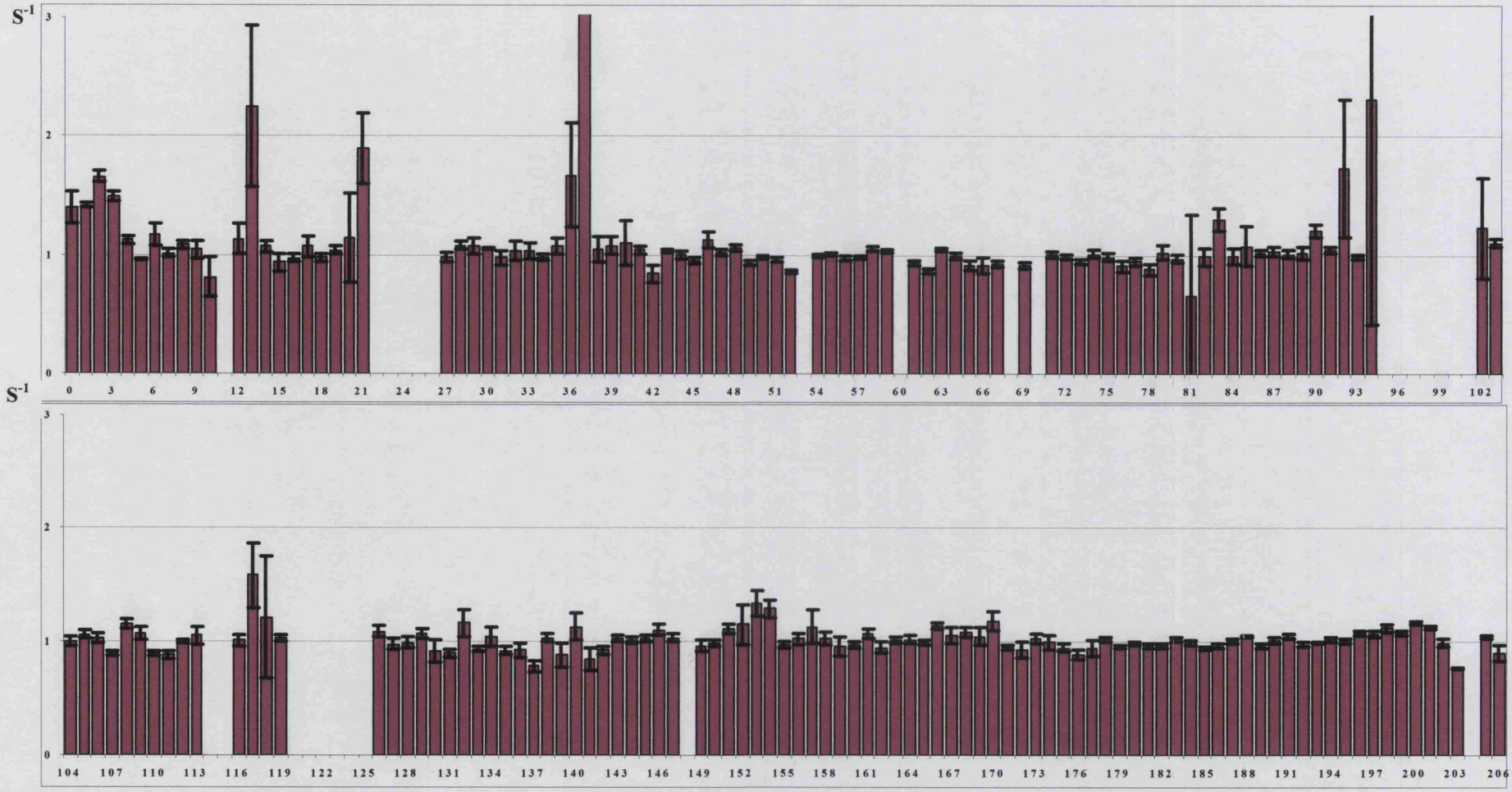

Figure 5.24 Backbone NH, $^{15}NR_1$ relaxation of $^{1}H^{15}N$-labelled Hsp90 N-terminal with AMP-PNP bound at 25°C. Error bars indicate the standard deviation for each residue.

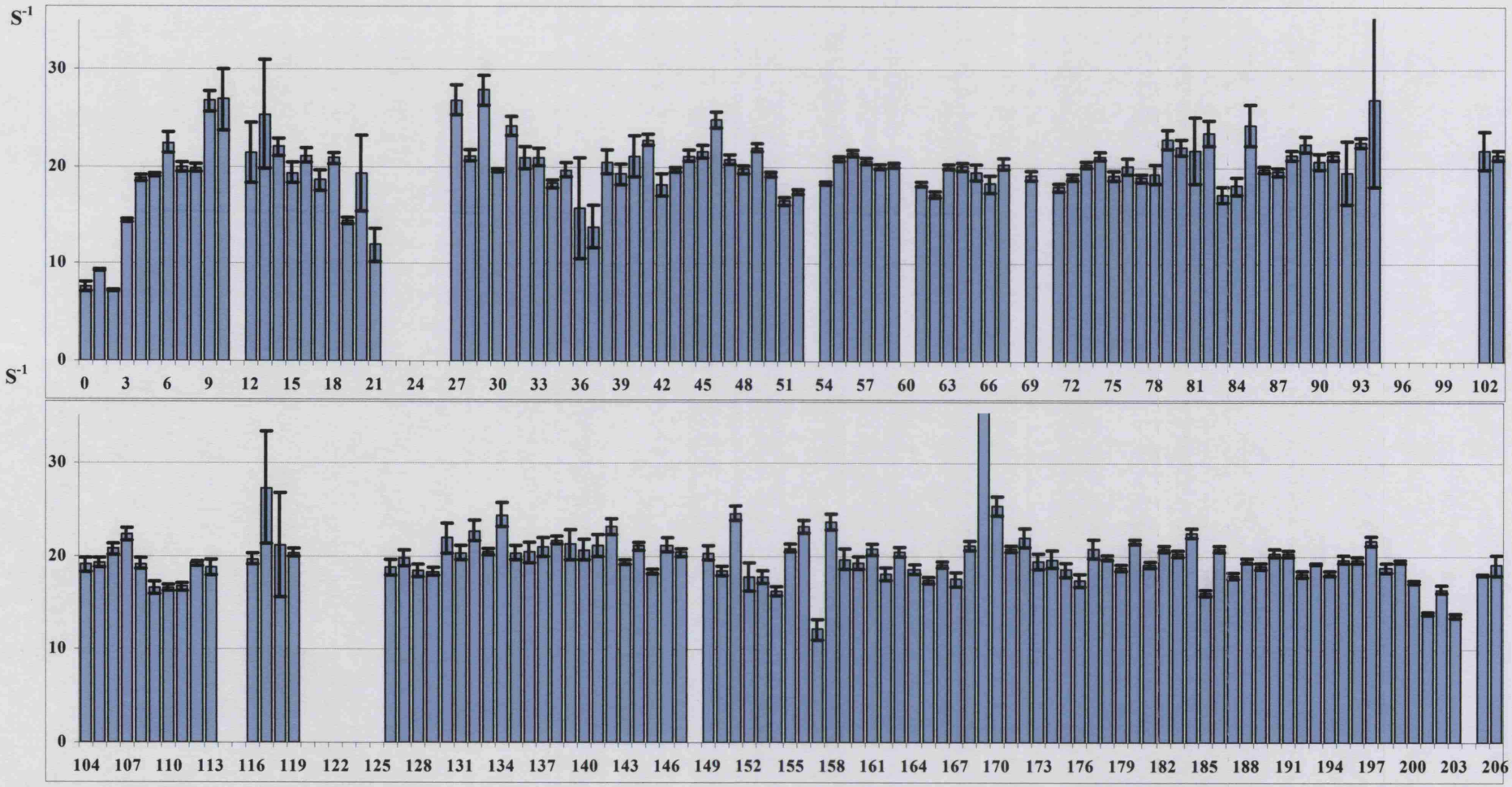

Figure 5.25 Backbone NH, $^{15}NR_2$ relaxation of $^{1}H^{15}N$-labelled Hsp90 N-terminal with AMP-PNP bound at 25°C. Error bars indicate the standard deviation for each residue. The unassigned residues are left as blanks. The T_2 values are in ms.

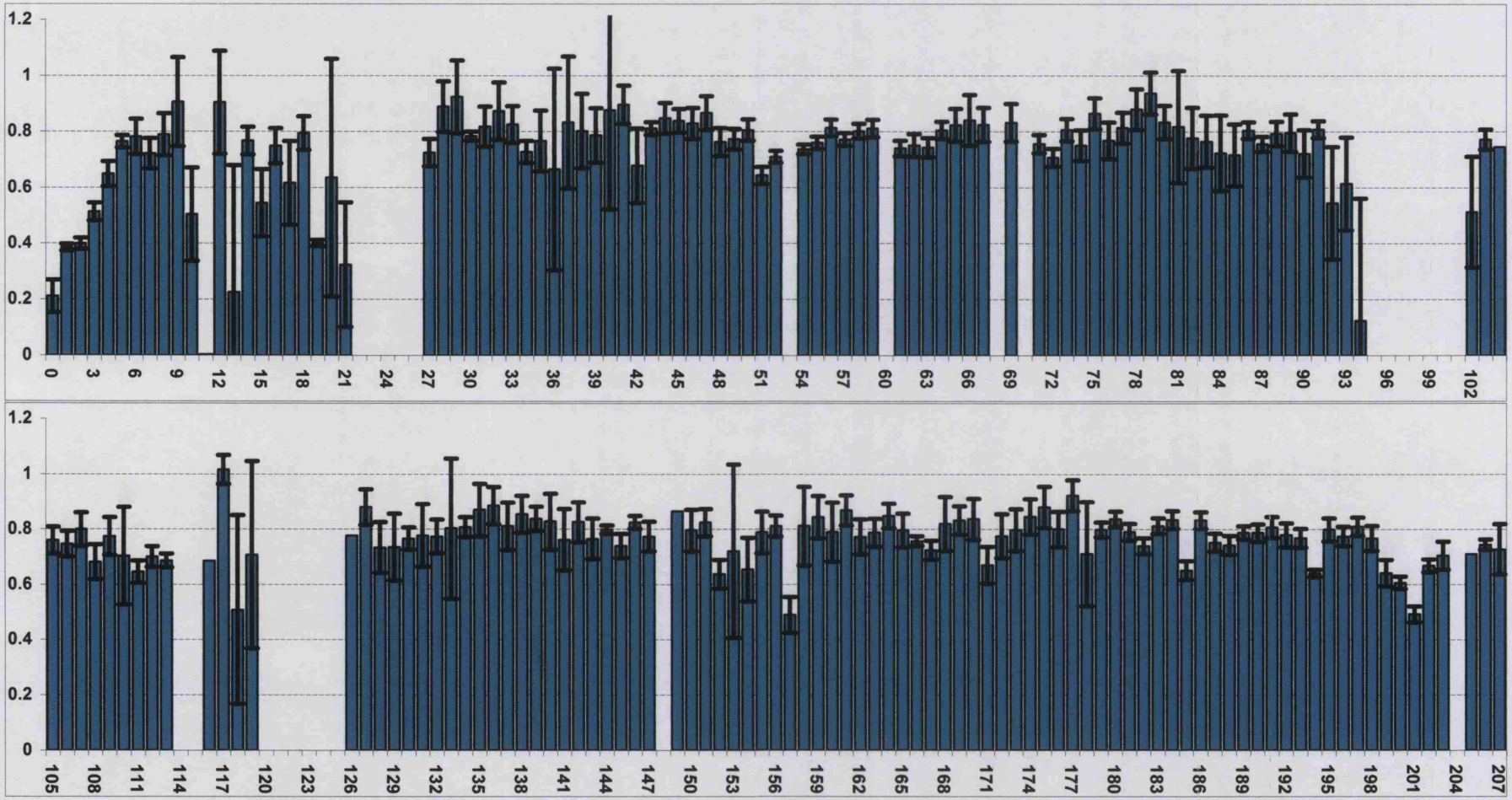

Figure 5.26 Backbone NH $\{^1H\}^{15}N$ heteronuclear NOE relaxation of $^1H^{15}N$-labelled Hsp90 N-terminal with AMP-PNP bound, at 25°C recorded at 600 MHz. Error bars indicate the standard deviation for each residue.

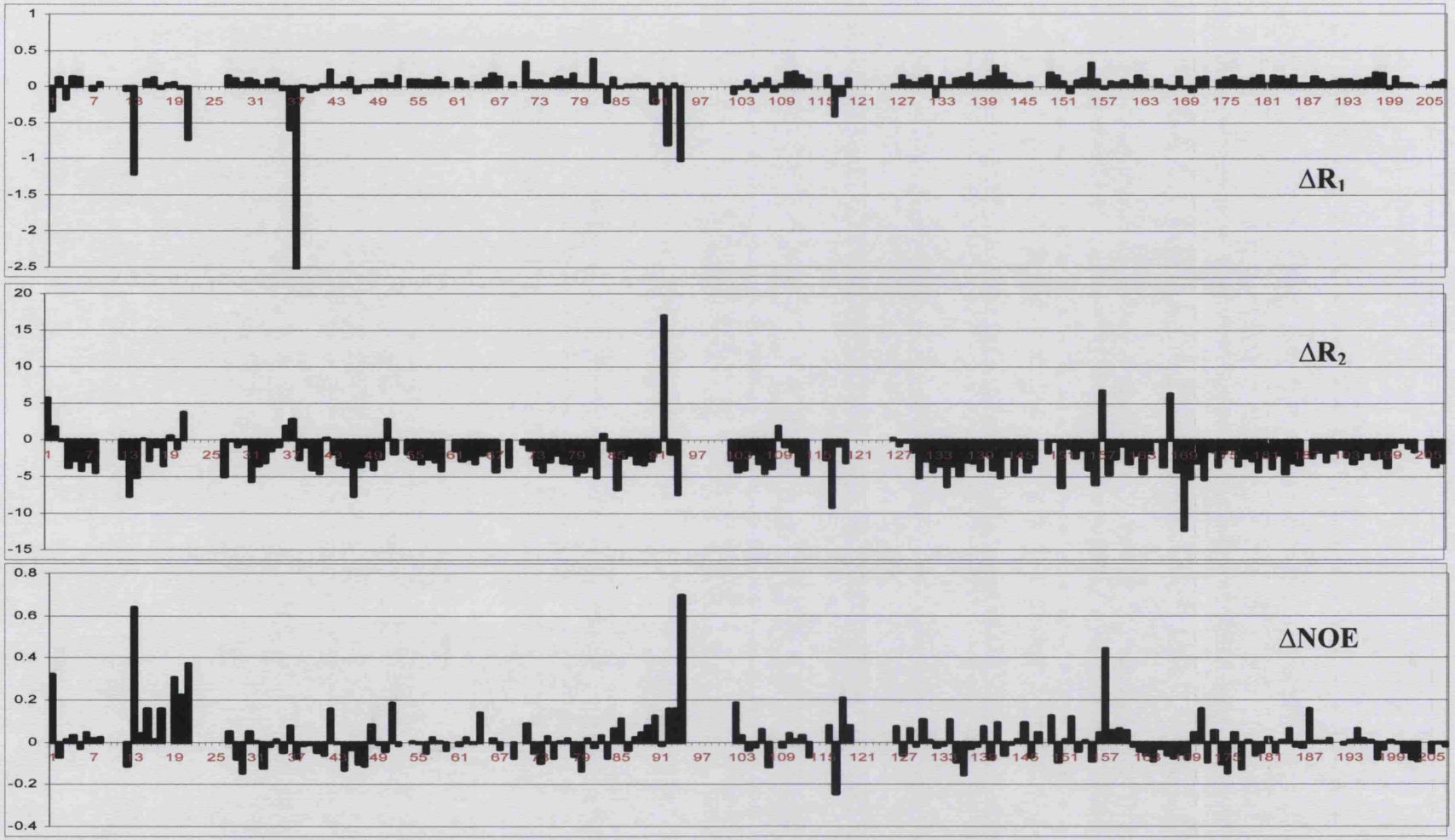

Figure 5.27 The relaxation rate difference of ΔR_1, ΔR_2 and ΔRNOE from the apo- and AMP-PNP bound Hsp90 N-terminal domain are compared.

different R_1 rate compared to the apo- sample are: 13, 21, 36, 37, 92, 94 and to lessser extent residue 117. None of these resides had a high R_1 rate in the apo- form indicating a decrease in the nanosecond time scale motion of these residues upon binding AMP-PNP to the protein (all of the above residues had a large chemical shift difference compared to the apo-form). This suggests that these residues in the AMP-PNP bound form were probably more restricted than in the apo- form. The differences between the apo- and AMP-PNP bound R_2 relaxation rates (ΔR_2) appears to demonstrate a general increase in the R_2 rate of the AMP-PNP bound form (Figure 5.27) with the exception being residues 21, 36, 37, 51, 83, 92, 157 and 167 having a decreased R_2 rate of the AMP-PNP bound complex. Residues exhibiting low R_2 values are generally believed to be involved in internal motion on a nanosecond time scale. Most of the above residues are involved in nucleotide and drug binding as described previously. Finally, the heteronuclear NOE values for the apo- and the AMP-PNP bound protein were compared. The median value did not changed for the AMP-PNP complex but the mobility of several secondary structures did change. Among the regions that became more mobile (reduced H-NOE value compared to apo-) are residues 13 to 21 on the first helix, residues 42, 51 and 64, residues 88 to 94 making the third helix, residues 102 and 118 on the ATP-lid and residue 157 located on the β-strand directly beneath the third helix.

The differences can be seen clearly in Figure 5.28 where heteronuclear NOE values are plotted on the X-ray crystal structure of the Hsp90 N-terminal domain. In this figure the residues with increased mobility are in red, highlighted using white arrows. Among these residues the most important are residues; 34, 36, 42, 84, 85, 92-94, 108, and 110-114. The unassigned residues are also shown in red

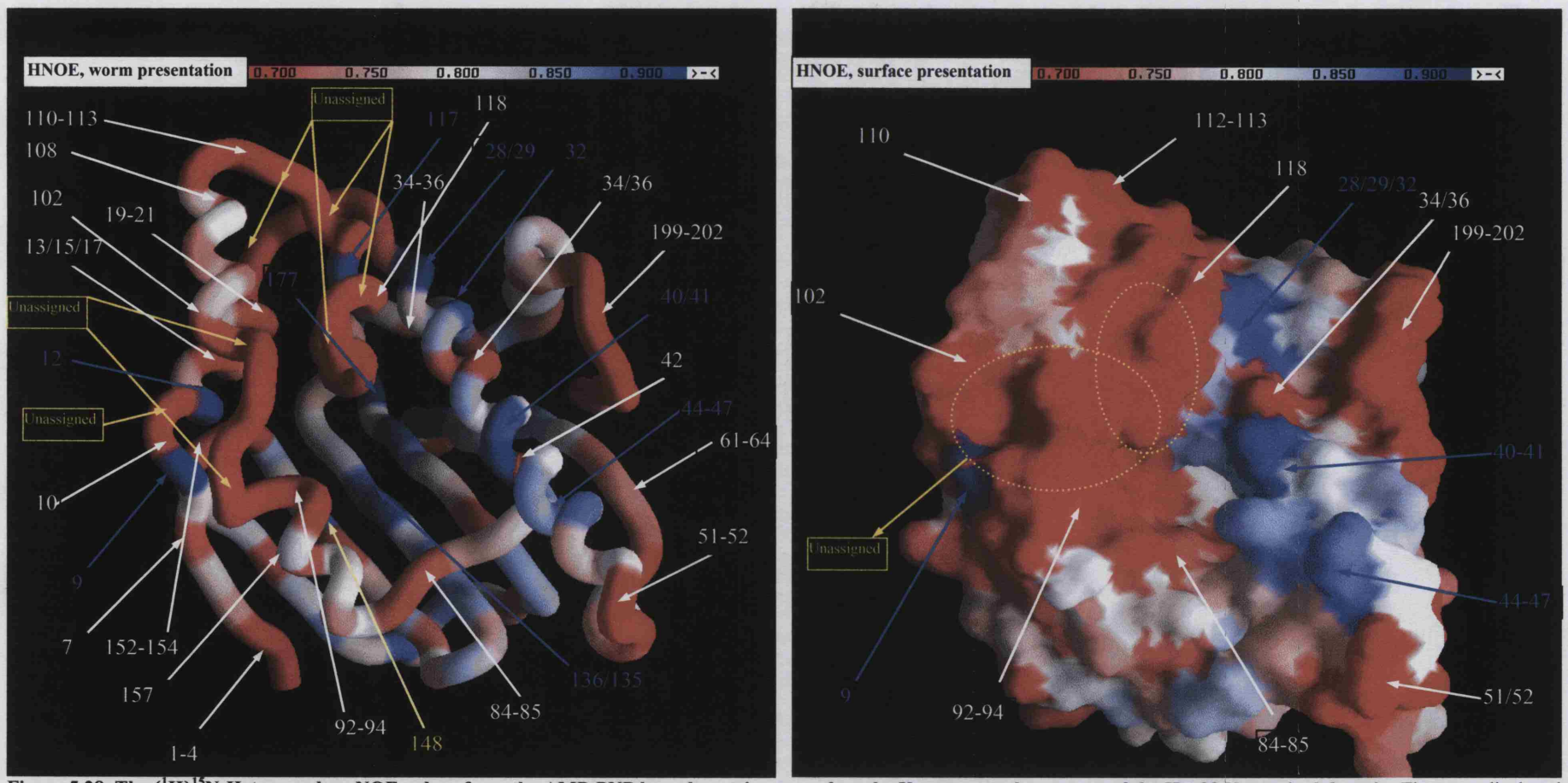

Figure 5.28. The {^{1}H}^{15}N-Heteronuclear NOE values from the AMP-PNP bound protein mapped on the X –ray crystal structure of the Hsp90 N-terminal domain. These are displayed in worm and surface area representation. Heteronuclear NOE values in red show the more mobile region (below 0.8) and in blue the least mobile (above 0.8) from the median NOE value (0.76). The unassigned residues are also displayed in red but separated using yellow arrows. (Also refer to Figure 4.8 for clarification of unassigned residues)

but separated using yellow arrows as the GRASP program used to display structures is unable to use more than two colours for visualization of the heteronuclear values. The residues with reduced heteronuclear NOE values are highlighted in blue.

Using the relaxation data, the τ_c for the AMP-PNP bound to the Hsp90 N-terminal domain was calculated. Residues 1-4, 10, 13, 15, 17, 19-21, 52, 92, 93, 102, 111, 118, 152, 157, 194 and 199-201 that predominantly belong to the flexible end or beginning of the sequence were omitted from the final calculation. As a result, an average τ_c of 14 ns was calculated from data of 155 residues. The observed increase in the τ_c could be due to a conformational change in the AMP-PNP bound form which may perhaps have changed the protein hydration resulting in a slower tumbling rate of the protein and hence an increase in τ_c. However, there does not appear to be a significant difference in the correlation time of the AMP-PNP bound protein compared to the apo-form.

5.10 Chapter summary

The main findings of this section were as follows:

- The chemical shift differences between the apo and AMP-PNP bound forms showed that the effect of AMP-PNP binding to Hsp90 was beyond the nucleotide pocket itself. This could suggest a possible conformational change that is likely to take place by nucleotide binding to the protein.
- Studies of the chemical shift changes in the 'ATP-lid' area showed that in the presence of AMP-PNP not all residues in this lid have been affected. This indicates that despite a conformational change, the closure of the lid on the

nucleotide as it was hypothesised does not occur in the presence of the AMP-PNP or in the N-terminal domain by itself.

- This could be due to:
  - The structure or conformation of the AMP-PNP itself which could possibly hinder the closure of the 'ATP-lid'.
  - The isolated N-terminal domain, which is not capable of dimerisation in solution, needs other domains (middle or C-terminal) to assist it with the conformational structural changes.
  - The requirement of other substrates or regulatory proteins to interact with the Hsp90 N-terminal domain 'ATP-lid'.
- The areas mostly affected by AMP-PNP binding were from helices 3, 4 and 5, and the second loop of the nucleotide binding pocket. This is in agreement to a degree, with what has been observed in the human Hsp90 N-terminal domain bound to GM in its closed form, but to a greater extent. The main difference is that the second loop remained mobile in the AMP-PNP bound form.
- Areas in the second helix, known from crystal structures to interact with the nucleotide, showed reduced mobility upon nucleotide binding. This suggests existence of flexibility in the second helix to accommodate and interact with the nucleotides.
- The first nucleotide binding loop, shown to be important in binding of the nucleotide, with surrounding flexible regions could be a site for interaction with other domains of Hsp90.
- Several locations that are good candidates for regulatory proteins to interact with have been found using dynamic results presented here which can potentially regulate Hsp90 N-terminal ATPase activity.

CHAPTER 6

Applications of backbone assignments

6.1 Chapter overview

In this chapter the application of the backbone assignments of the N-terminal ATPase domain of Hsp90 is demonstrated in investigations of a potential inhibitor, binding of interactions with domains of Hsp90 and of the effect of point mutation on Hsp90 structure and binding properties. First the binding of the antibiotic novobiocin with Hsp90 N-terminal domain was investigated to observe whether it was capable of binding to the protein. Next, the potential interaction of the N-terminal domain with that of the middle domain construct (which was used to solve the crystal structure of the Hsp90 middle domain, Meyer *et al.,* 2003) was investigated. Mutant constructs of the Hsp90 N-terminal domain, which have been previously shown to modify its enzymatic activity, were also investigated. Using the backbone assignment is the fastest and most accurate way for drug screening or finding compounds that interact with a protein. It is also extremely useful for investigated protein-protein interaction and mapping the interacting site on the protein structure.

6.2. Titration of novobiocin

It has previously been reported that novobiocin inhibits Hsp90 activity (Marcu *et al.,* 2000). The authors of that study suggested that this is due to novobiocin binding to an as yet uncharacterised ATP binding site in the Hsp90 C-terminal domain. However, the reported inhibition could also be explained by binding to the known N-terminal ATPase domain. The second hypothesis is particularly note worthy since the known bacterial target of novobiocin is the

ATPase domain of DNA gyrase B, which is homologous to the Hsp90 N-terminal domain. Consequently we decided to titrate novobiocin (with and without the presence of Mg^{2+}) to test the second possible explanation of Marcu *et al.* (2000), data.

Novobiocin was titrated using a 0.8 mM, ^{15}N-labelled sample of the Hsp90 N-terminal domain at 25°C and pH 8.0, using nine titration points with the spectra recorded on a 600 MHz proton frequency spectrometer. Seven aliquots of 5µl Novobiocin were added to the protein sample reaching a final concentration of 1 mM, with two extra points of 1.5 and 2.0 mM. Figure 6.1 shows six points out of nine titration points starting from the first titration point (top left in blue) moving from left to right to the final titration point at 2 mM novobiocin (bottom right in red). The superposition of the nine-titration points is shown in Figure 6.2. Comparison of the spectra confirms that novobiocin does not bind to the N-terminal domain of Hsp90. There are crosspeaks that have been shifted slightly during the titration and resonances which have disappeared. This could be due to dilution of the sample during titration, especially during the last points where the sample was diluted about 20%. Crosspeaks that are most affected belong to sidechains and residues that are sensitive to pH change (data not shown). Some of the residues affected during the titration are highlighted in Figure 6.2.

In addition to the previous experiment, a six-point titration of $MgCl_2$ was carried out on the same sample reaching a final Mg^{2+} concentration of about 1mM. Two extra points of 1.5 and 2 mM Mg^{2+} were also collected at the end of the titration. Figure 6.3 shows superposition of all the Mg^{2+} titration points in the presence of novobiocin. As expected Mg^{2+} had no effect on the sample, reasoning that novobiocin does not bind to the protein, with or without presence of Mg^{2+}.

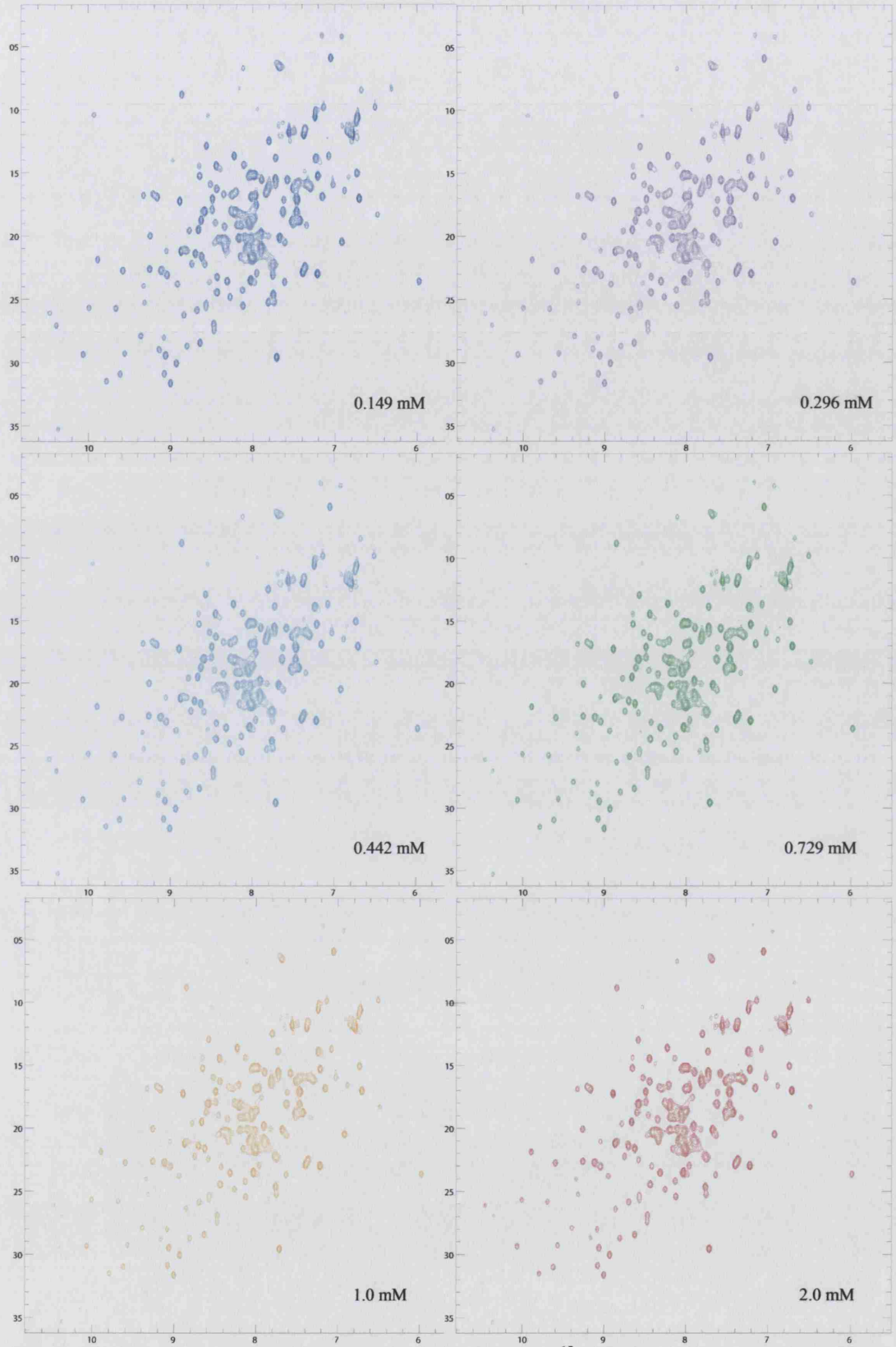

Figure 6.1. Six out of nine titration points for novobiocin in a ^{15}N-labelled sample of the Hsp90 N-terminal domain at pH 8.0, 25°C. The concentration of novobiocin is shown at the bottom right corner of each spectra.

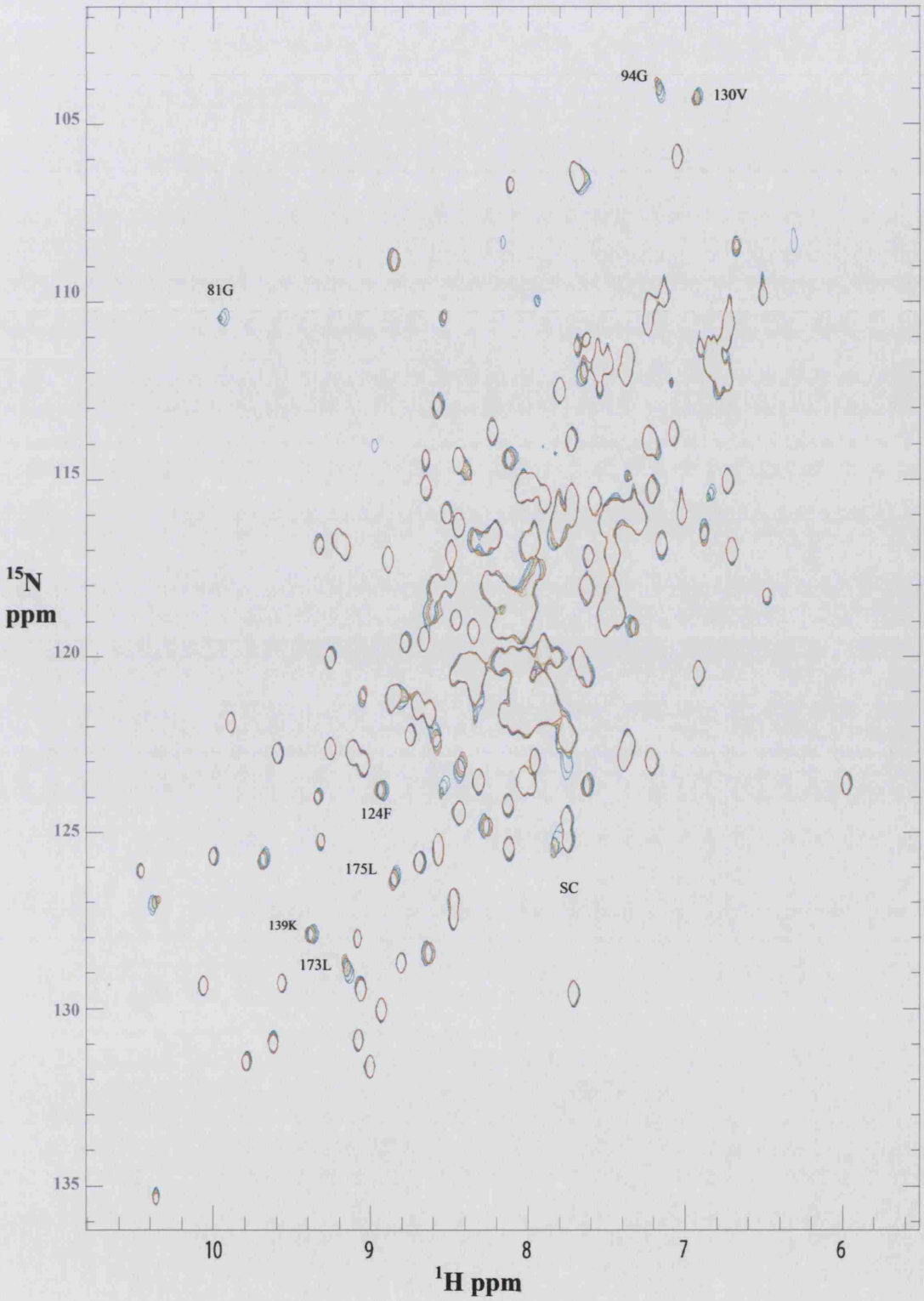

Figure 6.2. Superposition of all titration points for novobiocin against a ^{15}N-labelled sample of the Hsp90 N-terminal domain. Results show novobiocin does not bind to the protein. Some of the residues affected during the titration are highlighted. These are mostly pH sensitive residues, sidechains, or are affected as a result of sample dilution during the titration.

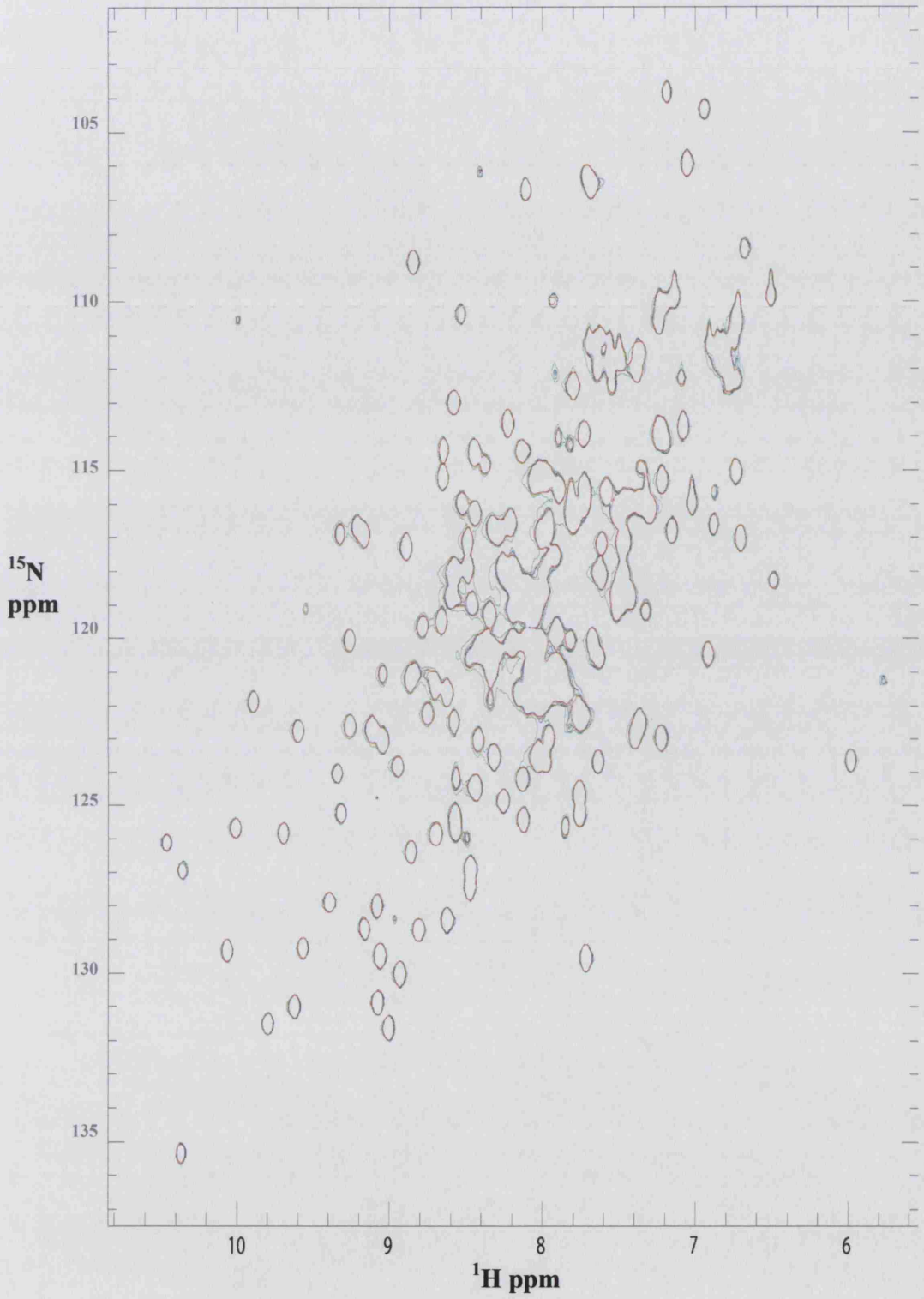

Figure 6.3. Superposition of the Mg^{2+} titration points in a ^{15}N-labelled sample of the Hsp90 N-terminal domain with novobiocin. Novobiocin does not bind to the protein neither with nor without presence of Mg^{2+}.

The structure of novobiocin is compared to the structures of GM and radicicol as shown in Figure 6.4. The possible reason for the failure of novobiocin to bind to the N-terminal domain of Hsp90 could be due to its inability to adapt the kinked formation that has been observed for the nucleotide and GM.

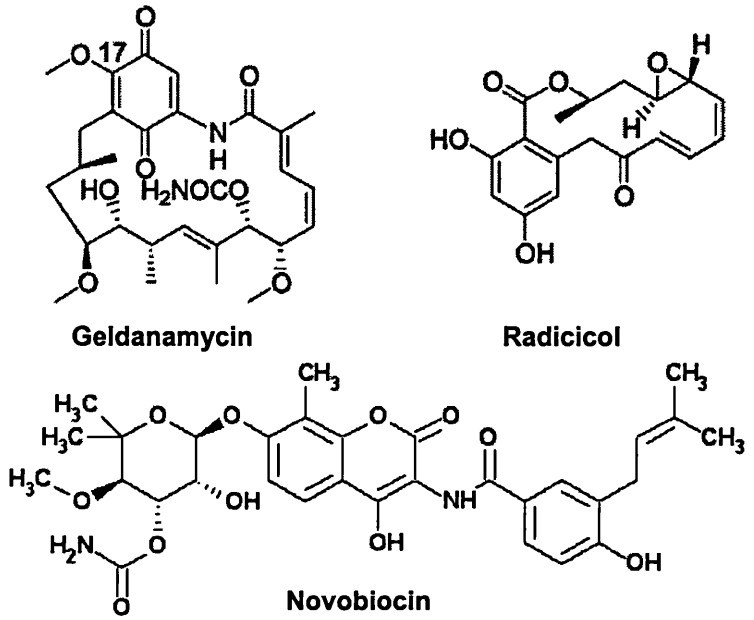

Figure 6.4. The structures of Geldanamycin and Radicicol are compared to that of Novobiocin.

This negative result eliminates the possibility of novobiocin binding the N-terminal as an explanation of its reported reduction of Hsp90 ATPase activity and consequently adds support to the idea of a second ATPase site in Hsp90.

6.3 Investigating the interaction of the middle domain (T560) construct with the N-terminal domain of Hsp90.

Meyer *et al.* (2003) have suggested in their model for Hsp90 activity that several residues from the middle domain construct of the protein interact with its N-terminal domain and could also be involved in its ATPase activity. To test this hypothesis an unlabelled sample and plasmid of the middle segment of Hsp90 (T560), which recently had its structure solved (Meyer *et al.*, 2003), was used to

investigate this. The T560 construct (kindly provided by Dr. Chris Prodromou, Institute of Cancer Research), a 36 KDa protein with an extinction coefficient of 32200 M^{-1} cm^{-1}, was measured using UV absorption at 280 nm to have a 0.4 mM concentration for 500 µl of protein. The sample was separated in two and its interaction with the ^{15}N labelled sample of the Hsp90 N- terminal domain was studied in the presence of various nucleotides.

The T560 protein was mixed with ^{15}N-labelled sample of Hsp90 N-terminal domain in the presence of Mg^{2+}, and a $^{1}H^{15}N$ HSQC spectrum was recorded at 25°C using a 600 MHz proton frequency spectrometer. The resultant spectrum is shown in Figure 6.5 (in red). This HSQC spectrum is similar to that of the apo-spectrum (shown in blue for comparison) and no obvious interaction between the two domains was observed. The crosspeaks in the N-terminal/middle domain mixed spectrum look broader than the apo- Hsp90 N-terminal domain HSQC spectrum alone. Only an extra sidechain crosspeak can be observed in the mixture spectrum, as highlighted by a black arrow in Figure 6.5.

Subsequently, AMP-PNP was added to the protein mixture and the spectra were compared to that of AMP-PNP and the N-terminal domain of Hsp90 alone. No interaction between the two domains in presence of 5 mM AMP-PNP and 5 mM Mg^{2+} was observed (Figure 6.6). Similar broadening of the crosspeaks and reduced resolution was observed in the complex spectrum compared to that of the N-terminal domain of Hsp90 and AMP-PNP. Finally ATP in presence of Mg^{2+} was added to the N-terminus/middle domain mixture and compared to that of the ATP and Hsp90 N-terminal domain. Similar to previous observation, no chemical shift differences between the two sets of experiments were observed as shown in Figure 6.7, apart from similar general crosspeak broadening.

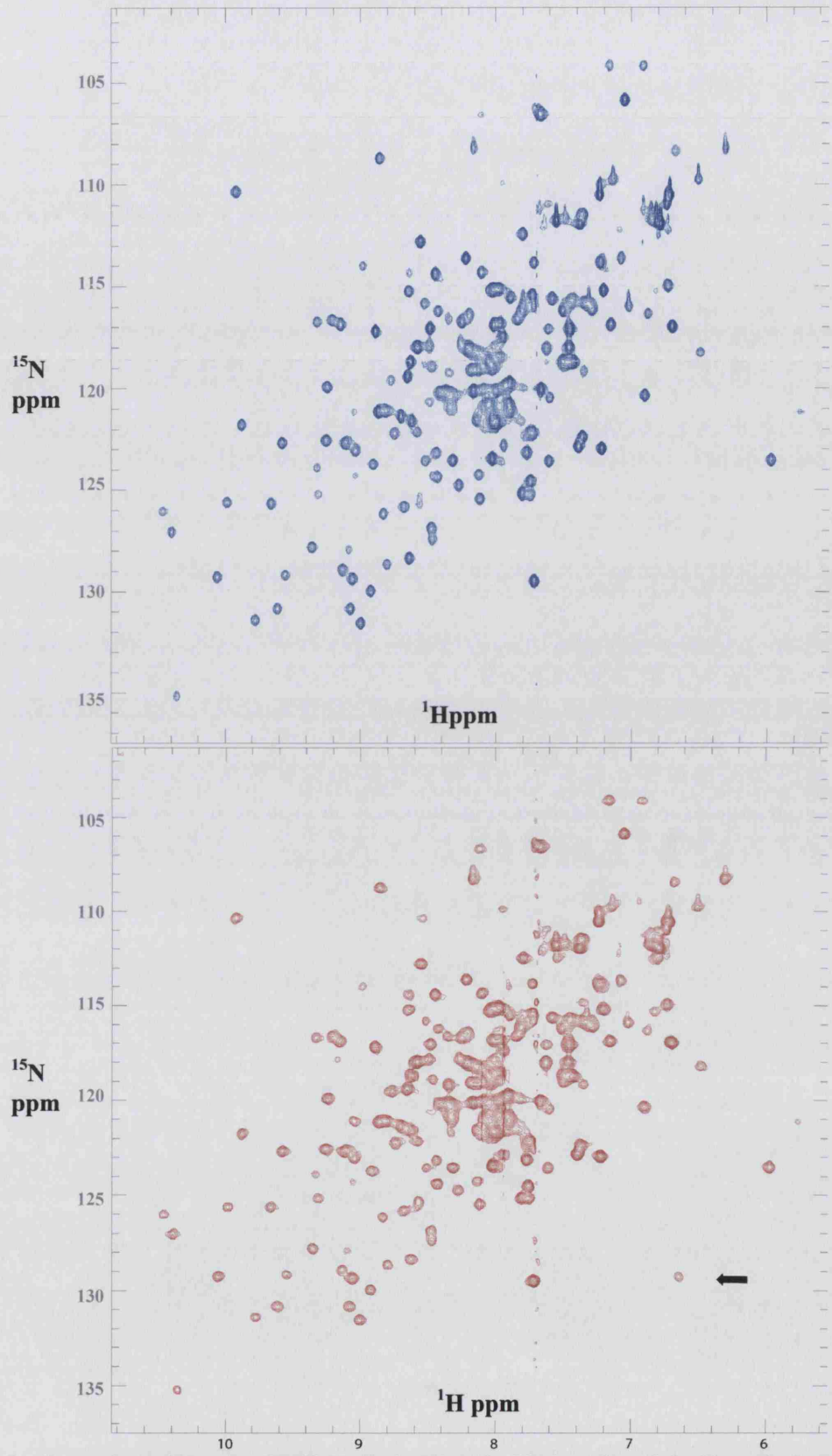

Figure 6.5. Comparison of the apo- Hsp90 N-terminal domain (blue) to that of the N-terminal and middle domain of Hsp90 (red). No interaction between the two domains was observed. The black arrow indicates presence of an extra sidechain crosspeak.

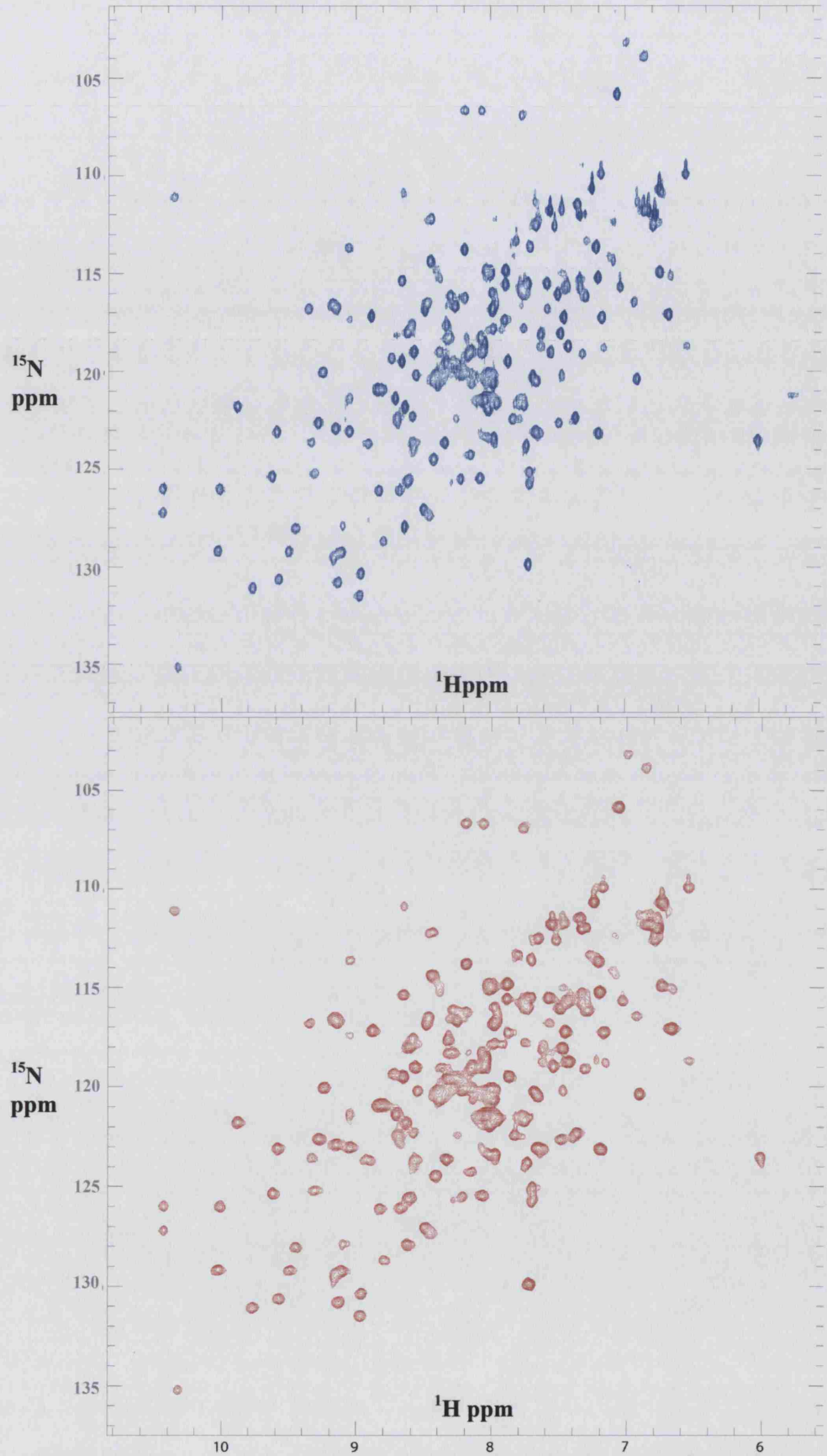

Figure 6.6. Comparison of the AMP-PNP bound Hsp90 N-terminal domain (blue) to that of the N-terminal and middle domain of Hsp90 (red) with AMP-PNP. No interaction between domains was observed.

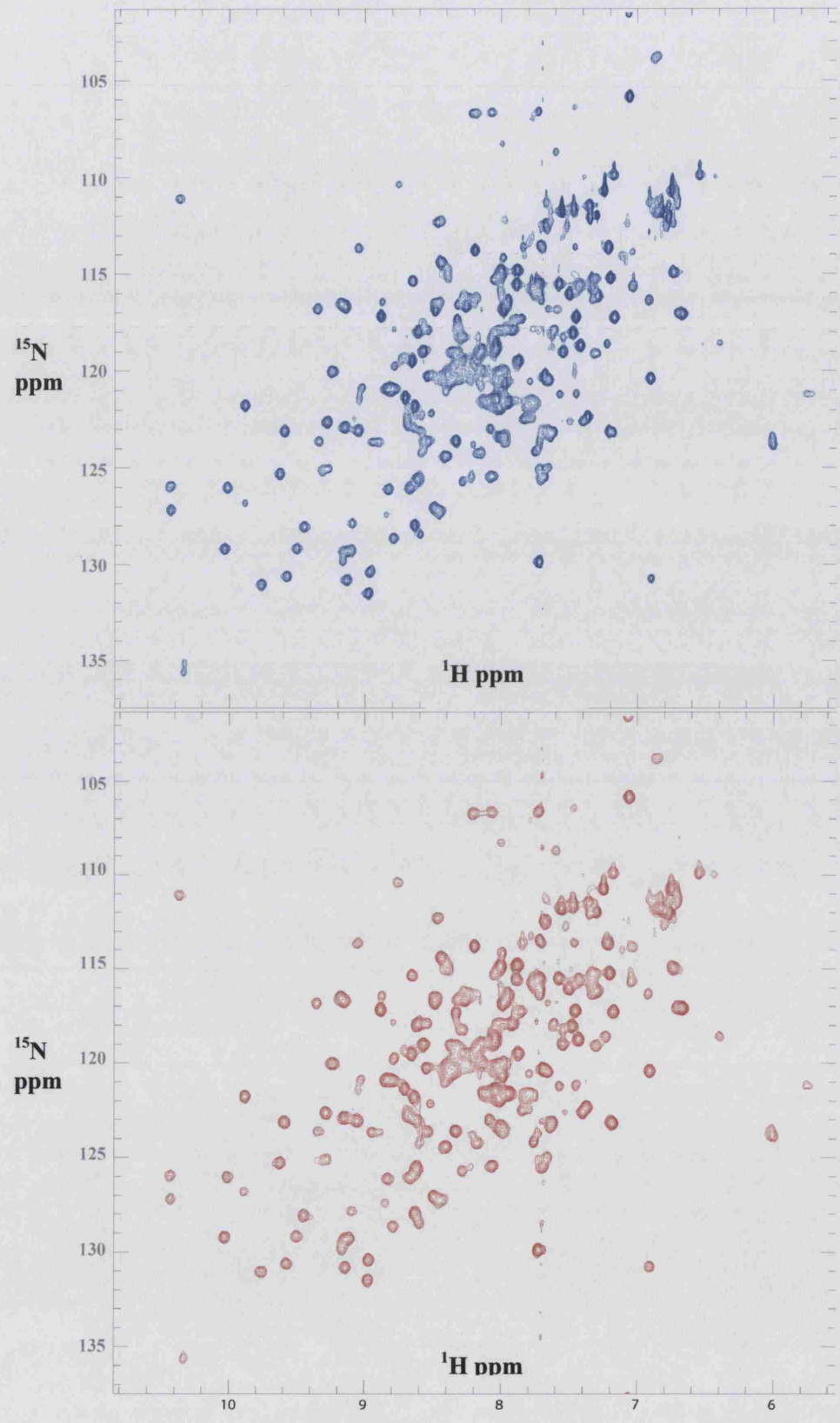

Figure 6.7. Comparison of the ADP bound Hsp90 N-terminal domain (blue) to that of the N-terminal and middle domain of Hsp90 (red) with ADP.

The cause of crosspeak broadening in all the above spectra could be due to a decrease in rotational correlation time for the labelled protein because of its interaction with the middle domain (possibly a hydrophobic interaction). All the spectra were processed as described previously in chapter 2 using similar parameters and settings.

A $^{1}H^{15}N$ HSQC spectrum of a ^{15}N-labelled sample of the T560 construct was recorded on a 600 MHz proton frequency spectrometer in 20 mM Tris in presence of Ca^{2+} (present in the crystal structure) at pH 8.0. The resultant spectrum was dominated by signals from unfolded parts of the protein in the centre of the spectrum. The existence of an unfolded region in the construct was confirmed by Dr. Chris Prodromou (personal communication) from the crystallography observations seen in the middle domain. Only about 50 resonances were observed in the spectrum (data not shown). The HSQC spectrum could be improved by making a shorter construct without the unfolded segments of the domain for future experiments on the middle domain.

6.4 Investigating the 'ATP-lid' using mutants of the Hsp90 N-terminal domain

The two mutant constructs, A107N and T101I of the Hsp90 N-terminal domain, were kindly provided by Prodromou *et al.* (2000), in order to investigate the possible different conformations that might affect the proposed 'ATP-lid' region. The residue Thr-101 is located at the beginning of one of the two helices present in the 'ATP-lid' while residue Ala-107 is located at the end of the same helix. The mutant T101I replaces a polar residue with a hydrophobic residue, whereby favouring hydrophobic interactions of isoleucine with hydrophobic

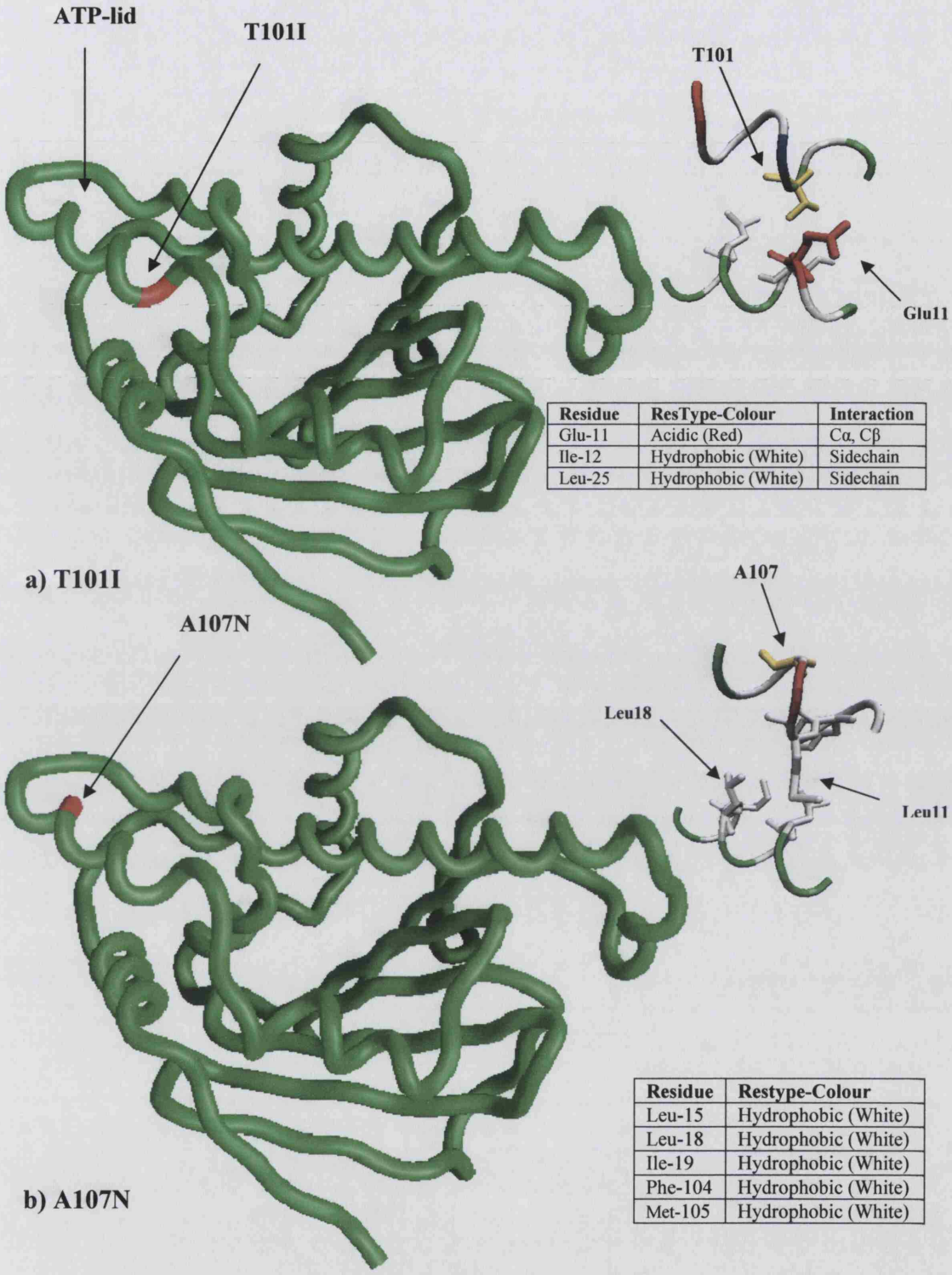

Residue	ResType-Colour	Interaction
Glu-11	Acidic (Red)	Cα, Cβ
Ile-12	Hydrophobic (White)	Sidechain
Leu-25	Hydrophobic (White)	Sidechain

Residue	Restype-Colour
Leu-15	Hydrophobic (White)
Leu-18	Hydrophobic (White)
Ile-19	Hydrophobic (White)
Phe-104	Hydrophobic (White)
Met-105	Hydrophobic (White)

Figure 6.8. The locations of the two mutated residues are shown in the X-ray crystal structure of the Hsp90 N-terminal domain. (a) Location of the T101I mutant and detail of the sidechain interaction are shown as inset with a table summarizing the interactions **(b)** location of the A101N mutant with the inset showing sidechain interactions. Mutated residues are in red in the backbone tube representation and yellow in the insert.

residues in the helix adjacent to the residue (the side chains of Ile-12 and Leu-15, and the Cα and Cβ of Glu 11) this would be anticipated to favour the 'open-lid' conformation. These interactions are shown in Figure 6.8 with details of sidechain interactions for the mutated residue inserted and summarized in a table. The mutant A107N replaces a hydrophobic residue with a polar residue with the objective of favouring the closed 'lid' conformation. The mutants studied in full-length Hsp90, had similar affinity for AMP-PNP close to that of the wild type, but with different ATPase activity and dimerisation. The effects of the mutations in the context of the full length protein are in accordance with the hypothesised 'open lid/ATPase inactive', 'closed lid/ATPase active' mechanism. The T101I had lower ATPase activity that was less able to dimerise, while the A107N showed an increase in its ATPase activity and dimerisation (Prodromou *et al.*, 2000).

In order to directly study the structural effects of the mutations, the two mutant proteins were expressed and purified in a manner similar to that of the Hsp90 N-terminal domain to yield a 0.8 mM ^{15}N-labelled sample of each mutant. The $^{1}H^{15}N$ HSQC spectra of the mutants in comparison to the apo- spectrum are shown in Figures 6.9 and 6.10. In the T101I mutant spectrum (in red) there are about 20-25 crosspeaks affected by the mutation occurring mainly in the 'lid' segment of the protein or structures close to it. Slightly more crosspeak differences (25-30) were observed between the apo- (black) and the A107N mutant (in blue) spectra (Figure 6.10). Ala-107 has been assigned in both apo- and AMP-PNP bound protein and shows a moderate shift difference between the two forms (Chapter 5). The location of Ala-107 in Figure 6.10 is highlighted using a red arrow. The amide assignment of the mutant resonances was carried out by moving the assigned crosspeaks to the closest chemical shift that could belong to the same

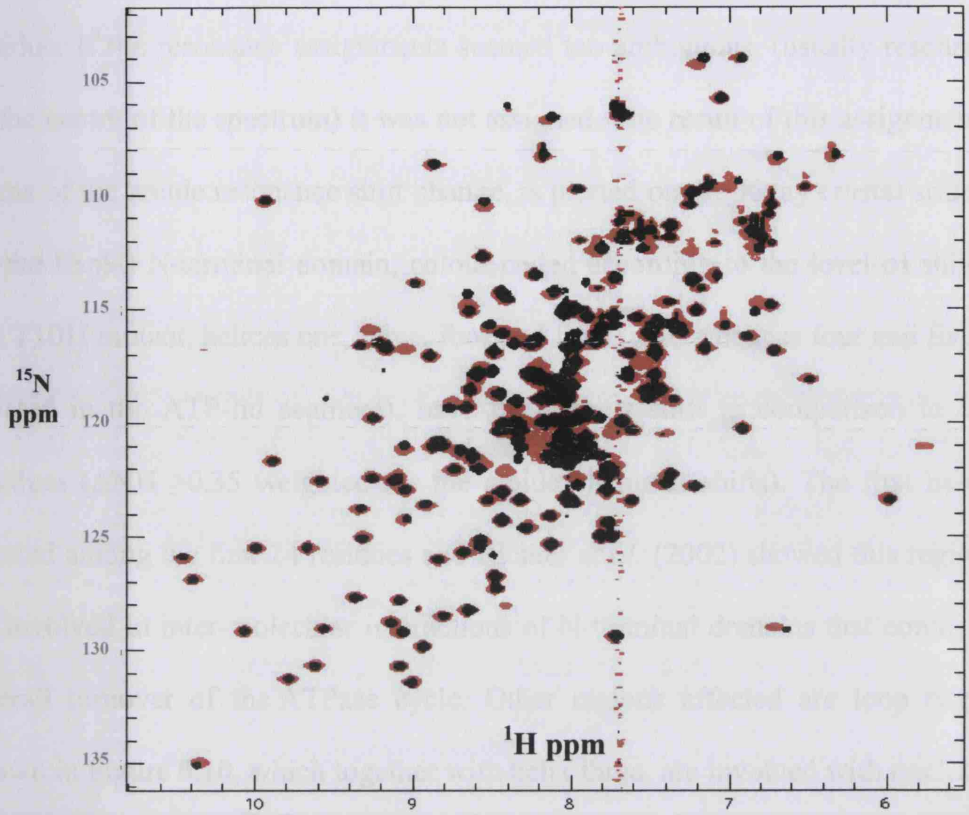

Figure 6.9. Comparison of the $^{1}H^{15}N$ HSQC apo- wildtype (black) to the T101I mutant (red) spectra (red).

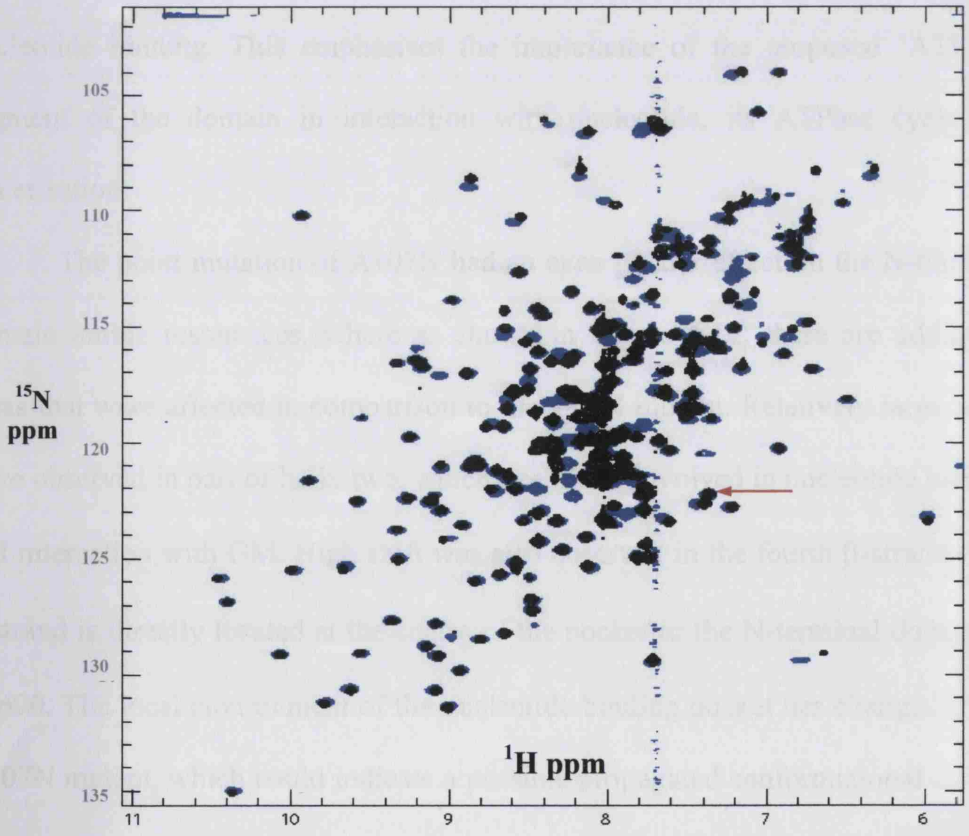

Figure 6.10. Comparison of the $^{1}H^{15}N$ HSQC apo- wildtype (black) to the A107N mutant (blue) spectra.
The red arrow indicates the location of Ala-107

residue. If the resonance assignments seemed too ambiguous, (usually resonances at the centre of the spectrum) it was not assigned. The result of this assignment, in terms of the amide resonance shift change, is plotted on the X-ray crystal structure of the Hsp90 N-terminal domain, colour coded according to the level of shift. In the T101I mutant, helices one, three, four and five, (where helices four and five are located in the ATP-lid segment), have the highest shift in comparison to other residues ($\Delta NH \geq 0.35$ weighted for the amide chemical shifts). The first helix is located among the first 24 residues and Richter *et al.* (2002) showed this region to be involved in inter-molecular interactions of N-terminal domains that control the overall turnover of the ATPase cycle. Other regions affected are loop two, as shown in Figure 6.10, which together with helix three, are involved with nucleotide binding. The pattern shown as a result of point mutation resembles that of nucleotide binding. This emphasises the importance of the proposed 'ATP-lid' segment of the domain in interaction with nucleotide, its ATPase cycle and dimerisation.

The point mutation of A107N had an even greater effect on the N-terminal domain amide resonances, where as shown in Figure 6.11, there are additional areas that were affected in comparison to the T101I mutant. Relatively large shifts were observed in part of helix two, which itself is in involved in nucleotide binding and interaction with GM. High shift was also observed in the fourth β-strand. This β-strand is directly located at the centre of the pocket in the N-terminal domain of Hsp90. The local environment of the nucleotide binding pocket has changed in the A107N mutant, which could indicate a possible propagated conformational change in the 'lid' segment due to the mutation. The above results could explain some of the alterations observed in the full-length protein, which result due to a change in

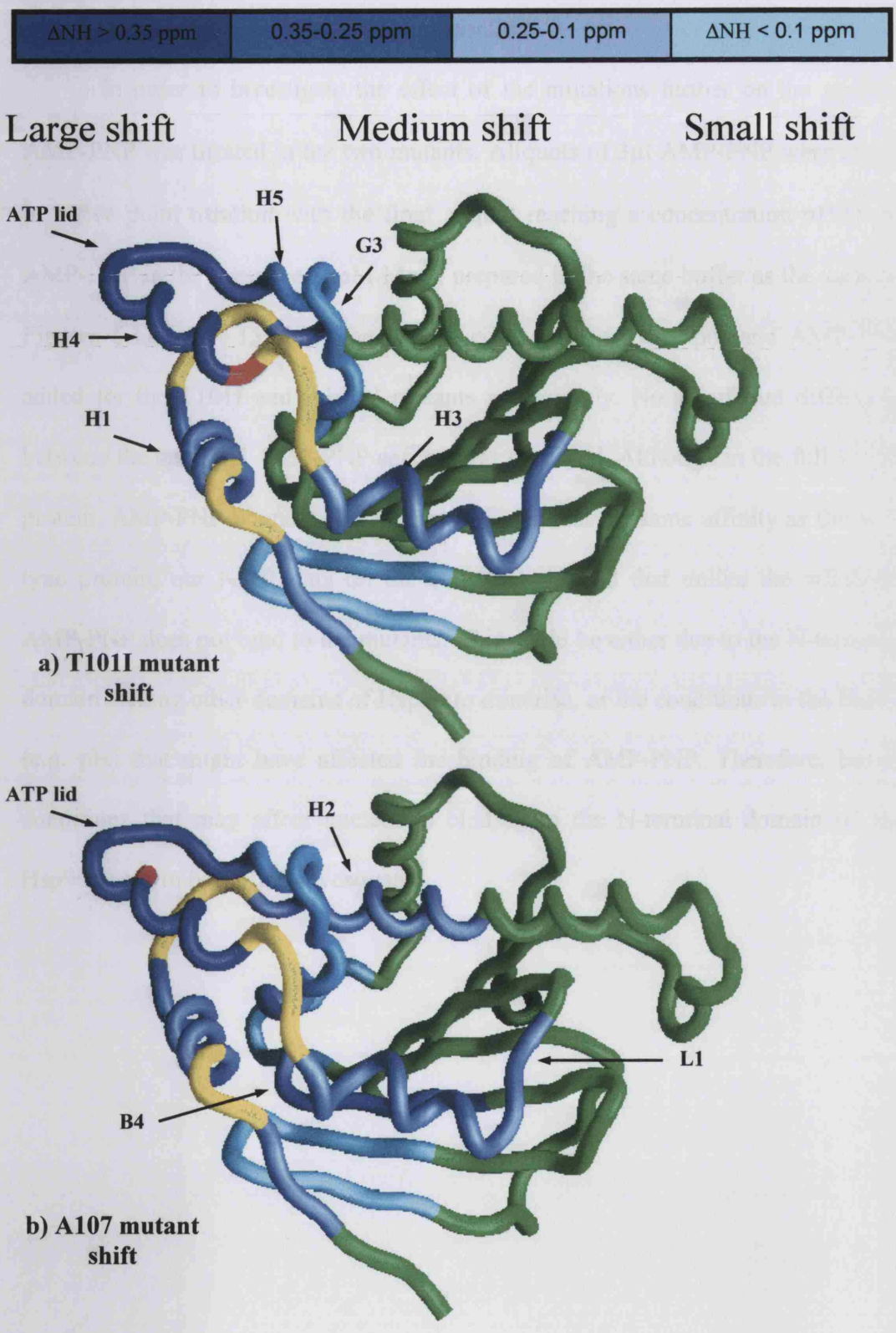

Figure 6.11. Areas affected by the mutation for the T101I (a) and A107N (b) mutants. The backbone is colour coded according to the size of the amide shift relative to wildtype. Unassigned areas are in yellow, whereas the mutation points are in red.

their ATPase activity and therefore dimerisation.

In order to investigate the effect of the mutations further on the protein, AMP-PNP was titrated in the two mutants. Aliquots of 3µl AMP-PNP were added in a five point titration with the final aliquot reaching a concentration of 5 mM AMP-PNP in the presence 5 mM Mg^{2+}, prepared in the same buffer as the sample. Figures 6.12 and 6.13 show the spectra comparison of the apo- and AMP-PNP added for the T101I and A107N mutants respectively. No significant difference between the apo- and AMP-PNP spectra was observed. Although in the full-length protein, AMP-PNP bound to the mutants with almost the same affinity as the wild type protein, our NMR data on the construct showed that unlike the wildtype, AMP-PNP does not bind to the mutants. This could be either due to the N-terminal domain lacking other domains of Hsp90 to dimerise, or the conditions in the buffer (e.g. pH) that might have affected the binding of AMP-PNP. Therefore, buffer conditions that may affect nucleotide binding to the N-terminal domain of the Hsp90 needs to be further investigated.

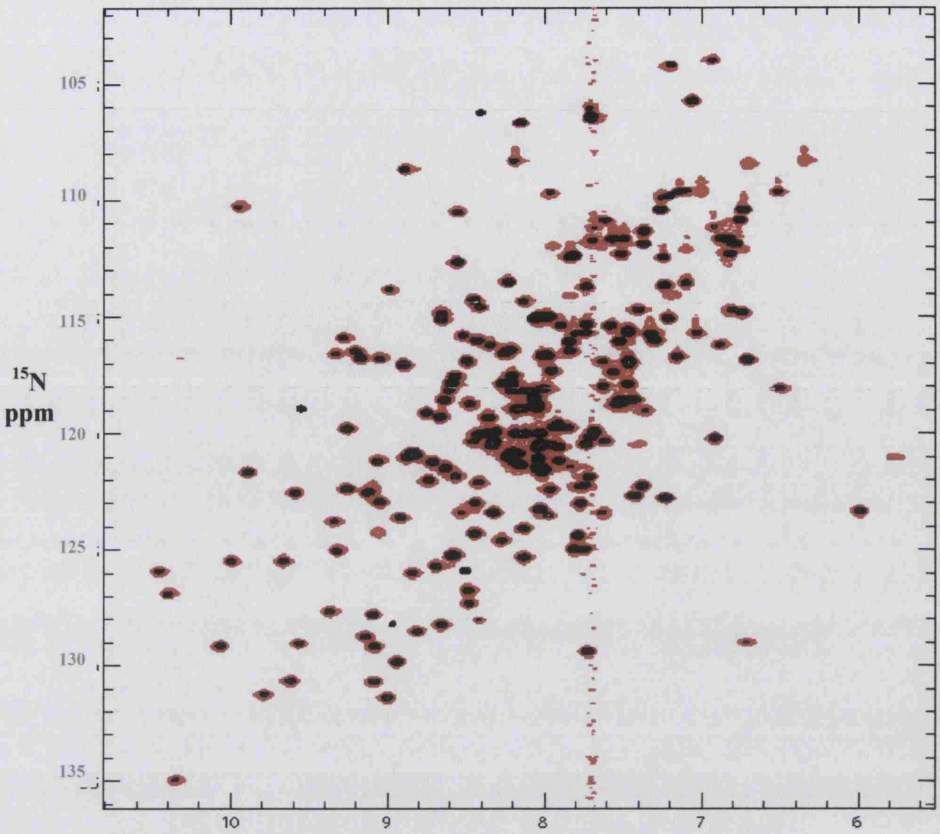

Figure 6.12. Comparison of the T101I mutant apo- (red) with AMP-PNP (black) spectra.

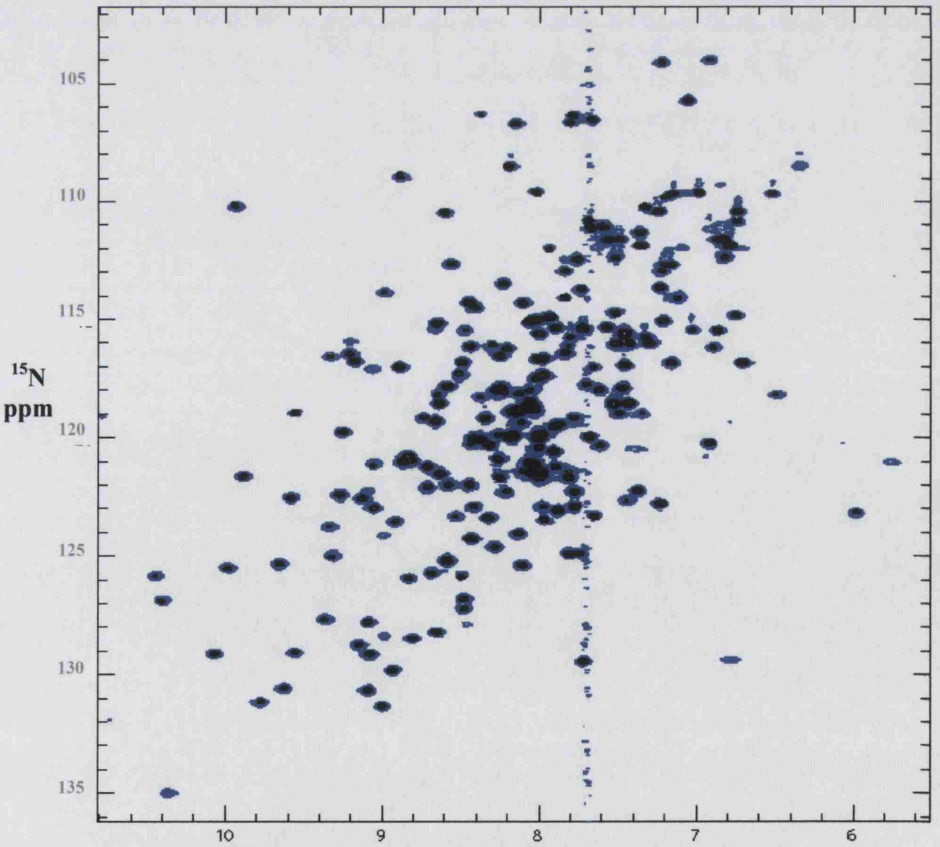

Figure 6.13. Comparison of the A107N mutant apo- (blue) with AMP-PNP (black) spectra.

6.5 Chapter summary

The main findings of this section were as follows:

- Novobiocin does not bind to the Hsp90 N-terminal domain, supporting the idea of a Novobiocin binding site elsewhere in Hsp90.
- No conformational change in the N-terminal domain of Hsp90 with the middle domain was observed, with or without presence of nucleotide, this may undermine the idea that the middle domain is involved in nucleotide binding
- Relatively large shifts in helices 3 and 4 and parts of the lid were observed as a result of the two point mutations. This suggests the importance of the interaction of the two mutated residues with the surrounding secondary structures for preference of the wild-type population.
- AMP-PNP was found not bind to the mutant constructs of the Hsp90 N-terminal domain, which is in conflict with reports of increased ATPase activity of the full length point mutant. Reconciliation of these observations will require further study perhaps of larger constructs.

CHAPTER 7

DISCUSSION

The structure of the human (Stebbins *et al.* 1997) and yeast (Prodromou *et al.* 1997) Hsp90 N-terminal domains haves been solved using X-ray crystallography. The human structure was also solved bound to GM, which showed conformational differences in 34 residues (residues 100 to 134) between the apo- and the drug bound structures of the human Hsp90. These differences began at the fourth helix, continuing to the second loop of the nucleotide binding pocket and ending at helices five and six which construct the 'ATP-lid'. The difference was initiated by movement of the second loop by about 9 Å, closing like a 'trap door' on GM which also resulted in displacement of the mentioned secondary structures (Stebbins *et al.* 1997). In contrast, despite high structural homology between the apo- human and yeast Hsp90 N-terminal domains, no significant structural differences (except rearrangement of the Lys-98 sidechain) were observed between the apo- and the ADP or ATP bound structures of the yeast domain.

Structural homology studies showed that the Hsp90 N-terminal domain is a member of an ATPase superfamily known as GHKL (Bergerat *et al.* 1997; Dutta and Inouye 2000). The homology studies combined with other biochemical observations suggested the possible presence of a conformational change in the ATPase domain of Hsp90 upon binding nucleotide, that might result in dimerisation of the protein (Prodromou *et al.* 2000). Prodromou *et al.* (1997) suggest a model based on the Hsp90 homologues in which a segment of the protein (residues Gly-100 to Gly-121) acts like a 'lid', with a hinge around the conserved glycine residues that closes on the nucleotide upon binding, resulting in association of the protein. This segment was consequently designated as the 'ATP-lid' (Prodromou *et al.* 2000). However this conformational change has not been observed in all of the X-ray crystal structures solved for the yeast Hsp90 to date. It

was therefore hypothesised that the constrains of the crystal structure prevented a motion that would occur *in vivo*.

In this thesis the aim was to investigate the nucleotide-binding domain of the yeast Hsp90 N-terminal domain in solution using NMR spectroscopy and to identify any potential conformational change upon nucleotide binding in solution. The initial comparison of the ATP and ADP bound spectra to that of the apo-HSQC spectrum showed large numbers of crosspeaks perturbed upon nucleotide binding with differences of about 25 resonances observed between the ATP and ADP spectra. Studies using size exclusion chromatography and 1D NMR diffusion experiments (temperatures ranging from 10°C to 35°C) confirmed earlier studies by Weikl *et al.* (2000) showing that the apo- N-terminal domain of Hsp90 in solution is a monomer in both apo- and nucleotide bound forms.

Time course titrations, beginning with an excess of a 20-fold protein concentration of ATP, at 25°C showed slow ATPase activity of the Hsp90 N-terminal domain with growth of the characteristic ADP bound resonances over time. Since the protein had an ATPase activity, ATP itself could not be used for a backbone assignment. Adding AMP-PNP to the protein sample in a separate experiment and comparison of the spectrum with that of the apo-, ATP and ADP spectra showed that it can be a good model for the ATP bound structure and was hence chosen for backbone assignment (AMP-PNP is a non-hydrolysable analogue of ATP). In order to investigate the conformational changes using NMR and to quantify it, the first step was to achieve the sequential backbone assignment of the apo- and AMP-PNP bound structures

A set of triple resonance 3D heteronuclear experiments (Yamazaki *et al.* 1994b) was applied to $^{2}H^{15}N^{13}C$ labelled sample and the resulting spectra were

used for the backbone assignment. As a result, a near complete amide backbone assignment for the apo- (197 resonance including 5 prolines out of 207 residues, 95%) and a less complete assignment for the AMP-PNP bound protein (187 out 207 including the prolines, 90%) in solution were achieved. Backbone assignments are the first step in solving protein structure using NMR and additionally provide a wealth of information about individual residues and secondary structures in the protein, their interaction with ligand and enable detection of any change in their local environment. The information from backbone assignments in combination with relaxation data are particularly useful in this case because an X-ray crystal structure of the protein is available, and the changes in residues chemical shift could be mapped on the Hsp90 N-terminal domain structure for analysis (Prodromou *et al.* 1997). Finally, comparison of the apo- with that of the AMP-PNP bound assignments made it possible to map areas affected by nucleotide binding, and to detect the areas involved in the protein conformational change. The chemical shifts of the assigned backbone and sidechain nuclei were also used in the estimation of the secondary structure of the protein in solution. The majority of the secondary structure was similar in the crystal and solution forms with some minor differences observed. The backbone assignments are also particularly useful in studying the effect of point mutation on the protein structure. Another potential use of the backbone assignments is in detecting protein-protein interactions and to determine regulatory areas in the proteins structure that are affected by cofactors. The NMR results for the Hsp90 N-terminal domain are presented here with different region of the protein presented as separate segment. In order to assist the discussion Figure 7.1 was used highlighting various segments of the protein highlighted thought the protein backbone in yellow or red.

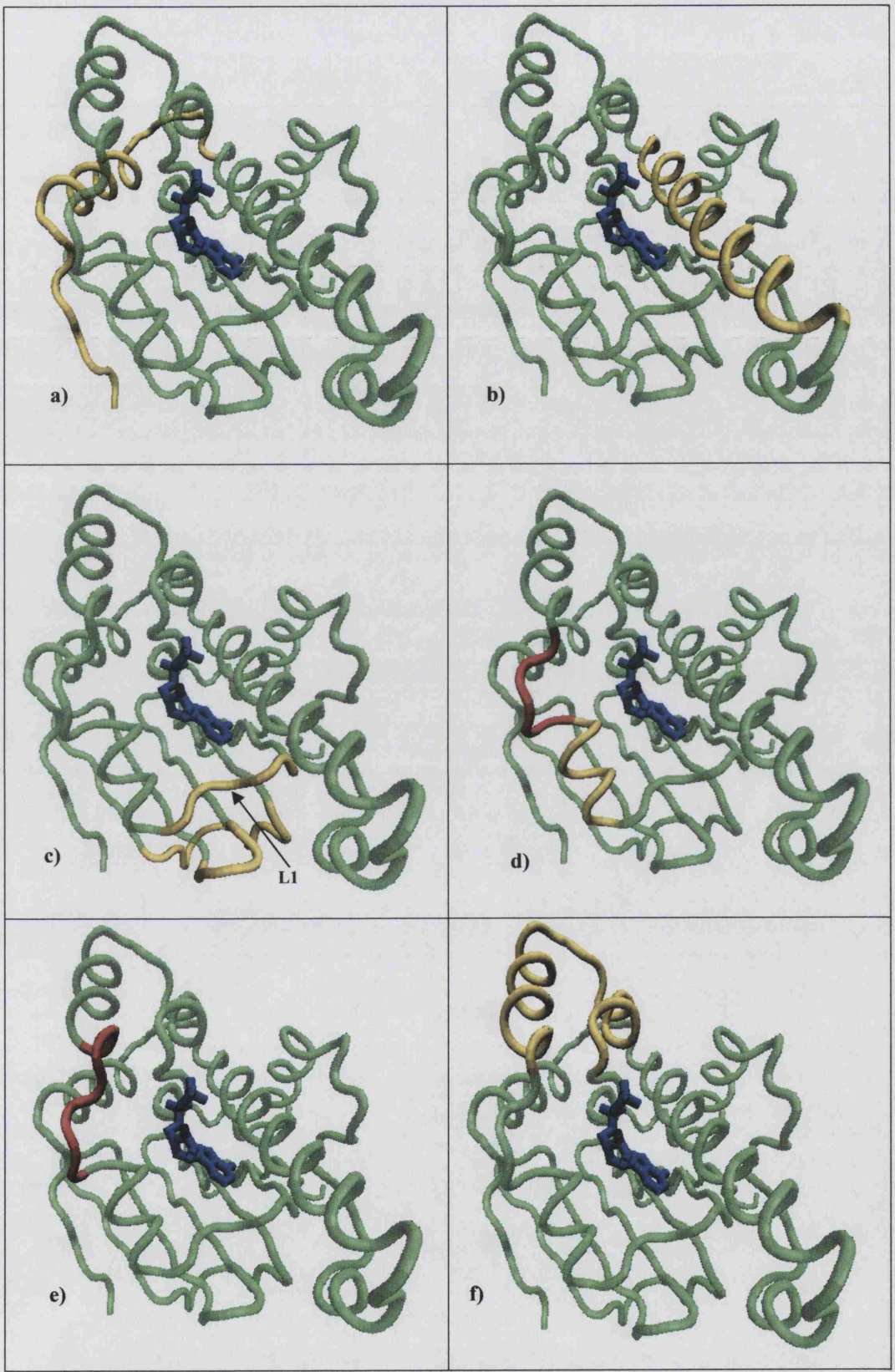

Figure 7.1. Various regions of the Hsp90 N-terminal domain highlighted on a tube representation. The transparent green regions show the entire backbone structure. Blue regions show the bound ADP and the highlighted red regions are suggested to have high mobility. The yellow segments correspond to residues considered further in the text. Representations (a-f) are referred to and discussed in sections 7.1–7.4.

7.1 Observations for residues 1 to 28

NMR results for the first 28 residues, highlighted in yellow in Figure 7.1.a, as well as earlier observations by Richter *et al.* (2001), suggests an importance role for the first 24 amino acids in ATPase activity and association of the N-terminal domain. The residues located on the first helix (residues 10 to 21) are not in direct contact with the nucleotide but were affected by AMP-PNP binding. The first helix is located directly beneath part of the 'ATP-lid' (helix four), with the loop connecting the first helix to the second helix lying beneath the loop segment of the lid. Relaxation data showed mobility more than average for this helix and its adjacent loop. A relationship between this region and the 'ATP-lid' must exist because the adjacent regions in both areas are affected by nucleotide binding. The amide chemical shift differences ($\Delta\delta$NH) also confirmed a change in the local environment of these residues during AMP-PNP binding. A secondary structure change was also predicted from the $^{13}C\alpha$ and $^{13}C\beta$ nuclei backbone chemical shift differences ($\Delta\delta^{13}C$) for the residues in this region.

The secondary structures predicted using the chemical shifts for the apo- and the AMP-PNP bound, predicted a larger helix (8-20) compared to the X-ray crystal structure (10-20). Supporting these assumptions were NMR observations for the A107N and T101I mutants. Both mutations caused an effect in relatively large areas of the protein, especially in the first, third and fourth helices with their relevant adjacent connecting loops. These mutants were designed, to favour either the open (T101I) or the closed (A107N) lid conformation on the basis of interactions between the fourth and the first helices (Prodromou *et al.,* 2000). Results also showed that neither of the two mutants were able to bind AMP-PNP

which could be due to disfavouring the open conformation of the protein, resulting in dominance of this disrupted population observed in the spectra, even in the presence of AMP-PNP. Changes caused by mutation in the interaction between the two helices might be the cause of this disruption.

The open conformation was dominant in all observed crystal structures solved so far for the Hsp90 N-terminal domain. Also, the thermo-sensitive mutant T22I which has a mutation located in the loop connecting the first helix to the second helix, caused a change in the ATPase activity of the protein (Prodromou *et al.* 2000). This is another example of the importance of this region in nucleotide binding. Part of this loop, residues 22 to 26, was not assigned in the apo- and the AMP-PNP bound structures suggesting mobility and/or exchange with local environment. This region (residues 20 to 27) could potentially be a good candidate for binding of ATPase regulatory proteins to the Hsp90 N-terminal domain, by potentially changing the flexibility of this segment and consequently its interaction with the ATP-lid and the nucleotide binding pocket itself. Residues 9 and 11 located at the beginning of the first helix were also not assigned and are presumed flexible. This region will be discussed together with the second loop of the nucleotide binding pocket.

7.2 The second α-helix

The second helix (residues 27 to 50 as shown in Figure 7.1.b) is one of the important secondary structures in the protein, which constructs one side of the nucleotide-binding pocket and according to the crystal structure is the longest α-helix structure present in the protein. The secondary structure predicted for this

helix, using chemical shifts suggested residue Ile-45 to be coil in both apo- and AMP-PNP bound structure. This can potentially break the second helix into one larger and one smaller helix towards the end of the secondary structure. Residues 44 to 46 in the apo- form had greater than average local motion, which was reversed by nucleotide binding. The Lys-44 sidechain interacts through solvent with the O2' and O3' oxygens of the ribose sugar of the nucleotide (Prodromou *et al.* 1997). The reduced mobility upon AMP-PNP binding could be explained by the interaction of this residue with the nucleotide. Residue 45 can provide a flexible point from which the end part of the second helix can potentially move towards the nucleotide in a breathing mechanism.

The relaxation studies also highlighted another mobile segment, around residues 34 to 36, in the same helix. Residue Glu-33 is located here which is believed to interact with the γ-phosphate of the ATP through a water molecule and initiates the hydrolysis of ATP (Panaretou *et al.,* 1998). The mobility of this region suggests existence of an inherent flexibility in this part of the helix that can accommodate a nucleotide or is capable of moving closer and interacting with it. Blocking this movement, potentially by drugs that bind to the protein, could disable the ATPase activity of the protein. The ΔδNH suggests a change in the local environment of these residues (34 to 40). The $\Delta\delta^{13}C$ from all three nuclei also confirmed a conformational change in the secondary structure of residues 33 to 40. The relaxation data for the AMP-PNP bound protein compared to the apo- form showed reduced flexibility for residues 40 and 41 which could be due to van der Waals interaction of residue 41 with the adenine base of the nucleotide and binding of the Asp-40 sidechain through water to the β-phosphate of the nucleotide. Residues 27 to 29 at the beginning of this helix were also affected and changed

during nucleotide binding, which could be due to their location (close to the first mobile loop and the ATP-lid) or secondary effect from the adjacent mobile loop. Residues 51 to 64 after the second helix, on average, showed flexibility that remained unchanged during nucleotide binding. This part will be further discussed in the next section.

7.3 The first nucleotide binding pocket loop and its neighbouring secondary structures

One important segment is the first loop of the nucleotide-binding pocket, which consists of residues 80 to 85 highlighted in yellow (L1) in figure 7.1.c. The ΔδNH for this region showed that the local environment for the whole segment was changed during nucleotide binding. The $\Delta\delta^{13}C$ showed a secondary structure change for residues 80 to 83 upon binding of AMP-PNP. The secondary structure for part of this segment (residues 83 to 85) was predicted as β-sheet in the AMP-PNP bound form compared to the coil predicted in the apo- and in the X-ray crystal structure. This suggests that parts of this region have become more structured upon ligand binding.

Residue Asp-79 located on the β-sheet connected to the loop has the only direct hydrogen bond to the nucleotide from its carboxylate sidechain to the exocyclic N6 group of the bound nucleotide. This residue had a relatively small ΔδNH and $\Delta\delta^{13}C$ in contrast to what was expected. This suggests that residues 80 to 84 may play a more important role in interacting with the adenosine, stabilising and binding of the nucleotide coupled with Asp-79. It is already known that Met-81

has a van der Waals interaction with adenosine of the nucleotide from crystal structure.

Most of the secondary structure located spatially adjacent to this segment have a slightly different secondary structure predicted, usually an extension to the β-strand making the bottom of the nucleotide binding pocket (residues 140 to 144 and 160 to 169) as shown in Figure 7.1.c. Also looking at the structure close to this loop, which mostly consists of loops and β-turns, this region seems to be affected by packing in the crystal structure, which could be due to the flexibility of residues, confirmed also from relaxation data presented here. The highest local motion observed in this region was for residues 160 to 169. In all, this could explain the slight deformity observed in the secondary structures of the region. These residues actually may be more aligned with the rest of the β–sheet, which makes the bottom of the nucleotide binding pocket, instead of protruding out as was seen in the crystal structure. The flexibility observed in this region suggests presence of another location for binding of regulatory proteins or a site with which other domains in the Hsp90 may interact.

7.4 Observation for the third helix and second nucleotide binding pocket loop

Another important region in the Hsp90 N-terminal domain is the third helix (residues 86 to 93, highlighted in yellow in Figure 7.1.d) and the second loop of the nucleotide-binding pocket (residues 94 to 98, highlighted in red in Figure 7.1.d). These two segments make the side of the nucleotide-binding pocket opposite to the second helix. Movement of the second loop has been observed in the human homolog of the Hsp90 N-terminal domain closing on GM and acting as trapdoor.

However, this local motion has not been reported so far for the yeast homologue even in presence of GM. No resonance for parts of this second loop extending to helix four (residues 97 to 101 in apo- and 95 to 101 in AMP-PNP bound) have been observed.

The surface representation of the X-ray crystal structure shows that the residues in this region are all on the surface and good candidates to have inherent flexibility, shown n rd in Figure 7.1.e. Because no resonance for residues in this region was observed it seems that it remains mobile even in the presence of nucleotides. This region is also important in the GHKL superfamily as a whole and plays a similar role by trapping the ligand via a conserved monovalent cation-binding site (Hu *et al.* 2003). Hu *et al.* (2003) also suggested that this monovalent cation-binding site is essential for ATPase activity in the GHKL superfamily. They have reported that a water molecule was present in the X-ray crystal structure of the Hsp90 N-terminal domain in the same locations as the monovalent cations in other GHKL members. Also, dependence of the ATPase activity of the protein with monovalent salt concentration has been reported (Weikl *et al.*, 2000). Residue Lys-98 according to the X-ray crystal structure has a direct ion pair or hydrogen bond to the β-phosphate group of the nucleotide (Prodromou *et al.* 1997). This residue, together with Asn-37 and Asp-40 in the second loop and residues 118 to 124 which make a hydrophobic patch could be responsible for the unusual kinked shape formation of the nucleotides as well as providing the contact interface with the phosphate groups of the nucleotide.

Sequence homology shows that Lys-98 is a conserved residue which, assisted by the motion of the second loop, could possibly also be responsible for the ATPase activity of the Hsp90 N-terminal domain or alternately play an

important role in ATPase activity due to its location. The highest chemical shifts were observed for residues in this region. This region is also located close to the first 12 resides, and together with unassigned residues 9 and 11, makes an unassigned area which could be due to flexibility of the residues in this region. This area at the surface of the protein can potentially coordinate interactions with other proteins, co-factors or Hsp90 domains that might have an effect on the ATPase activity of the protein (Sullivan *et al.,* 2002).

In the ATP-lid region the highest level of $\Delta\delta$NH and $\Delta\delta^{13}$C has been observed for most of the residues in this region, Figure 7.1.f, despite being away from the nucleotide-binding pocket. This suggests a possible conformational change of residues in the ATP-lid is very likely. However, this large shift is not uniform throughout the whole ATP-lid and varies for different residues.

The conclusion from studying the chemical shift differences and relaxation studies in this area is that the ATP-lid does not fold on the nucleotide binding pocket as hypothesised or that is unlikely to take place in presence of the AMP-PNP. Nevertheless, large parts of the lid will probably undergo a conformational change. The fourth helix together with the third helix and the second loop in the presence of AMP-PNP has the highest overall chemical shifts and most probably change as observed in the human homologue but to a possibly greater extent. Parts of the second helix and the first nucleotide binding pocket loops also go through a conformational change to accommodate the nucleotide. Unlike in the human Hsp90 N-terminal the second loop remains mobile when nucleotide is bound. No structural conformational change in human Hsp90 upon nucleotide binding has been reported to date. What is apparent is that binding of AMP-PNP to the Hsp90 N-terminal domain is not sufficient to cause lid closure. Results from AMP-PNP

cross-linking studies by Prodromou *et al.* (unpublished data) supports this view. It seems that to get lid closure other protein domains, particularly the middle domain, must also be present. A model based on the middle domain interacting with the γ-phosphate of ATP bound in the N-terminal domain has been proposed (Meyer *et al.,* 2003). This interaction with the ATP could potentially cause the changes in the Hsp90 N-terminal domain. However, NMR studies of interaction between the two separate domains of the N-termini and middle domain of the Hsp90 have shown no apparent interaction between the two separated domains. This could be due to an additional missing link required between the two domains for their interaction to take place.

Two $3_{.10}$ helices located right after the ATP-lid, consisting mostly of hydrophobic residues, are very important for interaction of the nucleotide phosphates with the protein. The signal for these residues (residues 114 to 120 and 123 to 129 in Figure 7.1.f) were broad and weak in the AMP-PNP bound complex compared to the apo- spectra, suggesting presence of conformational exchange for these residues or perhaps a helix-coil-helix transition.

7.5 Future Perspectives

NMR provides a detailed picture of the dynamic movements of a structure that are often vitally important to its function. Particularly important is the ability of NMR to monitor changes to structure and dynamics with changing solution conditions, particularly temperature, pH and salt concentration. One obvious benefit from understanding of the local motion of the protein secondary structures involved in nucleotide binding and the interaction of various residues with the

nucleotides is in the design of high-affinity drug compounds. Understanding this fundamental structure/function relationship is the ability to use structural information to determine the affinities and interaction of ligand with the protein. Rational drug design may achieve drugs that bind to the Hsp90 N-terminal domain that are more specific with less toxicity as a result of understanding the mechanism of protein function. The proven utility of NMR in the pharmaceutical industry for mapping ligand binding may well be extended towards screening for ligand interactions with the Hsp90 N-terminal domain.

Small molecule inhibitors of Hsp90 have been very useful in understanding Hsp90 biology and in validating this protein as a molecular target for anti-cancer drug development. The Hsp90 molecular chaperone has emerged as one of the most exciting targets for cancer drug development. Hsp90 is overexpressed in many malignancies, very likely as a result of the stress that is induced both by the hostile cancer microenvironment and also by the mutation and aberrant expression of oncoproteins. Inhibition of Hsp90 should therefore block multiple critical oncogenic pathways in the cancer cell, leading to inhibition of the hallmark traits of malignancy. This blockade of oncogenic targets should give rise to broad spectrum anti-tumour activity across multiple cancer types. Drug targeting of Hsp90 was confirmed by the discovery that the natural products geldanamycin and radicicol, which have anticancer activity, exert their biological effects by inhibiting the essential ATPase activity associated with the N-terminal domain. 17-allylamino-17-emethoxygeldanamycin (17-AAG), is a recent anticancer agent currently in clinical trials, shown to be capable of binding and disrupting the function of Hsp90. A growing understanding of the molecular, genetic and biochemical changes that occur during the process of cancer and other diseases have resulted in the focus of

drug development shifting towards therapeutics that act on specific molecular targets responsible for the malignant phenotype.

Future work could be carried out on the construct using the backbone assignment in combination with additional experiments such as usage of dipolar coupling to achieving a low-resolution solution structure of the protein. This would establish the exact conformational change in the protein structure upon nucleotide binding and possibly the difference between the structure bound to ATP and ADP in comparison to the apo- structure. Titration and binding of GM and other interacting drugs with Hsp90 could potentially provide us with additional information on the mechanism of the interaction of local structure and residues with its ligands.

APPENDIX

PUBLICATIONS ARISING FROM THIS RESEARCH

REFERENCES

Altieri, A. S., Hinton, D. P. and Byrd, R. A. (1995). Association of Biomolecular Systems via Pulsed Field Gradient NMR Self-Diffusion Measurements. *J. Am. Chem. Soc.* **117**: 7566-7567.

Ban, C. and Yang, W. (1998). Crystal structure and ATPase activity of MutL: implications for DNA repair and mutagenesis. *Cell* **95**: 541-552.

Ban, C., Junop, M. and Yang, W. (1999). Transformation of MutL by ATP binding and hydrolysis: a switch in DNA mismatch repair. *Cell* **97**: 85-97.

Bax, A. and Ikura, M. (1991). An efficient 3D NMR technique for correlating the proton and 15N backbone amide resonances with the alpha-carbon of the preceding residue in uniformly 15N/13C enriched proteins. *J Biomol NMR* **1**: 99-104.

Bax, A. (1994). Multidimensional nuclear magnetic resonance methods in protein studies. *Curr. Opin. Struct. Biol* **4**: 738-744.

Baxter, N. J. and Williamson, M. P. (1997). Temperature dependence of H^1 chemical shifts in proteins. *J. Biomol NMR* **9**: 359-369.

Bergerat, A., de Massy, B., Gadelle, D., Varoutas, P. C., Nicolas, A. and Forterre, P. (1997). An atypical topoisomerase II from Archaea with implications for meiotic recombination. *Nature* **386**: 414-417.

Beynon *et al.*, 1996. www.bi.umist.ac.uk/users/mjfrbn/buffers/makebuf.asp

Blagosklonny, M. V., Toretsky, J., Bohen, S. and Neckers, L. (1996). Mutant conformation of p53 translated in vitro or in vivo requires functional HSP90. *Proc Natl Acad Sci USA* **93**: 8379-8383.

Bodenhausen, G. and Ruben. D.J (1980). Natural abundance nitrogen-15 NMR by enhanced heteronuclear spectroscopy. *Chem Phys Lett* **69**: 185-189.

Boucher, W. (2002). AZARA version 2.7.

Brino, L., Urzhumtsev, A., Mousli, M., Bronner, C., Mitschler, A., Oudet, P. and Moras, D. (2000). Dimerization of Escherichia coli DNA-gyrase B provides a structural mechanism for activating the ATPase catalytic center. *J Biol Chem* **275**: 9468-9475.

Browne, D. T., Kenyon, G. L., Packer, E. L., Sternlicht, H. and Wilson, D. M. (1973). Studies of macromolecular structure by ^{13}C nuclear magnetic resonance. II. A specific labeling approach to the study of histidine residues in proteins. *J Am Chem Soc* **95**: 1316-1323.

Buchner, J. (1996). Supervising the fold: functional principles of molecular chaperones. *Faseb J* **10**: 10-19.

Buchner, J. (1999). Hsp90 & Co. - a holding for folding. *Trends Biochem Sci* **24**: 136-141.

Bukau, B. (1999). Molecular Chaperones and folding catalysts: Regulation, cellular function and mechanisms. Harwood Academic Publishers.

Caplan, A. J., Jackson, S. and Smith, D. (2003). Hsp90 reaches new heights. *EMBO Rep* **4**: 126-130.

Chadli, A., Ladjimi, M. M., Baulieu, E. E. and Catelli, M. G. (1999). Heat-induced oligomerization of the molecular chaperone Hsp90. Inhibition by ATP and geldanamycin and activation by transition metal oxyanions. *J Biol Chem* **274**: 4133-4139.

Chadli, A., Bouhouche, I., Sullivan, W., Stensgard, B., McMahon, N., Catelli, M. G. and Toft, D. O. (2000). Dimerization and N-terminal domain proximity underlie the function of the molecular chaperone heat shock protein 90. *Proc Natl Acad Sci USA* **97**: 12524-12529.

Chayen, N. E., Stewart, P. D. S. and Blow, D. M. (1992). Microbatch Crystallization under Oil - a New Technique Allowing Many Small-Volume Crystallization Trials. *J Cryst Growth* **122**: 176-180.

Chen, C. F., Chen, Y., Dai, K., Chen, P. L., Riley, D. J. and Lee, W. H. (1996). A new member of the hsp90 family of molecular chaperones interacts with the retinoblastoma protein during mitosis and after heat shock. *Mol Cell Biol* **16**: 4691-4699.

Chen, S. and Smith, D. F. (1998). Hop as an adaptor in the heat shock protein 70 (Hsp70) and hsp90 chaperone machinery. *J Biol Chem* **273**: 35194-35200.

Cho, C. H., Urquidi, J., Singh, S. and Robinson, G. W. (1999). Molecular-level description of temperature and pressure effects on the viscosity of water. *J Chem Phys* **111**: 10171-10176.

Cierpicki, T. and Otlewski, J. (2001). Amide proton temperature coefficients as hydrogen bond indicators in proteins. *J Biomol NMR* **21**: 249-261.

Clore, G. M. and Gronenborn, A. M. (1993). NMR of Proteins, CRC Press Inc, USA.

Clore, G. M. and Gronenborn, A. M. (1994). Multidimensional heteronuclear nuclear magnetic resonance of proteins. *Methods Enzymol* **239**: 349-363.

Clubb, R. T., Thanabal, V. and Wagner, G. (1992). A constant-time 3-dimensional triple-resonance pulse scheme to correlate intraresidue H-1(N), N-15, and C-13(') chemical shifts in N-15-C-13-labeled proteins. *J Magn Reson* **97**: 213-217.

Connell, P., Ballinger, C. A., Jiang, J., Wu, Y., Thompson, L. J., Hohfeld, J. and Patterson, C. (2001). The co-chaperone CHIP regulates protein triage decisions mediated by heat-shock proteins. *Nat Cell Biol* **3**: 93-96.

Creighton, T. E. (1992). Proteins: Structures and Molecular Properties. W. H.

Freeman Company.

Crespi, H. L., Rosenberg, R. M. and Katz, J. J. (1968). Proton magnetic resonance of proteins fully deuterated except for 1H-leucine side chains. *Science* **161**: 795-796.

Delaglio, F., Grzesiek, S., Vuister, G. W., Zhu, G., Pfeifer, J. and Bax, A. (1995). NMRPipe: a multidimensional spectral processing system based on UNIX pipes. *J Biomol NMR* **6**: 277-293.

Dingley, A. J., Mackay, J. P., Chapman, B. E., Morris, M. B., Kuchel, P. W., Hambly, B. D. and King, G. F. (1995). Measuring protein self-association using pulsed-field-gradient NMR spectroscopy: application to myosin light chain 2. *J Biomol NMR* **6**: 321-328.

Dutta, R. and Inouye, M. (2000). GHKL, an emergent ATPase/kinase superfamily. *Trends Biochem Sci* **25**: 24-28.

Felts, S. J., Owen, B. A., Nguyen, P., Trepel, J., Donner, D. B. and Toft, D. O. (2000). The hsp90-related protein TRAP1 is a mitochondrial protein with distinct functional properties. *J Biol Chem* **275**: 3305-3312.

Felts, S. J., Owen, B. A., Nguyen, P., Trepel, J., Donner, D. B. and Toft, D. O. (2000). The hsp90-related protein TRAP1 is a mitochondrial protein with distinct functional properties. J Biol Chem. **275:** 3305-3312.

Forsythe, H. L., Jarvis, J. L., Turner, J. W., Elmore, L. W. and Holt, S. E. (2001). Stable association of hsp90 and p23, but Not hsp70, with active human telomerase. *J Biol Chem* **276**: 15571-15574.

Freeman, R. (1997). A Handbook of nuclear magnetic resonance, Addison Wesley Longman Ltd, England.

Frydman, J. and Hohfeld, J. (1997). Chaperones get in touch: the Hip-Hop connection. *Trends Biochem Sci* **22**: 87-92.

Garcia-Cardena, G., Fan, R., Shah, V., Sorrentino, R., Cirino, G., Papapetropoulos, A. and Sessa, W. C. (1998). Dynamic activation of endothelial nitric oxide synthase by Hsp90. *Nature* **392**: 821-824.

Garnier, C., Lafitte, D., Tsvetkov, P. O., Barbier, P., Leclerc-Devin, J., Millot, J. M., Briand, C., Makarov, A. A., Catelli, M. G. and Peyrot, V. (2002). Binding of ATP to heat shock protein 90: evidence for an ATP-binding site in the C-terminal domain. *J Biol Chem* **277**: 12208-12214.

Gill, S. C. and von Hippel, P. H. (1989). Calculation of protein extinction coefficients from amino acid sequence data. *Anal Biochem* **182**: 319-326.

Grzesiek, S. and Bax, A. (1992a). Improved 3D triple-resonance NMR techniques applied to a 31 kDa protein. *J. Magn. Reson.* **96**: 432-440.

Grzesiek, S. and Bax, A. (1992b). An efficient experiment for sequential backbone assignment of medium sized isotopically enriched proteins. *J. Magn. Reson.* **99**: 201-207.

Grzesiek, S. and Bax, A. (1993). Amino acid type determination in the sequential assignment procedure of uniformly 13C/15N-enriched proteins. *J Biomol NMR* **3**: 185-204.

Guarne, A., Junop, M. S. and Yang, W. (2001). Structure and function of the N-terminal 40 kDa fragment of human PMS2: a monomeric GHL ATPase. *EMBO* **20**: 5521-5531.

Gupta, R. S. (1995). Phylogenetic analysis of the 90 kD heat shock family of protein sequences and an examination of the relationship among animals, plants, and fungi species. *Mol Biol Evol* **12**: 1063-1073.

Hansen, P. E. (1988). Isotope effects in nuclear shielding. *Prog. Nuc. Magn. Reson. Spetrosc.* **20**: 207-255.

Hartl, F. U. (1996). Molecular chaperones in cellular protein folding. *Nature* **381**: 571-579.

Hartson, S. D., Irwin, A. D., Shao, J., Scroggins, B. T., Volk, L., Huang, W. and Matts, R. L. (2000). p50(cdc37) is a nonexclusive Hsp90 cohort which participates intimately in Hsp90-mediated folding of immature kinase molecules. *Biochemistry* **39**: 7631-7644.

Hickey, E., Brandon, S. E., Smale, G., Lloyd, D. and Weber, L. A. (1989). Sequence and regulation of a gene encoding a human 89-kilodalton heat shock protein. *Mol Cell Biol* **9**: 2615-2626.

Hu, J., Toft, D. O. and Seeger, C. (1997). Hepadnavirus assembly and reverse transcription require a multi- component chaperone complex which is incorporated into nucleocapsids. *EMBO* **16**: 59-68.

Hu, X., Machius, M. and Yang, W. (2003). Monovalent cation dependence and preference of GHKL ATPases and kinases. *FEBS Lett* **544**: 268-273.

Ikura, M., Bax, A., Clore, G. M. and Gronenborn, A. M. (1990a). Detection of nuclear Overhauser effects between degenerate amide proton resonances by heteronuclear three-dimensional NMR spectroscopy. *J. Am. Chem. Soc.* **112**: 9020-9022.

Ikura, M., Kay, L. E. and Bax, A. (1990b). A novel approach for sequential assignment of ^{1}H, ^{13}C, and ^{15}N spectra of proteins: heteronuclear triple-resonance three-dimensional NMR spectroscopy. Application to calmodulin. *Biochemistry* **29**: 4659-4667.

Jakob, U., Lilie, H., Meyer, I. and Buchner, J. (1995). Transient interaction of Hsp90 with early unfolding intermediates of citrate synthase. Implications for heat

shock in vivo. *J Biol Chem* **270**: 7288-7294.

Jakob, U., Scheibel, T., Bose, S., Reinstein, J. and Buchner, J. (1996). Assessment of the ATP binding properties of Hsp90. *J Biol Chem* **271**: 10035-10041.

Johnson, B. D., Schumacher, R. J., Ross, E. D. and Toft, D. O. (1998). Hop modulates Hsp70/Hsp90 interactions in protein folding. *J Biol Chem* **273**: 3679-3686.

Johnson, B. D., Chadli, A., Felts, S. J., Bouhouche, I., Catelli, M. G. and Toft, D. O. (2000). Hsp90 Chaperone Activity Requires the Full-length Protein and Interaction Among Its Multiple Domains. *J Biol Chem.* **275:** 32499-32507

Kadkhodaei, M., Hwang, T. L., Tang, J. and Shaka, A. J. (1993). A Simple Windowless Mixing Sequence to Suppress Cross Relaxation in TOCSY Experiments,. *J Magn. Reson.* **105**: 104-107.

Kalbitzer, H. R., Leberman, R. and Wittinghoher, A. (1985). ^{1}H-NMR spectroscopy on elongation factor Tu from Escherichia coli. Resolution enhancement by perdeuteration. *FEBS Lett* **180**: 40-48.

Katz, J. J. and Crespi, H. L. (1966). Deuterated organisms: cultivation and uses. *Science* **151**: 1187-1194.

Kay, L. E., Ikura, M., Tschudin, R. and Bax, A. (1989a). Three-dimensional triple resonance NMR spectroscopy of isotopically enriched proteins. *J. Magn. Reson.* **89**: 496-514.

Kay, L. E., Torchia, D. A. and Bax, A. (1989b). Backbone dynamics of proteins as studied by 15N inverse detected heteronuclear NMR spectroscopy: application to staphylococcal nuclease. *Biochemistry* **28**: 8972-8979.

Kay, L. E., Ikura, M., Tschudin, R. and Bax, A. (1990). 3-Dimensional Triple-Resonance NMR-Spectroscopy of Isotopically Enriched Proteins. *J Magn. Reson.* **89**: 496-514.

Kimura, Y., Rutherford, S. L., Miyata, Y., Yahara, I., Freeman, B. C., Yue, L., Morimoto, R. I. and Lindquist, S. (1997). Cdc37 is a molecular chaperone with specific functions in signal transduction. *Genes Dev* **11**: 1775-1785.

Kraulis, P. J. (1989). ANSIG: A Program for the assignment of protein ^{1}H 2D NMR spectra by interactive graphics. *J. Magn. Reson.* **84**: 627-633.

Krone, P. H. and Sass, J. B. (1994). HSP 90 alpha and HSP 90 beta genes are present in the zebrafish and are differentially regulated in developing embryos. *Biochem Biophys Res Commun* **204**: 746-752.

Langer, T., Schlatter, H. and Fasold, H. (2002). Evidence that the novobiocin-sensitive ATP-binding site of the heat shock protein 90 (hsp90) is necessary for its

autophosphorylation. *Cell Biol Int* **26**: 653-657.

Laskey, R. A., Honda, B. M., Mills, A. D. and Finch, J. T. (1978). Nucleosomes are assembled by an acidic protein which binds histones and transfers them to DNA. *Nature* **275**: 416-420.

LeMaster, D. M. and Richards, F. M. (1988). NMR sequential assignment of Escherichia coli thioredoxin utilizing random fractional deuteriation. *Biochem* **27**: 142-150.

Lewis, J., Devin, A., Miller, A., Lin, Y., Rodriguez, Y., Neckers, L. and Liu, Z. G. (2000). Disruption of hsp90 function results in degradation of the death domain kinase, receptor-interacting protein (RIP), and blockage of tumor necrosis factor-induced nuclear factor-kappaB activation. *J Biol Chem* **275**: 10519-10526.

Lipari, G. and Szabo, A. (1982a). Model-free approach to the interpretation of nuclear magnetic resonance relaxation in macromolecules. 1. Theory and range of validity. *J. Am. Chem. Soc.* **104**: 4546-4559.

Lipari, G. and Szabo, A. (1982b). Model-free approach to the interpretation of nuclear magnetic resonance relaxation in macromolecules. 2. Analysis of experimental results. *J. Am. Chem. Soc.* **104**: 4559-4570.

Lotz, G. P., Lin, H., Harst, A. and Obermann, W. M. (2003). Aha1 binds to the middle domain of Hsp90, contributes to client protein activation, and stimulates the ATPase activity of the molecular chaperone. *J Biol Chem* **278**: 17228-17235.

Machius, M., Chuang, J. L., Wynn, R. M., Tomchick, D. R. and Chuang, D. T. (2001). Structure of rat BCKD kinase: nucleotide-induced domain communication in a mitochondrial protein kinase. *Proc Natl Acad Sci USA* **98**: 11218-11223.

Mandel, A. M., Akke, M. and Palmer, A. G., 3rd (1996). Dynamics of ribonuclease H: temperature dependence of motions on multiple time scales. *Biochemistry* **35**: 16009-16023.

Marcu, M. G., Chadli, A., Bouhouche, I., Catelli, M. and Neckers, L. M. (2000). The heat shock protein 90 antagonist novobiocin interacts with a previously unrecognized ATP-binding domain in the carboxyl terminus of the chaperone. *J Biol Chem* **275**: 37181-37186.

Markley, J. L., Putter, I. and Jardetzky, O. (1968). High-resolution nuclear magnetic resonance spectra of selectively deuterated staphylococcal nuclease. *Science* **161**: 1249-1251.

Markus, M. A., Dayie, K. T., Matsudaira, P. and Wagner, G. (1994). Effect of Deuteration on the Amide Proton Relaxation Rates in Proteins. *J Magn. Reson.* **105**: 192-195.

Maruya, M., Sameshima, M., Nemoto, T. and Yahara, I. (1999). Monomer arrangement in HSP90 dimer as determined by decoration with N and C-terminal

region specific antibodies. *J Mol Biol* **285**: 903-907.

Matsuo, H., Li, H. and Wagner, G. (1996). A Sensitive HN(CA)CO Experiment for Deuterated Proteins. *J Magn. Reson.* **110**: 112-115.

Mayer, M. P. and Bukau, B. (1999). Molecular chaperones: the busy life of Hsp90. *Curr Biol* **9**: R322-325.

McLaughlin, S. H., Smith, H. W. and Jackson, S. E. (2002). Stimulation of the weak ATPase activity of human hsp90 by a client protein. *J Mol Biol* **315**: 787-798.

Meyer, P., Prodromou, C., Hu, B., Vaughan, C., Roe, S. M., Panaretou, B., Piper, P. W. and Pearl, L. H. (2003). Structural and functional analysis of the middle segment of hsp90: implications for ATP hydrolysis and client protein and cochaperone interactions. *Mol Cell* **11**: 647-658.

Muhandiram, D. R., and Kay, L. E. (1994). Gradient-Enhanced Triple-Resonance Three-Dimensional NMR Experiments with Improved Sensitivity. *J Magn. Reson.* **103**: 203-216.

Ohnishi, M. and Urry, D. W. (1969). Temperature dependence of amide proton chemical shifts: the secondary structures of gramicidin S and valinomycin. *Biochem Biophys Res Commun* **36**: 194-202.

Panaretou, B., Prodromou, C., Roe, S. M., O'Brien, R., Ladbury, J. E., Piper, P. W. and Pearl, L. H. (1998). ATP binding and hydrolysis are essential to the function of the Hsp90 molecular chaperone in vivo. *EMBO* **17**: 4829-4836.

Peng, J. W. and Wagner, G. (1994). Investigation of protein motions via relaxation measurements. *Methods Enzymol* **239**: 563-596.

Pfuhl, M., Chen, H. A., Kristensen, S. M. and Driscoll, P. C. (1999). NMR exchange broadening arising from specific low affinity protein self-association: analysis of nitrogen-15 nuclear relaxation for rat CD2 domain 1. *J Biomol NMR* **14**: 307-320.

Pratt, W. B. and Toft, D. O. (1997). Steroid receptor interactions with heat shock protein and immunophilin chaperones. *Endocr Rev* **18**: 306-360.

Pratt, W. B. and Toft, D. O. (2003). Regulation of signalling protein function and trafficking by the hsp90/hsp70-based chaperone machinery. *Exp Biol Med* **228**: 111-133.

Prodromou, C., Piper, P. W. and Pearl, L. H. (1996). Expression and crystallization of the yeast Hsp82 chaperone, and preliminary X-ray diffraction studies of the amino-terminal domain. *Proteins* **25**: 517-522.

Prodromou, C., Roe, S. M., O'Brien, R., Ladbury, J. E., Piper, P. W. and Pearl, L. H. (1997). Identification and structural characterization of the ATP/ADP-binding site in the Hsp90 molecular chaperone. *Cell* **90**: 65-75.

Prodromou, C., Panaretou, B., Chohan, S., Siligardi, G., O'Brien, R., Ladbury, J. E., Roe, S. M., Piper, P. W. and Pearl, L. H. (2000). The ATPase cycle of Hsp90 drives a molecular 'clamp' via transient dimerization of the N-terminal domains. *EMBO* **19**: 4383-4392.

Prodromou, C. and L. H. Pearl (2003). Structure and functional relationships of Hsp90. *Curr Cancer Drug Targets* **3**(5): 301-23.

Queitsch, C., Sangster, T. A. and Lindquist, S. (2002). Hsp90 as a capacitor of phenotypic variation. *Nature* **417**: 618-624.

Richter, K., Reinstein, J. and Buchner, J. (2002). N-terminal residues regulate the catalytic efficiency of the Hsp90 ATPase cycle. *J Biol Chem* **277**: 44905-44910.

Richter, K., Muschler, P., Hainzl, O., Reinstein, J. and Buchner, J. (2003). Sti1 is a non-competitive inhibitor of the Hsp90 ATPase. Binding prevents the N-terminal dimerization reaction during the atpase cycle. *J Biol Chem* **278**: 10328-10333.

Roe, S. M., Prodromou, C., O'Brien, R., Ladbury, J. E., Piper, P. W. and Pearl, L. H. (1999). Structural basis for inhibition of the Hsp90 molecular chaperone by the antitumor antibiotics radicicol and geldanamycin. *J Med Chem* **42**: 260-266.

Rutherford, S. L. and Lindquist, S. (1998). Hsp90 as a capacitor for morphological evolution. *Nature* **396**: 336-342.

Schagger, H. and von Jagow, G. (1987). Tricine-sodium dodecyl sulfate-polyacrylamide gel electrophoresis for the separation of proteins in the range from 1 to 100 kDa. *Anal. Biochem.* **166**: 368-379.

Scheibel, T., Neuhofen, S., Weikl, T., Mayr, C., Reinstein, J., Vogel, P. D. and Buchner, J. (1997). ATP-binding properties of human Hsp90. *J Biol Chem* **272**: 18608-18613.

Scheibel, T., Weikl, T. and Buchner, J. (1998). Two chaperone sites in Hsp90 differing in substrate specificity and ATP dependence. *Proc Natl Acad Sci U S A* **95**: 1495-1499.

Scheibel, T., Siegmund, H. I., Jaenicke, R., Ganz, P., Lilie, H. and Buchner, J. (1999). The charged region of Hsp90 modulates the function of the N-terminal domain. *Proc Natl Acad Sci USA* **96**: 1297-1302.

Schnaider, T., Oikarinen, J., Ishiwatari-Hayasaka, H., Yahara, I. and Csermely, P. (1999). Interactions of Hsp90 with histones and related peptides. *Life Sci* **65**: 2417-2426.

Shao, W., S. C., Zuiderweg ER, Waskell L. (2003). Mapping the binding interface of the cytochrome b5-cytochrome c complex by nuclear magnetic resonance. *Biochemistry* 42(50): 14774-84

Silverstein, A. M., Grammatikakis, N., Cochran, B. H., Chinkers, M. and Pratt, W.

B. (1998). p50(cdc37) binds directly to the catalytic domain of Raf as well as to a site on hsp90 that is topologically adjacent to the tetratricopeptide repeat binding site. *J Biol Chem* **273**: 20090-20095.

Smith, D. F. (1993). Dynamics of heat shock protein 90-progesterone receptor binding and the disactivation loop model for steroid receptor complexes. *Mol Endocrinol* **7**: 1418-1429.

Song, H. Y., Dunbar, J. D., Zhang, Y. X., Guo, D. and Donner, D. B. (1995). Identification of a protein with homology to hsp90 that binds the type 1 tumor necrosis factor receptor. *J Biol Chem* **270**: 3574-3581.

Soti, C., Vermes, A., Haystead, T. A. and Csermely, P. (2003). Comparative analysis of the ATP-binding sites of Hsp90 by nucleotide affinity cleavage: a distinct nucleotide specificity of the C-terminal ATP-binding site. *Eur J Biochem* **270**: 2421-2428.

Spence, J., Cegielska, A. and Georgopoulos, C. (1990). Role of Escherichia coli heat shock proteins DnaK and HtpG (C62.5) in response to nutritional deprivation. *J Bacteriol* **172**: 7157-7166.

Stebbins, C. E., Russo, A. A., Schneider, C., Rosen, N., Hartl, F. U. and Pavletich, N. P. (1997). Crystal structure of an Hsp90-geldanamycin complex: targeting of a protein chaperone by an antitumor agent. *Cell* **89**: 239-250.

Stone, M. J., Chandrasekhar, K., Holmgren, A., Wright, P. E. and Dyson, H. J. (1993). Comparison of backbone and tryptophan side-chain dynamics of reduced and oxidized Escherichia coli thioredoxin using ^{15}N NMR relaxation measurements. *Biochemistry* **32**: 426-435.

Sullivan, W., Stensgard, B., Caucutt, G., Bartha, B., McMahon, N., Alnemri, E. S., Litwack, G. and Toft, D. (1997). Nucleotides and two functional states of hsp90. *J Biol Chem* **272**: 8007-8012.

Sullivan, W. P., Owen, B. A. and Toft, D. O. (2002). The influence of ATP and p23 on the conformation of Hsp90. *J Biol Chem* **277**: 45942-45948.

Tjandra, N., Feller, S. E., Pastor, R. W. and Bax, A. (1995). Rotational diffusion anisotropy of human ubiquitin from ^{15}N NMR relaxation. *J. Am. Chem. Soc.* **117**: 12562-12566.

Venters, R. A., Farmer, B. T., 2nd, Fierke, C. A. and Spicer, L. D. (1996). Characterizing the use of perdeuteration in NMR studies of large proteins: ^{13}C, ^{15}N and ^{1}H assignments of human carbonic anhydrase II. *J Mol Biol* **264**: 1101-1116.

Vuister, G. W. and Bax, A. (1992). Resolution Enhancement and Spectral Editing of Uniformly C-13- Enriched Proteins by Homonuclear Broad-Band C-13 Decoupling. *J Magn. Reson.* **98**: 428-435.

Weikl, T., Muschler, P., Richter, K., Veit, T., Reinstein, J. and Buchner, J. (2000).

C-terminal regions of Hsp90 are important for trapping the nucleotide during the ATPase cycle. *J Mol Biol* **303**: 583-592.

Welch, W. J. and Feramisco, J. R. (1982). Purification of the major mammalian heat shock proteins. *J Biol Chem* **257**: 14949-14959.

Wigley, D. B., Davies, G. J., Dodson, E. J., Maxwell, A. and Dodson, G. (1991). Crystal structure of an N-terminal fragment of the DNA gyrase B protein. *Nature* **351**: 624-629.

Wishart, D. S. and Sykes, B. D. (1994). The 13C chemical-shift index: a simple method for the identification of protein secondary structure using ^{13}C chemical-shift data. *J Biomol NMR* **4**: 171-180.

Wishart, D. S., Bigam, C. G., Yao, J., Abildgaard, F., Dyson, H. J., Oldfield, E., Markley, J. L. and Sykes, B. D. (1995). 1H, 13C and 15N chemical shift referencing in biomolecular NMR. *J Biomol NMR* **6**: 135-140.

Wolfram, S. (2002). Mathematica.

Yamazaki, T., Lee, W., Revington, M., Mattiello, D. L., Dahlquist, F. W., Arrowsmith, C. H. and Kay, L. E. (1994a). An HNCA Pulse Scheme for the Backbone Assignment of ^{15}N,^{13}C,^{2}H-Labeled Proteins: Application to a 37-kDa Trp Repressor-DNA Complex. *J. Am. Chem. Soc* **116**: 6464-6465.

Yamazaki, T., Lee, W., Arrowsmith, C. H. and Muhandiram, D. R., and Kay, L. E. (1994b). A Suite of Triple Resonance NMR Experiments for the Backbone Assignment of ^{15}N, ^{13}C, ^{2}H Labelled Proteins with High Sensitivity. *J. Am. Chem. Soc.* **116**: 11655-11666.

Yonehara, M., Minami, Y., Kawata, Y., Nagai, J. and Yahara, I. (1996). Heat-induced chaperone activity of Hsp90. *J Biol Chem* **271**: 2641-2645.

Young, J. C., Obermann, W. M. and Hartl, F. U. (1998). Specific binding of tetratricopeptide repeat proteins to the C-terminal 12-kDa domain of Hsp90. *J Biol Chem* **273**: 18007-18010.

Zhang, O., Kay, L. E., Olivier, J. P. and Forman-Kay, J. D. (1994). Backbone ^{1}H and ^{15}N resonance assignments of the N-terminal SH3 domain of drk in folded and unfolded states using enhanced-sensitivity pulsed field gradient NMR techniques. *J Biomol NMR* **4**: 845-858.

Zhu, G. and Bax, A. (1990). Improved linear prediction for truncated signals of known phase. *J. Magn. Reson.* **90**: 405-410.

Zou, J., Guo, Y., Guettouche, T., Smith, D. F. and Voellmy, R. (1998). Repression of heat shock transcription factor HSF1 activation by Hsp90 (Hsp90 complex) that forms a stress-sensitive complex with HSF1. *Cell* **94**: 471-480.